Natural Hazards and Risk Challenges to Civil Engineering 2020

Lead Guest Editor: Hugo Rodrigues
Guest Editors: Lars Abrahamczyk, André Barbosa, Haiyun Shi, and Tiago Ferreira

Natural Hazards and Risk Challenges to Civil Engineering 2020

Natural Hazards and Risk Challenges to Civil Engineering 2020

Lead Guest Editor: Hugo Rodrigues
Guest Editors: Lars Abrahamczyk, André Barbosa, Haiyun Shi, and Tiago Ferreira

Zhaofei Chu (iD), China
Wonseok Chung (iD), Republic of Korea
Donato Ciampa (iD), Italy
Gian Paolo Cimellaro, Italy
Francesco Colangelo, Italy
Romulus Costache (iD), Romania
Liviu-Adrian Cotfas (iD), Romania
Antonio Maria D'Altri, Italy
Bruno Dal Lago (iD), Italy
Amos Darko (iD), Hong Kong
Arka Jyoti Das (iD), India
Dario De Domenico (iD), Italy
Gianmarco De Felice (iD), Italy
Stefano De Miranda (iD), Italy
Maria T. De Risi (iD), Italy
Tayfun Dede, Turkey
Sadik O. Degertekin (iD), Turkey
Camelia Delcea (iD), Romania
Cristoforo Demartino, China
Giuseppe Di Filippo (iD), Italy
Luigi Di Sarno, Italy
Fabio Di Trapani (iD), Italy
Aboelkasim Diab (iD), Egypt
Thi My Dung Do, Vietnam
Giulio Dondi (iD), Italy
Jiangfeng Dong (iD), China
Chao Dou (iD), China
Mario D'Aniello (iD), Italy
Jingtao Du (iD), China
Ahmed Elghazouli, United Kingdom
Francesco Fabbrocino (iD), Italy
Flora Faleschini (iD), Italy
Dingqiang Fan, Hong Kong
Xueping Fan, China
Qian Fang (iD), China
Salar Farahmand-Tabar (iD), Iran
Ilenia Farina, Italy
Roberto Fedele, Italy
Guang-Liang Feng (iD), China
Luigi Fenu (iD), Italy
Tiago Ferreira (iD), Portugal
Marco Filippo Ferrotto, Italy
Antonio Formisano (iD), Italy
Guoyang Fu, Australia
Stefano Galassi (iD), Italy

Junfeng Gao (iD), China
Meng Gao (iD), China
Giovanni Garcea (iD), Italy
Enrique García-Macías, Spain
Emilio García-Taengua (iD), United Kingdom
DongDong Ge (iD), USA
Khaled Ghaedi, Malaysia
Khaled Ghaedi (iD), Malaysia
Gian Felice Giaccu, Italy
Agathoklis Giaralis (iD), United Kingdom
Ravindran Gobinath, India
Rodrigo Gonçalves, Portugal
Peilin Gong (iD), China
Belén González-Fonteboa (iD), Spain
Salvatore Grasso (iD), Italy
Fan Gu, USA
Erhan Güneyisi (iD), Turkey
Esra Mete Güneyisi, Turkey
Pingye Guo (iD), China
Ankit Gupta (iD), India
Federico Gusella (iD), Italy
Kemal Hacıefendioğlu, Turkey
Jianyong Han (iD), China
Song Han (iD), China
Asad Hanif (iD), Macau
Hadi Hasanzadehshooiili (iD), Canada
Mostafa Fahmi Hassanein, Egypt
Amir Ahmad Hedayat (iD), Iran
Khandaker Hossain (iD), Canada
Zahid Hossain (iD), USA
Chao Hou, China
Biao Hu, China
Jiang Hu (iD), China
Xiaodong Hu, China
Lei Huang (iD), China
Cun Hui (iD), China
Bon-Gang Hwang, Singapore
Jijo James (iD), India
Abbas Fadhil Jasim (iD), Iraq
Ahad Javanmardi (iD), China
Krishnan Prabhakan Jaya, India
Dong-Sheng Jeng (iD), Australia
Han-Yong Jeon, Republic of Korea
Pengjiao Jia, China
Shaohua Jiang (iD), China

Chayut Ngamkhanong (iD), Thailand
Trung Ngo, Australia
Tengfei Nian, China
Mehdi Nikoo (iD), Canada
Youjun Ning (iD), China
Olugbenga Timo Oladinrin (iD), United
Kingdom
Oladimeji Benedict Olalusi, South Africa
Timothy O. Olawumi (iD), Hong Kong
Alejandro Orfila (iD), Spain
Maurizio Orlando (iD), Italy
Siti Aminah Osman, Malaysia
Walid Oueslati (iD), Tunisia
SUVASH PAUL (iD), Bangladesh
John-Paris Pantouvakis (iD), Greece
Fabrizio Paolacci (iD), Italy
Giuseppina Pappalardo (iD), Italy
Fulvio Parisi (iD), Italy
Dimitrios G. Pavlou (iD), Norway
Daniele Pellegrini (iD), Italy
Gatheeshgar Perampalam (iD), United
Kingdom
Daniele Perrone (iD), Italy
Giuseppe Piccardo (iD), Italy
Vagelis Plevris (iD), Qatar
Andrea Pranno (iD), Italy
Adolfo Preciado (iD), Mexico
Chongchong Qi (iD), China
Yu Qian, USA
Ying Qin (iD), China
Giuseppe Quaranta (iD), Italy
Krishanu ROY (iD), New Zealand
Vlastimir Radonjanin, Serbia
Carlo Rainieri (iD), Italy
Rahul V. Ralegaonkar, India
Raizal Saifulnaz Muhammad Rashid,
Malaysia
Alessandro Rasulo (iD), Italy
Chonghong Ren (iD), China
Qing-Xin Ren, China
Dimitris Rizos (iD), USA
Geoffrey W. Rodgers (iD), New Zealand
Pier Paolo Rossi, Italy
Nicola Ruggieri (iD), Italy
JUNLONG SHANG, Singapore

Nikhil Saboo, India
Anna Saetta, Italy
Juan Sagaseta (iD), United Kingdom
Timo Saksala, Finland
Mostafa Salari, Canada
Ginevra Salerno (iD), Italy
Evangelos J. Sapountzakis (iD), Greece
Vassilis Sarhosis (iD), United Kingdom
Navaratnarajah Sathiparan (iD), Sri Lanka
Fabrizio Scozzese (iD), Italy
Halil Sezen (iD), USA
Payam Shafigh (iD), Malaysia
M. Shahria Alam, Canada
Yi Shan, China
Hussein Sharaf, Iraq
Mostafa Sharifzadeh, Australia
Sanjay Kumar Shukla, Australia
Amir Si Larbi (iD), France
Okan Sirin (iD), Qatar
Piotr Smarzewski (iD), Poland
Francesca Sollecito (iD), Italy
Rui Song (iD), China
Tian-Yi Song, Australia
Flavio Stochino (iD), Italy
Mayank Sukhija (iD), USA
Piti Sukontasukkul (iD), Thailand
Jianping Sun, Singapore
Xiao Sun (iD), China
T. Tafsirojjaman (iD), Australia
Fujiao Tang (iD), China
Patrick W.C. Tang (iD), Australia
Zhi Cheng Tang (iD), China
Weerachart Tangchirapat (iD), Thailand
Xiaxin Tao, China
Piergiorgio Tataranni (iD), Italy
Elisabete Teixeira (iD), Portugal
Jorge Iván Tobón (iD), Colombia
Jing-Zhong Tong, China
Francesco Trentadue (iD), Italy
Antonello Troncone, Italy
Majbah Uddin (iD), USA
Tariq Umar (iD), United Kingdom
Muahmmad Usman, United Kingdom
Muhammad Usman (iD), Pakistan
Mucteba Uysal (iD), Turkey

Ilaria Venanzi, Italy
Castorina S. Vieira, Portugal
Valeria Vignali, Italy
Claudia Vitone, Italy
Liwei WEN, China
Chunfeng Wan, China
Hua-Ping Wan, China
Roman Wan-Wendner, Austria
Chaohui Wang, China
Hao Wang, USA
Shiming Wang, China
Wayne Yu Wang, United Kingdom
Wen-Da Wang, China
Xing Wang, China
Xiuling Wang, China
Zhenjun Wang, China
Xin-Jiang Wei, China
Tao Wen, China
Weiping Wen, China
Lei Weng, China
Chao Wu, United Kingdom
Jiangyu Wu, China
Wangjie Wu, China
Wenbing Wu, China
Zhixing Xiao, China
Gang Xu, China
Jian Xu, China
Panpan, China
Rongchao Xu, China
HE YONGLIANG, China
Michael Yam, Hong Kong
Hailu Yang, China
Xu-Xu Yang, China
Hui Yao, China
Xinyu Ye, China
Zhoujing Ye, China
Gürol Yildirim, Turkey
Dawei Yin, China
Doo-Yeol Yoo, Republic of Korea
Zhanping You, USA
Afshar A. Yousefi, Iran
Xinbao Yu, USA
Dongdong Yuan, China
Geun Y. Yun, Republic of Korea

Hyun-Do Yun, Republic of Korea
Cemal YİĞİT, Turkey
Paolo Zampieri, Italy
Giulio Zani, Italy
Mariano Angelo Zanini, Italy
Zhixiong Zeng, Hong Kong
Mustafa Zeybek, Turkey
Henglong Zhang, China
Jiupeng Zhang, China
Tingting Zhang, China
Zengping Zhang, China
Zetian Zhang, China
Zhigang Zhang, China
Zhipeng Zhao, Japan
Jun Zhao, China
Annan Zhou, Australia
Jia-wen Zhou, China
Hai-Tao Zhu, China
Peng Zhu, China
QuanJie Zhu, China
Wenjun Zhu, China
Marco Zucca, Italy
Haoran Zuo, Australia
Junqing Zuo, China
Robert Černý, Czech Republic
Süleyman İpek, Turkey

Contents

Research Article

Forecasting of Hazard Zone due to Storm Surge Using SIND Model

Dong Hyun Kim ⬤**, Hyung Ju Yoo, and Seung Oh Lee** ⬤

Department of Civil Engineering, Hongik University, Seoul 04066, Republic of Korea

Correspondence should be addressed to Seung Oh Lee; seungoh.lee@gmail.com

We have developed the SIND (scientific interpolation for natural disasters) model to forecast natural hazard zone for storm surge. Most previous studies have been conducted to predict hazard zone with numerical simulations based on various scenarios. It is hard to predict hazard zone for all scenarios and to respond immediately because most numerical models are requested a long simulation time and complicated postprocess, especially in coastal engineering. Thus, in this study, the SIND model was developed to overcome these limitations. The principal developing methods are the scientific interpolation for risk grades and trial and error for parameters embedded in the governing equation. Even designed with hatch files, applying disaster characteristics such as the risk propagation, the governing equation for storm surge in coastal lines was induced from the mathematical solver, COMSOL Multiphysics software that solves partial differential equations for multiple physics using FEM method. The verification process was performed through comparison with the official reference, and the accuracy was calculated with a shape similarity indicating the geometric similarity of the hazard zone. It was composed of position, shape, and area criteria. The accuracy of about 80% in terms of shape similarity was archived. The strength of the model is high accuracy and fast calculation time. It took only less than few seconds to create a hazard map for each scenario. As future works, if the characteristics of other disasters would be understood well, it would be able to present risk propagation induced from each natural disaster in a short term, which should help the decision making for EAP.

1. Introduction

With the increasing extreme disasters including drought, heavy rain as well as ground heat, the ability to predict hazardous area affected by them has become more important. In the case of urban areas, man-made spaces were built such as impervious and underground spaces. These resulted in increasing the damage by natural disaster. Thus, many research studies have been carried out to respond to these extreme climate changes. Disaster measures to prevent extreme climate change can be divided into structural and nonstructural measures. In particular, the nonstructural measures generally include estimating the range or degree of each damage under various scenarios. Among them, a scenario-based hazard map is mainly made by governments and local public institutions to inform hazardous area to the residents.

In Korea, recently nonstructural measures have been taken to prevent natural disasters since there are many restrictions on structural measures such as land use, environmental effect, and so on. From the past, studies on countermeasures have been carried out, and the process of disaster damage to the area has been suggested by Cutter [1] and Lindell and Prater [2]. In Korea, the National Institute for Disaster Prevention [3] conducted a study on regional risk assessment and application for disaster management. The Seoul Institute [4] developed evaluation methods to prevent urban disasters in Seoul, Korea. Regarding coastal disasters, many countries have developed autonomously flood forecasting and disaster planning techniques to predict and respond to disasters. The NOAA (National Oceanic and Atmospheric Administration) is building a forecasting system for monitoring and supervising storm surges and tsunamis. In the United States Army Corps of Engineers, the

White Paper on Estimating Hurricane Inundation Probability (Hurricane Inundation Probability) is used to describe the storm events, the empirical simulation method, the empirical track model, and so on. In Japan, the Meteorological Agency has been building a remote magnetic detection device update and forecasting system to quickly and accurately grasp tsunami. It is constantly monitoring tsunami and storm surge throughout many countries. In addition, the local government area focusing on public relations by creating a coastal hazard map indicates areas and evacuation routes according to the intensity of typhoons. Meanwhile, numerical simulation has been the most essential element for making such hazard map.

It has been actively carried out on past disasters and virtual disaster scenarios in order to produce a hazard map. Scenarios of coastal disasters involve earthquakes and typhoons. However, since it is difficult to predict earthquakes and typhoons, most scenarios for the global scale are constructed based on past cases. It is not realistic to consider all parameters of typhoon which occurred in the global scale. It is not realistic to consider all parameters of typhoon which occurred in the global scale because of the diversity of sizes and routes of typhoons and the lack of numerical simulation capability and DB. Thus, the studies related to numerical simulations have been carried out continuously for forecasting risk. To forecast the inundation caused by the storm surge, it is important to calculate the initial wave height. The initial tidal-wave computation studies began in the mid-1990s, with brief empirical formulas based on observations (Conner et al. [5]; Harris [6]) or interpretations applied to simple waters (Proudman [7]; Doodson [8]; Heaps [9]). The development of high-performance computers could lead to numerical calculations of the governing equations in the 1960s, followed by a more detailed three-dimensional numerical model. Since the mid-1970s, numerical analysis on the theory and mechanism of storm surge have progressed in earnest, and simulation studies about spatial and temporal sea surface changes have begun (Simpson and Riehl [10]; Murty [11]; Pugh [12]). And the interpretation of sea level fluctuations requires an understanding of the action of complex oceanic elements such as tides, waves, oceanic winds, and sea surface pressure, and the importance of nonlinearity in relation to each element has been proposed by many researchers (Heaps [13]; Wolf et al. [14]; Tolman, [15]; Mastenbroek et al. [16]). The numerical simulations considering the interaction between the wave model and the storm surge model have been carried out in Li and Zhang [17] and Ozer et al. [18]. In addition, Peng et al. [19] analyzed the characteristics of storm surge and inundation according to changes of central air pressure, wind speed, and moving speed of each route after selecting 10 virtual storms in North Carolina Sea. There are various factors to define or simulate the inundation due to even single a storm surge. It is practically impossible to consider all of them, and also it heavily depends on the numerical simulation technique with various assumptions and boundary conditions.

On the other hand, in the step of disaster response, it is very important to simulate and analyze the initial wave height for making the hazard map. For this purpose, several considerations should be realized and computed in the numerical model such as the complexity of tidal, storm surge, and high waves, the effect of bottom friction in coastal submergence, and the smooth moving boundary layer calculation technique. There have been many cases related to flooding in coastal areas due to boundary and initial conditions on the outer seaside (Bates and De Roo [20]; Nicholls [21]; Brown [22]; Purvis et al. [23]). However, these models have many restrictions such as the calculation time with respect to corresponding accuracy. It is difficult to estimate the damage scenarios that do not exist and to forecast in a short time because the simulation time of most disaster prediction programs takes a long time. Brown [22] applied a rule-based method based on the geographic information system to derive future hazard areas due to large-scale climate change. The rule-based method enables rapid flood risk assessment compared with the hydrodynamic model. It could not consider the hydrodynamical effects such as storm surge. Therefore, in this study, we propose a methodology to produce hazard map of storm surge by the interpolation method using hazard map based on the hydrodynamic model.

In the field of weather and climate forecasting, the interpolation method has been traditionally used to estimate data for unmeasurable areas using statistical techniques such as spatial interpolation. It is meaningful in that it can provide a very good alternative method for estimating local phenomena with a small number of observational samples. However, it has a limitation that depends only on the number or values of available observed data. Many studies have been conducted to reduce the uncertainty and increase the accuracy of their estimations by using additional data that can reflect natural and physical characteristics to supplement these limitations (Yim and Lee [24]).

For instance, representative results of cokriging, when utilizing the altitude above sea level related to temperature, are compared with the estimation results of kriging, a traditional spatial interpolation method. Ishida and Kawashima [25] compared results from the cokriging method with the estimations of the kriging method in terms of the elevation above sea level which is a geographical climate factor highly related to temperature. Finally, it was found that the estimation results of the cokriging showed higher accuracy.

Fitria [26] used the interpolation method to analyze the spatial distribution of inundation according to initial tsunami heights. Several researchers also developed the interpolation techniques to determine the tsunami hazard zones (Islam et al. [27]; Maemunah et al. [28]; Fitria [26]). These researches also applied geostatistical approach through spatial interpolation with the kriging method. Fauzi and Mayasari [29] designed a tsunami hazard zone based on land use, slope, and distance from the shoreline using spatial modelling with GIS via the ordinary kriging method. However, the verification of the kriging model by the interpolation method was practically difficult, and there was a limit that the accuracy of such model cannot be evaluated.

Therefore, in this study, a model was developed using the interpolation method, and a shape similarity was introduced to quantitatively verify it. It was estimated for accuracy by

verifying the official hazard map and added physical meaning to the model by using additional data such as the characteristics of storm surge and the topography of the study area. Using this model, hazardous areas and risks are provided in a short time according to user-defined conditions so that a disaster situation can be determined as much as precisely for decision or policy maker.

2. Methodology

2.1. Scientific Interpolation and SIND Model. The SIND model was developed by using the interpolation method with the governing equation expressed by a partial differential equation (PDE). Interpolation is widely used in the various fields of mathematics, economics, medicine, meteorology, and engineering. For example, it is used to perform surface modelling or numerical topography modelling and to express linearly new data points. It has been used to understand the spatial structure of the target object and to design artificial organs which implanted in the human body. Also, it is known to simulate operation plan in the medical field (Lee [30]). The method from this study calculates new data with old data such as observation data and field measurements after establishing physical understanding, which is why we used "scientific" interpolation method. In detail, there are 3 reasons to explain that the "scientific" interpolation method was used in this study. First, the governing equation is not a simple PDE for a linear interpolation. It implies the meaning of risk transfer, of which form is similar to the heat transfer equation. Next, the transfer of risk grade depends on the topographical characteristics in the research area, which are embedded in the risk transfer equation. Finally, the input and boundary conditions are also defined by reflecting the physical characteristics of the storm surge after risk analysis was performed.

There are 3 steps to develop the SIND model as presented in Figure 1. First, the analysis of the hazard map is required to extract the main factor for each disaster. For storm surges, the hazard map was made by the government (MLTMA [32]) along the coastal line in Korea. However, they have only 4 hazard maps of each condition. This means that it could not predict the risk except the 4 wave height conditions. Next, the governing equation was derived using the hazard maps, and coefficients of the equation were decided by the trial and error method. Thus, this new prediction model for natural disaster can estimate the damage due to disaster with all conditions. Finally, it was verified by shape similarity and mounted on the disaster prediction system (see Figure 1). Since this equation is based on a database, the more reference data are accumulated, more accurate equation we can get. The component of the model was divided into "Activation Conditions" and "Usage Conditions." Each solver is performed based on these conditions. The users selected the degree or characteristics of disaster they want at the "Activation Conditions" (see Figure 1).

For a storm surge, the users can input conditions such as typhoon route, wind strength, and typhoon intensity, which are already selected by users as primary input variables. If they would set these conditions, the model would start to search the prebuilt database to check if there is the same condition of the data that they want. If not, the governing equation for prediction would be loaded. And the conditions entered by the user become a reference value for selecting the governing equation set for each condition in the "Usage condition" (see Figure 2), and the risk prediction is performed by the selected equation. All outcomes from this step are automatically stored in the database. In this model, the prediction accuracy of the risk is dominant by the selected equation for which we used the commercial program COMSOL Multiphysics to do the trial and error method.

2.2. Derivation of Governing Equation for Storm Surge. The derivation of governing equations for each disaster is the most important process to develop this model. First, we must analyze the hazard maps for disaster scenarios after collecting hazard maps related to the storm surge in Korea. They were computed with numerical models and presented by government (MLTMA [32]), and they officially have 4 maps with 4 conditions (see Table 1). These conditions are corresponding with the frequency of wave height caused by the typhoon in coastal area, 50-year, 100-year, 150-year, and 200-year wave height. The numerical model, KOSY (Kordi Operational Storm surge prediction sYstem) (MLTMA [32]), used to compute the wave height is basically a hydrodynamic model and includes the meteorological conditions of typhoons. It is an extension of the tidal model by the fractional step method and applied the shear stress caused by wind at the air-sea interface. Also, it is able to consider the horizontal pressure due to the spatial distribution of atmospheric pressure, the method of solving the long wave equation in which the momentum equation is vertically integrated. The size of the horizontal grid is about 300 m at the offshore and approximately 9 km at the open sea, respectively. The most basic and important factor in calculation of wave height is the establishment of precise bathymetry data. This is established by collecting data from the National Oceanographic Research Institute and global bathymetry data such as GEBCO 08, ETOPO1, and ETOPO2 of which horizontal resolution of these data is about 500 m~2 km. The time step of the numerical model is 1/3 sec~3 sec depending on the grid size.

The interpolation generally needed 3 reference data at least. So, we used the 3 maps to derive governing equation to predict risk grades for storm surge, 50-year, 150-year, and 200-year wave height. The other was used for verification of equation, 100-year wave height.

First, the basic form of equation was derived with physical meaning considering some assumptions. And the coefficients of the equation and boundary conditions were defined by the trial and error method. An independent variable of equation is set as the wave height frequency, and a dependent variable is the spatial distribution of the risk grades. Results from this model were put in the same conditions (50-year, 150-year, and 200-year wave height) with hazard map was compared with them to check whether this equation can exactly predict spatial distribution of risk
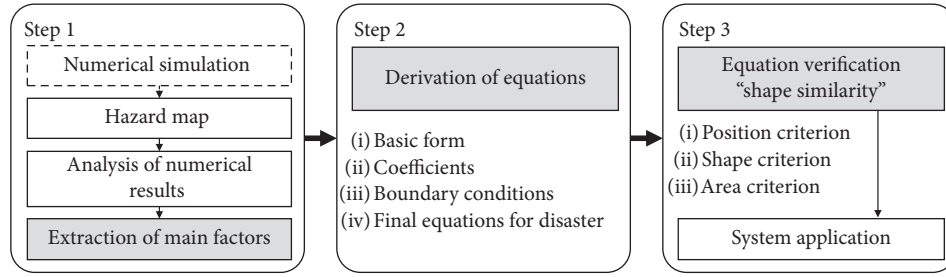
Figure 1: Progress of the SIND model (Kim et al. [31]).
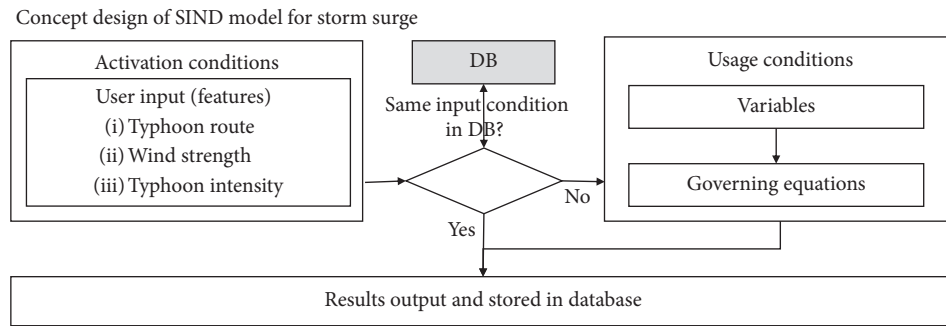
Figure 2: Concept design of the SIND model.

Table 1: Information of hazard maps.

	Hazard map
Format	Shape file (.shp), AutoCad file (.dxf, .dwg)
Agent	MLTMA (the Ministry of Land, Transport, and Maritime Affairs)
Program	Numerical model (physical model)
Year	2010
Conditions	50-year, 100-year, 150-year, 200-year

grade. The COMSOL Multiphysics program was used to perform the trial and error method for determining the equations and comparing the results. And the shape similarity was used to estimate accuracy of prediction by comparison of inundated area with official hazard map. Finally, the governing equation for predicting the risk of storm surges was derived (see Figure 3). After that, the result obtained using the same input conditions as the other map (100-year frequency) was compared with that of the map to verify the final equation.

2.2.1. COMSOL Multiphysics (Ver. 5.4). COMSOL Multiphysics developed by COMSOL AB (Multiphysics [33]) was used to derive governing equations for storm surges. COMSOL Multiphysics is a software that solves partial differential equations for multiple physics using the FEM method. The users can construct their own model and configure each part to enter or adjust values instantly. So, they can derive the equation with the change of conditions to make what they need. In other words, the property and boundary condition can be set as any function including space-time and dependent variables. COMSOL Multiphysics is equipped with governing equations that are frequently

used in the various fields of the heat transfer, flow, electromagnetic, structure, acoustic, chemical reactions, and equation-based module. Equation-based module allows users to construct their own governing equations to derive results. Nonlinear PDE-type equations can be classified into three types: coefficient form, general form, and weak form. In this study, coefficient form was used as follows:

$$e_a \frac{\partial^2 u}{\partial t^2} + d_a \frac{\partial u}{\partial t} - \nabla \cdot (c \nabla u + \alpha u - \gamma) + \beta \cdot \nabla u + au = f,$$

(1)

where e_a is the mass coefficient, d_a is a damping coefficient or mass coefficient, c is the diffusion coefficient, α is the conservative flux convection coefficient, β is the convection coefficient, a is the absorption coefficient, γ is the conservative flux source term, and f is the source term.

On the left-hand side of equation (1), it consists of terms of time, diffusion, convection, source, and absorption. It indicates a source term which can be used or selected according to the condition on the right-hand side. The users should select the coefficients c, α, γ, β, and a and the boundary term f.
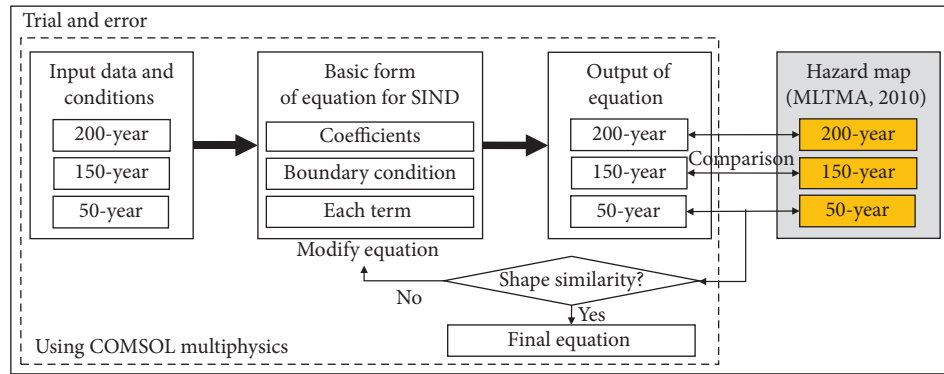
FIGURE 3: Process of derivation equation for storm surge in the SIND model.

2.2.2. Basic Form of Equation for Storm Surge. The risk grade for storm surge is based on the maximum inundation depth according to the typhoon grade. The hazard map is used as the database showing the maximum inundation depth in the coastal areas regardless of the occurrence time (MLTMA [32]). The risk propagation as the frequency of wave height is assumed that the absorption term is not significant. There is another assumption meaning that the initial risk grade determined by the typhoon grade is transmitted through the mediators such as geographical features. This mechanism is similar to the heat transfer equation. Thus, the governing equation for storm surge is shown compared with the heat transfer equation in Table 2.

The parameters of Table 2 are put in the coefficient form provided by COMSOL. Then, we assumed this equation as a steady state because it cannot consider the change over time due to the characteristics of the hazard map. Finally, eliminating the time term, the equation can be expressed as

$$\nabla \cdot (-k \nabla D) = Q, \tag{2}$$

where D is a risk grade and k is a resistance coefficient.

2.2.3. Assumptions. The coefficient required by the basic form is the resistance coefficient k and the boundary conditions which are the risk grade D_0 for coastal areas and D_{ext} for in land areas. An inundation caused by storm surge depends on the terrain characteristics. Thus, the resistance coefficient should be reflected to elevation (DEM). DEM provided by the National Geographic Information Institute in Korea was used to cover land topography with the scale of the DEM of 1 : 5000 and the grid size of 5 m. The wave height with frequency is the most important factor and boundary condition affecting inundation. The calculations of wave height can generally take into account the effects of tide, wind, and pressure fluctuations. The wave height used in the SIND model was calculated by considering the path, wind speed, and wind field of 201 typhoons for 56 years from 1951 to 2006. Wave heights were calculated according to each frequency with the KOSY. It is determined by typhoon grade and calculated as an initial risk grade on the boundaries. A regression analysis was performed to estimate the initial risk grades conditions for all scenarios, using 3 conditions of frequency (50-year, 150-year, and 200-year). The risk grades

on the land boundary are defined as the distance from the coast. The assumptions for the coefficients and each boundary condition are as follows:

(i) The resistance coefficient depends on the topographical conditions of the coastal area

(ii) Resistance constant (k) is inversely proportional to elevation (DEM)

(iii) The risk grade (D_0) at the coastal boundary depends on the grade of the typhoon and the wave height

(iv) The risk grade (D_{ext}) at the land boundary is lower as the distance from the coast increases

2.3. Validation of SIND Model with Shape Similarity. The hazard map depicts the hazardous areas and risk grades with inundation depth according to storm surge conditions. The area and location of the flooded zones are important factors and related to the shape of inundated zones. The comparison of shape of inundated area with the flooded zone in hazard map should be conducted to examine the accuracy of this SIND model. As a result, it is necessary to compare the position and shape of inundation areas to verify the result from the SIND model. It introduced the shape similarity method to quantify how much similar two figures or maps by comparing in their positions, shapes, and areas. It can express the degree of similarity using the geometrical properties of the spatial dataset. However, it does not consider the risk grades because it can just compare two-dimensional figures in terms of geometry only. To consider the risk grades, the hazardous areas for each risk grade were divided and compared again with the graded flood zone in hazard map. Thus, the shape similarity with risk grade is most efficient way to verify the results and to determine accuracy. Kim et al. [34] used a CRITIC method, one of the methods of calculating shape similarity, to select a matching criterion that can reflect geometric properties. The criteria for the similarity of spatial data are the position criterion that means the distance between the center of gravity and shape criterion that uses the shape index. An area criterion uses the ratio of overlapped areas (see Figure 4). For example, in Figure 4(a), when A is the result of hazard map and B is the result of SIND Model, two figures overlap each other based on a certain point. After that, the shape similarity is

TABLE 2: SIND for storm surge in coefficient form.

Parameter	Heat transfer	Risk grade for storm surge
U	Temperature, T	Risk grade (inundation), D
e_a	0	0
d_a	ρC_a	1
C	Conductivity coef. $-k$	Resistance coef. $-k$
γ	0	0
β	Velocity	Velocity
α	0	0
F	Heat flux, Q	Risk flux, Q
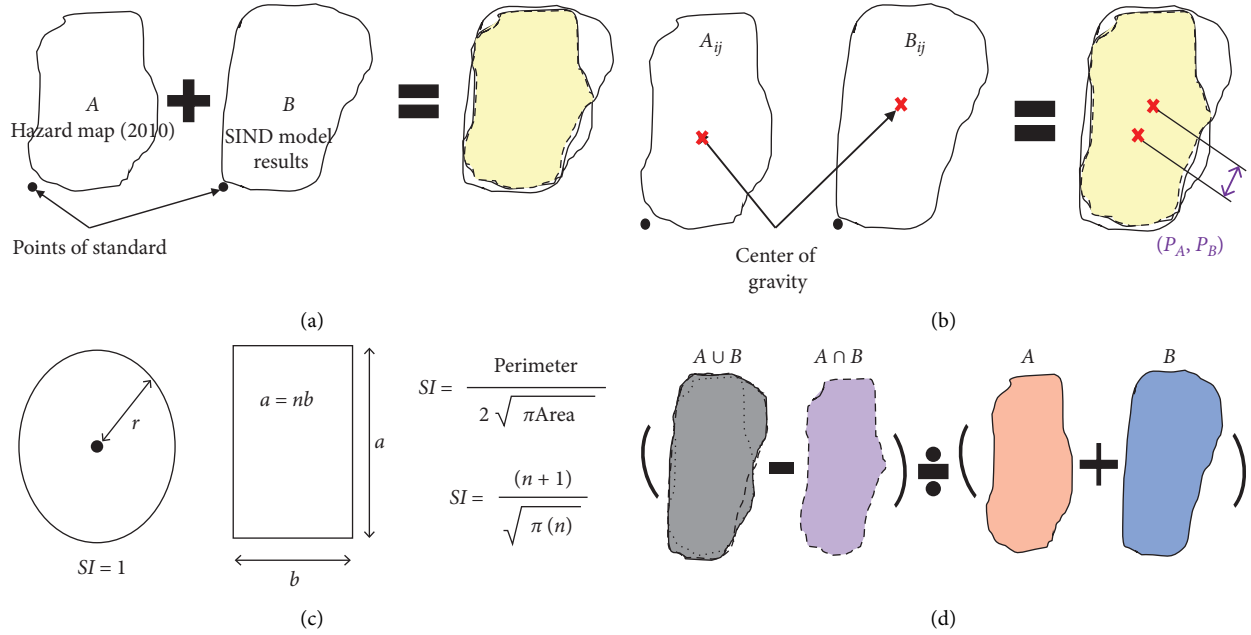
FIGURE 4: Concept of the CRITIC method. (a) Matching coupled object. (b) Position criterion: center of gravity. (c) Shape criterion: shape index. (d) Area criterion: ratio of overlapped area.

calculated using the location criteria (see Figure 4(b)), shape criteria (see Figure 4(c)), and area criteria (see Figure 4(d)).

2.3.1. Position Criterion (SP). The position criterion is evaluated as the distance between the centers of gravity of two objects. The closer the position criterion is to 1.0, the more similar the object of the SIND model is to the hazard map.

$$SP = 1 - \frac{P_c - P_m}{P_m} \ (0 \le SP \le 1), \tag{3}$$

where P_m is $\sqrt{(X_m - X_s)^2 + (Y_m - Y_s)^2}$ and P_c is $\sqrt{(X_c - X_s)^2 + (Y_c - Y_s)^2}$. X_m and Y_m are the center of gravity for the hazard map, and X_c and Y_c are the center of gravity for the SIND model.

2.3.2. Shape Criterion (SR). The CRITIC method is mainly used in GIS-based mapping field, and the shape of object is close to basic shape like rectangle and circle. There is a limitation to using this method because the shape of the hazardous area for storm surge shows a thin and long band shape. Thus, this method was modified by adding the RCCI index that can apply the elongated shape.

$$SR - I = 1 - \frac{R_c - R_m}{R_m} \ (0 \le SR - I \le 1),$$

$$SR - II = 1 - \frac{RCCI_c - RCCI_m}{RCCI_m} \ (0 \le SR - II \le 1), \tag{4}$$

$$SR = s_1 \times SR - I + s_2 \times SR - II \ (0 \le SR \le 1),$$

where R_m is $|P_m/(2\sqrt{\pi A_m})|$ and R_c is $|P_c/(2\sqrt{\pi A_c})|$. P_m is the perimeter of the shape in hazard map. P_c is the perimeter in the SIND model. RCCI is added shape index. Equation is

RCCI = $|A/\text{CA}|$. A_c and A_m are area of each shape. CA is circumscribed circle area. s_1 and s_2 are weights of 0.4 and 0.6, respectively.

2.3.3. Area Criterion (SA).

The area criterion was estimated using the ration of overlapped area between 2 maps.

$$SA = 1 - \left| \frac{(A_c \cup A_m) - (A_c \cap A_m)}{A_m + A_c} \right| \ (0 \le SA \le 1), \quad (5)$$

where A_m is the inundation area in hazard map and A_c is the inundation area in the SIND model.

2.3.4. Overall Shape Similarity (S).

The weights are calculated using the information amount and the correlation coefficient. The closer each criterion (SP, SR, and SA) is to 1.0, the overall shape similarity has higher value. That means the overall shape similarity (S) of the matching object is close to 1.0.

$$S = w_1 \times SP + w_2 \times SR + w_3 \times SA \ (0 \le S \le 1), \quad (6)$$

where w_1, w_2, and w_3 are the respective weights.

3. Results and Discussion

3.1. Coefficients and Boundary Conditions of SIND Model.

Using the trial and error method, the resistance coefficient (k), the risk grade (D_{ext}) at the land boundary, and the initial risk grade (D_0) at the coast boundary were calculated. The calculated coefficient and boundary conditions are considered with the characteristics of storm surge through assumptions. According to the assumptions, the distribution of k has something to do elevation (see Figures 5(a) and 6(a)). If k had low value, the propagation of risk is easier. The correlation is shown in the following equation:

$$k = \frac{c_1}{z}, \quad (7)$$

where c_1 is the empirical coefficient to be 0.5 and z is the elevation.

As shown in Figure 5(b), boundary conditions can be divided into coastal and land. The coastal boundary conditions used the wave height at the station through frequency analysis in the MLTMA report (see equation (8)). There is a restriction that all boundaries were estimated as 1 representative point. So, sections of boundary were divided according to the risk grade on the hazard map (see Figure 5(c) and Figure 4(d)). The wave height for storm surge was calculated through regression analysis to deal with all frequencies (see Figure 6(c)). The regression equation of the boundary condition in coastal line is shown in equation (9) and Figure 6(d). The risk grade of land boundary is expressed as distance d with the coastline, as shown in equation (10) and Figure 6(b):

$$H = 0.235 \ln(T) + 0.128, \quad (8)$$

$$D_0 = c_2 (4.25H - 0.54) + c_3 \quad (9)$$

$$D_{ext} = c_4 d \quad (10)$$

in coastal line boundary, in land boundary, where T is frequency of wave height, H is the wave height, c_2 is equivalent to 2.525 in sections A and B, c_3 is −1.293 in section A and −5.293 in section B, c_4 is constant, 0.25, c_2, c_3, and c_4 are empirical coefficients, and d is the distance from coastal line.

3.2. Results of Derivation Process.

The reference value is the criterion which determines similarity between the result of the equation and the hazard map. This value is 0.6, and it is used in the GIS-based mapping field. When the shape similarity is 0.6 or more, it is estimated that the results in the SIND model are implemented well. The detailed results are shown in Table 3. The results with each frequency are shown in Figure 7. The matching pairs above 0.6 are 73.7%, 62.0%, and 66.7%, respectively.

3.3. Short-Term Forecasting Hazard Zone.

The SIND model can predict the hazardous area caused by storm surges in a short time with simple input conditions. Table 4 shows the geometric results of each hazardous area. The result was very similar to the inundation area shape of the hazard map. However, the locally generated error between the two shapes is because the regional characteristics were not reflected due to the low resolution of the map.

3.4. Verification of SIND Model.

A corresponding wave height with 100-year frequency was entered for a model verification, and the results were compared with the hazard map at the same conditions: 100-year frequency of wave height. Shape similarity was used to calculate the accuracy of the SIND model. The wave height of 100-year frequency was calculated by regression equation.

3.4.1. Threshold of Shape Similarity.

A threshold is needed to determine whether two shapes are similar or not. In the CRITIC method, a subjective judgment process is necessary to calculate a threshold value. The matching pairs are directly divided into exact-matching and mismatching. The shape similarity of each matching pair is analyzed to estimate the threshold (see Figure 8). If the classification is well, the shape similarity values of the exact-matching pairs will generally be high and those of the mismatching pairs will be low. The threshold is defined as the value where the number of mismatching exceeds it of exact-matching. After the 3 maps used in derivation process were separated into exact-matching and mismatching, the shape similarity was analyzed. As a result, exact-matching pairs had a generally high shape similarity. The threshold where number of mismatching pairs exceeds those of exact-matching pairs is 0.55 (see Figure 9).

(a)

(b)

(c)

(d)
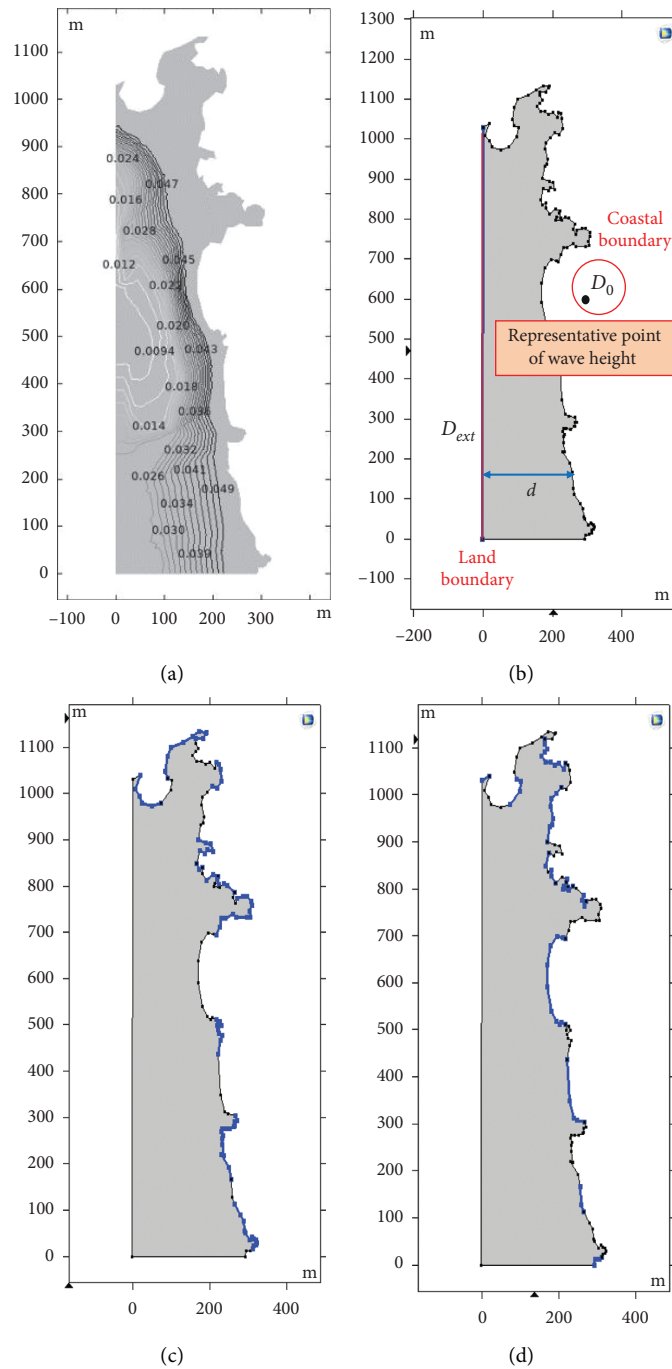
Figure 5: Coefficient and boundary conditions in the SIND model: (a) resistance coef; (b) B.C; (c) section A; (d) section B.

3.4.2. Results of Verification. It is necessary to obtain the accuracy of the area, center of gravity, and perimeter of each matching pair before calculating the overall shape similarity. Determination coefficients, root mean square error (RMSE), and Nash–Sutcliffe efficiency (NSE) were used for estimating indexes of shape characteristics. The determination coefficient is an index for evaluating the relationship between the observations and the model for the same variable. As a value is closer to 1.0 from 0.0, it indicates that the model results fit the observative values well. Nash–Sutcliffe efficiency is an index that is used as much as the determination coefficient.

The Nash–Sutcliffe efficiency is a technique that evaluates the efficiency of the model using the relationship between observations and the model. Ramanarayanan et al. [35] suggested the determination coefficient and the Nash-Sutcliffe efficiency when they simulate the natural phenomenon such as rainfall and temperature. If the determination coefficient was a value of 0.5 or more and the Nash-Sutcliffe efficiency is 0.4 or more, the model can be well-conducted. The root mean square error is a technique for calculating the amount of error, and it is the most intuitive and meaningful evaluation index. When it closed to

(a)

(b)

- ● BAJ1
- ○ BAJ2
- ■ BAJ3
- □ USN2
- × USN4

(c)

- ● Section A
- ○ Section B

(d)
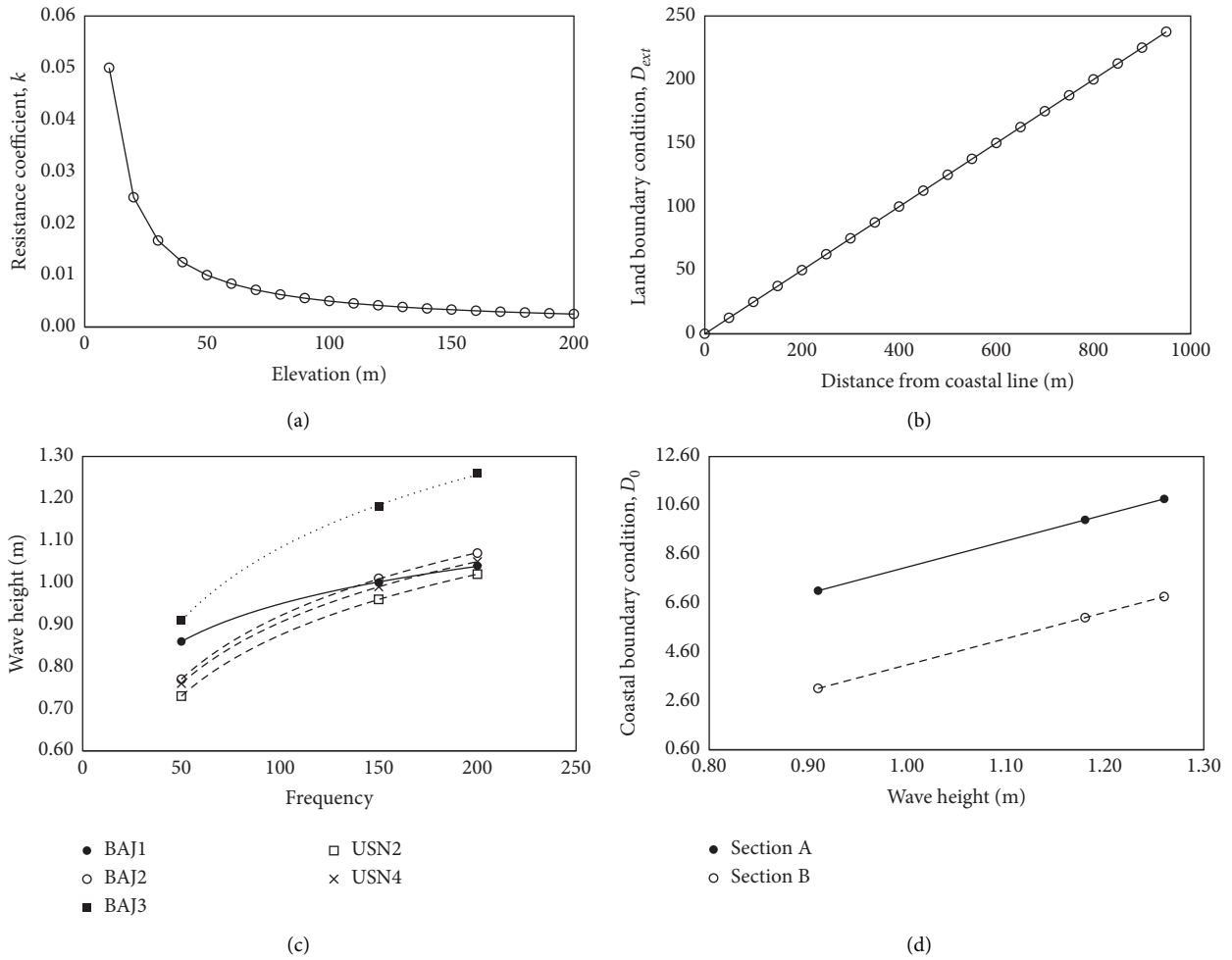
FIGURE 6: Results of coefficient and boundary conditions: (a) resistance coefficient with elevation; (b) land boundary conditions with d; (c) wave height with frequency; (d) coastal boundary conditions with H.

TABLE 3: Results of overall shape similarity (S).

	50-year	150-year	200-year
Total matching pairs	38	50	45
>0.6	28	31	30
Rate (%)	73.7	62.0	66.7

(a)

(b)
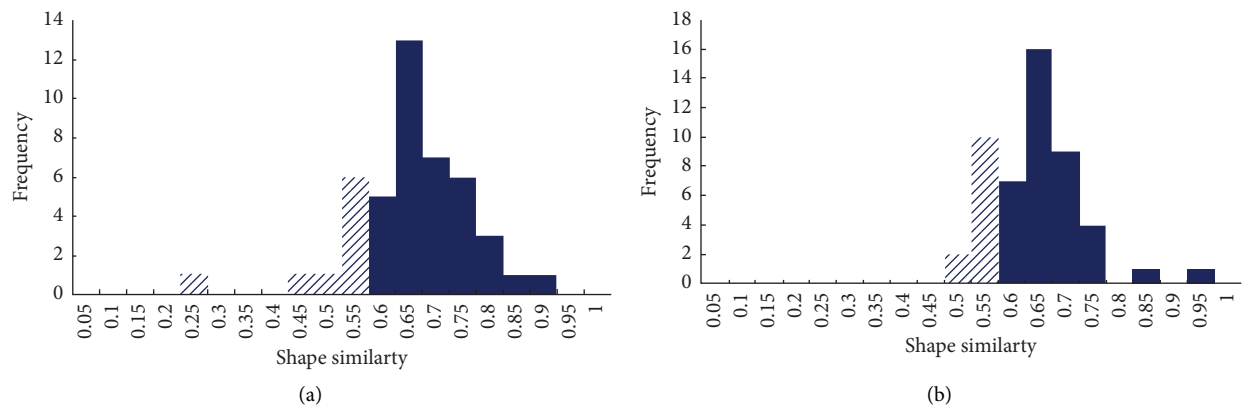
FIGURE 7: Continued.

(c)
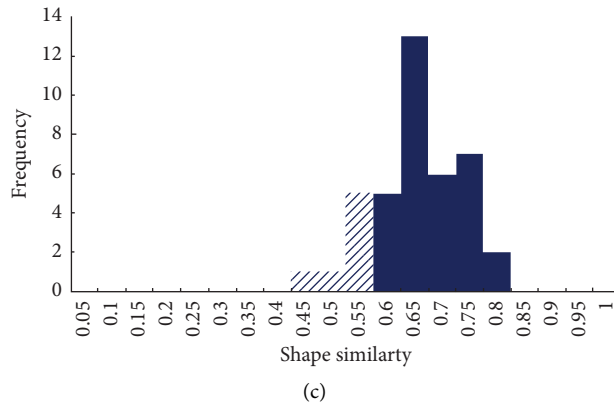
FIGURE 7: Results of shape similarity for each frequency: (a) 200-year; (b) 150-year; (c) 50-year.

TABLE 4: Overall results of the SIND model.

Grade	Distance between center of gravity	Area (km²)			Perimeter (km)	Ratio of overlapped area	Shape index	
		Each	Sum	Intersect			Each value	Difference
b1RA*	19.1	0.056	0.076	0.018	0.007	0.611	8.10	0.39
b1CA		0.038			0.006		8.49	
b2RA	176.5	0.029	0.051	0.013	0.005	0.601	8.50	0.87
b2CA		0.035			0.006		9.37	
b3RA	124.7	0.008	0.021	0.002	0.003	0.833	9.05	2.51
b3CA		0.015			0.003		6.55	
b4RA	14.9	0.006	0.018	0.001	0.002	0.857	6.63	2.37
b4CA		0.013			0.002		4.26	
b5RA	47.8	0.003	0.006	0.001	0.001	0.126	6.85	5.02
b5CA		0.034			0.001		1.84	

*b1RA-1st Grade in "A" section of "b" area of hazard map (1: risk grade; R: hazard map; C: results of SIND; A, b: name of area).
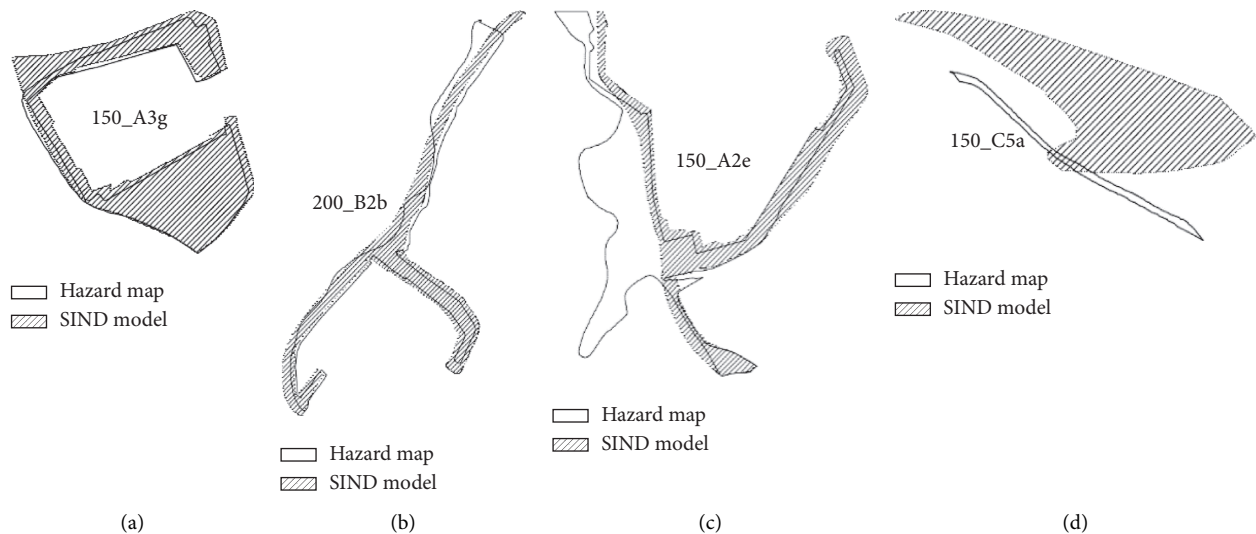
FIGURE 8: Examples of exact-matching and mismatching objects: (a) Exact 1; (b) Exact 2; (c) Mis 1; (d) Mis 2.

0.0, it has higher accuracy between model and observation. Each value of the shape characteristics at 100-year frequency condition is shown in Table 5 and Figure 10.

The accuracy of the results was verified at the random condition by using the thresholds. The shape similarity was calculated by matching the results with the hazard map for the wave height of 100-year frequency condition (see Table 6). A total of 41 pairs of matching pairs were made, and it was determined whether the shapes were similar based on the threshold. The number of exact-matching pairs was 33
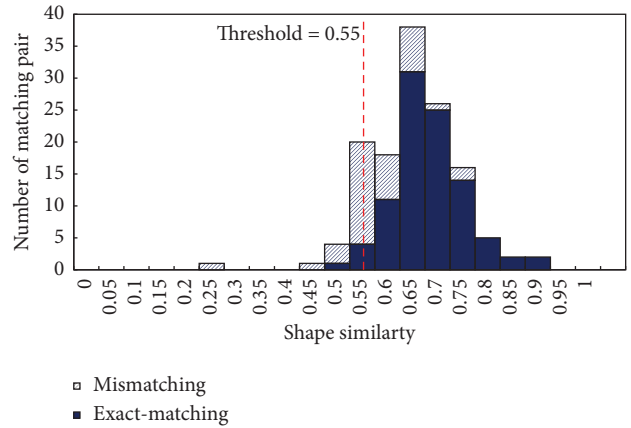
FIGURE 9: Threshold of the SIND model.

TABLE 5: Estimation of shape parameter.

Evaluation method	Center of gravity		A (km^2)	P (km)
	x (km)	y (km)		
R^2	0.9984	0.9986	0.8746	0.9061
RMSE	0.1937	0.1621	0.0176	1.0528
NSE	0.9962	0.9966	0.4538	0.8102
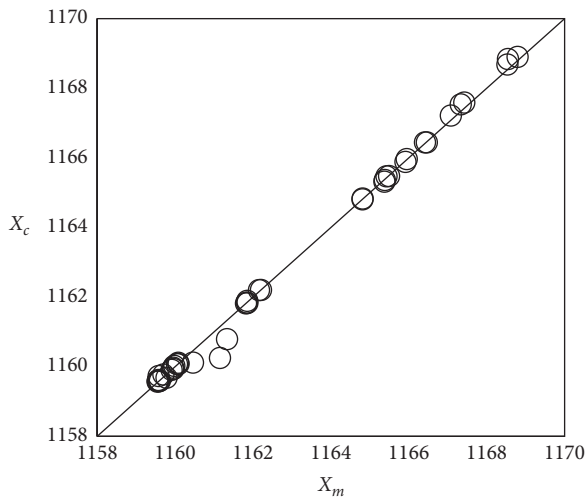
(a)
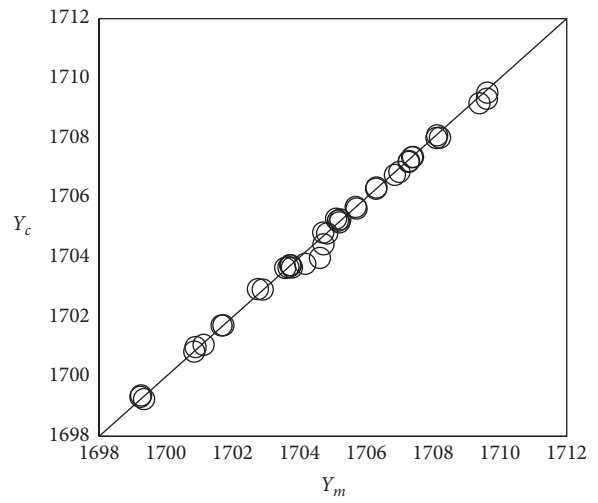
(b)

FIGURE 10: Continued.

(c)

(d)
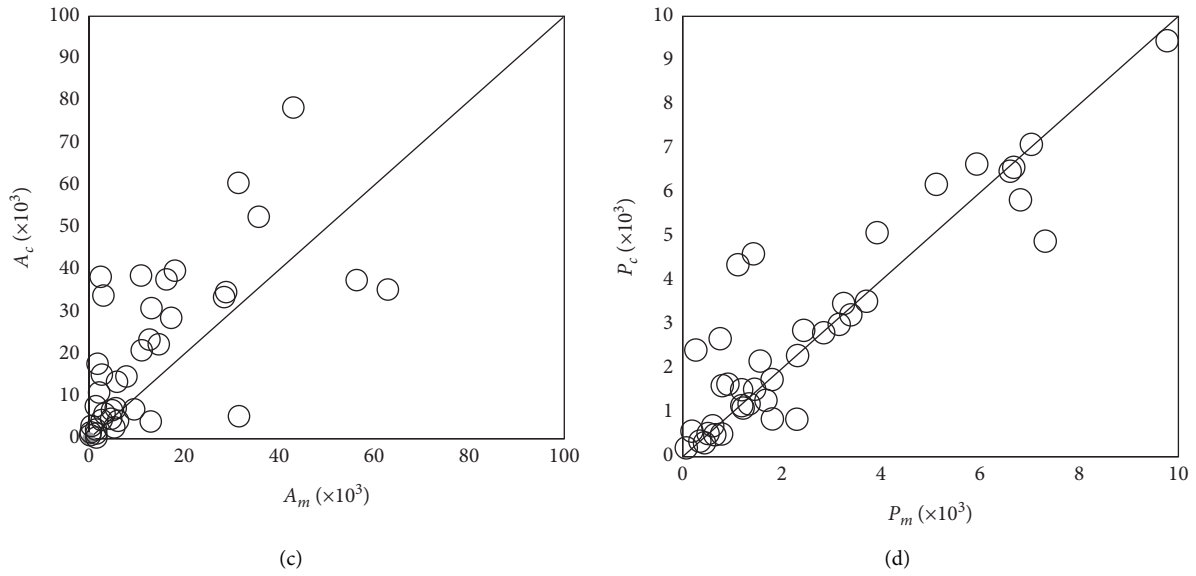
Figure 10: Scatter plot of (a) x-coordinate; (b) y-coordinate; (c) area; (d) perimeter.

Table 6: Estimation of shape similarity.

Grade	SP	SA	SR	S
b1RA b1CA	0.987	0.411	0.986	0.720
b2RA b2CA	0.883	0.421	0.973	0.685
b3RA b3CA	0.917	0.198	0.924	0.584
b4RA b4CA	0.990	0.174	0.926	0.599
b5RA b5CA	0.968	0.879	0.847	0.904

■ Exact-matching
▨ Mismatching
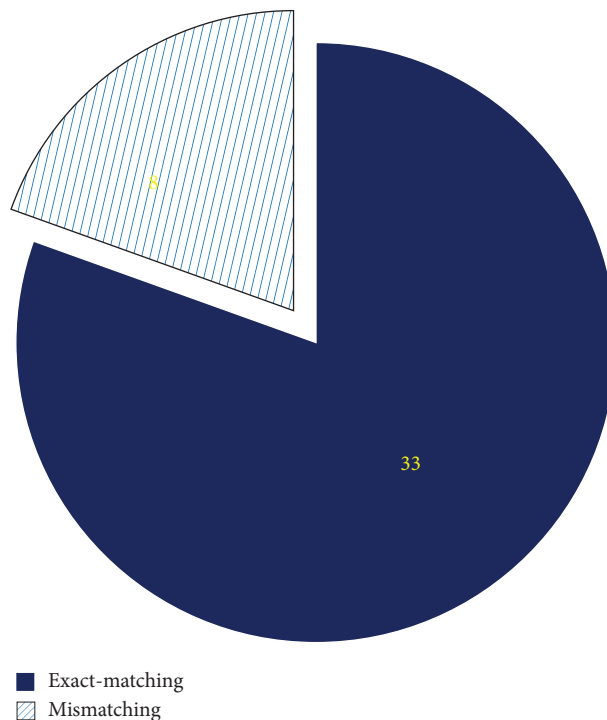
Figure 11: Verification results.

pairs. Thus, the accuracy is about 80.5%. Figure 11 shows the number of exact-matching and mismatching classified by the threshold.

4. Conclusions

Parallel to the hazard map made by the MLTMA [32], the SIND model, based on a scientific interpolation method, was devised with the guarantee of rapid and accurate estimation. The spatial distribution of the risk grades for inundation was presented after verification estimated with shape similarity between official hazard map and results from this model.

We reflect the physical characteristics of the disaster due to storm surge into this model by selecting PDE form as governing equation and setting the simple input and boundary conditions. The wave height, which is a representative input value, appears to be simple and robust, but it is calculated by the KOSY that can take into account the effects of tide, wind, and pressure fluctuations. And we used the trial and error method to decide coefficients of governing equation for storm surge. Thus, it can predict risk grades for all disaster scenarios with high accuracy and speed. The user can find out hazardous area within a few seconds (about 5 seconds) in any condition between 50-year and 200-year frequency of wave heights. As a result, this model can make up for the limits of scenario-based disaster countermeasures. The advantages of this model can be summarized in terms of convenience, speed, and accuracy. User does not require a complicated understanding of disaster mechanism. And there is no need for cornerstone work before simulating the numerical model. Thus, they can easily yield the results in the right time and right condition for the right decision making. Although the model was performed by simple procedures, it has a physical meaning reflected the disaster characteristics including initial wave height and geographical resistance. This model also improved computation time. As mentioned, it takes approximately 5 seconds for about $720,000\,km^2$ to present each hazard map while the Delft3D used commonly takes about 2 days in the same condition. And the accuracy of this model was about 80% for arbitrary condition. However, since we decided the threshold values under empirical estimations by classifying the exact-matching and mismatching, it is essential to prescribe the exact-matching and the mismatching through the clear criteria. And we would calibrate narrowly and adjust carefully multiobjects corresponding to one object so that the shape similarity will increase overall.

The SIND model shows the new approach of disaster prediction using the interpolation method with PDE representing physical characteristics of the target phenomenon. This model extenuated the complexity of the prediction for storm surge such as long simulation time and the occurrence of uncertain disasters, which were the well-known limitations in numerical modelling. Therefore, it is possible to predict disaster risk grades much quickly using this model, which should be very helpful for policy decisions to respond disaster. In fact, an early warning is very important to reduce human injury and property damage just prior to and immediately after occurrence of any event of specific disaster. Thus, the SIND model is capable of amply accurate and much rapid predicting at the early stage. Also, it is based on database like hazard maps, which can be composed of structured, semi-structured, and unstructured data. Therefore, it will be applicable to various disasters if more reliable database is acquired and higher accuracy is promised in the future.

And because this model used the results from numerical simulation or observation as input data for the scientific interpolation method, it does not consider the nonstationary of historical data. However, the historical data related to topography and climate are affected by extreme events as earthquakes. For instance, the change of topography will affect the occurrence of storm surge with physical laws. Thus, future works include the method how to regenerate risk grade considering such historical data.

Data Availability

The data used to support the findings of this study are available from the corresponding author upon request, and some of them would be restricted because of external security issues.

Conflicts of Interest

The authors declare that they have no conflicts of interest regarding the publication of this paper.

Acknowledgments

References

[1] S. Cutter, *Vulnerability to Environmental Hazards*, Progress in Hyman Geography, Thousand Oaks, CF, USA, 1957.

[2] M. K. Lindell and C. S. Prater, "Assessing Community Impacts of Natural Disasters," *Natural Hazards Review*, vol. 4, no. 4, p. 176, 2003.

[3] National Institute for Disaster Prevention, *A Study on the Regional Vulnerability Assessment and its Application for the Disaster Management*, National Emergency Management Agency, Seoul, Republic of Korea, 2003.

[4] Seoul Development Institute, *Developing a Risk Assessment Method for the Mitigation of Urban Disasters*, Seoul Metropolitan City, Seoul, Korea, 2009.

[5] W. C. Conner, R. H. Kraft, and D. L. Harris, "Empirical methods for forecasting the maximum storm tide due to hurricanes and other tropical storms," *Monthly Weather Review*, vol. 85, no. 4, pp. 113–116, 1957.

[6] D. L. Harris, *An Interim Hurricane Storm Surge Forecasting Guide*, US Department of Commerce, Washington, DC, USA, 1959.

[7] J. Proudman, "Note on the dynamics of storm-surges," *Geophysical Journal International*, vol. 7, pp. 44–48, 1954.

[8] A. T. Doodson, "Tides and storm-surges in a long uniform gulf," *Proceedings of the Royal Society of London. Series A*, vol. 237, no. 1210, pp. 325–343, 1956.

[9] N. S. Heaps, "Storm surges on a continental shelf. Phil. Trans. R. Soc. Lond. A," *Mathematical and Physical Sciences*, vol. 257, no. 1082, pp. 351–383, 1965.

[10] R. H. Simpson and H. Riehl, *The Hurricane and its Impact*, Louisiana State University Press, Baton Rouge, LA, USA, 2015.

[11] T. S. Murty, *Storm Surges: Meteorological Ocean Tide*, p. 897, Department of Fisheries and Oceans, Ottawa, Canada, 1984.

[12] D. T. Pugh, *Tides, Surges and Mean Sea-Level: A Handbook for Engineers and Scientists*, p. 472, John Wiley, Hoboken, NJ, USA, 1987.

[13] N. S. Heaps, "Storm surges, 1967-1982," *Geophysical Journal International*, vol. 74, no. 1, pp. 331–376, 1983.

[14] J. Wolf, K. P. Hubbert, and R. A. Flather, *A Feasibility Study for the Development of a Joint Surge and Wave Model*, Proudmen Oceanographic Laboratory, Liverpool, UK, 1988.

[15] H. L. Tolman, ""Wind wave propagation in tidal seas," Communications on Hydraulic and Geotechnical engineering," *Delft Univ. of Techn., Rep.*vol. 90, no. 1, 1990.

[16] C. Mastenbroek, G. Burgers, and P. A. E. M. Janssen, "The Dynamical coupling of a wave model and a storm surge model through the atmospheric boundary layer," *Journal of Physical Oceanography*, vol. 23, no. 8, pp. 1856–1866, 1993.

[17] Y. S. Li and M. Y. Zhang, "Dynamic coupling of wave and surge models by Eulerian–Lagrangian method," *Journal of Waterway, Port, Coastal, and Ocean Engineering*, vol. 123, no. 1, pp. 1–7, 1997.

[18] J. Ozer, R. Padilla-Hernandez, J. Monbaliu et al., "A coupling module for tides, surges and waves," *Coastal Engineering*, vol. 41, no. 1-3, pp. 95–124, 2000.

[19] M. Peng, L. Xie, and L. J. Pietrafesa, "A numerical study of storm surge and inundation in the Croatan-Albemarle-Pamlico Estuary System," *Estuarine, Coastal and Shelf Science*, vol. 59, no. 1, pp. 121–137, 2004.

[20] P. D. Bates and A. P. J. De Roo, "A simple raster-based model for flood inundation simulation," *Journal of Hydrology*, vol. 236, no. 1-2, pp. 54–77, 2000.

[21] R. J. Nicholls, "Rising sea levels: potential impacts and responses," in *Global Environmental Change: Issues in Environmental Science and Technology*, R. Hester and R. M. Harrison, Eds., vol. 17, pp. 83–107, Royal Society of Chemistry), Cambridge, UK, 2002.

[22] I. Brown, "Modelling future landscape change on coastal floodplains using a rule-based GIS," *Environmental Modelling & Software*, vol. 21, no. 10, pp. 1479–1490, 2006.

[23] M. J. Purvis, P. D. Bates, and C. M. Hayes, "A probabilistic methodology to estimate future coastal flood risk due to sea level rise," *Coastal Engineering*, vol. 55, no. 12, pp. 1062–1073, 2008.

[24] J. Yim and G. Lee, "Estimating urban temperature by combining remote sensing data and terrain based spatial interpolation method," *Journal of the Korean Cartographic Association*, vol. 17, no. 2, pp. 75–88, 2017.

[25] T. Ishida and S. Kawashima, "Use of cokriging to estimate surface air temperature from elevation," *Theoretical and Applied Climatology*, vol. 47, no. 3, pp. 147–157, 1993.

[26] N. Fitria, *Kajian Bahaya Tsunami Pada Variasi Ketinggian Run-Up Dan Arah Tsunami*, Artikel PIT MAPIN VII, Bandung, Indonesia, 2008.

[27] F. Islam, S. Subiyanto, and L. M. dan Sabri, "Penentuan resiko dan kerentanan tsunami di kebumen dengan citra alos," *Jurnal Geodesi*, vol. 3, no. 1, pp. 141–154, 2014.

[28] I. Maemunah, C. Sulaeman, and R. dan Robiana, "Identifikasi potensi kerawanan tsunami di wilayah Kabupaten Jember, Jawa Timur," *Jurnal Lingkungan Dan Bencana Geologi*, vol. 2, no. 2, pp. 141–152, 2011.

[29] Y. Fauzi and Z. M. Mayasari, "The run up tsunami modeling in bengkulu using the spatial interpolation of kriging technique," *Forum Geografi*, vol. 28, no. 2, pp. 103–112, 2014.

[30] J. E. Lee, *3-Dimensional Object Reconstruction of Medical Images Using Kriging and Markov Random Field Model*, Ewha University, Seoul, South Korea, 1996.

[31] D. H. Kim, H. J. Yoo, S. I. Jeong, and S. O. Lee, "Development for prediction model of disaster risk through try and error method: storm surge," *Journal of Korean Society of Disasters and Security*, vol. 11, no. 2, pp. 37–43, 2018.

[32] D. Y. Lee, *Development of Storm Surge and Tsunami Prediction System and Estimation of Design Water Level for Major Ports in Korea*, Ministry of Land, Transport and Maritime Affairs, Korea Ocean Research & Development Institute, Busan, Korea, 2006.

[33] C. O. M. S. O. L. Multiphysics, *Introduction to COMSOL Multiphysics®*, COMSOL Multiphysics, Burlington, MA, USA, 1998.

[34] J. Y. Kim, Y. Huh, D. S. Kim, and K. Y. Yoo, "A new method for automatic areal feature matching based on shape similarity using CRITIC method," *Journal of the Korean Society of Surveying, Geodesy, Photgrammetry, and Cartography*, vol. 29, no. 2, pp. 113–121, 2011.

[35] T. S. Ramanarayanan, J. R. Williams, W. A. Dugas, L. M. Hauck, and A. M. S. McFarland, *Using APEX to Identify Alternative Practices for Animal Waste Management*, ASAE Paper, Washington, DC, USA, 1997.

Review Article

Strong Far-Field Vertical Excitation and Building Damage: A Systematic Review and Future Avenues

Dipendra Gautam (iD)[1,2,3,4] **and Rewati Baruwal**[2]

[1]*Department of Civil Engineering, Cosmos College of Management and Technology, Lalitpur, Nepal*
[2]*Interdisciplinary Research Institute for Sustainability, IRIS, Kathmandu, Nepal*
[3]*Department of Civil Engineering, Institute of Engineering, Thapathali Campus, Kathmandu, Nepal*
[4]*Nepal Academy of Science and Technology, Lalitpur, Nepal*

Correspondence should be addressed to Dipendra Gautam; dipendra01@tcioe.edu.np

Strong vertical excitation may lead to detrimental consequences on structures and infrastructures. To date, the impacts of strong vertical shaking on structures and infrastructures are considered for near-field regions only. However, anomalies in terms of recorded evidence and damage occurrence in the central Himalayan earthquakes dragged the attention of the researchers to explore the possibility of strong vertical shaking in far-field regions as well. Systematic review approach is used to sum up the findings from scholastic works reported to date and juxtaposed the findings with the evidence from central Himalayan earthquakes. It is concluded that the strong vertical shaking in the far-field is undeniable, at least in the central Himalayas; thus, incorporation of strong far-field vertical shaking in structural analysis and design is required. This paper reports the evidence reported in the literature for strong vertical shaking and adds evidence from Nepal focusing on strong far-field vertical excitation.

1. Introduction

With an increasing availability of accelerometric records, experimental and numerical studies on the effects of strong vertical excitations are appearing more frequently nowadays. Although moderate to strong earthquakes rarely occur and instrumentation is not adequate across the active seismic regions, the impacts of vertical excitations were surfaced mainly after 1990s. For many years, vertical shaking is considered to be significant in the near-field regions only. Possibly, due to the fact that the effects would be detrimental in the near-field regions, consideration of vertical excitation in near-field regions deemed necessary. Many researchers conducted analyses on the seismic behavior of several types of structures considering the near-field strong motion records (e.g., [1–6], among others). In high-frequency scenario, the vertical-to-horizontal spectral ratio would be greater than 2/3, which is commonly considered [7], even for source to site distance up to 40 km [8]. Meanwhile, the V/H

ratio would be smaller than 2/3 for a long period as reported by several researchers (see, e.g., [9–11], among others). Several earthquakes worldwide depict that strong vertical shaking in the near-field would be detrimental in terms of structure and infrastructure damage [12–16]. As all the historical evidences coincide with the fact that the strong vertical shaking is prevalent in near-field regions, experimental as well as numerical studies on the effect of vertical excitation on structures and infrastructures are also limited to near-field regions. To the best of authors' knowledge, the far-field strong vertical shaking has not gotten adequate attention although there are some remarkable shreds of evidence to support this aspect. To this end, systematic review was conducted on the effect of strong vertical shaking on buildings to shed light on the necessity of strong far-field shaking pertaining to the recorded and descriptive evidence of the occurrence of strong or strongest vertical excitation in the far-field. This paper aims to report the effect of vertical excitation through extensive literature review and to propose

a new dimension of the promising research field in the future.

2. Methodology

The systematic review approach is used in this study to identify and synthesize the findings of published works that emerged in the past decades. Further details regarding the systematic review approach could be found elsewhere (see, e.g., [17]). The schematic diagram of the systematic review approach is shown in Figure 1. The first step involves the formulation of the pertinent research question(s). In this study, research questions were postulated as follows: is strong vertical excitation significant in far-field too? Thereafter, we explored repositories such as Scopus, Mendeley, ScienceDirect, ASCE Library, Taylor and Francis Online, Wiley Online, Springer, Sage, ResearchGate, and Google. The keywords such as "vertical shaking," "vertical excitation," "far-field motion," "near-field motion," "structure damage," and "building damage" among others were used to identify the potential works for literature review. Apart from the scholastic works, relevant codes and research works related to data and evidence for strong vertical shaking in near field were collected. In total 211 documents were prepared for initial assessment. Thereafter, initial screening was performed considering the quality of publication and publishers, indexation, duplication, and novelty of the works. After a thorough quality assessment, 118 documents from indexed journals, codes, data papers, reviewed reports, and reputed conferences papers were segregated. The papers from indexed journals, reviewed reports, and reputed conferences were used to perform an exhaustive literature review. It should be noted that our scope is limited to building damage due to strong vertical shaking; thus, infrastructure damages are not duly accounted. Thus, seismological aspects of strong vertical shaking and studies related to the effects of vertical shaking on bridges are not reported exhaustively, rather recognized only. The papers selected for review were screened to check the research alignment per our objective, and synopsis of findings from each reviewed content is presented. Critiques on existing studies are then delineated, and future insights and conclusions are formulated attributing the recent observations on far-field vertical shaking. The central Himalayan earthquakes were considered as the evidence to extend state-of-the-art practice to a new direction.

3. Effects of Vertical Shaking on Structures

One of the pioneering contributions in the effect of vertical shaking was made by Papazoglou and Elnashai in 1996 [18]. They critically analyzed the damages caused by the Kalamata, Greece, earthquake (1986) for the near-field damage analysis. They further noted that the historical earthquakes such as Skopje (1963), Managua (1972), Thessaloniki (1978), El-Asnam (1980), San Salvador (1986), and Spitak (1989) reflected the possibility of strong vertical shaking in the near-field regions. The Kalamata earthquake showed the V/H ratio up to 1.26 (for details, see [19, 20]) as reported by

[18]. Due to strong vertical shaking, the horizontal displacement of items had occurred without visible evidence of friction at the interface. Papazoglou and Elnashai [18] also presented field evidence of horizontally cracked reinforced concrete (RC) pedestal at midheight due to possible tensile action. Reports presented by several researchers (e.g., [20–24]) outlined the unusually high number of symmetric compression and shear-compression failures in columns and shear walls even in soft-story buildings. This evidence was not per the general expectation of the occurrence of bending failure; thus, researchers noted that strong vertical shaking would have been responsible for anomalous damage mechanisms. The soft-story construction is considered to have vulnerability concentrated to ground story, and occurrence of damage is generally expected due to formation of plastic hinges. The soft-story damage, strengthening, and seismic performance aspects are reported elsewhere (see, e.g., [25, 26]). Papazoglou and Elnashai [18] concluded that the discrepancy of vertical force was responsible for the reduction in shear strength due to loss/reduction of concrete contribution. Papazoglou and Elnashai [18] also presented the evidence of the 1994 Northridge and 1995 Hyogo Ken Nanbu earthquakes citing evidence of unusually strong vertical shaking and damage occurrence in modern buildings.

Several analytical investigations considering the effects of vertical shaking on buildings confirmed that varieties of buildings observe the same level of dynamic amplification due to vertical shaking as reported by Papazoglou and Elnashai [18] and analytical evidence presented by Georgantzis [27], Papadopoulou [28], Papaleontiou and Roesset [29], and Fardis [30]. The analysis conducted by Papadopoulou [28] highlighted that moment-resisting reinforced concrete (RC) frames show the variation of the vertical-to-horizontal fundamental period between 7 and 2.5 for 8- to 1-storied buildings. The analysis performed by Georgantzis [27] suggested that the behavior modification factor would be reduced by up to 30% when considering vertical excitation even though the V/H ratio is constrained to 2/3 [31, 32]. Thus, consideration of vertical motion would result in the failure of the upper story(s). Papazoglou and Elnashai [18] concluded that column shear failure would be the governing factor for the ultimate response when the vertical component is included in analyses. Analysis of steel frame building by Broderick et al. [33] showed that the inclusion of vertical shaking did not affect the interstory drift; however, a 12% increase in column rotation ductility demand was prevalent due to the occurrence of lower yield rotation. The beam would be the most affected due to vertical shaking. In 1996, Papazoglou and Elnashai [18] shed light on the necessity of inclusion of vertical excitation in earthquake-resistant designs and analyses. However, a broad literature review reflected that the topic is still vital to be explored even after 25 years. Elnashai and Papazoglou [34] presented a method to assess the behavior of RC buildings subject to vertical shaking deploying piecewise linear relationship. They derived bilinear and inelastic spectra and concluded that the net tensile forces and displacement may lead to the reduction in the shear resistance of RC columns. They proposed a modal
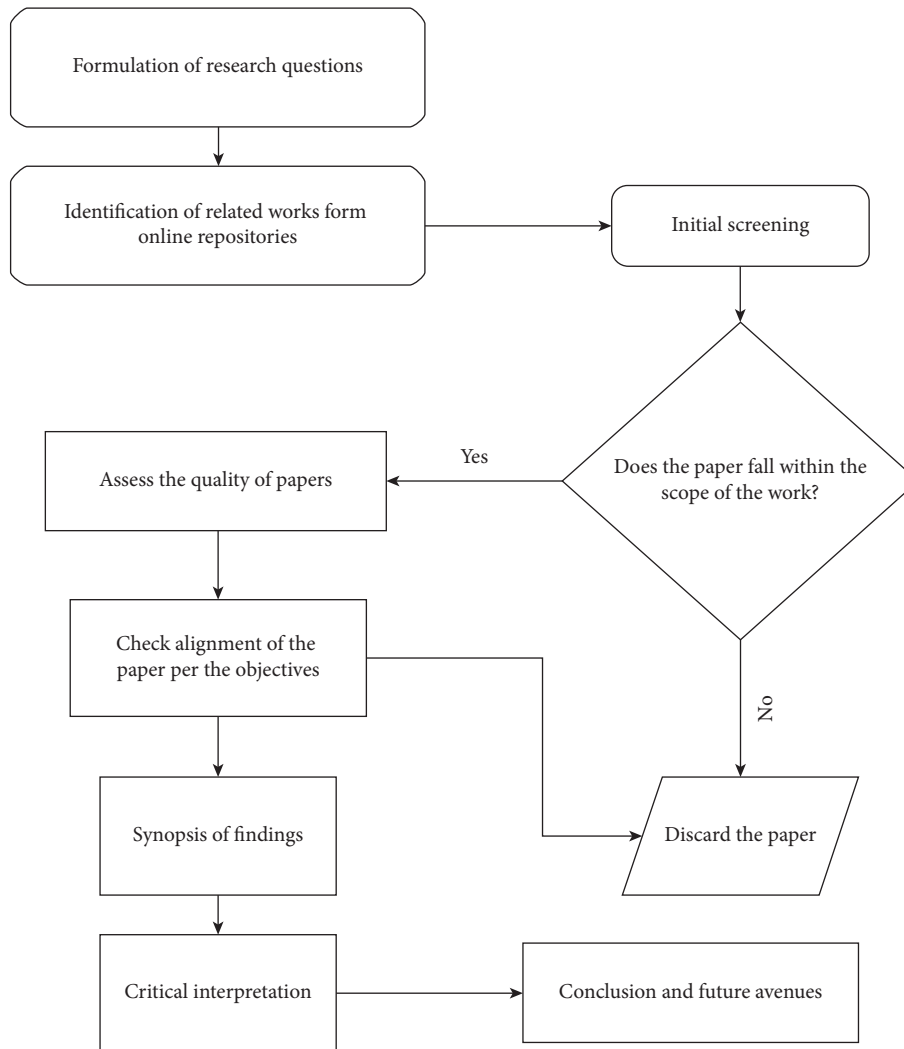
FIGURE 1: Systematic review approach implemented in the study.

analysis approach that could be deployed to estimate the vertical shaking forces. Their analysis highlighted that vertical excitation could lead to compression failure despite the safety factor for the fundamental load be in the range of 2.5. Ghobarah and Elnashai [35] presented the analysis in the contribution of vertical shaking on the seismic behavior of RC building considering low- and medium-rise RC buildings. They concluded that the vertical excitation would significantly affect the seismic performance of RC buildings. The vertical excitation was responsible for damage of existing nonductile RC moment-resisting frame building as well as the well designed RC building. The effect on drift was not severe when P-Δ effects become dominant. They further highlighted that 10–20% additional strength loss was attributed to the effects of vertical excitation. Similarly, the response modification factor was decreased by 30% when vertical excitation was accounted for. They reiterated that the near-field vertical shaking would lead to significant damage to the RC buildings.

In 2000, Diotallevi and Landi [36] presented an analysis of the vertical excitation in seismic response of a five-storied RC frame building using several strong motion records. They compared the response of building with and without the vertical excitation and concluded that the vertical shaking would be detrimental due to the adverse effects in column behavior. They further presented that the vertical excitation would lead to considerable fluctuations in the axial force, and hence the column behavior would be anomalous leading to a significant variation in global structural response. A greater roof displacement was prevalent, and the number of plasticized regions was greater in the columns. Significant reduction in the ductility was responsible for high axial compression, and the moment-curvature loops had become more random, and the greater axial force was responsible for greater peak values of moment and shear. Elgamal and He [8] denoted that the V/H response spectra would be strongly dependent on period and source to site distance and further concluded that the commonly used V/H ratio of 2/3 would be too conservative at high frequencies for up to 40 km source to site distance. They concluded that significantly high frequency (≥8 Hz) was prevalent in vertical excitations. However, their review

and analysis are more focused on seismological aspects rather than impacts of strong vertical shaking on buildings. Similar seismological studies regarding the strong vertical shaking in near-field regions are also performed by several researchers (see, e.g., [37–44]). Mazza and Vulcano [45] performed analysis on the effects of combined vertical and horizontal components of near-fault ground motions in the nonlinear dynamic response of the base-isolated building. They concluded that the compressive force exceeded the corresponding load for balanced failure in all the stories except the top. Loghman et al. [46] assessed the performance of base-isolated structures mounted on a triple concave friction pendulum (TCFP) bearing deploying the vertical excitation and concluded that the maximum error in calculating the base shear of structure would be 29.5%. They pointed out that if vertical excitation is not considered for superstructure with <0.6 sec period, the base shear would be underestimated. They further remarked that the inclusion of the vertical component is also critical in practical designs. Dana et al. [47] presented a comparative study considering code-based pseudo-static vertical excitation and nonlinear response history analysis which considers vertical ground excitation for a whole steel frame building and several 2D steel frame buildings. They concluded that the conventional code-based approach would give rise to conservative results as this underestimates the interior column compression demands by up to 40% with an average of ~20%. Similarly, the moments at the face of the columns were 65% greater than those for the code-based approach, and the magnitude difference was greater for upper stories when compared with the lower ones. Di Sarno et al. [48] performed finite element analysis of RC frame buildings using the recorded ground motions of the L'Aquila earthquake and concluded that the combination of horizontal and vertical ground motion is required for reliable seismic performance assessment. They highlighted the need for experimental and numerical assessment campaigns to rectify the mechanical models to evaluate the shear capacity of structural members. Mazza and Vulcano [49] and Mazza [50] depicted that the base isolators would sustain tensile loads under vertical excitation of the near-field earthquake. The consequence of such tensile loads may lead to the failure of the base isolation system due to large displacement. Recognizing the role of vertical seismic excitation in the modification of the axial stresses in masonry, Rinaldin et al. [51] performed nonlinear analyses of masonry structures to depict the lateral load resistance of masonry piers. They concluded that the inclusion of the vertical component may lead to an increase in demand/capacity ratio by an average value of 15% for the masonry piers. Liberatore et al. [52] performed the finite discrete element model of a masonry structure using recorded accelerograms. They concluded that vertical excitation induces more intense failures in masonry structures with small cohesion due to high-frequency content of the vertical shaking compared with the horizontal one. Elhifnawy et al. [53] considered four analysis schemes, viz., one horizontal component, two horizontal components, one horizontal and the vertical components, and two horizontal and the vertical components and found that the multiple components of the

earthquake significantly affect the axial forces and strain ductility factors of the columns. Meanwhile, the effect would not be considerable in terms of lateral deformation response. Abdollahiparsa et al. [54] analyzed the effects of vertical excitation considering soil-structure interaction in steel frame buildings. They concluded that the vertical excitation when combined with the soil-structure interaction effect may increase the axial force on columns by ~50%, maximum vertical displacement on beams by twofold, and story drift by ~40%. Asgarian et al. [55] performed nonlinear dynamic analysis of three moment-resisting frame buildings considering 15 recorded near-field accelerograms. They concluded that the vertical excitation does not significantly affect the dynamic response of the structure in the elastic range; however, they noted remarkable variation in the nonlinear range. Kim et al. [56] depicted that shear failure would be random when vertical excitation is considered in analyses. Wang et al. [57] obtained time histories of bending moment and shear capacities using numerical modeling and demonstrated that vertical excitation would affect both capacities due to high frequency and significant amplification leading to premature failure or anomalous failure modes and casted doubt in the use of capacity design approach. The shifting of brittle shear failure from ductile failure mode due to considerable variation in axial force and presence of tension in piers under near-field ground shaking was revealed by Hosseinzadeh [58] using numerical modeling and by Lee and Mosalam [59] using experimental approach.

As highlighted by Anderson and Bertero [60], seismic demand would increase in the case of coupling the horizontal and vertical components of strong ground motion due to increased lateral forces and P-Δ effects. Thus, many researchers felt the need for coupling the horizontal and vertical components of earthquakes to predict more realistic behavior. Ju et al. [61] proposed a methodology to perform three-dimensional dynamic analysis of buildings considering vertical excitation. They propose that four fundamental considerations such as division of the main girder into two elements, inclusion of secondary beams, avoidance of floor stiffness if the floor is too thick, and the use of 80% vertical effective mass led to precise results. With 1080 time-history analyses and 180 static analyses, they concluded that the relationships of extreme column axial forces and beam moments between vertical excitation and dead loads would be linearly proportional to the maximum acceleration taken from the response spectrum for the first vertical frequency. The method proposed by Collier and Elnashai [62] facilitates estimating the structural response under coupled vertical and horizontal components of strong ground motion. Gulerce and Abrahamson [63] and Gulerce et al. [64] developed and implemented the probabilistic seismic demand model and probabilistic seismic hazard assessment procedures to incorporate the randomness of strong ground motion and variation in structural characteristics. They also proposed that the ratio of vertical to horizontal motion would serve as the intensity measure for probabilistic seismic demand models. The study by Warn and Whittaker [65] highlighted that the direct sum of the peak axial forces

(vertical) that would be induced by the vertical excitation and overturning moment would overestimate the actual axial force on bearing. To this end, Wei et al. [66] highlighted that the simplified approaches may be effective in the estimation of seismic demands of structures but fail to incorporate the variation in moment capacity, shear capacity, and ductility related to the interactions of horizontal and vertical excitations. Recognition of vertical excitation led damages has also emerged after significant earthquakes as reported by Augenti and Parisi [67], Gautam and Chaulagain [68], Kim and Elnashai [69], Bovo et al. [70], Nadim et al. [71], and others. However, the majority of forensic interpretations and damage analyses lack explicit evidence regarding the effects of vertical shaking on structures. Meanwhile, Ambraseys and Simpson [11] and Kale and Akkar [72] have proposed vertical spectra for Europe. Ercolino et al. [73] performed forensic analysis and numerical modeling to assess the causes of roof damage during the Emilia-Romagna earthquake and justified that the collapse of roof elements was attributed to the vertical component of earthquake in the near-field region. Due to the occurrence of considerably large vertical excitation, high relative displacement and low frictional resistance were noted as uplift phenomena in nonlinear dynamic analysis considered by the authors. The effect of three components of earthquake excitation could be in particular more influential for low period structures with sliding support [74]. Similarly, Liauw et al. [75] highlighted that the vertical response of structure is the function of frictional stress that is governed by the supporting element on the foundation pad. They concluded that the inclusion of vertical excitation contributes in the sliding system. Similarly, Lin and Tadjbakhsh [76] confirmed that the vertical excitation can in particular affect the foundation system that is harmonically excited. The high-frequency content associated with the early period excitation due to vertical component of strong motion was reflected in several numerical studies (e.g., [51, 77–84]). Kim et al. [84] performed numerical studies of 13 RC buildings considering the effects of strong vertical shaking. With the variation of vertical-to-horizontal PGA ratio, they studied the effects on vertical excitation on axial force, shear capacity, and shear demand of RC columns. They finally concluded that the vertical excitation leads to the variation in axial force and shear capacity so that vertical excitation cannot be left behind for the purpose of seismic assessment and design of RC buildings. Tian et al. [83] concluded that the effect of vertical ground shaking will not be significant when considering interstory drift as a performance parameter; however, punching failure will dominantly occur, which is seldom expected in horizontal excitations only. They highlighted that the punching failure will reduce the lateral drift capacity by 23%. Lu et al. [85] conducted shake table testing of suspended ceilings. They observed the occurrence of damage to suspended ceilings due to both horizontal and vertical excitations. The experimental campaign concluded that damage to suspended ceilings is not governed by the horizontal shaking. On the contrary, the vertical shaking significantly contributed to the failure of the suspended ceiling-frame system [85]. Hosseini and Nezamabadi [86] studied the vertical response of Iranian steel buildings considering three-, four-, and five-storied steel buildings. Scenario analyses performed considering the vertical excitation and without considering it resulted considerable variation in compression and tension leading to noticeable uplift. They further justified that the effects of vertical shaking will be more pronounced in moment frames rather than the bracing members. The authors numerically validated that the effect of vertical component will be more concentrated in the upper stories rather the lower ones. Furthermore, the base shear ratio estimated for linear to nonlinear analysis scheme was obtained in between 0.34 and 1.89 [86]. Yamazaki et al. [87] also studied the effects of vertical excitations on steel frame constructions. They concluded that the fluctuation of axial force in weak columns is more significant than the same in weak beams. The numerical and experimental analyses highlighted that the ratio of vertical to horizontal fundamental vibration period was 0.2 or less [87]. Their analysis also highlighted that the vertical excitation would affect the interstory drift in the range of ±3%, which indicates that the horizontal excitation dominates the lateral displacement significantly than the vertical one. The authors concluded that the increase in axial force will give rise to significant reduction in shear capacity and thus aggravate the possibility of shear failure. Guo et al. [88] studied the combined effect of horizontal and vertical ground shaking on RC chimneys using fragility based assessment. They considered near-field ground motions to assess the seismic behavior and constructed fragility functions. They concluded that the likelihood of failure will be significantly increased when horizontal component of ground shaking intensity is significantly large. They recommend the use of combined horizontal and vertical excitations in seismic vulnerability assessment of RC chimneys. Similarly, Nezamabadi et al. [89] assessed performance of regular and mass asymmetric structures. They outlined that the near-fault vertical shaking will have significance, and thus the vertical design spectrum can be used to incorporate the effects arising from strong vertical shaking in near-fault regions. Furukawa et al. [90] conducted full scale shake table testing to assess the seismic response of base-isolated structure considering vertical excitation. The analysis performed by [91] showed that the displacements will be increased by up to 56% in a three-storied steel building when considering the vertical component of ground shaking. However, they used near-fault strike-normal strong ground motions only. They also noted that the vertical shaking will increase axial forces in column.

Several other studies perform analysis of building systems with base isolation to quantify the effects of vertical excitation (e.g., [49, 74, 92–95], among others). From the above discussions and broad literature review, it should be noted that the necessity of consideration of vertical excitation in design and code formulation is a must to capture the anomalous behavior of buildings during earthquakes. Furthermore, it is clear that the strong vertical shaking in the global context is confined to the near-field regions only. As limited studies have duly focused on the impacts of vertical shaking and have reiterated the need for formulation of

TABLE 1: Summary of strong motion records after some Himalayan earthquakes (modified from [113–115]).

Accelerometric station	Earthquake	Epicentral distance (km)	Recorded PGA (g)			V/H
			EW	NS	UD	
NSC	Gorkha (2015)	80	0.13	0.18	0.2	1.27
Kantipath	Gorkha (2015)	81	0.13	0.14	0.17	1.26
Kirtipur	Gorkha (2015)	80	0.25	0.15	0.12	0.58
Tribhuvan University	Gorkha (2015)	81	0.22	0.16	0.14	0.73
Patan	Gorkha (2015)	83	0.13	0.15	0.13	0.93
Thimi	Gorkha (2015)	87	0.12	0.15	0.18	1.33
NSC	Nepal-Sikkim border (2011)	272	0.032	0.05	0.018	0.43
Gangtok	Nepal-Sikkim border (2011)	70	0.15	0.16	0.13	0.84
Siliguri	Nepal-Sikkim border (2011)	115	0.16	0.2	0.12	0.66

vertical spectra for analysis, no significant improvements could be found in the existing literature regarding this regard. Although the scope of the paper is limited to building structures only, the authors recognize the notable contributions in the field of bridge engineering considering the effects of vertical excitation as reported elsewhere (see, e.g., [66, 96–101], among others). Despite buildings and bridges, many researchers have considered the vertical excitation to assess the seismic performance of various types of structures (e.g., [88, 102–106], among others).

4. Evidence and Avenues beyond Near-Field Regions

Virtually all existing literatures report the strong vertical shaking during an earthquake in the near-field region only. On the contrary, the focus of this paper is to drag the attention of the researchers towards strong vertical shaking in the far-field region. Studies by Collier and Elnashai [62], Ambraseys and Simpson [11], Ambraseys and Douglas [107], Kalkan and Gulkan [108], Gulerce and Abrahamson [63], and Boomer et al. [109] highlighted that the vertical to horizontal spectral ratio is the function of source to site distance as well as local soil condition. Accordingly, the Kathmandu Valley as well as other valleys that are located in the alluvial deposit may observe significant local site effects during earthquakes (see, e.g., [43]). In this case, vertical excitation would be dominant and may result in anomalous damage mechanisms. The first evidence of strong vertical shaking and associated damage in Nepal was reported by Rana in 1935 [110]. In the monograph, the author reported that despite being ~150 km away from the epicenter of the 1934 earthquake [111], buildings in Kathmandu Valley observed damage to the upper stories and also noted that the shaking was up down due to strong vertical shaking. Ground motion records in Nepal are available for 2011 and 2015 earthquakes only, so the account by Rana [110] cannot be numerically justified. Table 1 summarizes the peaks of horizontal and vertical components of recorded earthquakes in central Himalaya together with the epicentral distances and V/H ratios. As shown in Table 1, the 2011 earthquake was recorded at 70, 115, and 272 km from the epicenter. Notably, even the recording at 70 km shows V/H ratio as 0.84. Similarly, at 115 km, the ratio appears to be 0.66, and at 272 km from the epicenter (at Kathmandu), the ratio is still

0.43. Although significant damage did not occur in the instrumented location in Kathmandu Valley during the 2011 Sikkim-Nepal border earthquake, however, clear evidence of strong vertical shaking in the far-field was present. In 2015, Nepal was struck by a strong earthquake of moment magnitude 7.8. Several instrumental recordings are also available for the earthquake. As shown in Table 1, all except one recording in Kathmandu valley, which is more than 75 km far from the epicenter, depicted the V/H ratio more than 2/3 (Figure 2). At 80 km epicentral distance, the ratio is obtained as 1.33. The range of V/H in Kathmandu Valley is obtained between 0.58 and 1.33. This signifies that the central Himalayan earthquakes are likely to depict strong if not strongest vertical shaking even in the far-field regions. Figure 3 depicts that the frequency of vertical shaking was ~10 Hz which should have played a vital role in anomalous building damage as reported by Gautam et al. [111]. The accelerometric station is located on loose soil deposit area so there is also a possibility of seismic site effects. The Kathmandu basin is ~500 m deep, and interbedding of silts, sands, and clay is dominant [112]. This could be one of the possible reasons behind the strongest vertical shaking in central Kathmandu during the 1934 and 2015 earthquakes.

As opposed to the world earthquakes, as reported by Broderick et al. [33] and Elnashai et al. [116], the central Himalayan earthquakes depict relatively similar or greater V/H ratio even in the far-field regions when compared with the near-field records of Northridge and Kobe earthquakes. Apart from seismological evidence, the 2015 Gorkha earthquake in Nepal displayed exemplary evidence regarding the effects of strong vertical excitation in far-field. Figure 4 shows a soft-story building with a collapsed third story due to strong vertical shaking which is similar to the evidence presented by other researchers in the near-field regions. The excessive axial force due to vertical excitation that usually becomes more significant in upper stories should have caused the collapse. Except for the collapsed story, the building sustained minimal damage. Several cases of upper story collapse were reported in Kathmandu Valley, especially in the soft soil deposit locations. The V/H ratio also depicts the higher value especially in the case of soft soil locations such as Thimi and NSC (Table 1). Similarly, shear damage in the columns in the seventh story of a 14-storied apartment building was prevalent in the downtown of Kathmandu. It is pertinent to note that shear damage to
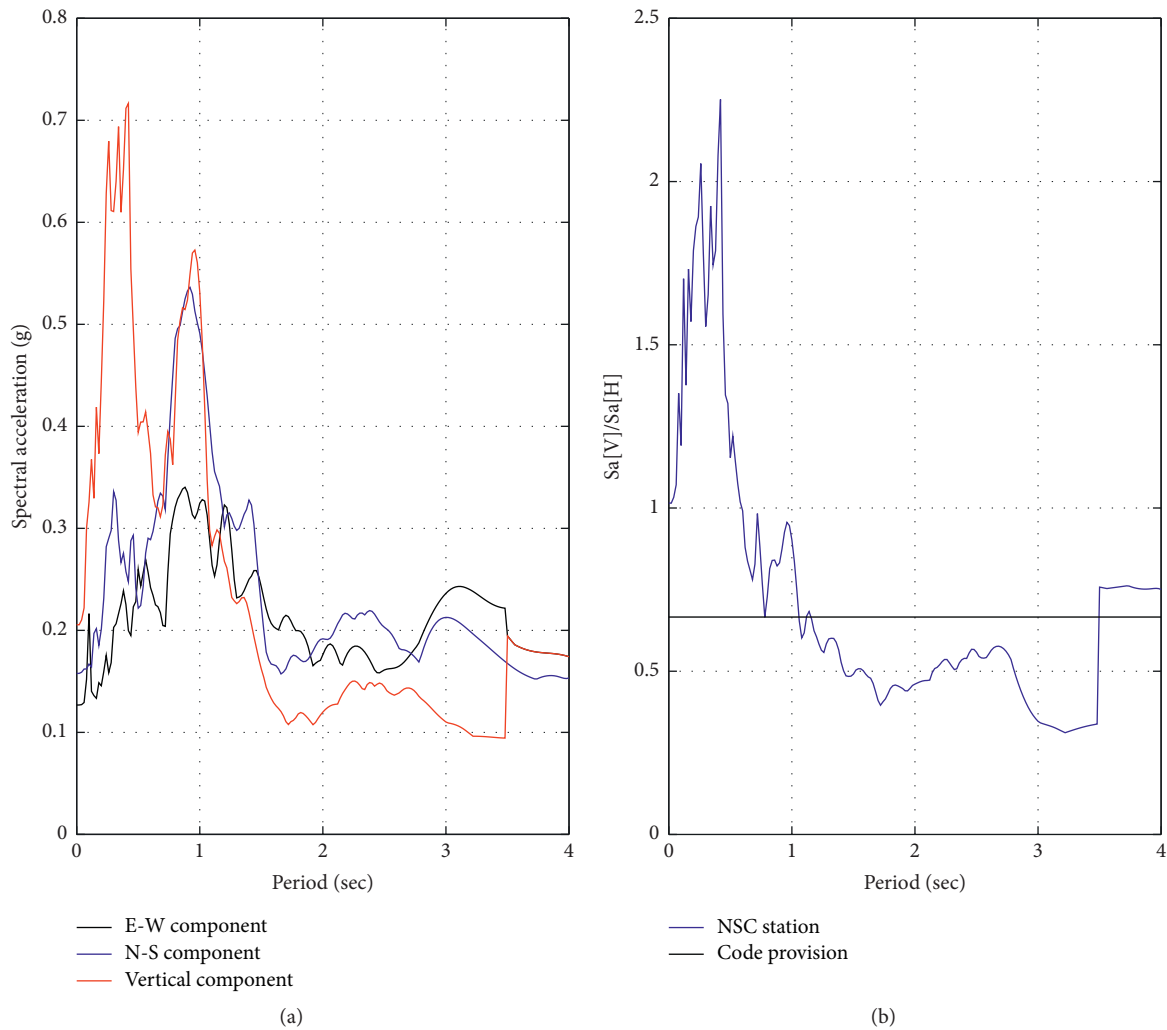
FIGURE 2: (a) Acceleration response spectra of the 2015 Gorkha earthquake recorded by National Seismological Center (NSC) [117] and (b) vertical to horizontal spectral ratio for the Gorkha earthquake.

columns in the location where maximum shear force is not expected (Figure 5), intermediate/upper story collapse (Figure 6), and shear-compression failure of internal columns among others clearly indicate the presence of strong vertical excitation during the Gorkha earthquake in the far-field regions. These shreds of evidence strongly demand due consideration of vertical excitation during seismic code formulation. The Nepal Building Code [31], on the contrary, does not account for the effects of the vertical shaking on building except for secondary structural elements. However, the earthquakes that struck Nepal Himalaya have consistently notified that the strong vertical shaking in far-field is significant. So, further research is needed to quantify the effects of strong far-field shaking beyond the conventional near-field analyses. To quantify the effects of strong far-field excitation, numerical studies and parametric analyses are required. We aim to perform studies based on finite element analysis considering strong far-field excitations considering parametric analyses. Furthermore, the effect of soil-

structure interaction in the case of far-field vertical excitation will be more influential in terms of foundation performance. So, studies that consider the effect of soil-structure interaction together with strong far-field vertical shaking are also important to capture the anomalous behaviors of buildings that were observed during several historical earthquakes. In the case of strong far-field excitation, the conventional design guidelines may not assure adequate seismic performance as shear damage in the middle portion of columns, higher axial force demand in the upper story column, and others could lead to unprecedented mechanisms and damages. Thus, experimental campaigns considering the effects of strong far-field vertical excitations will further advance the understanding regarding the mechanisms and possible remedial measures that could be implemented in building codes. To achieve the target performance of buildings in seismic areas, the occurrence and possible effects of strong far-field shaking should also be considered in contemporary seismic designs and assessments.

(a)

(b)

(c)

(d)
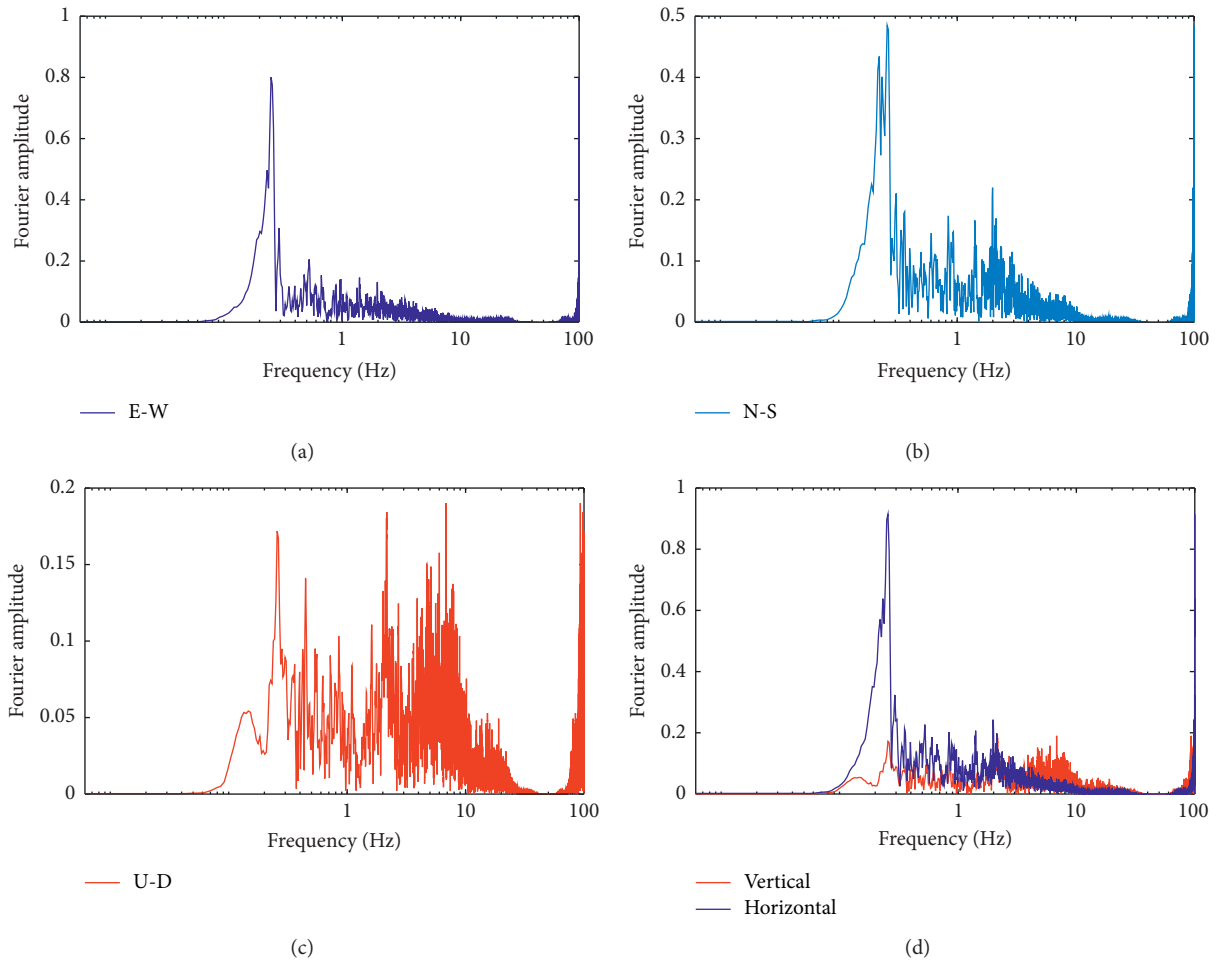
Figure 3: Fourier spectra of the Gorkha earthquake: (a) east-west (E-W) component, (b) north-south (N-S) component, (c) vertical (U-D) component, and (d) vertical and horizontal components.

Figure 4: Intermediate story collapse in a modern hotel building compliant to the prevalent code at Nagarkot, Bhaktapur, Nepal.

FIGURE 5: Shear damage of a column at midheight in Kathmandu due to the 2015 Gorkha earthquake.

FIGURE 6: Collapsed top story in a soft-story building in Kathmandu by the Gorkha earthquake.

5. Conclusion

A systematic review on the effect of vertical shaking on buildings is presented in this study. With the help of a broad literature review, the evidence for near-field and far-field vertical excitations is summarized. The sum of the reported evidence highlights that there are anomalous damage mechanisms that could not be explained by the conventional analyses. This supports the significance of inclusion of strong vertical excitation in the far-field regions too. Numerical simulation results presented by several researchers also highlight the clear evidence of detrimental impacts on

structures at least in terms of greater axial forces in the upper stories, occurrence of shear damage in noncritical regions, damage to interior columns, and variation in base shear, among others. However, virtually all previous works focused on the near-field regions only; thus, the strong far-field vertical excitation has not gotten adequate attention so far. The evidence from central Himalayan earthquakes shows that the strong/strongest vertical shaking is not limited to the near-field regions only and that may also lead to detrimental impacts on structures in the far-field regions. The damage mechanisms in far-field regions due to recent earthquakes are presented together with the V/H ratios of accelerometric records. It is concluded that there is a dire need for investigation regarding the occurrence of strong vertical shaking in the far-field regions as well and its impacts on structures and infrastructures. Further numerical and experimental campaigns are required to address this scenario. In addition, seismic codes should also consider the impacts of strong far-field vertical excitations. This study reports only a few pieces of evidence of occurrence of strong vertical excitation in the far-field regions and the related damages. The authors would perform numerical analysis using strong far-field vertical excitation to assess the seismic performance of RC buildings. Moreover, future works may also consider experimental studies implementing strong far-field vertical excitations.

Data Availability

The data used to support the findings of this study are included within the article.

Conflicts of Interest

The authors declare that they have no conflicts of interest.

References

[1] Z. P. Wen, Y. X. Hu, and K. T. Chau, "Site effect on vulnerability of high-rise shear wall buildings under near and far field earthquakes," *Soil Dynamics and Earthquake Engineering*, vol. 22, pp. 1175–1182, 2002.

[2] A. Aziminejad and A. S. Moghadam, "Fragility-based performance evaluation of asymmetric single-story buildings in near field and far field earthquakes," *Journal of Earthquake Engineering*, vol. 14, pp. 789–816, 2010.

[3] C. Jäger and C. Adam, "Influence of collapse definition and near-field effects on collapse capacity spectra," *Journal of Earthquake Engineering*, vol. 17, pp. 859–878, 2013.

[4] E. N. Farsangi, A. A. Tasnimi, and B. Mansouri, "Fragility assessment of RC-MRFs under concurrent vertical-horizontal seismic action effects," *Computers and Concrete*, vol. 16, no. 1, pp. 99–123, 2015.

[5] Y. Yazdani and M. Alembagheri, "Seismic vulnerability of gravity dams in near-fault areas," *Soil Dynamics and Earthquake Engineering*, vol. 102, 2017.

[6] F. S. Akhavan Hejazi and M. Khan Mohammadi, "Investigation on sloshing response of water rectangular tanks under horizontal and vertical near fault seismic excitations," *Soil Dynamics and Earthquake Engineering*, vol. 116, pp. 673–653, 2019.

[7] N. M. Newmark, J. A. Blume, and K. K. Kapur, "Seismic design spectra for nuclear power plants," *Journal of the Power Division*, vol. 99, no. 2, pp. 287–303, 1973.

[8] A. Elgamal and L. He, "Vertical earthquake ground motion records: an overview," *Journal of Earthquake Engineering*, vol. 8, pp. 663–697, 2004.

[9] Y. Bozorgnia and M. Niazi, "Distance scaling of vertical and horizontal response spectra of the Loma Prieta earthquake," *Earthquake Engineering and Structural Dynamics*, vol. 22, pp. 695–707, 1993.

[10] M. Niazi and Y. Bozorgnia, "Behaviour of near-source vertical and horizontal response spectra at smart-1 array, Taiwan," *Earthquake Engineering and Structural Dynamics*, vol. 21, pp. 37–50, 1992.

[11] N. N. Ambraseys and K. A. Simpson, "Prediction of vertical response spectra in Europe," *Earthquake Engineering and Structural Dynamics*, vol. 25, pp. 401–412, 1996.

[12] T. Furumura, "Destructive near-fault strong ground motion from the 2016 kumamoto prefecture, japan, m7.3 earthquake," *Landslides*, vol. 13, 2016.

[13] A. Rosti, M. Rota, and A. Penna, "Damage classification and derivation of damage probability matrices from L'Aquila (2009) post-earthquake survey data," *Bulletin of Earthquake Engineering*, vol. 16, 2018.

[14] A. Scala, G. Festa, and S. Del Gaudio, "Relation between near-fault ground motion impulsive signals and source parameters," *Journal of Geophysical Research: Solid Earth*, vol. 123, pp. 7707–7721, 2018.

[15] A. Akinci, L. Malagnini, and F. Sabetta, "Characteristics of the strong ground motions from the 6 April 2009 L'Aquila earthquake, Italy," *Soil Dynamics and Earthquake Engineering*, vol. 30, pp. 320–335, 2010.

[16] S. Ruiz, "Short-period rupture process of the 2010 mw 8.8 maule earthquake in Chile," *Earthquake Spectra*, 2012.

[17] K. S. Khan, R. Kunz, J. Kleijnen, and G. Antes, "Five steps to conducting a systematic review," *Journal of the Royal Society of Medicine*, vol. 96, no. 3, pp. 118–121, 2003.

[18] A. J. Papazoglou and A. S. Elnashai, "Analytical and field evidence of the damaging effect of vertical earthquake ground motion," *Earthquake Engineering and Structural Dynamics*, vol. 25, pp. 1109–1137, 1996.

[19] S. A. Anagnostopolous, D. Rinaldis, V. A. Lekidis, V. N. Margaris, and N. P. Theodulidis, "The Kalamata, Greece, earthquake of September 13, 1986," *Earthquake Spectra*, 1987.

[20] A. S. Elnashai and K. Pilakoutas, *The Kalamata (Greece) Earthquake of 13 September 1986*, London, 1986.

[21] A. J. Papazoglou, *Near-source Vertical Earthquake Ground Motion; an Assessment of Causes and Effects*, Imperial College, London, 1995.

[22] A. S. Elnashai and A. J. Papazoglou, *Vertical Earthquake Ground Motion; Evidence, Effects and Simplified Analysis Procedures*, 1995.

[23] A. S. Elnashai, K. Pilakoutas, and N. N. Ambraseys, "The Kalamata earthquake: performance of reinforced concrete buildings," in *SECED con$ on Ciuil Engineering Dynamics*, pp. 193–207, 1988.

[24] A. S. Elnashai, K. Pilakoutas, N. N. Ambraseys, and I. D. Lefas, "Lessons learnt from the Kalamata (Greece) earthquake of 13 september 1986," *European Journal of Environment and Earth Sciences*, vol. 1, pp. 11–19, 1987.

[25] G. M. Verderame, F. De Luca, P. Ricci, and G. Manfredi, "Preliminary analysis of a soft-storey mechanism after the

2009 L'Aquila earthquake," *Earthquake Engineering and Structural Dynamics*, vol. 40, pp. 925–944, 2011.

[26] H. Alinouri, F. A. Danesh, and S. B. Beheshti-Aval, "Effect of soft-storey mechanism caused by infill elimination on displacement demand in nonlinear static procedure using coefficient method," *Structural Design of Tall and Special Buildings*, vol. 22, pp. 1296–1309, 2013.

[27] M. Georgantzis, *Effect of Vertical Motion on Behaviour Factors*, Imperial College, London, 1995.

[28] O. Papadopoulou, *The Effect of Vertical Excitation on Reinforced Concrete Multi-Storey Structures*, Imperial College, London, 1989.

[29] C. Papaleontiou and J. M. Roesset, "Effect of vertical accelerations on seismic response of frames," in *Structural Dynamics EURODYN* vol. 93, pp. 19–26, 1993.

[30] M. Fardis, *Analysis and Design of Reinforced Concrete Buildings According to EC-2 and EC-8*, 1994.

[31] Government of Nepal, *Nepal National Building Code*, Government of Nepal, Nepal, 1994.

[32] Bureau of Indian Standards, *Indian Standard IS. IS 1893 (Part 1): 2002: Criteria for Earthquake Resistant Design of Structures*, Bureau of Indian Standards, India, 5th revision, 2002.

[33] B. M. Broderick, A. S. Elnashai, N. N. Ambraseys, J. J. Barr, R. G. Goodfellow, and E. M. Higazy, *The Northridge (California) Earthquake of 17 January 1994: Observations, Strong-Motion and Correlative Response Analyses*, London, 1994.

[34] A. S. Elnashai and A. J. Papazoglou, "Procedure and spectra for analysis of rc structures subjected to strong vertical earthquake loads," *Journal of Earthquake Engineering*, vol. 1, pp. 121–155, 1997.

[35] A. Ghobarah and A. S. Elnashai, "Contribution of vertical ground motion to the damage of RC building," in *Proceedings of the 11th European Conference on Earthqiake Engineering*, Paris, France, September 1998.

[36] P. P. Diotallevi and L. Landi, "Effect OF the axial force and OF the vertical ground motion component ON the seismic response OF R/C frames," ", in *Proceedings of the 12th World Conference in Earthquake Engineering*, p. 1026, Auckland, New Zealand, February 2000.

[37] T. Perea and L. Esteva, "Analysis of vertical ground motions of near source records in Mexico," in *Proceedings of the 13th World Conference on Earthquake Engineering*, p. 1852, Vancouver, BC, Canada, August 2004.

[38] A. S. Elnashai, L. He, and A. Elgamal, "Spectra for vertical earthquake ground motion," in *Proceedings of the 13th World Conference on Earthquake Engineering*, p. 2309, Vancouver, BC, Canada, August 2004.

[39] Y. Bozorgnia, K. W. Campbell, and M. Niazi, "Observed spectral characteristics OF vertical ground motion recorded during worldwide earthquakes from 1957 to 1995," in *Proceedings of the 12th World Conference in Earthquake Engineering*, p. 2671, Auckland, New Zealand, February 2000.

[40] I. A. Beresnev, A. M. Nightengale, and W. J. Silva, "Properties of vertical ground motions," *Bulletin of the Seismological Society of America*, vol. 92, no. 8, pp. 3152–3164, 2002.

[41] C. H. Loh and M. J. Ma, "Reliability assessment of structure subjected to horizontal-vertical random earthquake excitations," *Structural Safety*, vol. 19, no. 1, 1997.

[42] B. Fry, "Strong shaking in recent New Zealand earthquakes," *Eos (Washington. DC)*, vol. 92, no. 41, pp. 349–351, 2011.

[43] R. Rupakhety, S. Olafsson, and B. Halldorsson, "The 2015 Mw 7.8 Gorkha Earthquake in Nepal and its aftershocks: analysis of strong ground motion," *Bulletin of Earthquake Engineering*, vol. 15, 2017.

[44] R. Rupakhety, "Seismotectonic and Engineering Seismological Aspects of the M W 7.8 Gorkha, Nepal, Earthquake," in *Impacts and Insights of Gorkha Earthquake in Nepal*, pp. 19–45, Elsevier, 2018.

[45] F. Mazza and A. Vulcano, "Effects of the vertical acceleration on the response of base-isolated structures subjected to near-fault ground motions," in *Proceedings of the 13th World Conference on Earthquake Engineering*, p. 2934, Vancouver, BC, Canada, August 2004.

[46] V. Loghman, F. Khoshnoudian, and M. Banazadeh, "Effect of vertical component of earthquake on seismic responses of triple concave friction pendulum base-isolated structures," *JVC/Journal Vibration and Control*, 2015.

[47] M. Dana, "Effects of the seismic vertical component on structural behavior - an analytical study of current code practices and potential areas of improvement," in *Proceedings of the NCEE 2014 - 10th U.S. National Conference on Earthquake Engineering: Frontiers of Earthquake Engineering*, Anchorage, AL, USA, July 2014.

[48] L. Di Sarno, A. S. Elnashai, and G. Manfredi, "Assessment of RC columns subjected to horizontal and vertical ground motions recorded during the 2009 L'Aquila (Italy) earthquake," *Engineering Structures*, vol. 33, pp. 1514–1535, 2011.

[49] F. Mazza and A. Vulcano, "Effects of near-fault ground motions on the nonlinear dynamic response of base-isolated r.c. framed buildings," *Earthquake Engineering and Structural Dynamics*, vol. 41, pp. 211–232, 2012.

[50] F. Mazza, "Nonlinear dynamic response of RC buildings with different base isolation systems subjected to horizontal and vertical components of near-fault ground motions," *Open Construction and Building Technology Journal*, vol. 12, pp. 135–144, 2012.

[51] G. Rinaldin, M. Fasan, S. Noé, and C. Amadio, "The influence of earthquake vertical component on the seismic response of masonry structures," *Engineering Structure*, vol. 185, pp. 184–193, 2019.

[52] D. Liberatore, C. Doglioni, O. AlShawa, S. Atzori, and L. Sorrentino, "Effects of coseismic ground vertical motion on masonry constructions damage during the 2016 Amatrice-Norcia (Central Italy) earthquakes," *Soil Dynamics and Earthquake Engineering*, vol. 120, pp. 423–435, 2019.

[53] L. Elhifnawy, H. Abou-Elfath, and E. El-Hout, "Inelastic performance of RC buildings subjected to near-source multicomponent earthquakes," *Alexandria Engineering Journal*, vol. 56, pp. 511–522, 2017.

[54] H. Abdollahiparsa, P. Homami, and F. Khoshnoudian, "Effect of vertical component of an earthquake on steel frames considering soil-structure interaction," *KSCE Journal of Civil Engineering*, vol. 20, 2016.

[55] B. Asgarian, A. Norouzi, P. Alanjari, and M. Mirtaheri, "Evaluation of seismic performance of moment resisting frames considering vertical component of ground motion," *Advances in Structural Engineering*, vol. 15, no. 8, pp. 1439–1453, 2012.

[56] S. J. Kim, C. J. Holub, and A. S. Elnashai, "Analytical assessment of the effect of vertical earthquake motion on RC bridge piers," *Journal of Structural Engineering*, vol. 137, 2011.

[57] Z. Wang, L. Dueñas-Osorio, and J. E. Padgett, "Seismic response of a bridge-soil-foundation system under the combined effect of vertical and horizontal ground motions,"

Earthquake Engineering and Structural Dynamics, vol. 42, pp. 545–564, 2013.

[58] N. Hosseinzadeh, "Vertical component effect OF earthquake IN seismic performance OF reinforced concrete bridge piers," in *Proceedings of the 14th World Conference on Earthquake Engineering*, Beijing, China, October 2008.

[59] H. Lee and K. M. Mosalam, "Seismic evaluation of the shear behavior in reinforced concrete bridge columns including effect of vertical accelerations," *Earthquake Engineering and Structural Dynamics*, vol. 43, pp. 317–337, 2014.

[60] J. C. Anderson and V. V. Bertero, "Uncertainties in establishing design earthquakes," *Journal of Structural Engineering (United States)*, vol. 113, 1987.

[61] S. H. Ju, C. W. Liu, and K. Z. Wu, "3D analyses of buildings under vertical component of earthquakes," *Journal of Structural Engineering*, vol. 126, 2000.

[62] C. J. Collier and A. S. Elnashai, "A procedure for combining vertical and horizontal seismic action effects," *Journal of Earthquake Engineering*, vol. 5, pp. 521–539, 2001.

[63] Z. Gülerce and N. A. Abrahamson, "Site-specific design spectra for vertical ground motion," *Earthquake Spectra*, 2011.

[64] Z. Gulerce, E. Erduran, S. K. Kunnath, and N. A. Abrahamson, "Seismic demand models for probabilistic risk analysis of near fault vertical ground motion effects on ordinary highway bridges," *Earthquake Engineering and Structural Dynamics*, Article ID 1123, 2012.

[65] G. P. Warn and A. S. Whittaker, "Vertical earthquake loads on seismic isolation systems in bridges," *Journal of Structural Engineering*, vol. 134, 2008.

[66] B. Wei, C. Zuo, X. He, L. Jiang, and T. Wang, "Effects of vertical ground motions on seismic vulnerabilities of a continuous track-bridge system of high-speed railway," *Soil Dynamics and Earthquake Engineering*, 2018.

[67] N. Augenti and F. Parisi, "Learning from construction failures due to the 2009 L'Aquila, Italy, earthquake," *Journal of Performance of Constructed Facilities*, vol. 24, 2010.

[68] D. Gautam and H. Chaulagain, "Structural performance and associated lessons to be learned from world earthquakes in Nepal after 25 April 2015 (M_W 7.8) Gorkha earthquake," *Engineering Failure Analysis*, vol. 68, 2016.

[69] S. J. Kim and A. S. Elnashai, "Characterization of shaking intensity distribution and seismic assessment of RC buildings for the Kashmir (Pakistan) earthquake of October 2005," *Engineering Structure*, vol. 31, no. 12, 2009.

[70] M. Bovo, A. Barbaresi, D. Torreggiani, and P. Tassinari, "Collapse and damage to vernacular buildings induced by 2012 Emilia earthquakes," *Bulletin of Earthquake Engineering*, vol. 18, no. 3, 2020.

[71] F. Nadim, "The bam earthquake of 26 december 2003," *Bulletin of Earthquake Engineering*, vol. 2, no. 2, 2004.

[72] Ö. Kale and S. Akkar, "A new formulation for a code-based vertical design spectrum," *Earthquake Engineering and Structural Dynamics*, vol. 49, pp. 936–980, 2020.

[73] M. Ercolino, G. Magliulo, and G. Manfredi, "Failure of a precast RC building due to Emilia-Romagna earthquakes," *Engineering Structure*, vol. 118, 2016.

[74] H. Shakib and A. Fuladgar, "Response of pure-friction sliding structures to three components of earthquake excitation," *Computers and Structures*, vol. 81, no. 4, 2003.

[75] T. C. Liauw, Q. L. Tian, and Y. K. Cheung, "Structures on sliding base subject to horizontal and vertical motions," *Journal of Structural Engineering*, vol. 114, no. 9, 1988.

[76] B. C. Lin and I. Tadjbakhsh, ""Effect of vertical motion on friction-driven isolation systems," *Earthquake Engineering and Structural Dynamics*, vol. 14, no. 4, 1986.

[77] E. Lim, L. Jiang, and N. Chouw, "Dynamic response of a non-structural component with three supports in multi-directional earthquakes," *Engineering Structure*, vol. 150, 2017.

[78] Y. Xiang, Y. Feng Luo, Z. Chen Zhu, and Z. Yan Shen, "Estimating the response of steel structures subjected to vertical seismic excitation: idealized model and inelastic displacement ratio," *Engineering Structure*, vol. 148, 2017.

[79] Y. Xiang and Q. L. Huang, "Damping modification factor for the vertical seismic response spectrum: a study based on Japanese earthquake records," *Engineering Structure*, vol. 179, 2019.

[80] J. Náprstek and C. Fischer, "Dynamic stability of a vertically excited non-linear continuous system," *Computers and Structures*, vol. 155, 2015.

[81] K. Ren, "Assessing the reliability, resilience and vulnerability of water supply system under multiple uncertain sources," *Journal of Cleaner Production*, vol. 252, Article ID 119806, 2020.

[82] V. V. Bertero, S. A. Mahin, and R. A. Herrera, "Aseismic design implications of near-fault san fernando earthquake records," *Earthquake Engineering and Structural Dynamics*, vol. 6, no. 1, 1978.

[83] Y. Tian, X. Liu, and S. George, "Effects of vertical ground motion on seismic performance of reinforced concrete flat-plate buildings," *Journal of Structural Engineering*, vol. 146, no. 12, 2020.

[84] S. Kim, S. J. Kim, and C. Chang, "Analytical assessment of the effect of vertical ground motion on RC frames designed for gravity loads with various geometric configurations," *Advances in Civil Engineering*, vol. 2018, Article ID 4029142, 11 pages, 2018.

[85] Y. Lu, G. Mosqueda, Q. Han, and Y. Zhao, "Shaking table tests examining seismic response of suspended ceilings attached to large-span spatial structures," *Journal of Structural Engineering*, vol. 144, no. 9, 2018.

[86] M. Hosseini and M. F. Nezamabadi, "A study on the effect of vertical ground on the seismic response of steel buildigns," in *Proceedings of the 13th World Conference on Earthquake Engineering*, vol. 1368, pp. 3–8, Vancouver, BC, Canada, August 2004.

[87] S. Yamazaki, S. Minami, H. Mimura, and K. Udagawa, "Effects of vertical ground motions on earthquake response of of steel frames," in *Proceedings of the 12th World Conference on Earthquake Engineering*, p. 0663, Auckland, New Zealand, 2000.

[88] X. Guo, W. Chen, and J. Yu, "Combined effect of vertical and horizontal ground motions on failure probability of RC chimneys," *Advances in Civil Engineering*, vol. 2018, Article ID 9327403, 11 pages, 2018.

[89] M. F. Nezamabadi and F. Y. Vayeghan, "Development of seismic criteria for seismic responses of regular and irregular structures in plan considering vertical component of the nearfield records," *Journal of Structural Engineering*, vol. 5, no. 1, pp. 9–20, 2015.

[90] S. Furukawa, E. Sato, Y. Shi, T. Becker, and M. Nakashima, "Full-scale shaking table test of a base-isolated medical facility subjected to vertical motions," *Earthquake Engineering and Structural Dynamics*, vol. 42, no. 13, 2013.

[91] G. MacRae, D. Fields, I. Turkman, and H. Tagawa, "Effect of shaking characteristics on steel moment-resisting frames," *Structural Congress 2000*, vol. 103, pp. 1–8, 2004.

[92] W. Eltahawy and K. L. Ryan, "Performance of flexible frame building with horizontal and 3D seismic isolation when subjected to 3D ground shaking," *Earthquake Spectra*, vol. 36, no. 4, 2020.

[93] B. L. Khan, M. Azeem, M. Usman, S. H. Farooq, A. Hanif, and M. Fawad, "Effect of near and far field earthquakes on performance of various base isolation systems," *In Procedia Structural Integrity*, vol. 18, 2019.

[94] D. Liu, Y. Liu, D. Sheng, and W. Liao, "Seismic response analysis of an isolated structure with QZS under near-fault vertical earthquakes," *Shock Vibration*, vol. 2018, Article ID 9149721, 12 pages, 2018.

[95] Y. N. Huang, A. S. Whittaker, R. P. Kennedy, and R. L. Mayes, "Response of base-isolated nuclear structures for design and beyond-design basis earthquake shaking," *Earthquake Engineering and Structural Dynamics*, vol. 42, no. 3, 2013.

[96] S. H. Kim and M. Q. Feng, "Fragility analysis of bridges under ground motion with spatial variation," *International Journal of Non-Linear Mechanics*, vol. 38, pp. 705–721, 2003.

[97] K. H. Abdelkareem and A. MachidA, "No TitleEffect of vertical motion of earthquake on failure mode and ductility of RC bridge piers," in *Proceedings of the 12th World Conference in Earthquake Engineering*, Auckland, New Zealand, February 2000.

[98] M. Zahedi, G. Ghodrati Amiri, and M. Akbarzadeh, "Characteristics of vertical spectrum in near-field region and investigation of its effects on the dynamic response of bridges," in *Proceedings of the 4th International Conference on Earthquake Geotechnical Engineering*, p. 1535, Thessaloniki, Greece, June 2007.

[99] K. D. Makan, Y. Chen, T. Larkin, and N. Chouw, "The influence of vertical seismic ground motion on structures with uplift," in *Proceedings of the 2013NZSEE Conference*, Wellongton, New Zealand, 2013.

[100] S. K. Kunnath, E. Erduran, Y. H. Chai, and M. Yashinsky, "Effect of near-fault vertical ground motions on seismic response of highway overcrossings," *Journal of Bridge Engineering*, vol. 13, 2008.

[101] A. M. Abdel-Ghaffar and L. I. Rubin, "Vertical seismic behaviour of suspension bridges," *Earthquake Engineering and Structural Dynamics*, vol. 11, no. 1, 1983.

[102] S. Zhang and G. Wang, "Effects of near-fault and far-fault ground motions on nonlinear dynamic response and seismic damage of concrete gravity dams," *Soil Dynamics and Earthquake Engineering*, vol. 53, 2013.

[103] M. Breccolotti and A. L. Materazzi, "The role of the vertical acceleration component in the seismic response of masonry chimneys," *Materials and Structures*, vol. 49, no. 1-2, pp. 29–44, 2016.

[104] F. Faridafshin and G. McClure, "Seismic response of tall guyed masts to asynchronous multiple-support and vertical ground motions," *Journal of Structural Engineering*, vol. 134, no. 8, pp. 1374–1382, 2008.

[105] D. Konstantinidis and N. Makris, "Experimental and analytical studies on the response of freestanding laboratory equipment to earthquake shaking," *Earthquake Engineering and Structural Dynamics*, vol. 38, no. 6, 2009.

[106] A. M. Sweedan and A. A. El Damatty, "Equivalent models of pure conical tanks under vertical ground excitation," *Journal of Structural Engineering*, vol. 131, no. 5, 2005.

[107] N. N. Ambraseys and J. Douglas, "Near-field horizontal and vertical earthquake ground motions," *Soil Dynamics and Earthquake Engineering*, vol. 23, pp. 1–18, 2003.

[108] E. Kalkan and P. Gülkan, "Empirical attenuation equations for vertical ground motion in Turkey," *Earthquake Spectra*, 2004.

[109] J. J. Bommer, S. Akkar, and Ö. Kale, "A model for vertical-to-horizontal response spectral ratios for Europe and the middle east," *Bulletin of the Seismological Society of America*, vol. 101, pp. 1783–1806, 2011.

[110] B. Rana, *The Great Earthquake of Nepal, I*, Jorganesh Press, Kathmandu, Nepal, 1935.

[111] D. Gautam, G. Fabbrocino, and F. Santucci de Magistris, "Derive empirical fragility functions for Nepali residential buildings," *Engineering Structure*, 2018.

[112] D. Gautam, G. Fabbrocino, and F. Santucci de Magistris, "Derive empirical fragility functions for Nepali residential buildings," *Engineering Structure*, vol. 171, pp. 617–628, 2018.

[113] D. Gautam, F. S. de Magistris, and G. Fabbrocino, "Soil liquefaction in Kathmandu valley due to 25 April 2015 Gorkha, Nepal earthquake," *Soil Dynamics and Earthquake Engineering*, vol. 97, 2017.

[114] D. Gautam, "Seismic performance of world heritage sites in Kathmandu valley during Gorkha seismic sequence of april-may 2015," *Journal of Performance of Constructed Facilities*, vol. 31, no. 5, 2017.

[115] Earthquake Engineering Research Institute, *The Mw 6.9 Sikkim-Nepal Border Earthquake of September 18, 2011*, Earthquake Engineering Research Institute, California, CA, USA, 2012.

[116] A. S. Elnashai, J. J. Boomer, C. I. Baron, D. Lee, and A. I. Salama, *Selected Engineering Seismology and Structural Engineering Studies of the Hyogo-Ken-Nanbu (Great Hanshin) Earthquake of 17 January 1995*, London, 1995.

[117] National Seismological Center, *Recent Earthquakes*, Online https://www.seismonepal.gov.np/, 2015.

Research Article

HSE Risk Assessment of Major Sewage Transport Tunnel Projects at the Construction Stage Based on the Structural Entropy Weight Method and the Cloud Model

Han Wu [ID],[1] **Sen Liu** [ID],[1] **Denghui Liu** [ID],[2] **and Junwu Wang** [ID][1]

[1]*School of Civil Engineering and Architecture, Wuhan University of Technology, Wuhan 430070, China*
[2]*China Construction First Group Corporation Limited, Beijing 100161, China*

Correspondence should be addressed to Junwu Wang; junwuwang@163.com

The health, safety, and environment (HSE) risk assessment of major sewage transport tunnel projects (MSTTPs) is of great significance to guarantee sewage treatment, ecological environment protection, and sustainable development. To accurately evaluate the HSE risk of MSTTPs at the construction stage and effectively deal with their randomness and ambiguity, a risk assessment model based on the structural entropy weight method (SEWM) and the cloud model is put forward in this paper. First, an index system for MSTTPs was constructed via a literature review and expert interviews, and the rough sets method was used to filter the indicators. Then, weights were calculated by the SEWM, which is able to consider both subjective and objective factors of the weight calculation. Finally, to clarify the randomness and ambiguity in the evaluation, the HSE risk level was determined by the cloud similarity. The model was applied to the Donghu Deep Tunnel Project in Wuhan, China, and the results demonstrated that its HSE risk level was medium, which was acceptable. The index related to construction safety had the largest weight. A humid environment, improper power utilization, and sludge and mud pollution were found to be the most influential risk indicators. The risk level could be intuitively and qualitatively judged by the figure evaluation cloud, providing a vivid and rapid evaluation tool for the emergency decision-making of project managers, and the risk level could be quantitatively judged by the calculation of cloud similarity. Moreover, through the comparison with gray correlation degree, set pair analysis, and fuzzy comprehensive evaluation method evaluation results, we prove the scientificity and effectiveness of the proposed model. The research results provide a valuable reference for the project management of MSTTPs at the construction stage.

1. Introduction

In the past 30 years, urbanization in developing countries, especially China, has progressed rapidly, resulting in increased difficulties in urban sewage treatment and environmental pollution problems [1]. Moreover, the capacity for sustainable development has been severely restricted. To solve these problems, major cities in developing countries are initiatively building major sewage transport tunnels under the core areas of the cities [2]. At present, a large number of major sewage transport tunnel projects (MSTTPs) are being built in China, and the total investment has exceeded 15 billion RMB [3].

MSTTPs are usually located 30–60 m underground and their construction sites are typically closed construction

environments, which have great impacts on occupational safety. The construction processes of MSTTPs are characterized by complicated technology, a strict construction period, high mechanization, and complex construction safety risk [4]. The accidents and pollution incidents caused by these risk factors may result in huge economic losses and casualties, making the MSTTPs unable to be completed on time.

Health, safety, and the environment (HSE) is a concept that was originally generated in the petrochemical industry [5]. In recent decades, HSE has been gradually applied to high-risk industries [5] and the management of major projects [6] with established results. In combination with the research purposes of this study, the HSE risk of MSTTPs is

defined as the occupational health risk of workers, the construction safety risk, and the environmental pollution risk caused by the construction of MSTTPs. The occupational health risk of workers (the H risk factor) is geared toward the research category of public health science [7]. Safety risk management during construction, which is related to the S risk factor, belongs to the research areas of civil engineering and management science. The adverse effects of construction operations on the surrounding environment, which are related to the E risk factor, are part of the research fields of environmental engineering and civil engineering.

Referring to the general risk assessment process, the HSE risk assessment of MSTTPs in the present study includes three components, namely, the determination of risk indexes, weight calculations, and the selection of assessment methods.

At present, the existing research on HSE has primarily considered the HSE performance management of enterprises and the HSE risk management system of projects. Based on three elements, namely, time, scope, and type, Amir-Heidari et al. [8] comprehensively classified the HSE performance evaluation methods of enterprises and put forward a new HSE performance evaluation method from both positive and negative aspects. Lu and Li [9] studied the importance of the teamwork culture of construction teams in the HSE risk management system. Via a case analysis of a large prefabrication plant, it was proven that ensuring the HSE risk management system in an immersed tube prefabrication plant is of great significance to its smooth implementation. A team's strength could be mobilized and all construction workers could be motivated to participate in vocational education and safety production training. Zhang and Li [10] systematically studied the construction risk of the subsea tunnel of the Hong Kong-Zhuhai-Macao Bridge via HSE risk management. The LEC, an operation condition risk assessment, was used as the evaluation method for the analysis of the HSE risk level of the subsea tunnel, and the corresponding risk response measures were stated. However, the quantitative analysis and calculation process of the LEC method are subjective and do not provide a clear logical relationship between the values of risk indexes and the risk response measures. In addition, to the best of the authors' knowledge, a study on the HSE risk assessment of MSTTPs has not yet been reported. The main reason for the lack of prior research might be that the MSTTPs have only been restarted in the past few years, and many completed MSTTPs, such as the famous Thames Tunnel in London, were completed over a century ago.

The structural entropy weight method (SEWM) is a combined subjective and objective weight method that has been extensively used in recent years. Based on the characteristics of a large number of risk indicators for coalbed methane development and their complex relationships, Wang et al. [11] used the SEWM to process questionnaire survey results for weight calculation. The results were consistent with the actual situation of the case project. By employing the SEWM to calculate the weights of indexes, Liang et al. [12] not only effectively solved the problem of the lack of statistical data in the risk assessment of pipeline damage to the goaf, but also better handled the limitations of expert experience. Sun et al. [13] effectively adopted the SEWM to calculate the weights of the bearing capacity evaluation indexes of water resources.

For the selection of a risk assessment method, as one of the key steps in risk assessment, the characteristics of risk factors and assessment should be fully considered. Rezaee et al. [14] pointed out that the uncertainty of risk factors and the objectivity of assessment results are the key issues in the field of HSE risk assessment in the chemical industry. The failure mode and effects analysis (FMEA) and the fuzzy data envelopment analysis (DEA) were used to deal with these problems, but the randomness and fuzziness of the risk factors and risk assessment were neither further explored nor analyzed. The grey relational degree [15], set pair analysis [16], and fuzzy comprehensive evaluation [17] have been frequently used in risk assessment; while they have achieved sound results, it remains difficult for them to accurately describe randomness and fuzziness.

The cloud model is able to analyze both qualitative descriptions and quantitative data and can handle both fuzziness and randomness of a risk system. In recent years, it has become increasingly more widely used in the field of risk assessment. Liu et al. [18] combined the cloud model with an artificial neural network and proposed a new method of urban flood risk assessment that could effectively deal with the randomness and fuzziness of urban flood risk factors. Peng [19] used the positive cloud generator and the reverse cloud generator to construct a risk assessment model of a cable-stayed bridge; the risk assessment results based on the cloud model were found to be more stable and reasonable. Liu et al. [20] employed the cloud model to improve the traditional FMEA method, and their case study results proved the effectiveness of this amendment.

The present paper proposes a risk assessment model of MSTTPs based on the SEWM and the cloud model. The main contributions of this paper are as follows. (1) For the first time, a HSE risk evaluation index system was constructed from three aspects of health, safety, and environment by using the methods of literature research and questionnaire survey. Based on the genetic reduction algorithm of rough set theory, this paper retained the core evaluation index, effectively reduced the workload of the evaluation process, and enhanced the practicability of this method. (2) In this paper, the structural entropy weight method with the advantages of strong explanatory power and high accuracy of calculation results was used to calculate the weights of indexes. (3) Considering the fuzziness and randomness in the evaluation process, the qualitative concept of HSE risk evaluation index and the conversion of quantitative data were realized by the cloud model, which made the evaluation more reasonable. In addition, the risk level could be intuitively and qualitatively judged by the figure evaluation cloud, providing a vivid and rapid evaluation tool for the emergency decision-making of project managers, and the risk level could be quantitatively judged by the calculation of cloud similarity. (4) This paper revealed for the first time that, among the health, safety, and

environment, the index related to safety had the largest weight, while the index affecting the environment had the smallest weight. This weight distribution was the same as the current research situation; the main research focused on the construction safety risks, while the research on analysis of construction's environmental impact risks was less. A humid environment, improper power utilization, and sludge and mud pollution were found to be the most influential risk indicators.

The remainder of this paper is organized as follows. Section 2 focuses on the research materials and methods, including the index system and the risk assessment method based on the SEWM and the cloud model. The process of the case analysis is presented in Section 3, Section 4 details the discussion of the results, and the conclusions are presented in Section 5.

2. Materials and Methods

2.1. The Index System of HSE Risk Assessment of Major Sewage Transport Tunnel Projects

2.1.1. Preliminary Selection of HSE Risk Index Indicators of MSTTPs. According to the principles of scientificity, systematicness, effectiveness, and operability, risk indicators of the categories of health, safety, and the environment were preliminarily identified via research of the existing literature. Table 1 presents references for each risk indicator.

2.1.2. Determination of HSE Risk Index Indicators of MSTTPs. At present, there only exist a handful of MSTTPs that have been constructed around the world. As many were built long ago, they are of little significance for investigation. In addition, China and other countries have just begun to construct MSTTPs. Therefore, the available engineering data of MSTTPs is scarce. Considering this, the expert interview method was chosen to score the importance of the 42 HSE risk indicators that have been identified. According to the index score, the rough set was used to filter the index with the help of Rosetta.

In the questionnaire developed for this research, experts scored each indicator on a 5-point Likert scale. Each secondary indicator has five degrees of attributes for its primary indicator, which are "very strong" (5 points), "strong" (4 points), "average" (3 points), "weak" (2 points), and "very weak" (1 point).

The questionnaire was distributed to twenty-five experts with rich theoretical and practical experience. Eight experts were affiliated with universities, eleven were affiliated with construction enterprises of MSTTPs, and five were affiliated with MSTTP design units. Seventeen experts had the title of senior engineer or associate professor, while the other eight experts had the title of deputy senior engineer. Twenty experts had participated in the Donghu Deep Tunnel Project in Wuhan, which is the case study object of this article. Eleven experts had participated in more than three MSTTPs. These characteristics of the experts ensure the rationality of the survey results.

TABLE 1: Identification results of HSE risk indicators.

Criteria layer	Preliminary indicator	References
Health	Construction noise	[21]
	Construction dust	[22]
	Humid environment	[23]
	High ambient temperature	[23]
	Irregular lifestyle	[24]
	Toxic and harmful chemicals	[7]
	Whole body vibration	[7]
	Radiation	[25]
Safety	Unreasonable tunneling parameters	[26]
	Excessive deformation	[26]
	Improper use of transportation	[2]
	Wear failure of the shield cutter head	[27]
	Improper power utilization	[28]
	Unqualified shield segments	[29]
	Improper operation of shield segments	[30]
	Random stacking	[2]
	Incorrect protection	[31]
	Failure of bearing seal	[32]
	Failure of hoisting jack	[32]
	Clogging at the exit of slurry	[32]
	Bad grouting effect	[32]
	Improper selection of TBM machine	[33]
	Inadequate fastening of bolt	[34]
	Anchor bolt quality	[34]
	Imprecise installation of launching base	[34]
	Deviation of TBM from target shaft	[34]
	Formation of "mud cake" during excavation	[34]
	Derailment or collision of electric cart	[34]
	Grout pipe blockage	[34]
	Improper grouting amount	[34]
	Improper control of grouting coefficient	[34]
	Leakage of pipe piece joints	[35]
	Shield tail seal leakage	[35]
	Segment seal failure	[36]
Environment	Domestic waste pollution	[37]
	Exhaust pollution	[38]
	Wastewater pollution	[37]
	Sludges and muds pollution	[39]
	Pollution from vehicles	[40]
	Impact on groundwater level	[41]
	Excessive surface subsidence	[42]
	Destruction of the ecological structure	[43]

After twenty-five experts had completed scoring for all 42 secondary indicators, the results of the questionnaire were collected.

Rough sets theory is a mathematical method proposed by the Polish scientist Z. Pawlak to deal with inaccurate, uncertain, and incomplete data [44]. In the process of rough set reduction, the relationship between evaluation indicators and decision indicators can be established according to methods such as self-information and mutual information, so as to determine the importance of conditional attributes and calculate weights [45]. The Rosetta system is a tabular logic data tool based on the rough set theoretical framework.

It was developed by the Department of Computer and Information Science of the Norwegian University of Science and Technology and the Institute of Mathematics, University of Warsaw, Poland. This software is not aimed at a specific research field, but a general tool for simplifying models.

In this paper, rough sets theory was used to screen indicators with the help of Rosetta system; the index screening results are shown in Table 2.

2.1.3. Construction of HSE Risk Index System of MSTTPs.
According to the identified indicators of the HSE risk of MSTTPs, an index system including 3 primary indicators and 13 secondary indicators was constructed, as shown in Table 2. In addition, based on the characteristics and actual situations of MSTTPs, the connotation of each secondary indicator was analyzed, as presented in Table 2.

2.1.4. HSE Risk Assessment Criteria of MSTTPs.
Currently, no uniform HSE risk evaluation standard does exist [46]. In this paper, the HSE risk was divided into five levels, namely, lower risk, low risk, medium risk, high risk, and higher risk. The scoring interval was set as [0, 100]. According to the opinions of experts, the risk levels were divided and are presented in Table 3. The concepts and calculations of Ex, En, and He are described in the subsequent section.

Lower risk indicates that the risk is negligible. Low risk indicates that the risk is low, but project managers must check the existing risk management measures. Medium risk indicates that the risk is moderate and acceptable, but further measures should be considered. High risk indicates that the risk is serious and mitigation measures should be taken immediately. Finally, higher risk indicates that the risk is the most serious and completely unacceptable and construction should be stopped immediately.

2.2. The Assessment Model of HSE Risk Assessment of Major Sewage Transport Tunnel Projects

2.2.1. Introduction of the SEWM.
The SEWM combines both qualitative analysis and the quantitative analysis of weight calculation [11]. Its basic logic is as follows. First, the Delphi expert survey method and fuzzy analysis method are combined to form a quantitative order that fully considers the subjective judgments of experts. Then, entropy computing and cognitive blind degree analysis are used to analyze the quantitative order, and the statistical processing of potential data that may produce deviation is conducted with the modified uncertainty of the subjective judgments of experts. Finally, the weights of indexes are obtained via normalization.

2.2.2. Introduction of the Cloud Model.
The cloud model was first proposed by Li et al., a Chinese scholar. It realizes the two-way transformation of qualitative concepts and quantitative values [47]. By applying the cloud model to the evaluation of complex systems, the randomness and fuzziness of indicators and evaluation are fully considered [18].

A qualitative concept can be described by Ex (expected value), En (entropy), and He (hyper entropy), which are also recorded as (Ex, En, and He) [19].

(1) Ex represents the basic certainty of the qualitative concept. It is the mathematical expectation of the cloud drop in the spatial distribution of the domain. It also denotes the center value of the evaluation index in a certain grade score interval.

(2) En represents the uncertainty measure of the qualitative concept and is determined by both randomness and ambiguity of the concept. It evaluates the degree of fuzziness of the index grade boundary.

(3) He is the uncertainty of entropy and reflects the degree of deviation of the random variable corresponding to the qualitative concept from the normal distribution.

2.2.3. Risk Assessment Method of MSTTPs Based on the SEWM and the Cloud Model.
The flow chart of this evaluation method is illustrated in Figure 1.

The specific steps of the risk assessment method of MSTTPs based on the SEWM and the cloud model are as follows.

Step 1. Determine the standard cloud of each risk level.

There are 5 subintervals shown in Table 1. Let the subinterval i be $[C_i^{min}, C_i^{max}]$, and the digital characteristic values are

$$\begin{cases} Ex_i = \dfrac{\left(C_i^{max} + C_i^{min}\right)}{2}, \\ \\ En_i = \dfrac{\left(C_i^{max} - C_i^{min}\right)}{(2\sqrt{2In2})}, \\ \\ He_i = k, \end{cases} \tag{1}$$

where k is a constant that is usually assigned the value of 0.5 [47].

Step 2. Calculate the weights by the SEWM.

The detailed steps for determining the weights are as follows [13].

(1) Determine the Quantitative Order Based on Expert Opinions.
According to the operating procedures of the Delphi method, k experts with rich theoretical and practical experience are selected and sent a questionnaire. The questionnaire must be completed anonymously.

Experts score the importance of each index by using the integer of $(1 - n)$, where 1 is the most important index and n is the least important index. The number of indicators is n. The index ranking matrix **A** is obtained as follows:

TABLE 2: The index system for the HSE risk assessment of MSTTPs.

Criteria layer	Indicator layer	Indicator interpretation
Health	Construction noise H1	Shield machines and vehicles in tunnels generate noise, which can give hearing damage to construction workers.
	Humid environment H2	The humidity in the tunnel is exceedingly high, which may lead to skin dipping and erosion of construction workers.
	High ambient temperature H3	Excessive ambient temperature may cause heatstroke in workers.
	Toxic and harmful chemicals H4	Cement, paint, and other items may cause workers to suffer from occupational diseases such as contact dermatitis.
Safety	Excessive deformation S1	Excessive deformation leads to the destruction of the original structure, leading to safety accidents.
	Improper power utilization S2	If the temporary power management is improper, it may easily give rise to an electric shock accident.
	Improper operation of shield segments S3	The improper operation of the construction personnel would end up in segments falling, causing object strike accidents.
	Imprecise installation of launching base S4	The launch base was installed incorrectly and the shield machine could not launch normally, resulting in a safety accident.
Environment	Domestic waste pollution E1	Domestic waste in office and living areas may cause damage to the surrounding environment.
	Exhaust pollution E2	The construction of tunnels uses a lot of machinery, and waste gas will be generated during use. If it is not properly treated, it will pollute the atmosphere.
	Sludges and muds pollution E3	Due to inexperience, it is difficult to achieve zero discharge of construction waste such as engineering sludges and muds.
	Impact on groundwater E4	The earth pressure is not set properly, which may compact the surrounding soil and cause the groundwater level to rise significantly.
	Excessive surface subsidence E5	During the construction of the shield, the surrounding soil is disturbed greatly, and the ground surface has a large settlement.

TABLE 3: Standard risk level classification and corresponding cloud models.

Risk level	Standards	Ex	En	He
Lower risk	[0, 25]	12.5	10.616	0.5
Low risk	(25, 50]	37.5	10.616	0.5
Medium risk	(50, 75]	62.5	10.616	0.5
High risk	(75, 90]	82.5	6.369	0.5
Higher risk	(90, 100]	95.0	4.246	0.5

$$\mathbf{A} = \begin{bmatrix} a_{11} & \cdots & a_{1n} \\ \vdots & \ddots & \vdots \\ a_{k1} & \cdots & a_{kn} \end{bmatrix}, \qquad (2)$$

where a_{ij} indicates the importance evaluation of expert i $(1 \leq i \leq k)$ for indicator j $(1 \leq j \leq n)$.

(2) Perform Weight Correction on the Quantitative Order. According to the concept of the entropy weight method, the uncertainty of the quantitative order is corrected [11]:

$$\mu(I) = -\frac{\ln(m - I)}{\ln(m - 1)}, \qquad (3)$$

where I is the qualitative ranking number given by experts. If the ranking number given is 1, then I is 1. If the ranking number is 2, then I is 2. Additionally, m is the conversion parameter, which is generally considered as $m = j + 2$.

After including a_{ij} in (3), the ordering quantitative conversion value b_{ij} is obtained. Assuming that all experts have the same weights in the evaluation system, the average cognitive degree is defined as [12]

$$b_{ij} = \frac{(b_{1j} + b_{2j} + \cdots + b_{kj})}{k}. \qquad (4)$$

The uncertainty of experts' cognition is defined as knowledge blindness, and its parameter Q_j is as given by the following equation [12]:

$$Q_j = \left| \frac{\left\{ \left[\max\{b_{1j}, b_{2j}, \ldots, b_{kj}\} - b_j \right] + \left[\min\{b_{1j}, b_{2j}, \ldots, b_{kj}\} - b_j \right] \right\}}{2} \right|. \qquad (5)$$

The overall cognition degree of indicator j by k experts is defined as [13]

$$x_j = b_j(1 - Q_j). \qquad (6)$$
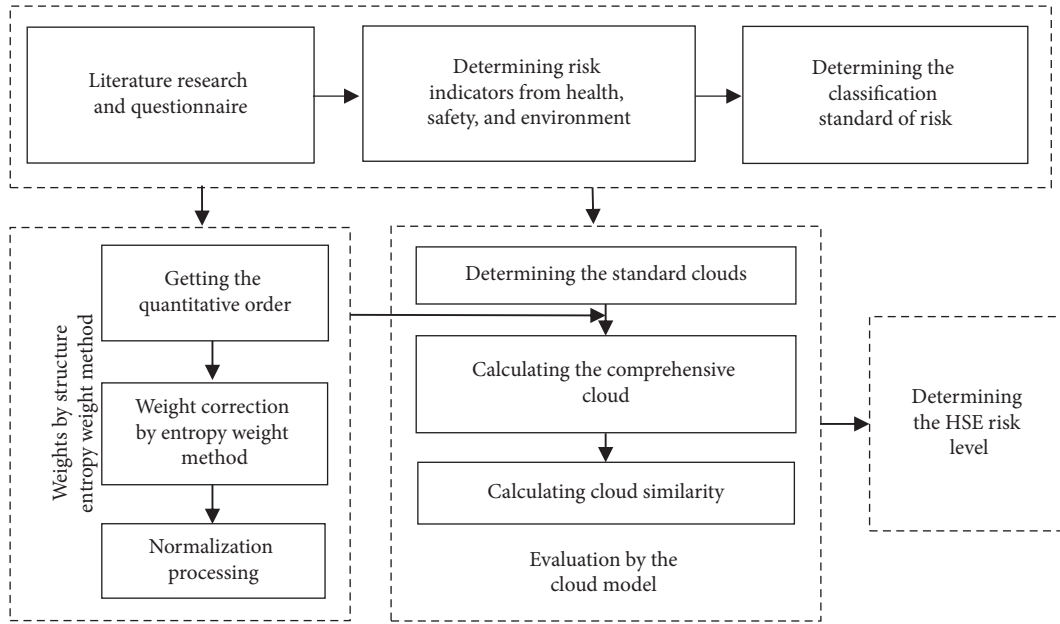
FIGURE 1: Flow chart of risk assessment method of MSTTPs based on the SEWM and the cloud model.

(3) Perform Normalization to Determine the Weights.

$$\omega_j = \frac{x_j}{\sum_{j=1}^n x_j}. \tag{7}$$

Step 3. Calculate the clouds of the evaluation factors and the comprehensive cloud.

By substituting the scores of all experts $[z_{ij}]_{k \times m}$ into the following equations, the clouds of the evaluation factors are obtained [19]:

$$Ex_j = \frac{1}{k} \sum_{i=1}^k z_{ij}, \tag{8}$$

$$En_j = \sqrt{\frac{\pi}{2}} \times \frac{1}{k} \sum_{i=1}^k \left| z_{ij} - Ex_j \right|, \tag{9}$$

$$He_j = \sqrt{\left| S_j^2 - En_j^2 \right|}. \tag{10}$$

The weights $\mathbf{W} = (\omega_1, \omega_2, \ldots, \omega_n)^{\mathrm{T}}$ obtained in Step 2 are substituted into the clouds of the evaluation factors (Ex_j, En_j, He_j). The comprehensive cloud of the HSE risk of the MSTTP is determined by the following equation [19]:

$$\begin{cases} Ex = \sum_{j=1}^n Ex_j \cdot \omega_j, \\ En = \sqrt{\sum_{j=1}^n En_j^2 \cdot \omega_j}, \quad He = \sum_{j=1}^n He_j \cdot \omega_j. \end{cases} \tag{11}$$

By drawing the comprehensive cloud and five standard clouds in the same image, the HSE risk level of an MSTTP can be qualitatively judged.

Step 4. Determine the HSE risk level by the cloud similarity.

The steps for the calculation of δ_i, which is the cloud similarity between the clouds of the evaluation factors and the comprehensive cloud, are as follows [47]:

(1) Generate $Ex_p = \mathrm{Norm}(En, He^2)$.

(2) Generate $x_p = \mathrm{Norm}(Ex, Ex_p^2)$.

(3) Substitute into (12) to calculate μ_p:

$$\mu_p = e^{-\left(\left(x_p - Ex_i^2 \right)^1 / \left(2En_i^2 \right) \right)}. \tag{12}$$

(4) Repeat Steps 2 and 3 to generate μ_p, where $q \in [10, 30]$. Then, δ_i can be calculated as follows:

$$\delta_i = \frac{1}{q} \sum_{p=1}^q \mu_p. \tag{13}$$

The greater the value of δ_i is, the closer the HSE risk level of the MSTTP is to the evaluation level. In this way, the HSE risk level of an MSTTP can be calculated quantitatively.

3. Results

3.1. Engineering Background. The case selected in this article is the Donghu Deep Tunnel Project in Wuhan, which is the largest MSTTP in China. Its recent service scope covers the core area of Wuhan, which is about $130.35 \, \mathrm{km}^2$, and its long-term control service range is about $200.25 \, \mathrm{km}^2$. Its total length is about $17.5 \, \mathrm{km}$ via shield construction, the tunnel diameters are D3000-D3400 mm, and the buried depths are 30–50 m. When this project is successfully completed, the sewage from the core area of Wuhan will be directly transferred to the Beihu Sewage Treatment Plant, which is the largest sewage treatment plant in

China. The Donghu Deep Tunnel not only can elevate the capacity and efficiency of urban sewage transport, but can also effectively avoid the problem of the mixture of rain and sewage, thereby improving the water environment of Shahu Port, Luojia Port, and Donghu Port. To achieve the smooth implementation of this project, it is necessary to carry out a typical HSE risk assessment.

Current data of MSTTPs was difficult to obtain, so the data used for the computations of the weights and risk levels in the case study were obtained by questionnaires. The 10 invited experts were the experts who selected the HSE risk indicator system in the preliminary study. The 10 experts scored the indexes on the basis of fully understanding the site situation, construction content, and process of the Donghu Deep Tunnel Project. According to (1), three digital clouds of the characteristics of each level were computed and are presented in Table 1.

3.2. Determination of Indicator Weights.
After a questionnaire survey, the results of the importance scores of the 3 primary indicators and 15 secondary indicators by the twenty-five experts were substituted into (2)–(7), and the calculation results of the weights of the 3 primary indexes (Table 4), 4 secondary indexes related to the health indicator (Table 5), 4 secondary indexes related to the safety indicator (Table 6), and 5 secondary indexes related to the environment indicator (Table 7) were obtained.

From Table 4, it can be seen that the safety indicator has the largest weight of the primary indexes, while the environment indicator has the smallest weight. This weighting explains the phenomenon of most previous research focusing on construction safety risks instead of environmental risks.

Table 5 shows that the humid environment index (H2) has the largest weight, while the high ambient temperature (H3) has the least weight. These results are consistent with the construction content of MSTTPs, in which earth pressure balance shield machines are used for shield construction and typically create a high-humidity environment. However, MSTTPs are mostly constructed underground and with good ventilation. So, high temperature conditions will not occur.

As presented in Table 6, the weight of the improper power utilization index (S2) is the largest of the 6 secondary indexes related to safety, and the weight of the imprecise installation of launching base (S4) is the smallest. The construction safety risk management of MSTTPs should therefore focus on improper power utilization.

As presented in Table 7, the sludge and mud polarization index (E3) has the largest weight. The reason for this is that the main pollutants produced during the shield construction of the Donghu Deep Tunnel Project in Wuhan are sludge and mud.

3.3. Calculations of the Clouds of Evaluation Factors and the Comprehensive Cloud.
Via the questionnaire survey results of 25 experts, the scores of the 13 secondary indexes of the Donghu Deep Tunnel Project were averaged and introduced into (8)–(10). The evaluation cloud model of each index was obtained, as presented in Table 8.

TABLE 4: The weights of primary indexes.

No.	H	S	E
Expert 1	2	1	3
Expert 2	1	2	3
Expert 3	2	1	3
Expert 4	3	1	2
Expert 5	2	1	3
Expert 6	2	1	3
...	...	...	...
Expert 24	2	1	3
Expert 25	1	2	3
b_j	0.7687	0.9253	0.5985
Q_j	0.0187	0.0291	0.1515
x_j	0.7543	0.8984	0.5078
ω_j	0.3491	0.4158	0.2350
Ranking	2	1	3

TABLE 5: The weights of 4 secondary indexes related to health.

No.	H1	H2	H3	H4
Expert 1	1	3	2	4
Expert 2	2	1	3	4
Expert 3	2	1	4	3
Expert 4	3	1	4	2
Expert 5	3	1	4	2
Expert 6	2	3	4	1
...	...	...	...	...
Expert 24	2	3	4	1
Expert 25	3	2	1	4
b_j	0.8101	0.9159	0.5929	0.6446
Q_j	0.0948	0.0746	0.1224	0.0708
x_j	0.7333	0.8476	0.5203	0.5990
ω_j	0.2716	0.3139	0.1927	0.2218
Ranking	2	1	4	3

TABLE 6: The weights of 6 secondary indexes related to safety.

No.	S1	S2	S3	S4
Expert 1	3	2	1	4
Expert 2	4	1	2	3
Expert 3	2	1	3	4
Expert 4	4	2	1	3
Expert 5	4	1	3	2
Expert 6	4	1	2	3
...	...	...	...	...
Expert 9	3	2	1	4
Expert 10	3	1	2	4
b_j	0.6485	0.9191	0.8274	0.5741
Q_j	0.0668	0.0778	0.1120	0.1413
x_j	0.6052	0.8476	0.7347	0.4930
ω_j	0.2258	0.3162	0.2741	0.1839
Ranking	3	1	2	4

After substituting the weight calculation results and the clouds of the evaluation factors into (11), the comprehensive cloud was found to be 67.8774, 7.3989, and 1.4578, and this is shown in Figure 2.

It can be easily and intuitively seen that the HSE risk level of the Donghu Deep Tunnel Project was found

TABLE 7: The weights of 5 secondary indexes related to the environment.

No.	E1	E2	E3	E4	E5
Expert 1	5	4	1	3	2
Expert 2	4	3	2	1	5
Expert 3	4	5	1	2	3
Expert 4	3	5	2	1	4
Expert 5	5	4	3	1	2
Expert 6	4	5	1	2	3
. . .	. . .	. . .	. . .	. . .	. . .
Expert 24	4	5	2	1	3
Expert 25	5	4	1	3	2
b_j	0.5483	0.5621	0.9272	0.8453	0.7891
Q_j	0.0320	0.1314	0.0403	0.0388	0.0956
x_j	0.5308	0.4882	0.8898	0.8126	0.7136
ω_j	0.1545	0.1421	0.2590	0.2366	0.2077
Ranking	4	5	1	2	3

TABLE 8: The clouds of evaluation factors.

Indicator	Average score	Ex	En	He
H1	78.80	78.80	7.798650	1.617801
H2	84.84	84.84	5.120245	0.503215
H3	56.56	56.56	8.103378	2.329037
H4	73.96	73.96	8.556462	0.003187
S1	70.48	70.48	6.639879	2.580660
S2	55.48	55.48	7.008761	0.473030
S3	71.24	71.24	6.864416	0.826566
S4	79.44	79.44	6.287035	0.010070
E1	66.80	66.80	9.021574	2.986067
E2	61.84	61.84	7.483897	2.767690
E3	52.28	52.28	9.657094	3.233065
E4	54.48	54.48	6.371236	3.124658
E5	56.60	56.60	9.342341	2.485330

to be the closest to moderate risk [18, 38]. The cloud model could therefore effectively deal with the randomness and ambiguity in the HSE risk evaluation of MSTTPs.

3.4. Determination of the HSE Risk Level by the Cloud Similarity. After introducing the obtained comprehensive evaluation cloud (67.8774, 7.3989, and 1.4578) into (12) and (13), the cloud similarities δ_i between the comprehensive evaluation cloud and the five standard clouds were obtained and are presented in Table 9. In (12), q is an important parameter ($q \in [10, 30]$). δ_i under three different values of q was calculated in Table 9.

The cloud similarity between the comprehensive evaluation cloud and the standard Cloud 3 was the largest, which indicates that the HSE risk level of the Donghu Deep Tunnel Project is medium risk.

4. Discussion

The weight calculation in risk assessment often only considers subjective or objective factors, thereby making the weights inaccurate. Moreover, the common risk evaluation methods cannot reasonably take into account the

randomness and ambiguity in the evaluation process, thereby making the risk evaluation results inaccurate. Currently, MSTTPs are under construction in large quantities, but there is little research on the risk of MSTTPs, and research on the HSE risk assessment of MSTTPs has not yet been reported.

To fill this gap, a typical risk evaluation index system of MSTTPs was constructed in this study for the first time. Then, to ensure the accuracy of the weight calculations, the SEWM, in which both subjective and objective factors in the weight calculation are comprehensively considered, was used to calculate the weights. Finally, an evaluation method based on the cloud model was adopted to describe the randomness and ambiguity of the HSE risk assessment of MSTTPs. The research results obtained in this study can help ensure the smooth implementation of MSTTPs and are of great significance for ensuring wastewater treatment, ecological environment protection, and sustainable development.

Because there are no existing research results on the HSE risk of MSTTPs, this paper compared the results of case analysis with the results of common risk assessment methods (the grey relational degree [15], set pair analysis [16], and fuzzy comprehensive evaluation [17]). The grey relational degree calculation results of each risk level are shown in Table 10. According to the calculation result of the index weight of Donghu Deep Tunnel Project and the average of the scores of each risk index, the gray correlation degree of Donghu Deep Tunnel Project was 0.428, which belonged to medium risk. The calculation result of the five-element connection number of Donghu Deep Tunnel Projects calculated by set pair analysis is shown in Table 11. When the confidence $\in [0.50, 0.70]$, the HSE risk of Donghu Deep Tunnel Project was medium risk. The evaluation results of fuzzy comprehensive evaluation are shown in Table 12. According to the principle of maximum membership degree of comprehensive evaluation, the HSE risk was medium risk.

The grey relational degree, set pair analysis, and fuzzy comprehensive evaluation results of HSE risk of Donghu Deep Tunnel Project belonged to the medium risk, and the direct evaluation results were basically consistent
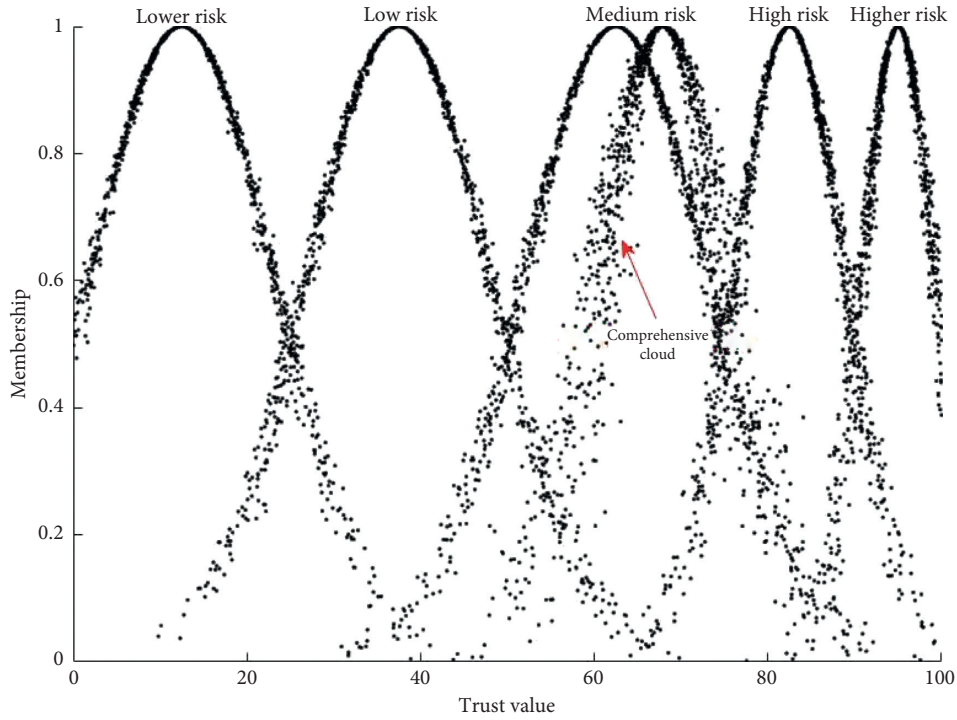
Figure 2: Cloud of comprehensive evaluation.

Table 9: Calculation results of the cloud similarity.

Standard cloud	q	Cloud 1	Cloud 2	Cloud 3	Cloud 4	Cloud 5
Cloud similarity δ_i	10	0.003	0.121	0.614	0.262	0.010
Cloud similarity δ_i	20	0.002	0.120	0.620	0.251	0.007
Cloud similarity δ_i	30	0.000	0.125	0.615	0.254	0.006

Table 10: Comprehensive grey relational degree.

Risk level	Lower risk	Low risk	Medium risk	High risk	Higher risk
Grey relational degree	0.6667	0.5000	0.4000	0.3571	0.3333

Table 11: The results of Donghu Deep Tunnel Project' five-element contact numbers.

Five-element contact numbers	f_1	f_2	f_3	f_4	f_5	Level
Donghu deep tunnel project	0.0000	0.1080	0.5009	0.3569	0.0342	Medium risk

Table 12: Evaluation results of the Donghu Deep Tunnel Project.

Risk level	Lower risk	Low risk	Medium risk	High risk	Higher risk
Membership	0.000	0.1107	0.5931	0.2787	0.0175

with the evaluation results of the cloud model. The gray correlation model solved the ambiguity of indicators, but it was difficult for it to deal with the randomness and uncertainty of indicators [15, 47]. When many pieces of data and information were used, the evaluation of indicators always carried a certain degree of uncertainty and randomness. In the application process of the set pair analysis method, it was difficult to determine the ambiguity of the index difference coefficient, so it was not able

to be widely promoted in actual evaluation [16]. In practical applications, the fuzzy synthesis method often used the membership function to calculate the membership degree of each index and forcibly incorporated the fuzziness of the index into the category of precise mathematics. These characteristics made it difficult to deal with the randomness and uncertainty of indicators. The method in this article used the cloud model to consider the ambiguity and randomness in the HSE

evaluation work, and the cloud diagram of the model in the article vividly and intuitively depicted these characteristics of the evaluation [47]. The calculation results are displayed in two ways: similarity and cloud graph, which is convenient for decision makers to use evaluation information.

5. Conclusions

To accurately evaluate the HSE risk of MSTTPs and effectively deal with their randomness and ambiguity, the SEWM and the cloud model were employed. In this paper, for the first time, an index system for MSTTPs at the construction stage was constructed from three aspects of health, safety, and environment via a literature review and expert interviews. Based on the genetic reduction algorithm of rough set theory, this paper retained the core evaluation index, effectively reduced the workload of the evaluation process, and enhanced the practicability of this method. Then, weights were calculated by the SEWM with the advantages of strong explanatory power and high accuracy of calculation results. To clarify the randomness and ambiguity in the evaluation, the HSE risk level was determined by the cloud similarity. This model was applied to the Donghu Deep Tunnel Project in Wuhan, China, and the results demonstrated that its HSE risk level was medium, which was acceptable. The index related to construction safety had the largest weight. A humid environment, improper power utilization, and sludge and mud pollution were found to be the most influential risk indicators, which should be key points in HSE risk management of MSTTPs. The risk level could be intuitively and qualitatively judged by the figure evaluation cloud, providing a vivid and rapid evaluation tool for the emergency decision-making of project managers, and the risk level could be quantitatively judged by the calculation of cloud similarity. Through the comparison with gray correlation degree, set pair analysis, and fuzzy comprehensive evaluation method evaluation results, we prove the scientificity and effectiveness of the proposed model.

The construction process of MSTTPs has obvious stages and is highly dynamic, so the HSE risk factors and risk levels also have obvious stages and are highly dynamic. The accurate description of these stages and dynamics will further improve the application and promotion value of the research results achieved in this paper. Due to the difficulty in obtaining engineering data, qualitative indicators were used in this research. Therefore, determining how to select and use quantitative indicators to describe the HSE risk of MSTTPs will be explored in future research.

Data Availability

The case analysis data used to support the findings of this study are available from the corresponding author upon request.

Conflicts of Interest

The authors declare that there are no conflicts of interest regarding the publication of this paper.

References

[1] H. Wang, C. Mei, J. Liu, and W. Shao, "A new strategy for integrated urban water management in China: Sponge city," *Science China Technological Sciences*, vol. 61, no. 3, pp. 317–329, 2018.

[2] G. H. Wang, Y. Chen, J. H. Zhou et al., "Discussion on application and development trend of deep tunnel drainage technology," *China Water and Wastewater*, vol. 32, no. 22, pp. 1–13, 2016.

[3] J. Liu, L. Xia, H. Wang, W. Shao, and X. Ding, "Typical case analysis of deep tunnel drainage system in urban area," *Chinese Science Bulletin*, vol. 62, no. 27, pp. 3269–3276, 2017.

[4] M. L. Huang, Z. E. Zhang, and Z. S. Tan, "Construction model of deep tunnel for urban flood control and drainage in China," *China Civil Engineering Journal*, vol. 50, no. 1, pp. 76–81, 2017.

[5] A. Dewan, P. Soren, R. B. N. Mathias, and O. Jacob, "Why does the offshore wind industry need standardized HSE management systems? An evidence from Denmark," *Renewable Energy*, vol. 136, pp. 691–700, 2019.

[6] A. Motaghifard, M. Omidvari, and A. Kaazemi, "Introducing a conceptual model for evaluating health safety environmental performance of residential buildings using the fuzzy decision-making approach," *Environmental Monitoring and Assessment*, vol. 192, no. 1, p. 19, 2020.

[7] A. Hamid, W. Saleem, G. Yaqub, and M. U. D. Ghauri, "Comparative assessment of respiratory and other occupational health effects among elementary workers," *International Journal of Occupational Safety and Ergonomics*, vol. 25, no. 3, pp. 394–401, 2019.

[8] P. Amir-Heidari, R. Maknoon, B. Taheri, and M. Bazyari, "A new framework for HSE performance measurement and monitoring," *Safety Science*, vol. 100, pp. 157–167, 2017.

[9] Q. Z. Lu and D. H. Li, "Analysis on the role of team culture construction in HSE management," *Highway*, vol. 63, no. 8, pp. 135–137, 2018.

[10] Z. G. Zhang and J. F. Li, "Application and demonstration of health-safety-environment risk management to underwater tunnel of Hong Kong-Zhuhai-Macao Link," *Tunnel Construction*, vol. 39, no. 2, pp. 189–196, 2019.

[11] W. Q. Wang, S. R. Lyu, Y. D. Zhang, and S. Q. Ma, "A risk assessment model of coalbed methane development based on the matter-element extension method," *Energies*, vol. 12, no. 20, pp. 3931–3960, 2019.

[12] X. Liang, W. Liang, L. Zhang, and X. Guo, "Risk assessment for long-distance gas pipelines in coal mine gobs based on structure entropy weight method and multi-step backward cloud transformation algorithm based on sampling with replacement," *Journal of Cleaner Production*, vol. 227, pp. 218–228, 2019.

[13] Y. R. Sun, Z. C. Dong, Y. Zhou, and S. N. Feng, "Evaluation of water resources carrying capacity in lower reaches of Yangtze River based on structural entropy method: a case study of Nanjing," *Yangtze River*, vol. 49, no. 7, pp. 47–51, 2018.

[14] M. J. Rezaee, S. Yousef, M. Eshkevari, M. Valipour, and M. Saberi, "Risk analysis of health, safety and environment in chemical industry integrating linguistic FMEA, fuzzy

inference system and fuzzy DEA," *Stochastic Environmental Research and Risk Assessment*, vol. 40, no. 2, pp. 231–242, 2019.

[15] J. F. Zhou, S. Y. Hu, J. K. An et al., "Research on key indexes of power supply level of medium-voltage distribution network based on entropy-weighted method and grey relational degree," *Bulletin of Science and Technology*, vol. 35, no. 12, pp. 101–104, 2019.

[16] Q. Wu, L. Wang, N. Jin, N. Li, and X. Hu, "Social stability risk evaluation of major water conservancy projects in fragile eco-environment regions," *Applied Ecology and Environmental Research*, vol. 17, no. 4, pp. 9097–9111, 2019.

[17] X. Q. Yang and S. C. Zhang, "Manned space engineering project based on fuzzy analytic hierarchy process-particle swarm optimization research on identification of important processes," *Science and Technology Management Research*, vol. 39, no. 24, pp. 217–224, 2019.

[18] D. Liu, D. Wang, J. Wu et al., "A risk assessment method based on RBF artificial neural network—cloud model for urban water hazard," *Journal of Intelligent & Fuzzy Systems*, vol. 27, no. 5, pp. 2409–2416, 2014.

[19] K. K. Peng, "Risk evaluation for bridge engineering based on cloud-clustering group decision method," *Journal of Performance of Constructed Facilities*, vol. 33, no. 1, Article ID 04018105, 2019.

[20] H.-C. Liu, L.-E. Wang, Z. Li, and Y.-P. Hu, "Improving risk evaluation in FMEA with cloud model and hierarchical TOPSIS method," *IEEE Transactions on Fuzzy Systems*, vol. 27, no. 1, pp. 84–95, 2019.

[21] C. L. Themann and E. A. Masterson, "Occupational noise exposure: a review of its effects, epidemiology, and impact with recommendations for reducing its burden," *The Journal of the Acoustical Society of America*, vol. 146, no. 5, pp. 3879–3905, 2019.

[22] E. Jonsson, B. Järvholm, and M. Andersson, "Silica dust and sarcoidosis in Swedish construction workers," *Occupational Medicine*, vol. 69, no. 7, pp. 482–486, 2019.

[23] P. Wolkoff, "Indoor air humidity, air quality, and health—an overview," *International Journal of Hygiene and Environmental Health*, vol. 221, no. 3, pp. 376–390, 2018.

[24] F. M. Fischer, C. A. Silva, R. H. Griep et al., "Working time society consensus statements: psychosocial stressors relevant to the health and wellbeing of night and shift workers," *Industrial Health*, vol. 57, no. 2, pp. 175–183, 2017.

[25] G. Cucchi, A. Lisardi, D. Mostacci, L. Tositti, F. Tugnoli, and S. Vichi, "Radiation protection issues in the excavation of road and railway tunnels, a preliminary assessment," *Radiation Effects and Defects in Solids*, vol. 171, no. 9-10, pp. 801–807, 2016.

[26] Y. S. Jiang, Z. Y. Sun, and Z. Y. Yang, "Construction risk monitoring system and parameter warning of EPB shield," *Tunnel Construction*, vol. 39, no. 7, pp. 1083–1089, 2019.

[27] Y. R. Yan, "Risk analysis of cutter head failure of composite EPB shield," *Rock and Soil Mechanics*, vol. 30, no. 8, pp. 2324–2330, 2007.

[28] G. H. Chen, W. S. Wu, S. Y. Xu, and K. Liu, "Assessment HSE risk of during sea-crossing bridges project construction based on WBS-RBS and AHP," *China Safety Science Journal*, vol. 23, no. 9, pp. 51–57, 2013.

[29] W. Q. Wei, L. Chen, and H. B. Luo, "Geological safety evaluation of cross-river metro tunnel based on clustering analysis," *Journal of Civil Engineering and Management*, vol. 32, no. 1, pp. 72–76, 2015.

[30] Z. M. Ding, Q. L. Liao, and C. Y. Li, "Study on risk of the construction of earth-pressure-balanced shield in metro engineering," *Construction Technology*, vol. 41, no. 24, pp. 64–67, 2012.

[31] B. R. Fortunato, M. R. Hallowell, M. Behm, and K. Dewlaney, "Identification of safety risks for high-performance sustainable construction projects," *Journal of Construction Engineering and Management*, vol. 138, no. 4, pp. 499–508, 2012.

[32] H. Lu, M. Y. Wang, B. H. Yang, and X. L. Rong, "Study on the application of the kent index method on the risk assessment of disastrous accidents in subway engineering," *Scientific World Journal*, vol. 2013, Article ID 360705, 10 pages, 2013.

[33] K.-C. Hyun, S. Min, H. Choi, J. Park, and I.-M. Lee, "Risk analysis using fault-tree analysis (FTA) and analytic hierarchy process (AHP) applicable to shield TBM tunnels," *Tunnelling and Underground Space Technology*, vol. 49, pp. 121–129, 2015.

[34] W. Liu, T. Zhao, W. Zhou, and J. Tang, "Safety risk factors of metro tunnel construction in China: an integrated study with EFA and SEM," *Safety Science*, vol. 105, pp. 98–113, 2018.

[35] H. Lu, Y. H. Shi, and X. L. Rong, "Discussion on safety risk assessment of shield construction in underwater tunnel," *Strategic Study of CAE*, vol. 15, no. 10, pp. 91–96, 2013.

[36] W. Liu, T. S. Zhao, Y. J. Zhang, Y. K. Chen, and W. Zhou, "Analysis of risk factors and countermeasures for metro shield construction," *China Safety Science Journal*, vol. 27, no. 10, pp. 130–136, 2017.

[37] T. Huang, F. Shi, H. Tanikawa, J. Fei, and J. Han, "Materials demand and environmental impact of buildings construction and demolition in China based on dynamic material flow analysis," *Resources, Conservation and Recycling*, vol. 72, pp. 91–101, 2013.

[38] O. K. M. Ouda, H. P. Peterson, M. Rehan, Y. Sadef, J. M. Alghazo, and A. S. Nizami, "A case study of sustainable construction waste management in Saudi Arabia," *Waste and Biomass Valorization*, vol. 9, no. 12, pp. 2541–2555, 2017.

[39] W. S. Guo, K. S. Liang, and Y. F. You, "Study of the main risks and countermeasures for the sea-crossing shield tunnel of the Taishan nuclear power station," *Modern Tunnelling Technology*, vol. 52, no. 6, pp. 195–202, 2015.

[40] L. Szwarcfiter, F. E. Mendes, and E. L. La Rovere, "Enhancing the effects of the brazilian program to reduce atmospheric pollutant emissions from vehicles," *Transportation Research Part D: Transport and Environment*, vol. 10, no. 2, pp. 153–160, 2005.

[41] F. M. Shaqour and S. E. Hasan, "Groundwater control for construction purposes: a case study from Kuwait," *Environmental Geology*, vol. 53, no. 8, pp. 1603–1612, 2008.

[42] K.-I. Song, G.-C. Cho, and S.-B. Chang, "Identification, remediation, and analysis of karst sinkholes in the longest railroad tunnel in South Korea," *Engineering Geology*, vol. 135-136, no. 15, pp. 92–105, 2012.

[43] Y. X. Lv, Y. J. Jiang, W. Hu, M. Cao, and Y. Mao, "A review of the effects of tunnel excavation on the hydrology, ecology, and environment in karst areas: current status, challenges, and perspectives," *Journal of Hydrology*, vol. 586, Article ID 124891, 2020.

[44] Z. Pawlak and A. Skowron, "Rough sets and Boolean reasoning," *Information Sciences*, vol. 177, no. 1, pp. 41–73, 2007.

[45] C. Wang, M. Shao, B. Sun, and Q. Hu, "An improved attribute reduction scheme with covering based rough sets," *Applied Soft Computing*, vol. 26, pp. 235–243, 2015.

[46] U. K. Chakrabarti and J. K Parikh, "Risk-based route evaluation against country-specific criteria of risk tolerability for hazmat transportation through Indian State Highways,"

Journal of Loss Prevention in the Process Industries, vol. 26, no. 4, pp. 723–736, 2017.

[47] Y. P. Li, M. Q. Liu, F. Wang, and R. G. Li, "Safety performance assessment of fabricated building project based on cloud model," *China Safety Science Journal*, vol. 27, no. 6, pp. 115–120, 2017.

Research Article

Study on the Seismic Performance of Different Combinations of Rubber Bearings for Continuous Beam Bridges

Yumin Zhang [1,2] **Jiawu Li** [2] **Lingbo Wang** [2] **and Hao Wu** [2]

[1]*Department of Civil Engineering, Xi'an Shiyou University, Xi'an 710065, China*
[2]*Shaanxi Key Laboratory of Highway, Bridge and Tunnel, Highway College of Chang'an University, Xi'an 710064, China*

Correspondence should be addressed to Yumin Zhang; zhangyumincorn@163.com

Rubber isolation bearings have been proven to be effective in reducing the seismic damage of bridges. Due to the different characteristics of isolation bearings, the mechanical properties of bridges with different combinations of rubber bearings are complex under the action of earthquakes. This paper focuses on the application of combinations of rubber isolation bearings on seismic performance of continuous beam bridges with T-beams. The seismic performances of continuous beam bridges with different combinations of rubber isolation bearings, pier height, and span length were studied by the dynamic time history analysis method. It was found that the bridges with natural rubber bearings (NRBs) have the largest seismic responses compared to the other types of bearings. The continuous beam bridge with isolation bearings, such as lead rubber bearings (LRBs) and high damping rubber bearings (HDRBs), has approximately 20%~30% smaller seismic response than that with NRBs under the action of earthquakes due to the hysteretic energy of the bearings, indicating that the isolation bearings improve the seismic performance of the bridge. The continuous beam bridges with both NRBs and LRBs or NRBs and HDRBs have larger seismic response of the piers than those with a single type of isolation bearings (LRBs or HDRBs) but smaller seismic response of the piers than those with only NRBs. For a continuous beam bridge with shorter span and lower pier, it is not economical to use LRBs or HDRBs underneath every single girder, but it is more reasonable to use cheaper NRBs underneath some girders. The larger difference in stiffness of the bearings between the side and middle piers leads to the more unbalanced seismic response of each pier of the bridge structure. The results also show that with increasing pier height and span length, the difference in the seismic response value between the cases gradually increases.

1. Introduction

Among the seismic performance of a continuous beam bridge, traffic safety is of great concern [1, 2]. In recent years, rubber materials have been widely used for the bearings of bridges because of their excellent deformation characteristics. They play an important role in the seismic design of continuous beam bridges [3–6]. Research on the material and mechanical properties of different rubber bearings is helpful to understand the seismic performance of rubber bearings in bridge structures, thereby guaranteeing no serious damage to the continuous beam bridge under the action of earthquakes [7, 8].

Numerous studies have proved the efficiency of rubber bearings in reducing the seismic-induced forces of bridge systems [9, 10]. The common types of rubber isolation bearings include low damping natural rubber bearings (LDRs) [1], natural rubber bearings (NRBs) [3, 6], lead rubber bearings (LRBs) [7], and high damping rubber bearings (HDRBs) [2, 8]. At present, the seismic performance of the aseismic bearings for continuous beam bridges is mainly studied for the mechanical behavior of various rubber bearings under earthquakes [11, 12], by utilizing the finite element method and shaking table test methods [13–16]. Yamamoto et al. [17] investigated the seismic characteristics of the isolation bearings of bridge structure and found that for a structure under instantaneous load, the isolation bearings can effectively reduce the seismic input and can affect the characteristics of the structure in the frequency domain. Pradilla and Cho [18] presented a

comparison of the seismic behavior of simply supported bridges by using three types of isolators, including HDRBs, LRBs, and a friction pendulum system. Losanno et al. [19] analyzed the seismic performance of a three-span continuous bridge designed with different isolation systems, including simply supported, LRBs, isolated with rubber isolators and 10% damping, and isolated with rubber isolators and a 70% supplemental damping ratio. Six near-fault ground motion records were used to analyze the seismic performance of a bridge by the direct time history integration method. Tubaldi et al. [8] revealed that in simply supported multispan bridges, the HDRBs typically placed in two lines of support and eccentric with the pier axis induces a coupled horizontal vertical response of the bearings. Wang et al. [20] investigated the seismic response of a typical continuous beam bridge isolated with friction sliding bearings in the Hong Kong-Zhuhai-Macao Link Project of China. Li et al. [2] performed the shaking table array test of a two-span isolated continuous bridge specimen with the scale of 1 : 3 to study the seismic response characteristics of the continuous bridge with HDR bearings. Zheng et al. [21] investigated the seismic performance of the bridges with a sliding-lead rubber bearing (LRB) isolation system under the action of near-fault earthquakes. For the bridges with tall piers, Chen and Li [11] investigated the effect of different seismic retrofitting measures including LRBs and rocking foundations on mitigation of their seismic responses. Anajafi et al. [22] investigated the effect of LRBs on improvement of the seismic performance of the bridges with flexible piers in near-field and far-field earthquakes. Their studies show that for far-field ground motions, the LRBs used significantly reduce not only the substructure responses but also the displacement response of the girder. For near-fault excitations, their studies show that there is an optimum range of bearing parameters that can reduce the substructure force demand and keep the girder displacement demand in practice. Zhen et al. [23] used a high-speed multispan continuous beam bridge with equal section as the engineering background to discuss the seismic isolation effect of LRBs and fluid viscous dampers by the dynamic time history analysis method. Current research mainly focuses on the mechanical behaviors of a single type of bearings. The combination of different bearings is seldom studied. To save the construction cost, many kinds of bearings are used for the bridges in practice.

Additionally, the continuous beam bridge with a combination of different bearings has more complicated response to earthquakes because (1) LRBs and HDRBs have nonlinear horizontal stiffness, quite different from NRBs especially at high shear strain amplitudes, and (2) some factors, such as pier height and span length, also influence the seismic performance of the bridges [24–26]. Researchers have investigated the failure modes and seismic performance of a continuous beam bridge with a combination of different bearings during strong ground motions [21, 27]. However, the influencing factors are studied very rarely based on a combination of different bearings. What is more, the importance of the combinations of different bearings has not been clarified.

In this paper, the seismic performance of continuous beam bridges with combinations of different rubber bearings, such as a combination of NRBs, LRBs, HDRBs, NRBs, and LRBs, and a combination of NRBs and HDRBs, were studied; the bridges with such combinations were compared to the bridges without bearings; the influence of bearing combination, pier height, and span length on the seismic response, including the displacement and energy dissipation of bearings, the displacement of the girder, the displacement of the top of the piers, and the bending moment and shearing force of the bottom of the piers, were discussed. The isolation design method for the continuous beam bridges with T-beams was provided; the effects of different combinations of rubber bearings on the mechanical performance of the bridges were studied in order to further understand the optimal configuration of different pier heights and span lengths and provide rational suggestions for selection of bearings for the continuous bridges with T-beams.

2. Materials and Mechanical Properties of Rubber Bearings

2.1. Material Properties of Rubber Bearings. Rubber is a highly elastic synthetic polymer material, including natural and synthetic rubber [28]. The mechanical properties of rubber materials are relatively complex; the stress-strain relationship of rubber materials is approximately linear in the case of small strain but nonlinear in the case of large strain [29]. Among synthetic rubbers, high damping rubber is an effective isolation material typically filled with carbon black, oils, or resins, which can enhance the seismic performance of structures due to its higher damping properties, energy dissipation capability, and flexible stiffness [30, 31].

Rubber material has been widely used in the bearings of bridge structures, and isolation rubber bearings are especially suitable for the design of the seismic isolation for bridges because of their seismic properties [8]. HDRBs consist of high damping rubber layers, providing bearings with horizontal flexibility, reinforced with steel layers that provide vertical stiffness [32], as shown in Figure 1(a). The shape and high damping characteristics of LRBs are similar to that of HDRBs; the difference is that LRBs have lead cores vertically inserted into the bearings, as shown in Figure 1(b). The lead cores can change the damping characteristics of the bearings so that they can adopt antiseismic and energy absorption properties during earthquakes [33].

Both LRBs and HDRBs have high horizontal stiffness and damping at low shear strains, which can reduce the response of bridges within a reasonable range under service loads and small earthquakes. Furthermore, their horizontal stiffness changes after the bearings yield with large horizontal shear force and displacement during larger earthquakes, and so the bearings can absorb seismic energy [23, 30]. A high damping ratio is also an important characteristic of LRBs and HDRBs in addition to the nonlinear constitution relation of conventional rubber materials.
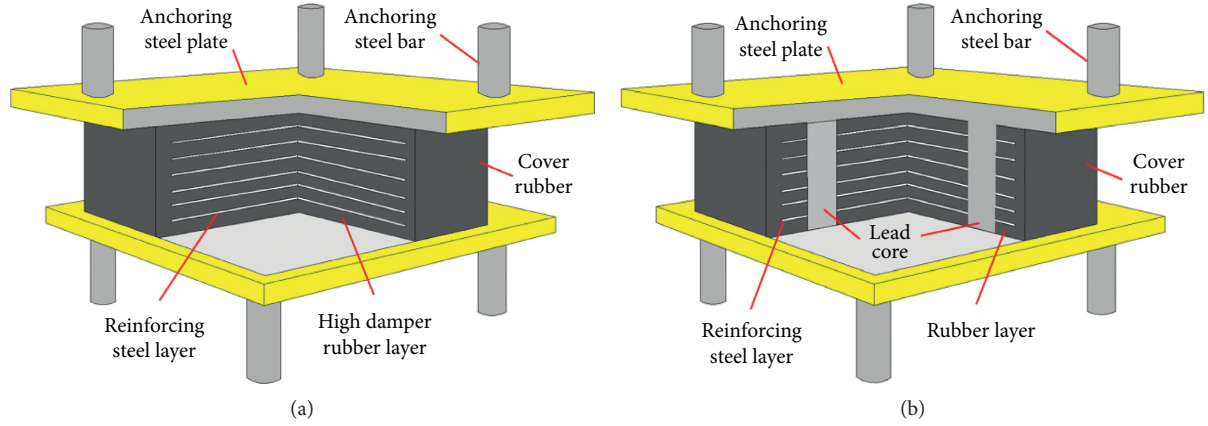
Figure 1: Structural composition of isolation bearings: (a) HDRB; (b) LRB.

2.2. Mechanical Properties of Rubber Bearings.

Rubber bearings not only need to support the superstructure of a bridge but also satisfy the deformation demand of the bridge under the action of external forces. Especially under the action of large earthquakes, bridge structures have a larger displacement and the bearings have a larger shear deformation [34]. LRBs and HDRBs can extend the overall period of the bridge structure by yielding, effectively avoiding the outstanding period of the earthquake, and reducing the seismic response of the superstructure based on the high damping characteristics, so as to achieve the effect of isolation [27]. The shear performance curve of LRBs and HDRBs under horizontal load is shown in Figure 2.

The equivalent horizontal stiffness, K_h, of LRBs and HDRBs is calculated according to the equation below:

$$K_h = G_{eq}(\gamma)\frac{A}{T_r}, \tag{1}$$

where G_{eq} is the equivalent shear modulus at the shear strain of γ; A is the plane area of the rubber inside the bearing, i.e., the effective area; and T_r is the total thickness of the rubber of the bearing.

The initial horizontal stiffness is calculated according to the following equation:

$$K_i = \frac{2 \cdot U(\gamma) - \pi \cdot h_{eq}(\gamma)[1 - U(\gamma)]}{2 \cdot U(\gamma) - \pi \cdot h_{eq}(\gamma)} \cdot K_h, \tag{2}$$

where $U(\gamma)$ is the ratio of yield force to shear force at the shear strain of γ and $h_{eq}(\gamma)$ is the equivalent damping ratio. $U(\gamma)$ and $h_{eq}(\gamma)$ are calculated according to equations (3) and (4), respectively:

$$U(\gamma) = \frac{Q_d}{K_h(T_r\gamma)}, \tag{3}$$

$$h_{eq}(\gamma) = \frac{W_d}{2\pi K_h(T_r\gamma)^2}, \tag{4}$$

where the yield force, Q_d, is experimentally determined, and W_d is the energy consumed for each loading cycle, i.e., the envelope area of the hysteresis curve of LRBs and HDRBs.

The postyield stiffness, K_d, is calculated according to the following equation:

$$K_d = [1 - U(\gamma)]K_h. \tag{5}$$

From the viewpoint of dynamics, the dynamic equation of bridge structures under the action of the earthquakes can be expressed as follows [35]:

$$m\ddot{x}(t) + c\dot{x}(t) + kx(t) = -m\ddot{x}_0(t), \tag{6}$$

where $\ddot{x}(t)$, $\dot{x}(t)$, and $x(t)$ are the acceleration, velocity, and displacement response of the bridge structure, respectively; $\ddot{x}_0(t)$ is the acceleration time history of the ground motion on the bridge structure, m is the mass of the structure, c is the damping, and k is the rigidity.

It can be seen from the dynamic equation that for a bridge structure with isolation bearings, its seismic response under the action of an earthquake can be changed by changing $m, c,$ and k. For example, by changing the damping, c, and the rigidity, k, of the bridge structures, LRBs and HDRBs can reduce the seismic response and thereby avoid seismic damage to the bridge structures.

3. Model of a Bridge

3.1. Physical Model of a Bridge.
Figure 3 shows the simplified geometry and a detailed structural drawing of the continuous beam bridge studied in this paper. Figure 3(a) shows a 3×50 m physical model of a continuous beam bridge, for which the piers are 50 m tall. The compressive strength of the concrete used for the girder and piers are 50 MPa and 40 MPa, respectively. Figure 3(b) shows that the girder of the bridge is composed of six T-beams; the bridge has a total width of 12.25 m, and the T-beams are 2.8 m tall; the deck pavement is composed of 8 cm thick C40 cement concrete and 10 cm thick asphalt concrete. Figure 3(c) shows the transverse, longitudinal and cross-sectional views of the pier from left to right. The piers are thin-walled and hollow with a sectional area of 6×4 m, a minimum section wall thickness of 0.5 m, and a maximum section wall thickness of 1 m. The yield strength of the steel used for piers is 400 MPa (according to Chinese code GB50010-2010) [23]. The pier
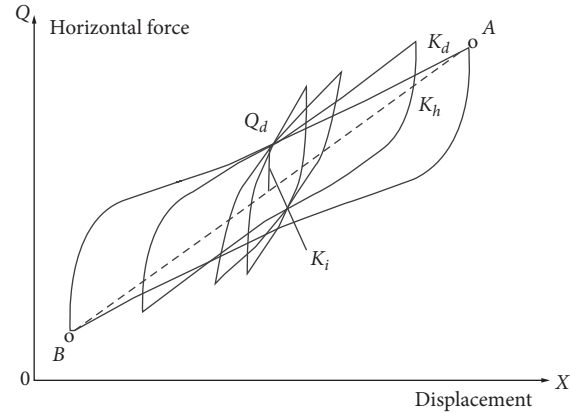
FIGURE 2: Shear performance curve of LRBs and HDRBs.

cap beams are 11.8 m long, 4.2 m wide, and 2.4 m tall; the caps are 8.3×8.3 m quadrates and 3 m tall.

3.2. Finite Element Model.

A 3-D model of the bridge structure was created by the nonlinear finite element program MIDAS [36, 37]. The simplified analysis model of the bridge is shown in Figure 4(a). The superstructure and substructure of the bridge were simulated by the lumped mass system and the small discrete segment method. The appropriateness of such a modeling approach for a bridge has been proven by the research of Choi et al. [38]. Zhang and Huo [39] verified the accuracy of the program by comparing the test results of static and dynamic loading experiments. In the bridge structure modeling, the girder was simulated by using elastic beam elements, while the bearings and piers were simulated by nonlinear elements. In the modeling details of the bridge system, piers, and bearings, as shown in Figure 4(b), elastic linear beam-column elements were used for girder; bilinear link elements were used for the bearings; rigid elements were used to connect the girder and piers with bearings; and fibre-based nonlinear elements were used to model the piers [40, 41]. The details of fibre-based nonlinear elements and the stress-strain relationship of unconfined concrete, confined concrete, and longitudinal steel reinforcement used for the pier sections are shown in Figure 4(c). The compressive strength of the unconfined concrete, confined concrete, and the yield stress of the steel reinforcement are 26.8 MPa, 29.2 MPa, and 345 MPa, respectively [23, 37]. The base of the pier, fixed as the interaction effect of the soil and the structure, was neglected [42]. The model had a total of 572 nodes, 48 nonlinear beam-columns, 600 elastic linear beam-columns, and 24 bilinear link elements.

3.3. Model for Rubber Bearings.

In this paper, the aseismic performance of different combinations of rubber bearings for the bridges was studied. According to the recommendations for the parameters of 50 m T-beam bearings in the Chinese standard, three different types of bearings, NRBs, LRBs and HDRBs, were selected for the bridge structure, respectively [6–8].

All of the bearings were simulated by bilinear elastic plastic spring element. The restoring force model of the sliding and fixed NRBs is shown in Figure 5(a). K_0 is the bearing stiffness, x_{0y} is the yield displacement, and Q_{0y} is the sliding frictional force [43]. The stiffness of LRBs and HDRBs is nonlinear, which was simulated by a mechanical model of bilinear restoring force as shown in Figure 5(b). K_1 is the preyield stiffness, K_2 is the postyield stiffness, K_h is the equivalent horizontal stiffness, x_y is the yield displacement, x_d is the limiting displacement, Q_y is the yield force, and Q_d is the limiting shear force of bearings [36, 44].

4. Case Setting

4.1. Case Setting of Bearings.

As the reaction forces of each pier are different, different combinations of bearings for the bridge were selected according to their vertical bearing force [45]. Based on the static analysis, the support reacting force of the bearings of the four piers was nearly symmetric [46–48]. The characteristics, such as bearings constructability, availability, and technique, are also very important to build a bridge, but the safety of the bridge, especially seismic performance, was studied in this paper [49]. Therefore, the No. 1 pier and No. 4 pier adopted the same type of bearing, while the No. 2 and No. 3 piers had the same type of bearings [37, 50, 51]. The study cases were as follows:

Case 1: without bearings

Case 2: NRBs used for the four piers (NRBs)

Case 3: LRBs used for the four piers (LRBs)

Case 4: NRBs used for the No. 1 and No. 4 piers and LRBs used for the No. 2 and No. 3 piers (NRBs + LRBs)

Case 5: HDRBs used for four the piers (HDRBs)

Case 6: NRBs used for the No. 1 and No. 4 piers and HDRBs used for the No. 2 and No. 3 piers (NRBs + HDRBs)

The case setting of the bearings are shown in Table 1.

The bearings were mainly selected according to the static analysis results, and the material properties and physical parameters of each bearing are shown in Table 2 (according to the Chinese codes JTT 4-2019, JTT 822-2011, and JTT 842-2012) [24, 44, 52]. The LRBs and HDRBs have nonlinear

(a)

(b)

(c)
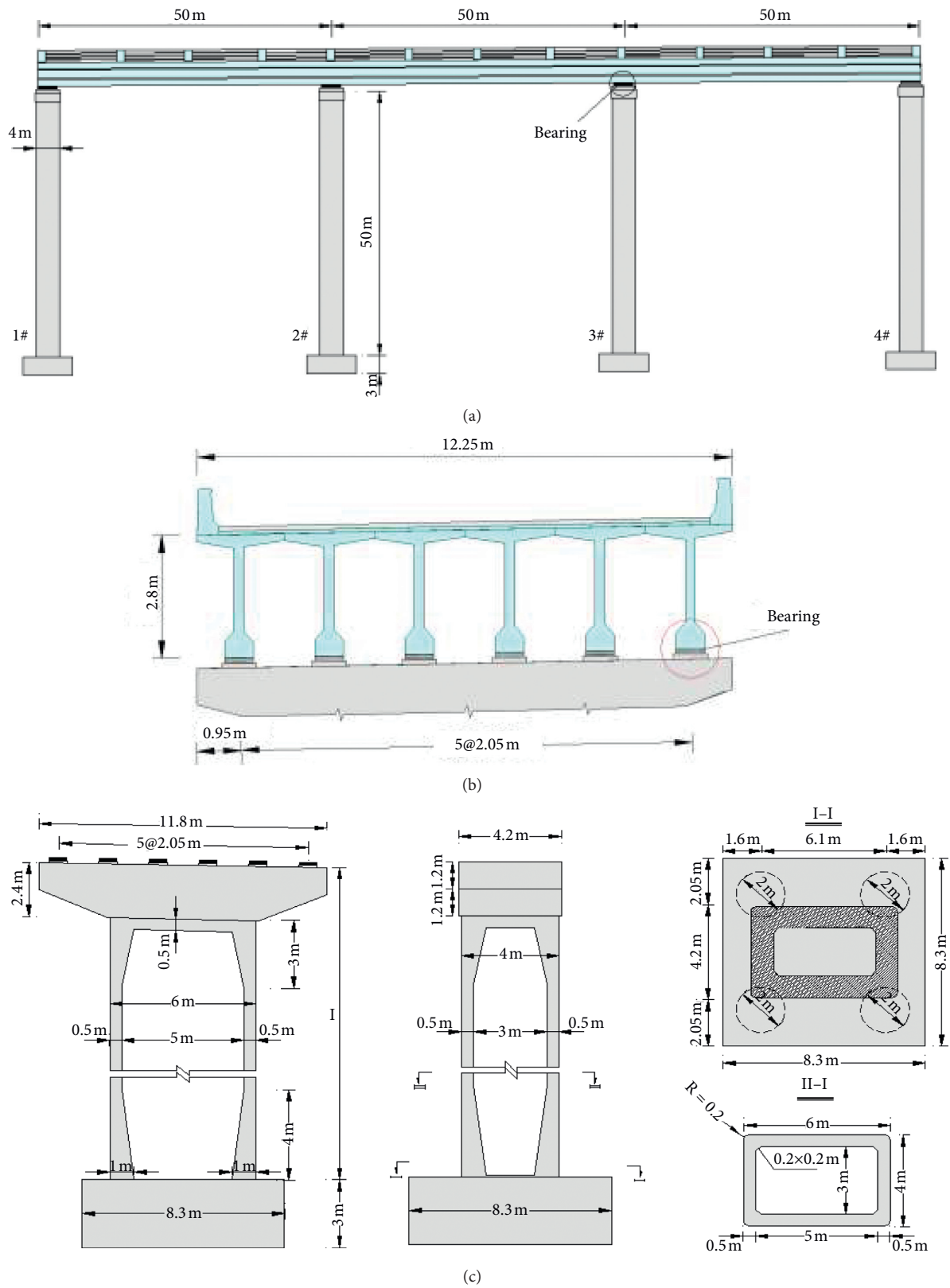
FIGURE 3: Simplified bridge geometry: (a) longitudinal view of the bridge; (b) transverse view of the superstructure; (c) details of the piers.

horizontal stiffness; as the bearing is subjected to a horizontal seismic force that exceeds its yield force, the preyield stiffness of the bearing becomes postyield stiffness [7, 8].

Considering that the horizontal stiffness of bearings is an important parameter during selection of the design parameters of the bearings, one horizontal equivalent stiffness
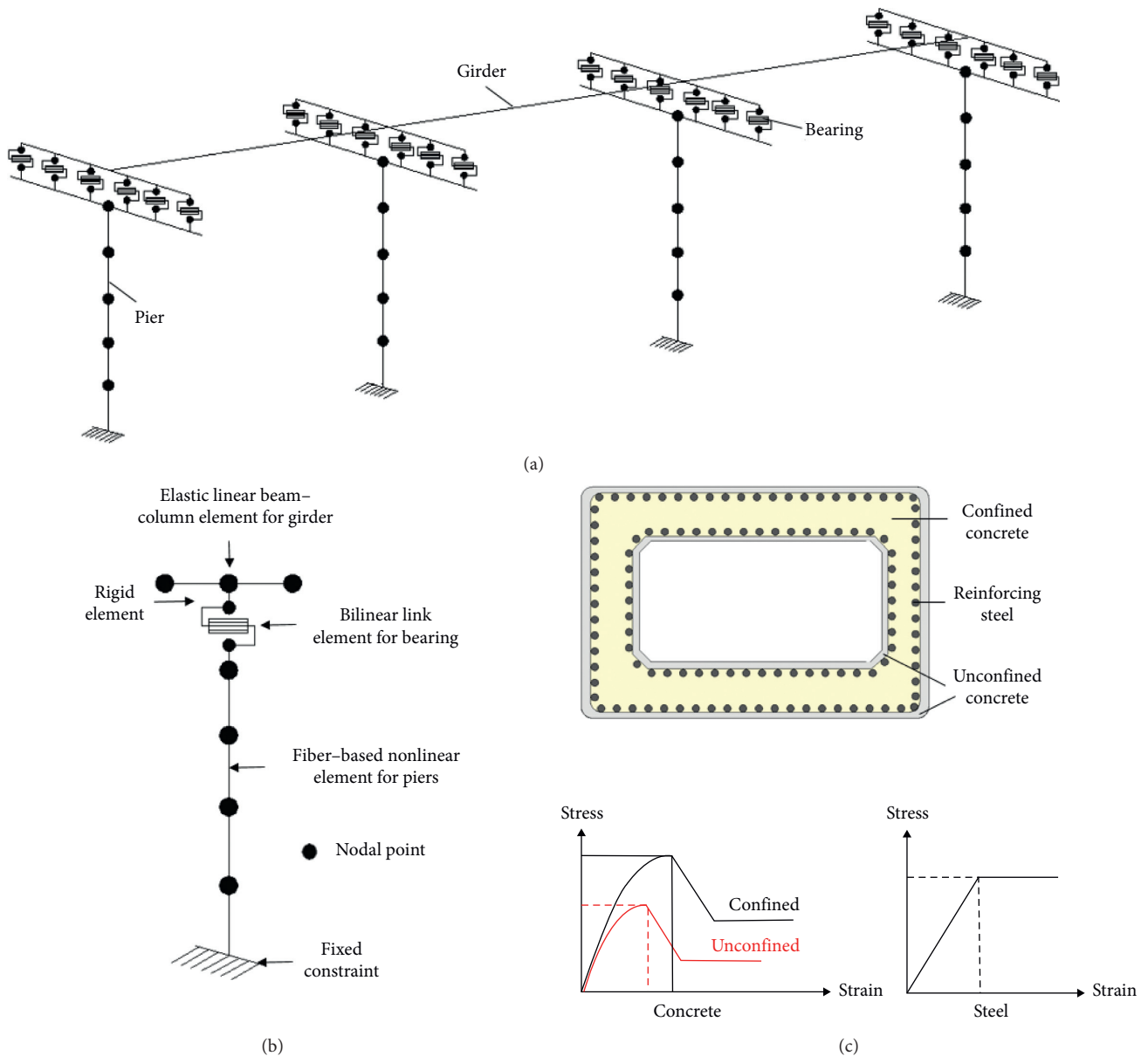
Figure 4: Analytical model: (a) 3-D finite element model of the total bridge system (girder and deck elements are not shown for clarity); (b) modeling details of an external bridge pier including the nonlinear model used for bearings; (c) details of the fibre-based nonlinear elements used for the pier sections.

value is taken for the bearings on side piers and middle piers through conversion, while the other stiffness parameters of the bearings are converted by the equivalent ratio to facilitate the analysis and comparison.

4.2. Earthquakes. The continuous beam bridge in this study is located in Yan'an city, Shaanxi province in China. The seismic fortification intensity of the site area is 7, while the site classification of the bridge is III, and the remarkable cycle of the site for small and large earthquakes is 0.56 s and 0.78 s, respectively [53, 54]. In order to analyze all of the responses of the bridge structure under different magnitudes of earthquake, time history dynamic

analysis was carried out using earthquakes with a probability of 40% and 2% in 100 years at the bridge site (three seismic waves in small and large earthquakes, respectively). In addition, there is an autocorrelation between three seismic waves of both small earthquake and large earthquake. Figure 6(a) shows the three seismic time history waves (401, 402, and 403) of small earthquakes, with a peak acceleration value of $0.431 \, \text{m/s}^2$, $0.436 \, \text{m/s}^2$, and $0.43 \, \text{m/s}^2$, respectively. Figure 6(b) shows the three seismic time history waves (21, 22, and 23) of large earthquakes, with a peak acceleration value of $1.542 \, \text{m/s}^2$, $1.548 \, \text{m/s}^2$, and $1.545 \, \text{m/s}^2$, respectively. The maximum values of the seismic response of the bridge obtained from the time history analysis with the three seismic waves were
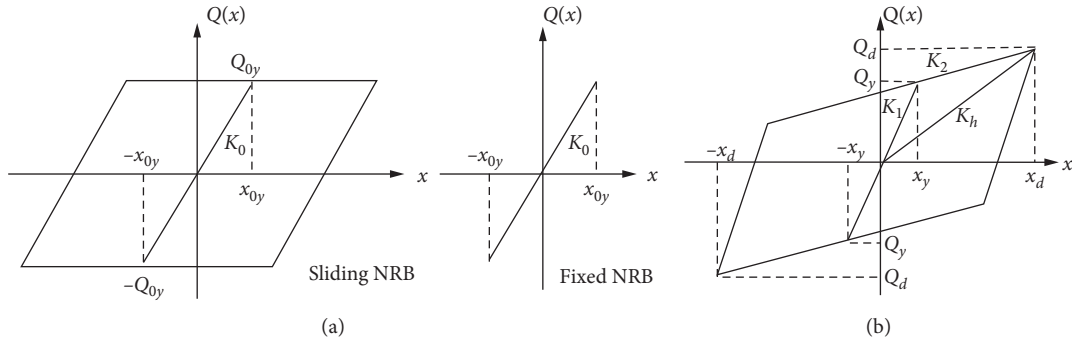
FIGURE 5: Layout and restoring force model of bearings: (a) restoring force model of NRB; (b) bilinear restoring force model of LRBs and HDRBs.

TABLE 1: Case setting of bearings.

Cases		1	2	3	4	5	6
Pier Nos.	No. 1, No. 4	—	NRB-1	LRB-1	NRB-1	NRB-1	HDRB-1
Pier Nos.	No. 2, No. 3	—	NRB-2	LRB-2	LRB-2	HDRB-2	HDRB-2

used to be discussed (according to the Chinese code JTG/T B02-01-2008) [34, 50].

5. Verification

The verification of a mathematical model is a key step for the simulation research [55, 56]. The shaking table test in reference [57] was analyzed by numerical simulation in this paper, in order to verify the correctness of the numerical model adopted in this paper. A two-span simply supported bridge model was built, as shown in Figure 7(a), with a 30 m long span and an 880 ton girder. All of the pier columns were the same height (8 m) and diameter (1.6 m). Circular laminated-rubber bearings with the diameter of 600 mm were used to support the beam. The specified yield strength of the steel reinforcement used in the model was 335 MPa, and that of the concrete was 40 MPa. The scale model for the shaking table test is shown in Figure 7(b), with the scale of 1/4 to the prototype bridge. The column diameter and the clear height of the piers were 0.4 m and 2 m, respectively. The Northridge earthquake recorded by the New Hall Fire Station with a peak acceleration of 0.59 g was used to analyze the seismic response of the bridge. The peak ground accelerations of ground motions were applied in increasing earthquake intensity, varying from 0.1 to 0.6 g. The displacement of the bearings was measured by the shaking table test, as shown in Figure 7(c).

The results show that under the action of earthquakes, the trend of the analytical bearing displacements is consistent with that of the experimental displacements, as can be seen in Figure 7(d). Figure 7(e) further presents the displacement errors in different intensities of the Northridge earthquake and shows that the errors between the analytical results and the experimental results are less than 13%, which meets the requirement for accuracy in this study [58, 59]. The difference may be due to the measuring instrument used

for the test, which cannot achieve accurate simulation in numerical analyses [4].

6. Analysis of the Results

6.1. Seismic Response of the Bridge

6.1.1. Displacement of the Bearings. Rubber bearings of bridges deform and thereby reduce the seismic load onto the structure in an earthquake, and their deformation capacity and hysteretic deformation under the action of earthquakes can directly reflect their aseismic effect. Figure 8 shows the displacement of the bearings at each pier in different cases under the action of small and large earthquakes. On the whole, the No. 1 and No. 4 piers have much higher bearing displacements than the No. 2 and No. 3 piers; the No. 3 pier basically has the same bearing displacements as the No. 2 pier in different cases; the displacement of the bearings under the action of large earthquakes is about 8 times that under the action of small earthquakes.

Figures 8(a) and 8(c) show the longitudinal displacement of each bearing under the action of small and large earthquakes, respectively. The displacement of the bearings of the different piers changes in the same trend. The displacement of the bearings of the No. 1 pier is larger; that at the No. 2 pier decreases and is close to that of the No. 3 pier; and that of the No. 4 pier increases and is close to that of the No. 1 pier. The bearing displacement of the No. 1 and No. 4 piers is generally larger than that of the No. 2 and No. 3 piers mainly due to the larger stiffness of the bearings of the No. 2 and No. 3 piers. However, the maximum displacement of the bearings under the action of large earthquakes is 42.09 cm in Case 2, which exceeds the limiting deformation of NRB-1. In several cases, the displacement of the bearings of the No. 1 and No. 4 piers exceeds the ultimate displacement, meaning that damage has occurred to the bearings. Under the action of small earthquake and large earthquakes, the bearings have the maximum displacement in Case 1. In Case 3, the longitudinal displacement

TABLE 2: Physical parameters of bearings.

Bearings	NRB-1	NRB-2	LRB-1	LRB-2	HDRB-1	HDRB-2
Height of bearings (mm)	96	112	154	234	137	187
Total thickness of rubber layer (mm)	67	82	76	125	70	110
Vertical bearing force (kN)	1258	2701	1417	3510	1360	3489
Vertical stiffness, K_v (kN/m)	689183	1168633	806791	1382812	875000	1427000
Preyield stiffness, K_1 (kN/m)	—	—	7225	12810	4690	7510
Postyield stiffness, K_2 (kN/m)	—	—	1133	1930	1340	2150
Equivalent stiffness, K_0, K_h(kN/m)	1700	2720	1700	2720	1700	2720
Yield force, Q_{0y}, Q_y(kN)	25	—	106	190	53	133
Shear modulus, G (MPa)	1.0	1.0	1.0	1.0	1.0	1.0
Damping ratio, ξ (%)	—	—	19.1	16.7	12	12
Limiting displacement (mm)	90	150	227	376	210	330

(a)

(b)
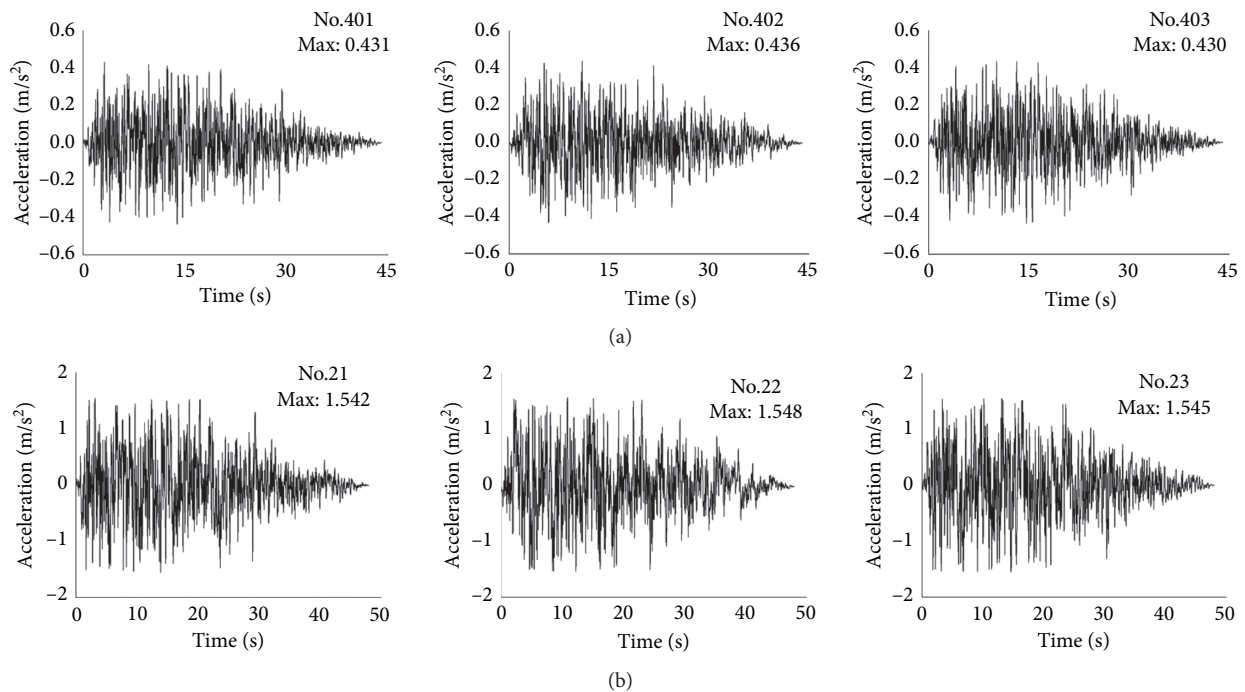
FIGURE 6: Time history and acceleration response spectrum of the earthquakes: (a) time history of the small earthquakes; (b) time history of the large earthquakes.

of each bearing is approximately 30% and 60% of maximum displacement under small and large earthquakes, respectively. In Case 5, the longitudinal displacement of each bearing is approximately 50% and 65% of the maximum displacement under the action of small and large earthquakes, respectively.

Figures 8(b) and 8(d) show the lateral displacement of each bearing under the action of small and large earthquakes, respectively. In different cases, the No. 1 and No. 4 piers have larger displacement of their bearings, while the No. 2 and No. 3 piers have similar displacement of their bearings, which is lower than that of the No. 1 and No. 4 piers. Under the action of small earthquake and large earthquakes, the bearings have maximum displacement in Case 2, which is much larger than that in other cases. The displacement of the bearings exceeds the limiting displacements under the action of large earthquake in Case 2, indicating that damage has occurred to bearings under the action of earthquake. In Case 3, the lateral displacement of

each bearing is approximately 30% and 40% of the maximum displacement under the action of small and large earthquakes, respectively. In Case 5, the lateral displacement of each bearing is approximately 35% and 45% of the maximum displacement under the action of small and large earthquakes, respectively.

In Cases 4 and 6, both the longitudinal and the lateral displacements of the bearings of the No. 1 and No. 4 piers are almost 2 times than those of the No. 2 and No. 3 piers under the action of small earthquakes due to the preyield stiffness of the bearings of the latter two piers being much larger than the NRBs of the former two piers. The displacements of NRB-1 exceed the limiting displacements under the action of large earthquakes in Cases 4 and 6. In Cases 3 and 5, as LRBs and HDRBs were set on all of the piers, the longitudinal and lateral bearing displacements under the action of earthquakes are smaller than in the other cases. The displacements of the LRBs and HDRBs are within the limiting

(a)

(b)

(c)

(d)

(e)
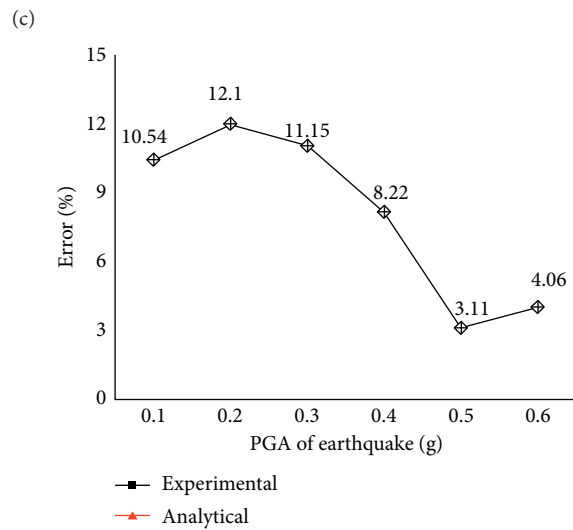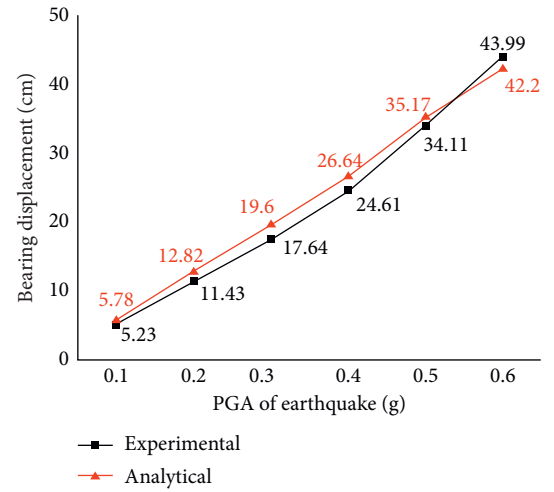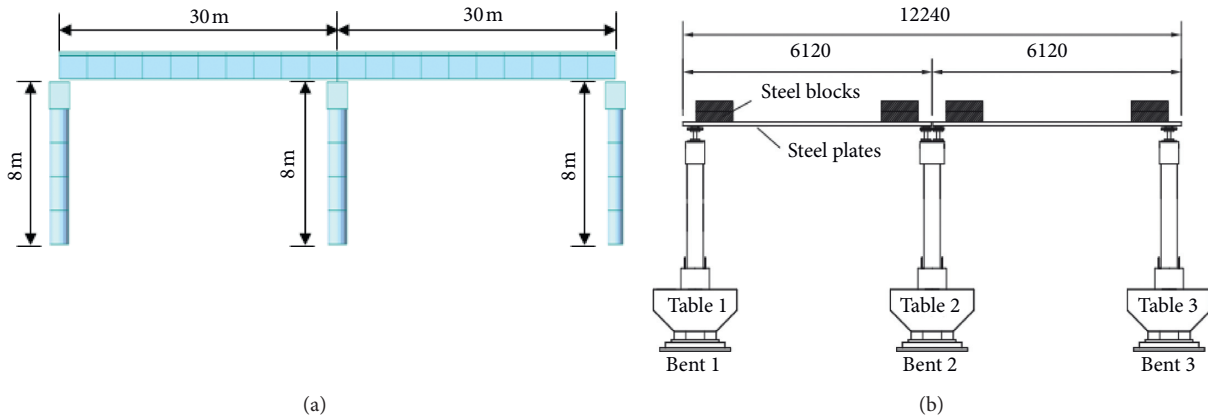
Figure 7: Models and results: (a) analytical model; (b) experimental model; (c) model for the shaking table test; (d) seismic response under different intensities of Northridge earthquake; (e) error analysis of the test and numerical simulation.

displacements under the action of large earthquake. Moreover, according to the pushover analysis results, the LRBs and HDRBs do not yield under the action of large earthquakes.

6.1.2. Hysteresis Curve of the Bearings. The hysteretic curve can characterize the deformation and energy characteristics of isolation bearings. Figure 9 shows the hysteretic curves of the LRBs and HDRBs of the No. 2 pier in different cases under the action of the small earthquake (401) and the large earthquake (23). The mechanical properties of the LRBs and HDRBs were nonlinear, as the horizontal seismic force at the bearings exceeds their yield force, and thus the bearings yield and dissipate seismic energy.

Figure 9(a) shows the hysteretic curves of the LRB-2 bearings of the No. 2 piers under the action of small and large earthquakes in Case 3. The hysteretic curves of LRB-2 in Case 3 are different under the action of small and large earthquakes. The LRB-2 bearings of the No. 2 pier have the maximum displacement of 1.17 cm and 22.26 cm and the maximum horizontal shear force of 121 kN and 572 kN under the action of small and large earthquakes, respectively. As the bearings never yield under the action of small earthquakes, the energy consumption is less (63,154 kJ), while the bearings yield under the action of large earthquakes and play a great role in the aseismic effect and energy consumption, with an energy consumption of 3,903,502 kJ.

Compared to Case 3, the hysteretic curves of LRB-2 in Case 4 under the action of small and large earthquakes are plumper. The LRB-2 bearings of the No. 2 pier have a maximum displacement of 1.47 cm and 28 cm, a maximum horizontal shear force of 149 kN and 683 kN, and an energy consumption of 94,186 kJ and 6,473,746 kJ under the action of small and large earthquakes, respectively. It can be seen from Figures 9(a) and 9(b) that the bearings of the No. 2 pier in Case 4 have larger (approximately 1.5 times) displacement, horizontal shear force, and energy consumption than those in Case 3 mainly because the bearings (NRB-1) of the No. 1 and No. 4 piers in Case 4 have much smaller stiffness and thereby larger shear deformation than the bearings (LRB-1) in Case 3 under the action of earthquakes.

Figures 9(c) and 9(d) show the hysteretic curves of HDRB-2 of the No. 2 piers under the action of small and large earthquakes in Cases 5 and 6, respectively. The HDRB-2 bearings of the No. 2 pier in Case 5 have a maximum displacement of 1.81 cm and 25 cm, a maximum horizontal shear force of 110 kN and 633 kN, and an energy consumption of 121,453 kJ and 548,017 kJ under the action of small and large earthquakes, respectively. In Case 6, the HDRB-2 bearings have a maximum displacement of 2.68 cm and 30.2 cm, a maximum horizontal shear force of 146 kN and 744 kN, and an energy consumption of 126,942 kJ and 8,629,838 kJ under the action of small and large earthquakes, respectively. The bearings of the No. 2 pier in Case 6 have larger (approximately 1.3

times) displacement, horizontal shear force, and energy consumption than those in Case 5, which are slightly larger than those in Case 4. This indicates that the LRBs in Case 4 have a better isolation effect than the HDRBs in Case 3.

6.1.3. Bending Moment of the Bottom of the Piers. The bending moment of a pier affects the seismic safety of the substructure of a bridge under the action of earthquakes. Theoretically, a smaller bending moment of the bottom of a pier leads to a higher seismic safety of the said pier. Figure 10 shows the bending moments of the bottom of the piers in the longitudinal and lateral directions of the bridge with different bearings under the action of small and large earthquakes. Figure 10(a) shows the bending moments of the bottom of the piers in the longitudinal direction of the bridge in different cases under the action of small earthquake. In Case 1, the change trend of the bottom bending moments of the four piers is similar to the displacement of the top of the piers. The No. 1 and No. 4 piers have maximum bending moments of their bottoms of 58,836 kN·m and 58,696 kN·m in Case 1, respectively. In the other cases, the No. 2 and No. 3 piers have higher bending moments of the bottom of the piers than the No. 1 and No. 4 piers. In Case 2, the four piers have the lowest bending moments of their bottoms; in Cases 4 and 6, the bending moments of the bottom of the No. 2 and No. 3 piers are almost 1.6 times bigger than those of the No. 1 and No. 4 piers. In Cases 3 and 5, the bending moments of the bottom of the piers are relatively small. Figure 10(b) shows that, in different cases, the bending moments of the bottom of the piers have similar trends, and the No. 2 and No. 3 piers have bigger bending moments of the pier bottoms than the No. 1 and No. 4 piers. In Case 1, the four piers have the biggest bending moments of their bottoms. In Cases 4 and 6, the No. 1 and No. 4 piers have almost 1.8 times bigger bending moments than the No. 2 and No. 3 piers. Due to the fact that the NRBs of the No. 1 and No. 4 piers have smaller stiffness and that the HDRBs of the No. 2 and No. 3 piers have higher stiffness, more seismic loads are transmitted to the No. 2 and No. 3 piers. The piers have smaller bending moments of their bottoms in Case 5, meaning that the HDRBs show a relatively better isolation effect under the action of small earthquake.

Figure 10(c) shows the longitudinal bending moment of the bottom of the piers under the action of large earthquakes. The bending moment increases first and then decreases in different cases. The bending moments of the bottoms of the different piers with LRBs and HDRBs (Cases 3–6) are similar and smaller than those with NRBs (Case 2). The bending moments of the bottom of the piers in Cases 3 and 5 are approximately 60% and 70% of those in Case 2, meaning that the LRBs and HDRBs have good aseismic effect and reduce the seismic load of the bridge, especially under the action of large earthquake. Although the same bearings were used for the No. 2 and No. 3 piers in Cases 3 and 4, the piers have bigger bending moments of their bottoms in Case 4 than in Case 3. The piers have almost

(a)

(b)

(c)

(d)
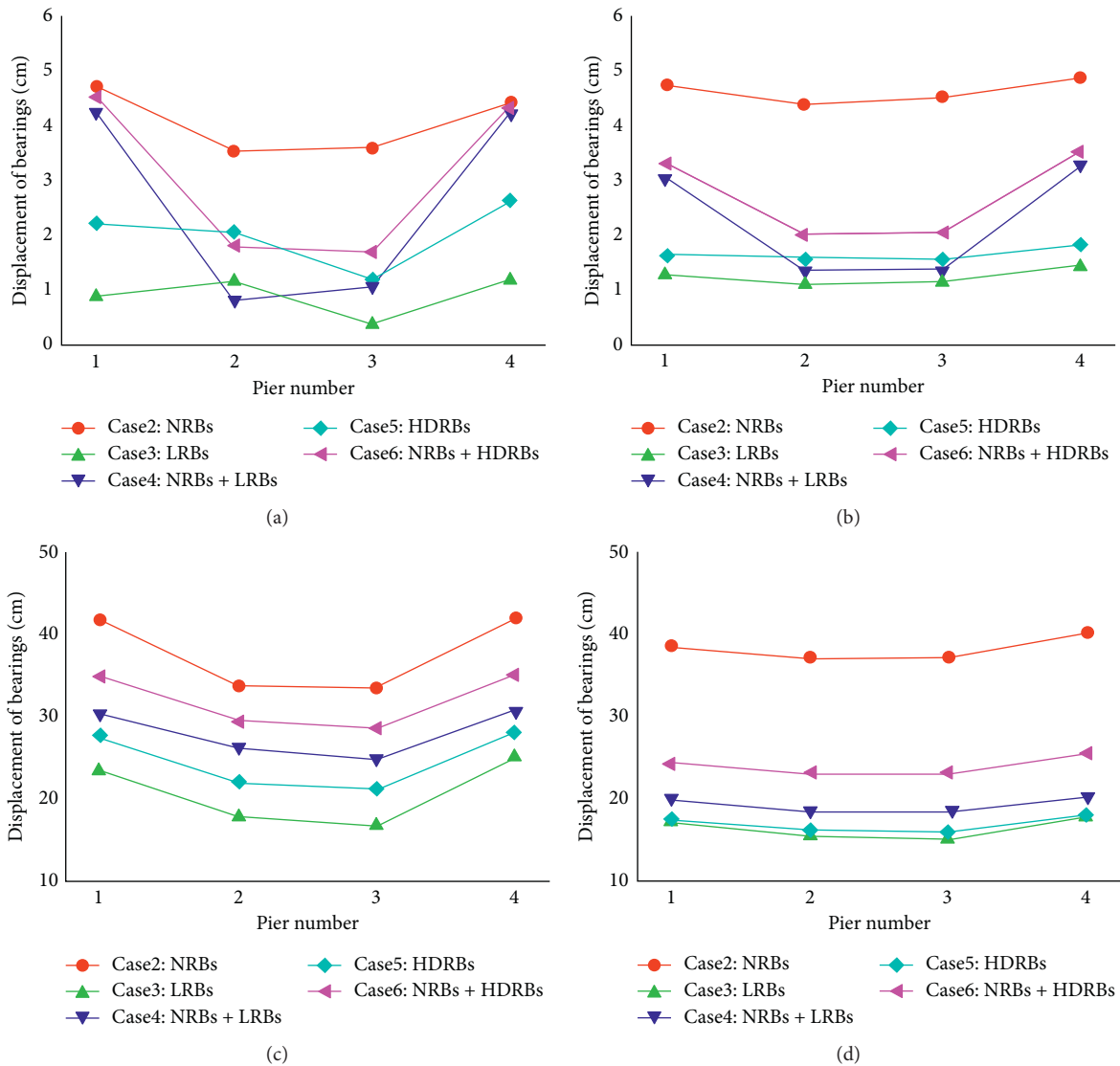
Figure 8: Displacement of bearings in different cases: (a) longitudinal displacement under the action of small earthquake; (b) lateral displacement under the action of small earthquake; (c) longitudinal displacement under the action of large earthquake; (d) lateral displacement under the action of large earthquake.

minimum bending moments of their bottoms in Case 1, and the bending moments of the bottom of the piers exceed the yield moment (292,468 kN·m) in Cases 1 and 2. Figure 10(d) shows the bending moments of the bottom of the piers in the lateral direction of the bridge under the action of large earthquake. The lateral bending moments of the bottom of the piers are almost the biggest in Cases 1 and 2. The other piers have smaller bending moments of their bottoms in the lateral directions of the bridge. The bending moments of the bottom of the piers in Cases 3 and 5 are almost 60% of that without bearings (Case 1). The bottom bending moments of the No. 2 and No. 3 piers exceed the yield moment in Cases 1 and 2, indicating that the use of isolation bearings can prevent the piers from being damaged under the action of large earthquakes.

According to the static elastoplastic pushover analysis results, the bottoms of the piers have lower longitudinal and lateral bending moments than maximum bending yield strength in different cases under the action of large earthquake.

6.1.4. Shear Force of the Bottom of the Piers. Figure 11 shows the shear forces of the bottom of the piers in the longitudinal and lateral directions of the bridge with different bearings under the action of small and large earthquakes, respectively. Figure 11(a) shows that in Case 1, No. 2 and No. 3 piers have smaller shear force of their bottoms than the No. 1 and No. 4 piers, and the piers have the maximum shear force of their bottoms in Case 1. In the other cases, the No. 2 and No. 3 piers have bigger shear force of their bottoms than the No. 1

(a)

(b)

(c)

(d)
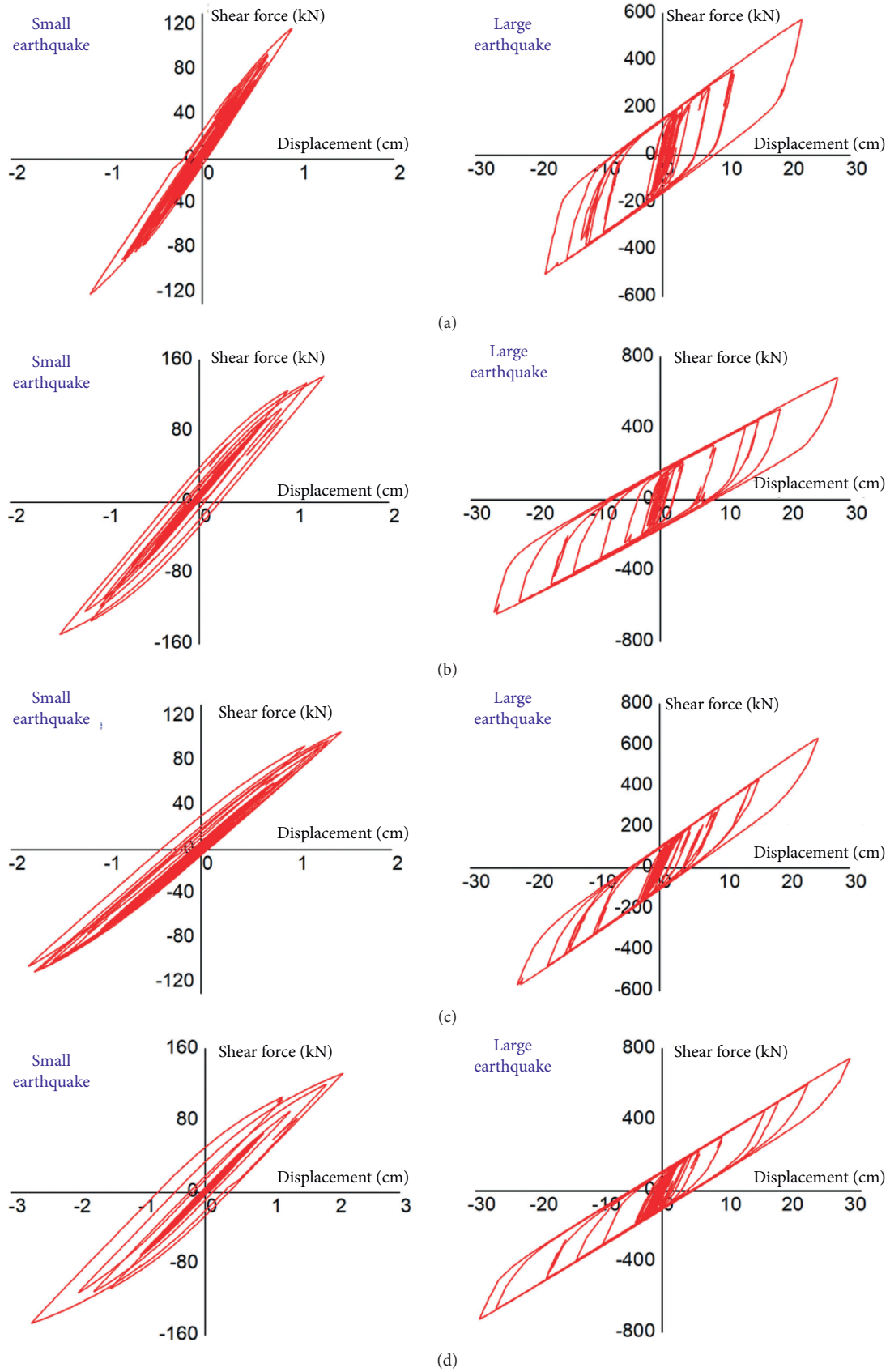
FIGURE 9: Hysteresis curve of bearings of the No. 2 pier: (a) LRB-2 in Case 3; (b) LRB-2 in Case 4; (c) HDRB-2 in Case 5; (d) HDRB-2 in Case 6.
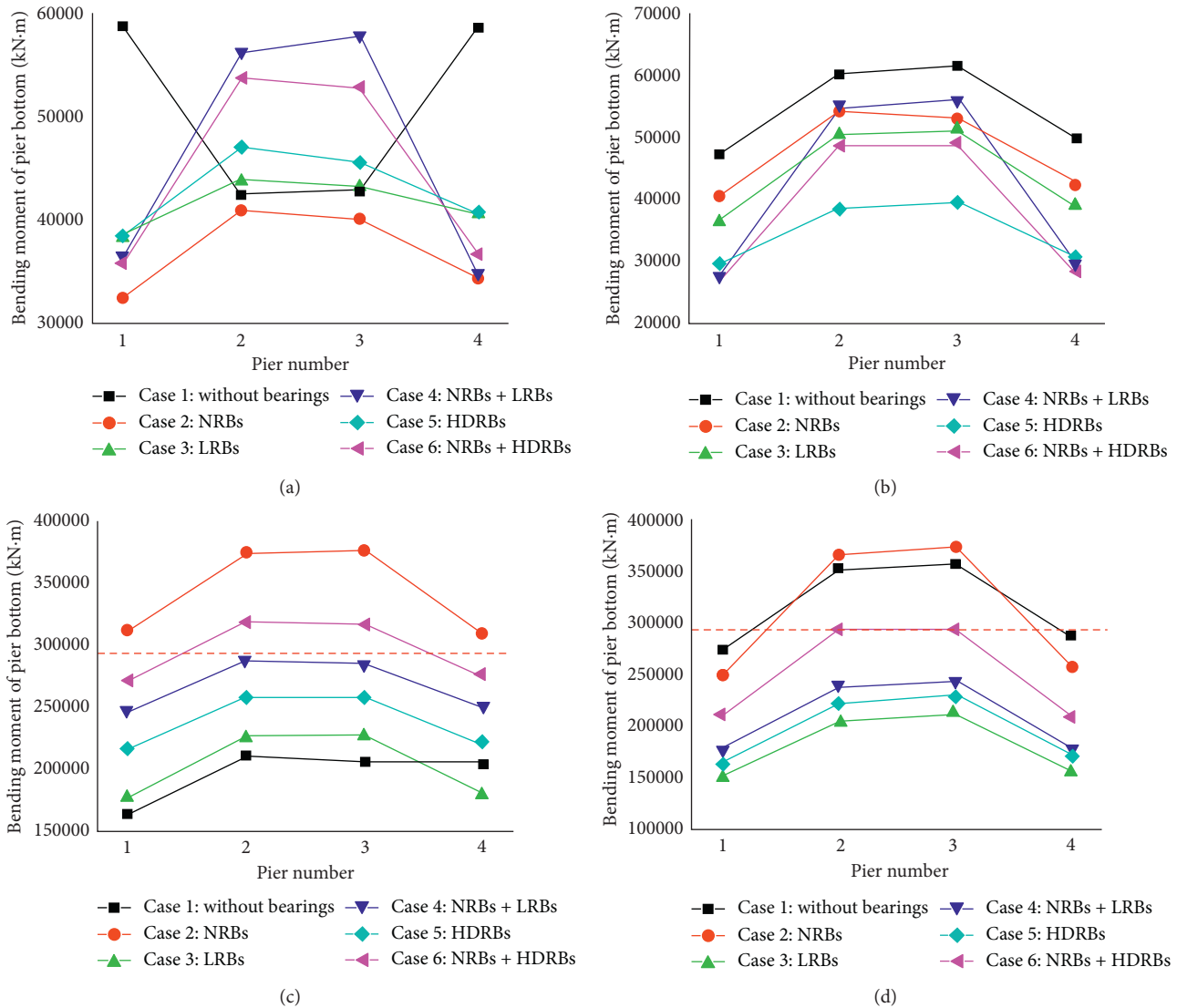
FIGURE 10: Bending moments of the bottom of the pier in different cases: (a) longitudinal moment under the action of small earthquake; (b) lateral moment under the action of small earthquake; (c) longitudinal moment under the action of large earthquake; (d) lateral moment under the action of large earthquake.

and No. 4 piers. The piers have smaller shear force of their bottoms in Case 2, which is approximately 60% of maximum shear force of the bottom of the piers in Case 1. Figure 11(b) shows the shear force of the bottom of the piers in the lateral direction of the bridge under the action of small earthquakes. In different cases, the shear force of the bottom of the piers increases first and then decreases in different cases. The overall shear force of the bottom of the piers is bigger in Case 1 and smaller in Case 5. The No. 2 and No. 3 piers have bigger shear force of their bottoms than the No. 1 and No. 4 piers in Cases 4 and 6 due to the fact that the LRBs and HDRBs do not yield under the action of small earthquakes and have bigger preyield stiffness than the NRBs in Case 2.

Figure 11(c) shows the shear force of the bottom of the piers in the longitudinal direction of the bridge under the

action of large earthquakes. The shear force of the bottoms of the four piers in Case 2 is 6821 kN, 7883 kN, 7947 kN, and 6927 kN, respectively, bigger than that of the corresponding piers in the other cases. The shear force of the bottoms of the piers with aseismic bearings (Cases 3 and 5) is approximately 70% of that without aseismic bearings (Case 2). The shear force of the bottoms of the piers in Cases 4 and 6 is approximately 85% of that in Case 2. Figure 11(d) shows the shear force of the bottoms of piers in the lateral direction of the bridge under the action of large earthquakes. The four piers in Case 2 have bigger shear force of their bottoms than in other cases. The piers in Case 3 have almost the smallest shear force of their bottoms, which is 65% of the shear force of those in Case 2; the shear force of the bottom of the piers in Case 1 is between that in Case 2 and Case 6.

(a)

(b)

(c)

(d)

Figure 11: Shear force of the bottom of the piers in different cases: (a) longitudinal shear force under the action of small earthquake; (b) lateral shear force under the action of small earthquake; (c) longitudinal shear force under the action of large earthquake; (d) lateral shear force under the action of large earthquake.

In summary, the use of isolation bearings can effectively reduce the shear force of the bottom of the piers of the bridge under the action of large earthquake, meaning that the LRBs and HDRBs have a better isolation effect. Under the action of small earthquakes, the bridge structure has the biggest overall seismic response in Case 1 without bearings because the bearings deformed and created an isolation effect in the other cases. In Cases 4 and 6, the bottom shear force of the No. 1 and No. 4 piers is smaller than that in Cases 3 and 5 under the action of small earthquakes, but the shear force of the No. 2 and No. 3 piers is bigger than that in Cases 3 and 5 due to the fact that bearings of the No. 2 and No. 3 piers do not yield and have bigger preyield stiffness under the action of small earthquakes. Under the action of large

earthquakes, the shear force of the bottom of the piers in Cases 4 and 6 is larger than that in Cases 3 and 5.

It is confirmed in the conclusion of the experimental study in reference [2] that the side and middle piers of the continuous beam bridge have quite different seismic response. Only HDRBs were used for each pier to investigate the acceleration response of the bridge in their studies.

6.1.5. Displacement of the Top of the Piers. In an earthquake, a larger displacement of the top of a pier leads to greater damage to a bridge. Thus, controlling the displacement of the top of a pier in a reasonable range is important to guaranteeing the stability of a bridge. Figure 12 shows the
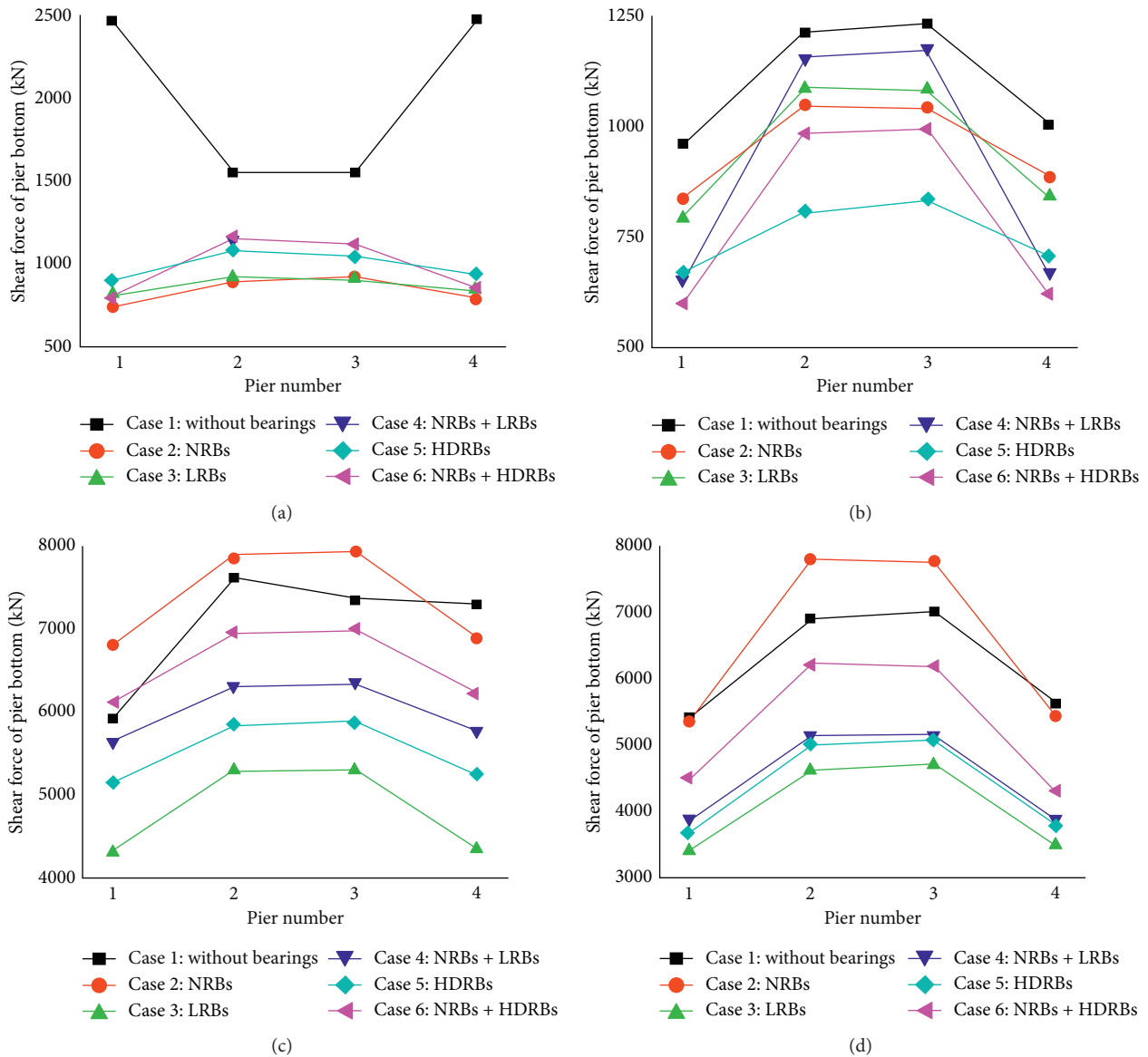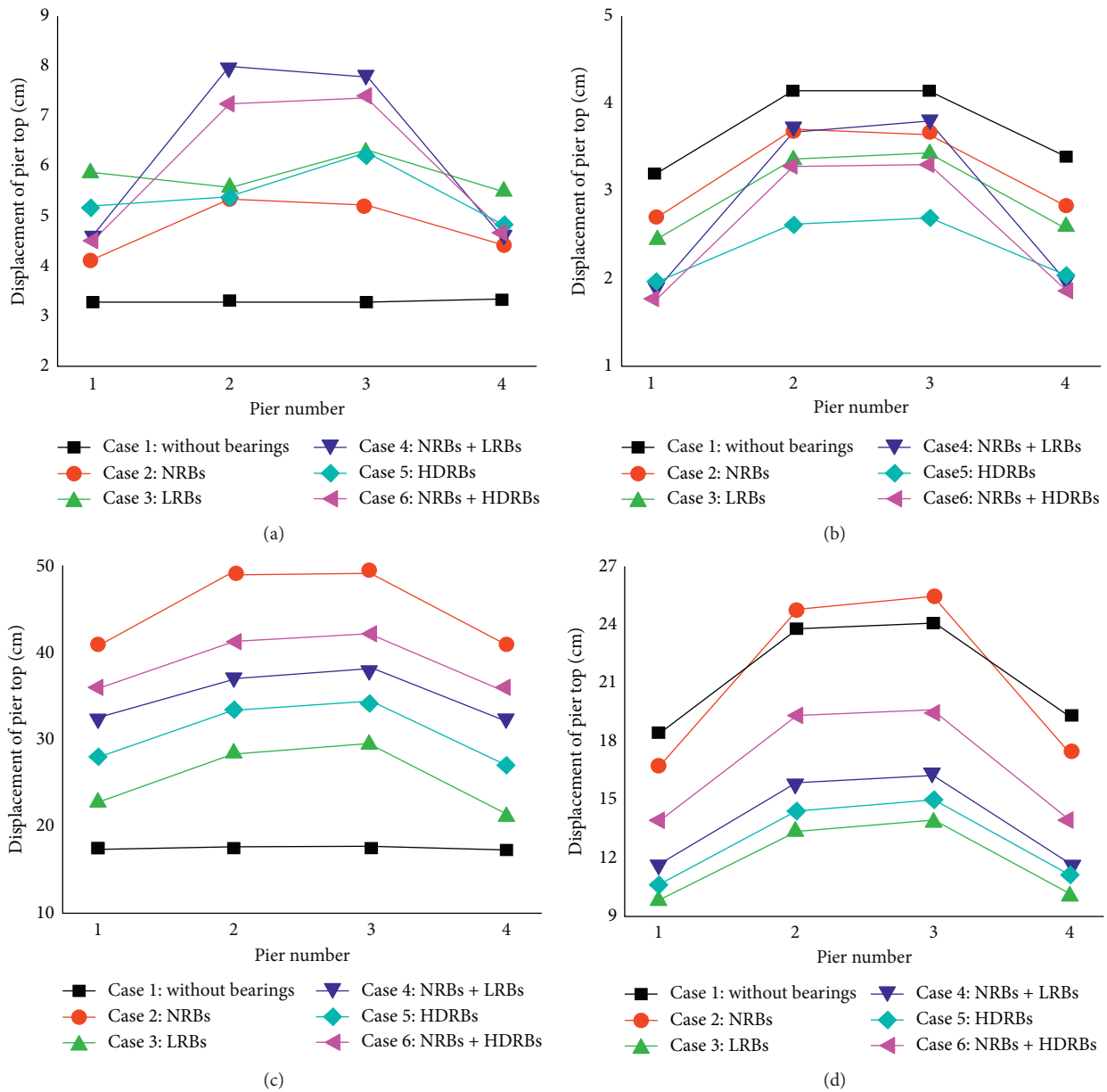
FIGURE 12: Displacement of the pier top in different cases: (a) longitudinal shear force under the action of small earthquake; (b) lateral shear force under the action of small earthquake; (c) longitudinal shear force under the action of large earthquake; (d) lateral shear force under the action of large earthquake.

displacement of the top of the piers in different cases under the action of small and large earthquakes. In the different cases, the No. 2 and No. 3 piers generally have bigger displacement of their tops than the No. 1 and No. 4 piers, and the piers at the two sides of the bridge have similar or much smaller displacement of their tops than the two piers in the middle of the bridge mainly due to the fact that the No. 2 and No. 3 piers have higher rigidity and thereby bear larger seismic load.

Figure 12(a) shows the longitudinal displacement of the top of the piers under the action of small earthquakes. The piers have the lowest displacement of their tops in Case 1, as the longitudinal stiffness of the bridge without bearings

is much bigger than in other cases. The piers generally have bigger displacement of their tops in Cases 4 and 6 than in the other cases, and the No. 2 and No. 3 piers have bigger displacement of their tops; meanwhile, the No. 1 and No. 4 piers have the biggest displacement of their tops in Case 3—5.84 cm and 5.53 cm, respectively. The No. 2 and No. 3 piers have the biggest displacement of their tops in Case 4—8.02 cm and 7.80 cm, respectively; the displacement of the top of the piers in Case 2 is lower than in the other cases, except in Case 1 (without bearings). Figure 12(b) shows the lateral displacement of the top of the piers under the action of small earthquakes; the lateral displacement of the action of the four piers increases first and then decreases in

different cases. The piers have a larger displacement of their tops in Case 1 than in the other cases, and smaller displacement of their tops in Case 3, which is almost 80% of the maximum displacement.

Figure 12(c) shows the longitudinal displacement of the top of the piers under the action of large earthquakes. The four piers have the lowest displacement of their tops in Case 1; and the biggest displacement in Case 2, i.e., 40.93 cm, 49.01 cm, 49.28 cm, and 40.72 cm, respectively. The piers with aseismic bearings have similar displacement of their tops; the displacement of the top of the piers in Case 3 is approximately 60% of the displacement in Case 2. Figure 12(d) shows the lateral displacement of the top of piers under the action of large earthquakes. The four piers in Cases 1 and 2 have almost the biggest displacement of their tops. The lateral displacement of the top of piers in Cases 3 and 5 is approximately 60% of that without bearings (Case 1). This means that aseismic bearings can effectively reduce the displacement of the piers, especially under the action of large earthquake, and LRBs have a better isolation effect than HDRBs. The results are similar to the research of Wang et al. [20], but they mainly focus on friction pendulum bearings.

6.1.6. Displacement of the Girder. Figure 13 shows the displacement of the girder in the longitudinal and lateral directions of the bridge in different cases under the action of small and large earthquakes. In different cases, the displacement of the girder is over 9 times bigger under the action of large earthquake than under the action of small earthquake. In Case 1, the girder has the lowest displacement, that is, 3.5 cm and 18 cm in the longitudinal direction and 4.5 cm and 26 cm in the lateral direction under the action of small and large earthquakes, respectively. In Case 2, the girder has the biggest displacement, namely, 8.9 cm and 83 cm in the longitudinal direction and 8.2 cm and 63 cm in the lateral direction under the action of small and large earthquakes, respectively. The girder displacement in Cases 4 and 6 is approximately 50% of that in Case 2, showing that LRBs and HDRBs have a better aseismic effect and effectively reduce the seismic load on the substructure of the bridge. The displacement of the girder in Cases 3 and 5 is approximately 80% of that in Cases 4 and 6. In all cases except Case 1, the longitudinal displacement of the girder is significantly greater than the lateral direction displacement.

6.2. Seismic Response of the Bridges with Different Pier Heights and Span Lengths. Section 6.1 studies the law of influence of different combinations of rubber bearings on the seismic performance of the continuous beam bridge with a span length and pier height of 50 m. In order to explore the applicability of the research conclusion, this section analyzes the isolation effect of various bearing combinations on continuous girder bridges with different pier heights and span lengths.

6.2.1. Seismic Response of the Bridge with Different Pier Heights. In order to compare the impact of the change in pier height on the seismic response of the structure, the span length of the bridge remained at 50 m and the pier heights were 10 m, 20 m, 30 m, 40 m, 50 m, and 60 m, i.e., with an increment of 10 m. As the seismic response, such as the bottom bending moment, the bottom shear force, and the top displacement of each pier similarly vary with the change of pier height, the seismic responses of the No. 2 pier under the action of large earthquakes were analyzed.

Figure 14 shows the trend of the longitudinal and lateral bending moments of the No. 2 pier in different cases as the pier height changes. Figure 14(a) shows that the longitudinal bottom bending moment of the No. 2 pier in different cases almost increases with the increase of pier height. In Case 1, when the height of the pier is 50 m, the bending moment of the bottom of the pier reduces to a certain extent. When the height of the pier is lower, the difference of the bottom bending moment of the pier is smaller in each case, which the largest is in Case 1. With the increase in pier height, the difference between the bending moments of the bottom of the piers in various cases gradually becomes obvious. When the pier height is 60 m, the difference in the pier's bottom bending moment decreases. With different pier heights, the bending moment of the bottom of the pier is the biggest in Case 2, as NRBs were used; the bending moments of the bottom of the pier in Cases 3 and 5 are approximately 60%–70% of that in Case 2, and in Cases 4 and 6, it is approximately 70%–80%.

As shown in Figure 14(b), the lateral bottom bending moments of the No. 2 pier in different cases present an increasing trend with the increase in pier height. When the pier height is 10–40 m, the maximum bending moment of the bottom of the pier is in Case 1; the maximum bending moment appears in Case 2 when the pier is 50–60 m high, which is slightly bigger than that in Case 1. The laws of other seismic response of the bridges are similar to the law of the longitudinal bending moment of the bottom of the pier.

Figure 15 shows the trend of the longitudinal and lateral girder displacements changing with pier height in different cases. The displacement of girder increases with the increase in pier height, and the girder displacement in Case 1 is the smallest. In the cases that the bridge has bearings, the displacement of the girder in Case 2 is the maximum, while the girder displacement in Cases 3 and 5 is approximately 60%–70% of that in Case 2, and in Cases 4 and 6, it is approximately 70%–80% of that in Case 2.

Figure 16 shows that the longitudinal and lateral displacements of the bearings of the No. 2 pier vary with the pier height in different cases. In Case 3, the bearing displacement is the smallest, while in Case 2, the bearing
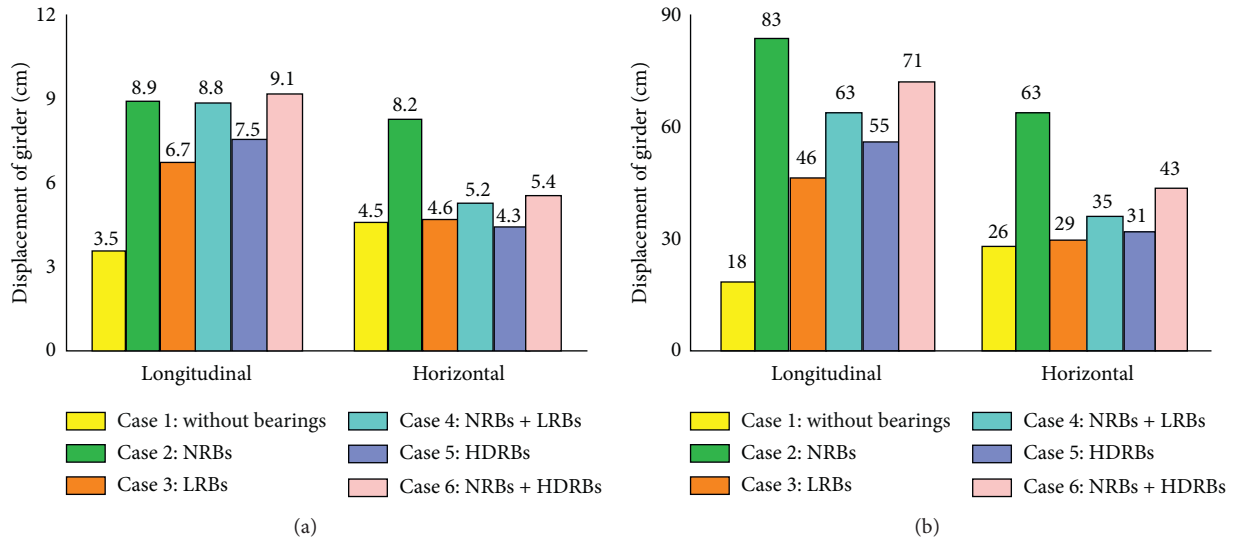
FIGURE 13: Displacement of the girder in different cases: (a) under the action of small earthquake; (b) under the action of large earthquake.
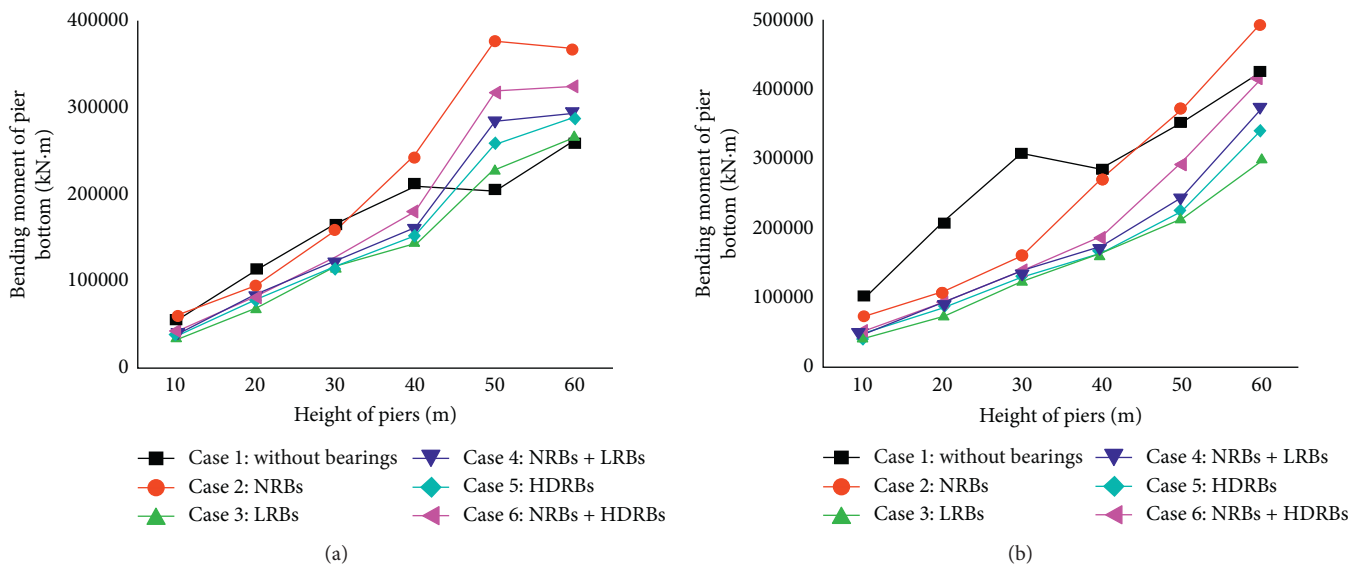
FIGURE 14: Bottom bending moments of the piers with the change of pier height in different cases: (a) longitudinal; (b) lateral.

displacement is the largest. In Figure 16(a), the longitudinal displacement of the bearings at the No. 2 pier basically increases first and then decreases with the increase of pier height. When the pier height is 60 m, the displacement of the bearing decreases greatly. In Figure 16(b), the lateral bearing displacement basically increases, and only the bearing displacement in Case 2 exceeds its limiting displacement.

6.2.2. Seismic Response of the Bridges with Different Span Lengths. In this section, the pier height of the bridge remained 50 m and the span lengths of the bridge were 35 m,

40 m, 45 m, 50 m, 55 m, and 60 m, i.e., with an increment of 5 m. Figure 17 shows that the longitudinal and lateral bending moments of the No. 2 pier in the different cases basically increase with the increase of span length. In the cases that the bridge with bearings, the bending moment at the bottom of the pier in Case 2 is the largest, while that in Cases 3 and 5 is approximately 60%–70% of that in Case 2, and in Cases 4 and 6, it is approximately 70%–80% of that in Case 2. In Case 1, when the bridge is without bearings, the longitudinal bending moment of the bottom of the pier is smaller than that in the other cases, while the lateral bending moment of the bottom of the pier is larger than that in other
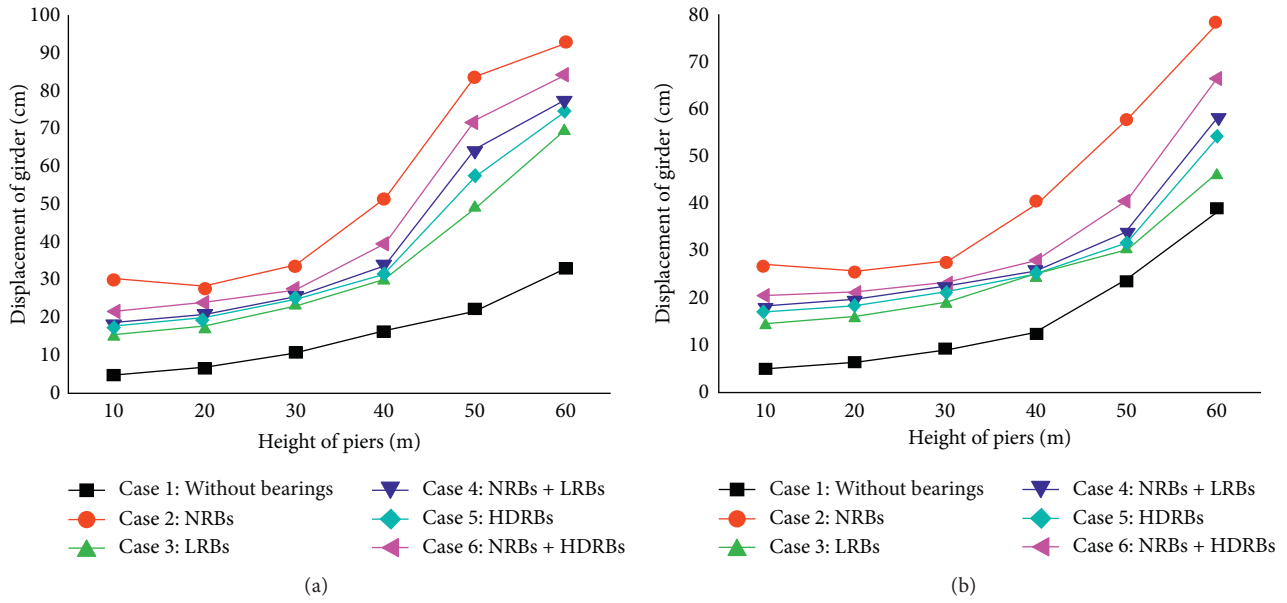
FIGURE 15: Displacement of girder with the change of pier height in different cases: (a) longitudinal; (b) lateral.
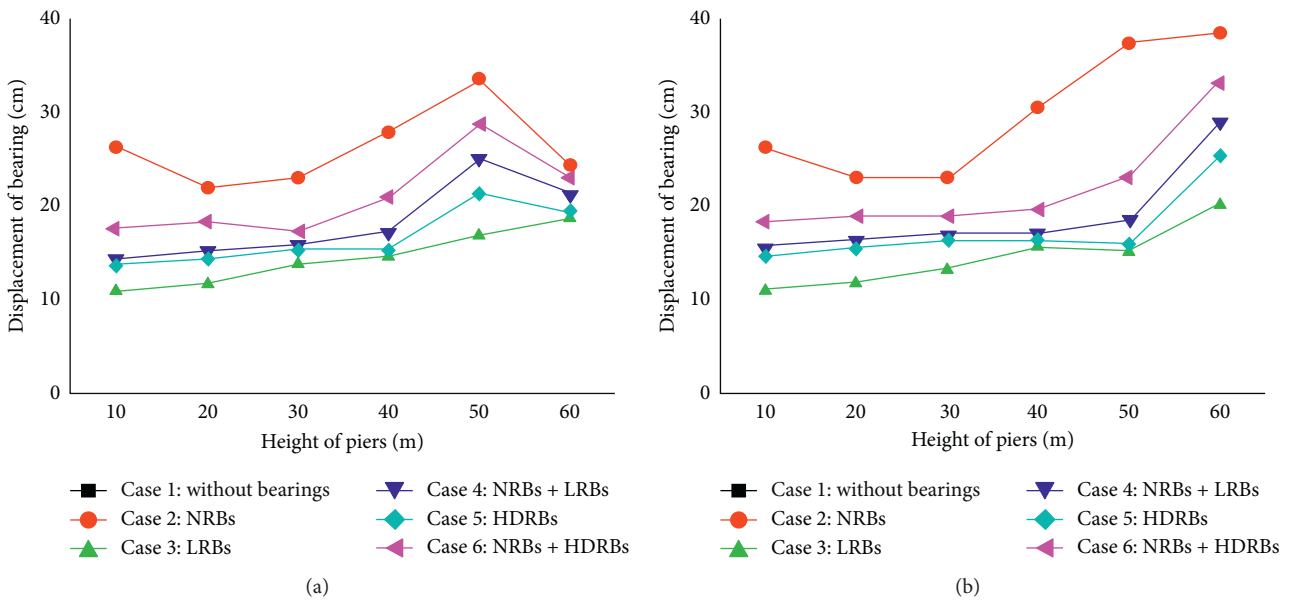
FIGURE 16: Displacement of bearings with the change of pier height in different cases: (a) longitudinal; (b) lateral.

cases. With the increase of span length, the difference in the bending moment of the bottom of the pier in various cases gradually becomes obvious. When the span length is 60 m, the difference of the longitudinal bending moment of the bottom of the pier decreases slightly.

Figure 18 shows that the longitudinal and lateral displacements of the bearings of the No. 2 pier vary with the change of span length in different cases. In Case 2, the bearing displacement is the maximum, while in Case 3, the bearing displacement is the minimum, which is 50%–60% of that in Case 2. The longitudinal and lateral displacements of the bearings both increase with the increase of span length. When the span length is 60 m, the bearing displacement decreases slightly in Case 2. However, the displacements of NRB-2 exceed the limiting displacements under the action of large earthquake in Case 2 with different span lengths.
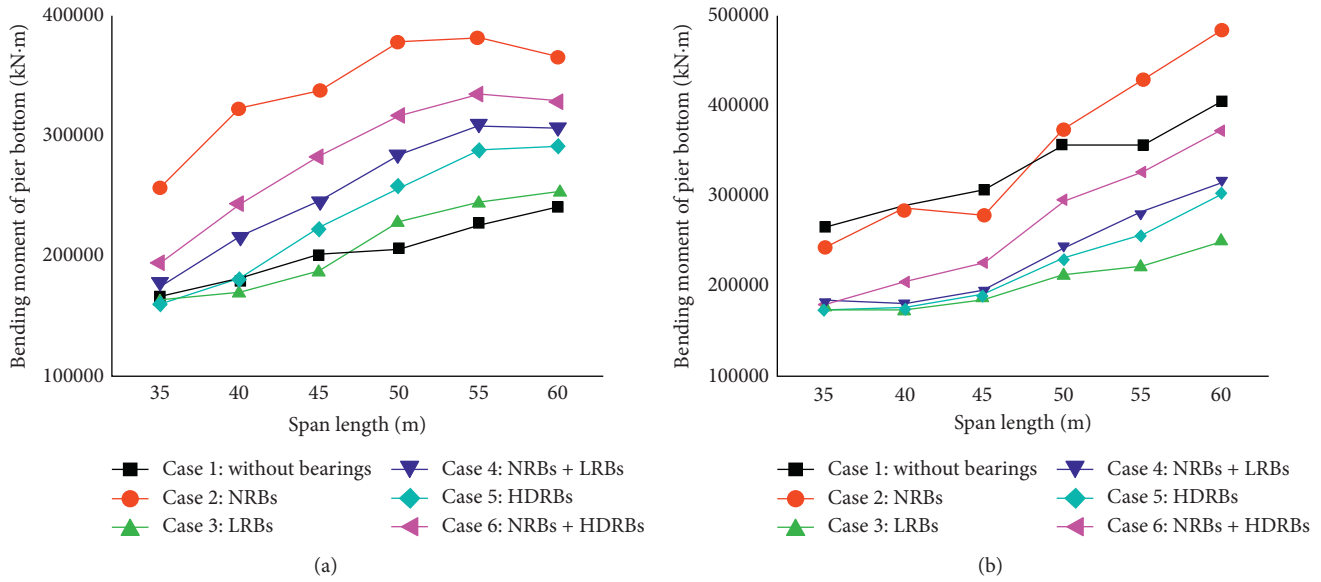
FIGURE 17: Bottom bending moment of the pier with the change of span length in different cases: (a) longitudinal; (b) lateral.
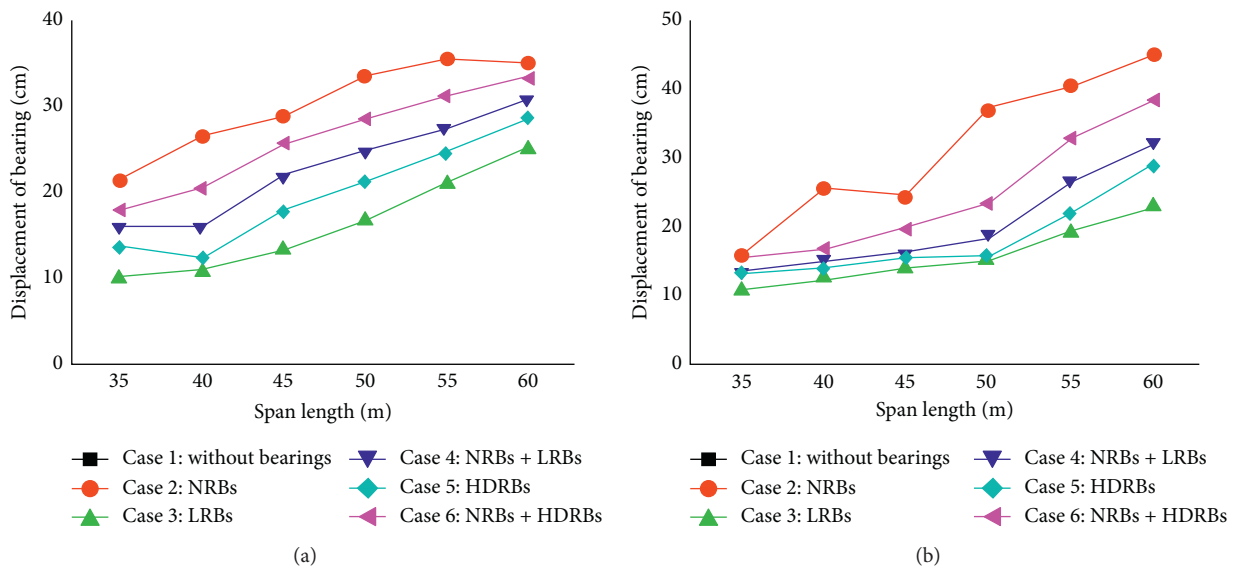
FIGURE 18: Displacement of bearings with the change of span length in different cases: (a) longitudinal; (b) lateral.

7. Conclusions

In this paper, the seismic performance of different combinations of rubber isolation bearings for the continuous beam bridges with different pier heights and span lengths under the action of small and large earthquakes was studied. The seismic effects of the different combinations of rubber bearings on the displacement, bending moment of pier, and girder displacement of the bridge under the action of earthquakes were analyzed. The main conclusions are as follows:

(1) Due to the nonlinear horizontal stiffness of LRBs and HDRBs, it was proved that the cases in which the bridge uses LRBs and HDRBs were more effective than cases with NRBs in reducing the seismic response of the continuous bridges with T-beams under the action of earthquakes. LRBs and HDRB dissipate seismic energy through yield and damping effects and show excellent isolation performance under the action of large earthquakes compared to that of other bearings.

(2) The seismic response of the bridge was lower in Cases 3 and 5 (LRBs and HDRBs) than in Cases 4 and 6 (NRBs + LRBs and NRBs + HDRBs), and much lower than in Case 2 (NRBs). The values of the

physical quantities in Cases 3 and 5 were approximately 60%–70% of those in Case 2. The seismic response of the bridge in Cases 4 and 6 are mostly between those in Case 2 and those in Cases 3 and 5 (approximately 70%–80% of those in Case 2). However, Cases 4 and 6 were more economical than Cases 3 and 5, as the unit price of NRBs is relatively cheaper than that of LRBs and HDRBs.

(3) No. 2 and No. 3 piers generally have bigger displacement of the tops and bigger shear force and the bending moments of the bottoms than No. 1 and No. 4 piers, especially in Cases 4 and 6 under the action of small earthquakes. More seismic loads are transmitted to the No. 2 and No. 3 piers due to the fact that No. 1 and No. 4 piers have smaller stiffness of the bearings than No. 2 and No. 3 piers. However, the bearings with lower stiffness have larger displacement than those with higher stiffness under the action of earthquakes. The larger difference in stiffness of the bearings between the side and middle piers leads to more unbalanced seismic response of each pier of the bridge structure.

(4) No matter how the pier height or the span length of the bridge changes, the law of influence of the bearing combinations on the seismic response of a bridge is similar. The seismic response of the bridge in each case was relatively close to each other when the pier height and span length were small, and the difference in the seismic response values of each case gradually increased as the pier height and span length increased. LRBs and HDRBs on all the piers are more suitable for isolation design for the continuous beam bridge with longer span and higher pier. In Cases 4 and 6, the use of cheaper NRBs underneath some girders is more reasonable for the continuous beam bridge with shorter span and lower pier.

(5) In Case 1, the piers and the girder were fixed without bearings. When the pier height was lower, the pier stiffness was larger, and the bottom bending moment of the pier was larger; as the pier height increased, the bending moment of the bottom of the pier decreased, along with the pier stiffness, which was more obvious when the pier height was 40 m.

In this paper, the influence of the collision of adjacent bridges and different site conditions for the isolation effect of the bridge is not considered. In the future, studies will be carried out on the constructability, availability, and technical soundness of the isolation bearings for continuous beam bridges.

Data Availability

All the data used to support the findings of this study are included in the paper.

Conflicts of Interest

The authors declare that they have no conflicts of interest.

References

[1] N. Xiang and M. Shahria Alam, "Comparative seismic fragility assessment of an existing isolated continuous bridge retrofitted with different energy dissipation devices," *Journal of Bridge Engineering*, vol. 24, no. 8, Article ID 0001425, 2019.

[2] Y. Li, Z. Zong, and B. Yang, "Experimental study on seismic performance of concrete continuous bridge with HDR bearings," *Journal of The Institution of Engineers: Series A*, vol. 101, pp. 1–22, 2020.

[3] N. Xiang, M. S. Alam, and J. Li, "Shake table studies of a highway bridge model by allowing the sliding of laminated-rubber bearings with and without restraining devices," *Engineering Structures*, vol. 171, pp. 583–601, 2018.

[4] Y. Zhang, Y. Shi, and D. Liu, "Seismic effectiveness of multiple seismic measures on a continuous girder bridge," *Applied Sciences*, vol. 10, no. 2, p. 624, 2020.

[5] A. K. M. T. A. Khan, M. A. R. Bhuiyan, and S. B. Ali, "Seismic responses of a bridge pier isolated by high damping rubber bearing: effect of rheology modeling," *International Journal of Civil Engineering*, vol. 17, no. 11, pp. 1767–1783, 2019.

[6] N. Xiang and J. Li, "Experimental and numerical study on seismic sliding mechanism of laminated-rubber bearings," *Engineering Structures*, vol. 141, pp. 159–174, 2017.

[7] A. M. Billah and B. Todorov, "Effects of subfreezing temperature on the seismic response of lead rubber bearing isolated bridge," *Soil Dynamics and Earthquake Engineering*, vol. 126, Article ID 105814, 2019.

[8] E. Tubaldi, S. A. Mitoulis, and H. Ahmadi, "Comparison of different models for high damping rubber bearings in seismically isolated bridges," *Soil Dynamics and Earthquake Engineering*, vol. 104, pp. 329–345, 2018.

[9] W. Zhang, H. Wu, H. Hwang et al., "Bearing behavior of reinforced concrete column-isolated footing substructures," *Engineering Structures*, vol. 200, Article ID 109744, 2019.

[10] L.-P. Guay and N. Bouaanani, "Assessment of low temperature exposure for design and evaluation of elastomeric bridge bearings and seismic isolators in Canada," *Canadian Journal of Civil Engineering*, vol. 43, no. 9, pp. 851–863, 2016.

[11] X. Chen and C. Li, "Seismic performance of tall pier bridges retrofitted with lead rubber bearings and rocking foundation," *Engineering Structures*, vol. 212, Article ID 110529, 2020.

[12] F. Paolacci, R. Giannini, and M. De Angelis, "Seismic response mitigation of chemical plant components by passive control techniques," *Journal of Loss Prevention in the Process Industries*, vol. 26, no. 5, pp. 924–935, 2013.

[13] W. Wang and X. Wang, "Tests, model, and applications for coned-disc-spring vertical isolation bearings," *Bulletin of Earthquake Engineering*, vol. 18, no. 1, pp. 357–398, 2020.

[14] N. Nakata, R. Erb, and M. Stehman, "Mixed force and displacement control for testing base-isolated bearings in real-time hybrid simulation," *Journal of Earthquake Engineering*, vol. 23, no. 6, pp. 1055–1071, 2019.

[15] F. Mazza and A. Vulcano, "Experimental tests and analytical modelling of a scaled isolated structure on sliding and elastomeric bearings," *Advances in Materials Science and Engineering*, vol. 2016, Article ID 2942194, 15 pages, 2016.

[16] N. D. Oliveto, A. A. Markou, and A. Athanasiou, "Modeling of high damping rubber bearings under bidirectional shear loading," *Soil Dynamics and Earthquake Engineering*, vol. 118, pp. 179–190, 2019.

[17] K. Yamamoto, K. Fujita, and I. Takewaki, "Instantaneous earthquake input energy and sensitivity in base-isolated building," *The Structural Design of Tall and Special Buildings*, vol. 20, no. 6, pp. 631–648, 2011.

[18] L. R. Pradilla and G. C. Cho, "Uso de aisladores de base en puentes de concreto simplemente apoyados," *Tecnura*, vol. 16, no. 34, pp. 103–124, 2012.

[19] D. Losanno, H. A. Hadad, and G. Serino, "A case study on performance of isolated bridges under near-fault ground motion," *Urban and Civil Engineering*, vol. 11, no. 4, pp. 387–392, 2017.

[20] B. Wang, Q. Han, and J. Jia, "Seismic response analysis of isolated offshore bridge with friction sliding bearings," *Earthquakes and Structures*, vol. 16, no. 6, pp. 641–654, 2019.

[21] W. Zheng, H. Wang, H. Hao et al., "Performance of bridges isolated with sliding-lead rubber bearings subjected to near-fault earthquakes," *International Journal of Structural Stability and Dynamics*, vol. 20, no. 2, Article ID 2050023, 2020.

[22] H. Anajafi, K. Poursadr, M. Roohi, and E. Santini-Bell, "Effectiveness of seismic isolation for long-period structures subject to far-field and near-field excitations," *Frontiers in Built Environment*, vol. 6, Article ID 00024, 2020.

[23] L. Zhen, L. Dejian, P. Leihua, L. Yao, C. Kepei, and W. Qianqiu, "Study on the damping efficiency of continuous beam bridge with constant cross-section applied by lead rubber bearings and fluid viscous dampers," *Noise & Vibration Worldwide*, vol. 51, pp. 85–92, 2020.

[24] T. Takeuchi, M. Uchida, and R. Matsui, "Response characteristics of spherical sliding bearings and superstructure subject to bidirectional ground motions," *Journal of Structural and Construction Engineering (Transactions of AIJ)*, vol. 82, no. 739, pp. 1339–1347, 2017.

[25] Y. Bao, T. C. Becker, T. Sone, and H. Hamaguchi, "To limit forces or displacements: collapse study of steel frames isolated by sliding bearings with and without restraining rims," *Soil Dynamics and Earthquake Engineering*, vol. 112, pp. 203–214, 2018.

[26] F. H. Dezfuli and M. Shahria Alam, "Performance-based assessment and design of FRP-based high damping rubber bearing incorporated with shape memory alloy wires," *Engineering Structures*, vol. 61, no. 61, pp. 166–183, 2014.

[27] P. Tan, J.-d. Huang, C.-M. Chang, and Y. Zhang, "Failure modes of a seismically isolated continuous girder bridge," *Engineering Failure Analysis*, vol. 80, pp. 57–78, 2017.

[28] H. S. Gu and Y. Itoh, "Ageing behaviour of natural rubber and high damping rubber materials used in bridge rubber bearings," *Advances in Structural Engineering*, vol. 13, no. 6, pp. 1105–1113, 2010.

[29] B. D. Liu, S. Z. Yang, W. L. Li, and M. Q. Zhang, "Damping dissipation properties of rubberized concrete and its application in anti-collision of bridge piers," *Construction and Building Materials*, vol. 236, Article ID 117286, 2020.

[30] J.-C. Li, H.-S. Zhang, X.-Y. Zhao et al., "Development of high damping natural rubber/butyl rubber composites compatibilized by isobutylene-isoprene block copolymer for isolation bearing," *Express Polymer Letters*, vol. 13, no. 8, pp. 686–696, 2019.

[31] A. A. Markou and G. D. Manolis, "Numerical solutions for nonlinear high damping rubber bearing isolators: newmark's method with newton-raphson iteration revisited," *Journal of Theoretical and Applied Mechanics*, vol. 48, no. 1, pp. 46–58, 2018.

[32] W. Wei, P. Tan, Y. Yuan, and H. Zhu, "Experimental and analytical investigation of the influence of compressive load on rate-dependent high-damping rubber bearings," *Construction and Building Materials*, vol. 200, pp. 26–35, 2019.

[33] Q. Rong, "Optimum parameters of a five-story building supported by lead-rubber bearings under near-fault ground motions," *Journal of Low Frequency Noise, Vibration and Active Control*, vol. 39, no. 1, pp. 98–113, 2020.

[34] K. Bhowmik and P. Saha, "Seismic response control of benchmark highway bridge using passive hybrid control systems," *International Journal of Materials and Structural Integrity*, vol. 11, no. 4, pp. 155–174, 2017.

[35] G. Augusti, "Dynamics of structures: theory and applications to earthquake engineering," *Meccanica*, vol. 31, no. 6, pp. 719-720, 1996.

[36] J. Guo, J. Zhong, X. Dang, and W. Yuan, "Influence of multidirectional cable restrainer on seismic fragility of a curved bridge," *Journal of Bridge Engineering*, vol. 24, no. 3, Article ID 04019001, 2019.

[37] H. Gou, W. Zhou, Y. Bao, X. Li, and Q. Pu, "Experimental study on dynamic effects of a long-span railway continuous beam bridge," *Applied Sciences*, vol. 8, no. 5, p. 669, 2018.

[38] E. Choi, R. Desroches, and B. Nielson, "Seismic fragility of typical bridges in moderate seismic zones," *Engineering Structures*, vol. 26, no. 2, pp. 187–199, 2004.

[39] J. Zhang and Y. Huo, "Evaluating effectiveness and optimum design of isolation devices for highway bridges using the fragility function method," *Engineering Structures*, vol. 31, no. 8, pp. 1648–1660, 2009.

[40] M. S. Alam, M. A. Youssef, and M. Nehdi, "Analytical prediction of the seismic behaviour of superelastic shape memory alloy reinforced concrete elements," *Engineering Structures*, vol. 30, no. 12, pp. 3399–3411, 2008.

[41] F. D. Julian, T. Hayashikawa, and T. Obata, "Seismic performance of isolated curved steel viaducts equipped with deck unseating prevention cable restrainers," *Journal of Constructional Steel Research*, vol. 63, no. 2, pp. 237–253, 2007.

[42] A. H. Billah and M. S. Alam, "Seismic performance of concrete columns reinforced with hybrid shape memory alloy and fiber reinforced polymer bars," *Construction and Building Materials*, vol. 28, no. 1, pp. 730–742, 2012.

[43] N. Xiang and J. Li, "Utilizing yielding steel dampers to mitigate transverse seismic irregularity of a multi-span continuous bridge with unequal height piers," *Engineering Structures*, vol. 205, Article ID 110056, 2020.

[44] C. P. Providakis, "Effect of LRB isolators and supplemental viscous dampers on seismic isolated buildings under near-fault excitations," *Engineering Structures*, vol. 30, no. 5, pp. 1187–1198, 2008.

[45] S. A. Mitoulis, "Uplift of elastomeric bearings in isolated bridges subjected to longitudinal seismic excitations," *Structure and Infrastructure Engineering*, vol. 11, no. 12, pp. 1600–1615, 2015.

[46] D. Cardone, M. Dolce, and G. Palermo, "Direct displacement-based design of seismically isolated bridges," *Bulletin of Earthquake Engineering*, vol. 7, no. 2, pp. 391–410, 2009.

[47] Z. Li, Ri Gao, and W. Jia, "Design and experimental study on shock-absorbing steel bar with limit function for bridges," *Shock and Vibration*, vol. 2019, Article ID 3096291, 10 pages, 2019.

[48] L. Jiang, X. Kang, C. Li, and G. Shao, "Earthquake response of continuous girder bridge for high-speed railway: a shaking

table test study," *Engineering Structures*, vol. 180, pp. 249–263, 2019.

[49] K. Kalfas, S. A. Mitoulis, and D. Konstantinidis, "Influence of the steel reinforcement on the vulnerability of elastomeric bearings," *ASCE Journal of Structural Engineering*, vol. 146, no. 10, Article ID 04020195, 2020.

[50] Y. Li, J. J. Wang, and J. B. Liu, "Seismic performance of a multi-span rc highway bridge with high damping rubber bearings," *Key Engineering Materials*, vol. 540, pp. 69–78, 2013.

[51] K. N. Kalfas, S. A. Mitoulis, and K. Katakalos, "Numerical study on the response of steel-laminated elastomeric bearings subjected to variable axial loads and development of local tensile stresses," *Engineering Structures*, vol. 134, pp. 346–357, 2017.

[52] X. Wang, B. Zhu, and S. Cui, "Research on collapse process of cable-stayed bridges under strong seismic excitations," *Shock and Vibration*, vol. 2017, Article ID 7185281, 18 pages, 2017.

[53] A. R. Bhuiyan and M. Shahria Alam, "Seismic performance assessment of highway bridges equipped with superelastic shape memory alloy-based laminated rubber isolation bearing," *Engineering Structures*, vol. 49, pp. 396–407, 2013.

[54] C. Lu, M. Gui, and S. Lai, "A numerical study on soil–group-pile–bridge-pier interaction under the effect of earthquake loading," *Journal of Earthquake and Tsunami*, vol. 8, no. 1, Article ID 1350037, 2014.

[55] M. A. R. Bhuiyan and M. Shahria Alam, "Seismic vulnerability assessment of a multi-span continuous highway bridge fitted with shape memory alloy bars and laminated rubber bearings," *Earthquake Spectra*, vol. 28, no. 4, pp. 1379–1404, 2012.

[56] L. Wang, J. Su, Z. Gu et al., "Numerical study on flow field and pollutant dispersion in an ideal street canyon within a real tree model at different wind velocities," *Computers and Mathematics With Applications*, 2020.

[57] J. Li, N. Xiang, H. Tang, and Z. Guan, "Shake-table tests and numerical simulation of an innovative isolation system for highway bridges," *Soil Dynamics and Earthquake Engineering*, vol. 86, pp. 55–70, 2016.

[58] J. Yi, H. Yang, and J. Li, "Experimental and numerical study on isolated simply-supported bridges subjected to a fault rupture," *Soil Dynamics and Earthquake Engineering*, vol. 127, Article ID 105819, 2019.

[59] Y.-I. Kim and G.-J. Park, "Nonlinear dynamic response structural optimization using equivalent static loads," *Computer Methods in Applied Mechanics and Engineering*, vol. 199, no. 9–12, pp. 660–676, 2010.

Research Article

Effect of Earthquake Ground Motion Duration on the Seismic Response of a Low-Rise RC Building

Martin O. Martineau, Alvaro F. Lopez [ID], and Juan C. Vielma

Escuela de Ingeniería Civil, Pontificia Universidad Católica de Valparaíso, Valparaíso 2362804, Chile

Correspondence should be addressed to Alvaro F. Lopez; alvaro.lopez@pucv.cl

This paper investigates the effect of earthquake ground motion duration on the seismic response of a low-rise reinforced concrete shear wall building. Two sets of spectrally equivalent ground motion sets were determined to isolate the effect of duration from other earthquake record characteristics. A numerical model that accounts for P-delta effects and degradation of strength and stiffness of the structural elements was used. Detailed nonlinear dynamic analysis for both the design and collapse levels of shaking was performed, considering the spectral acceleration at the fundamental period of vibration with intensity measure and material strains as engineering demand parameters. The results showed that at the design level of shaking, slightly larger interstory drifts were obtained under the short-duration events. However, the maximum values for interstory drifts were small, and minor damage is expected in the structure. When both seismic record sets were incrementally scaled until collapse, a slight increase in the material strains was found under the short-duration seismic events. Overall, it is indicated that ground motion duration does not influence the seismic response of low-rise buildings with low deformation capacity.

1. Introduction

In recent years, there has been a resurgence interest in studying the effect of ground motion duration on the seismic performance and collapse assessment of structures. This topic's interest has been primarily due to the field observation after large-magnitude long-duration earthquakes such as the 2010 Maule, Chile (M_w8.8), and the 2011 Tohoku, Japan (M_w9.0), megathrust earthquakes, which caused significant structural damage to critical infrastructures like bridges and buildings [1–4]. Moreover, such events and others from subduction regions have made available new long-duration strong motion records allowing a better study of the effects of earthquake duration on structural performance. For instance, the lack of available long-duration ground motion records in the past required the generation of artificial records to address this topic adequately [5–7]. The previous events have shown that ground motion duration should be duly considered in structural design. However, the effect of ground motion duration is not yet explicitly considered as a parameter in current seismic design codes [8–10] and performance assessment throughout the world [11, 12].

A vast number of research studies on the effects of ground motion duration on structural performance have been reported in the literature in the past decades, often with inconclusive results due to the parameters used. On the one hand, investigations using cumulative response measures, such as the number of inelastic cycles or energy dissipation, showed a good correlation between duration and damage [13–16]. On the other hand, research studies using only peak response measures, such as peak deformation or peak interstory drift, did not show a significant influence of duration on structural response [15, 17, 18]. However, the inadequacy of structural models in capturing the effect of energy capacity degradation, cyclic and in-cycle strength degradation, and scarcity of long-duration ground motion records made it difficult to address duration effects in previous research adequately [19]. Likewise, the problem of isolating duration from other key explanatory variables of the ground motion, such as frequency content, spectral

amplitude, and spectral shape, added another challenge since the spectral content of the earthquake record can be modified [20]. In this regard, using spectrally equivalent ground motion pairs for isolating the effect of duration has made available a more robust way of analyzing ground motions for nonlinear dynamic analyses since the spectral content is almost not altered [21, 22].

More recent investigations employing numerical models that captured structural components' degradation have shown that long-duration ground motions can induce higher deformations and affect the structural collapse capacity [22–25]. Chandramohan et al. [22] presented results showing that long-duration records induce higher deformations for large shaking intensities. By analyzing 2D models of a modern 5-story steel special moment frame and a single reinforced concrete (RC) bridge pier, they concluded that the median collapse capacity of the structural systems could experience a reduction of 29% and 17%, respectively, when the structures are subjected to long-duration motions. Raghunandan and Liel [23] studied the influence of duration on the collapse capacity of eight non-ductile RC frames and nine modern ductile RC frames, using 2D nonlinear models. The authors concluded that earthquake duration plays a significant role in the collapse resistance of the structural systems. They reported reductions in the collapse resistance ranging from 26% to 56% due to duration effects, impacting the buildings' vulnerability. Barbosa et al. [24] quantified the influence of duration on the damage (i.e., not only at collapse stage) of 3-, 9-, and 20-story steel buildings designed according to pre-Northridge codes. Spectrally equivalent records from subduction and crustal earthquakes were used as input in the 2D nonlinear models. It was concluded that the increase in energy dissipation demands in the structures subjected to long-duration motions significantly increased the expected levels of structural damage at the higher intensities of shaking. Belejo et al. [26] studied the seismic behavior of a substandard plan-asymmetric RC framed building through 3D nonlinear modeling and found that ground motion duration influence is evident only for intensities leading to the collapse of the structure. This result agrees with the conclusions reported by Raghunandan and Liel [23] since structural systems with low ductile capacity are not influenced by earthquake duration due to the inability to reach large deformations and dissipate energy before failure. Bravo-Haro and Elghazouli [25] analyzed 50 steel moment frames through detailed nonlinear dynamic analysis using a suite of 77 spectrally equivalent pairs of short and long earthquake records. Similar to previous studies, they reported that the effects of duration are significant for structures showing high rate of cyclic degradation levels. Reductions of about 20% on the collapse capacity were observed due to duration, reaching up to a 40% reduction in buildings with a high cyclic degradation rate. Samanta and Pandey [27] studied the effect of duration on a 15-story RC building, and they found that earthquake duration can become a determining factor in the levels of maximum peak story drift ratio under low hazard levels. Bhanu et al. [19] found a reduction in ductile RC framed structures' dynamic deformation capacity under the increased cyclic demands imposed by long-duration ground motions. Vega and Montejo [28] found that long-duration records impose larger inelastic

demands and that the effect of duration is more detrimental in relatively rigid structures and poorly detailed flexible structures. Liapopoulou et al. [29] investigated the effect of duration on a series of ductile SDOF models and reported up to 60% reduction in the collapse capacity due to duration effects in the case of flexible bilinear systems under low levels of P-Δ effect.

On the other hand, the structural response to long-duration events is directly related to ductility, a property necessary to study under earthquake-induced deformations on buildings. Nonetheless, traditional analysis methods do not consider the effects of earthquake duration and the use of deteriorating structural models that directly affect the structure's demand [19, 30]. Therefore, the assessment of the effects of earthquake ground motion duration on these structures is not feasible. As a matter of fact, current seismic design practice for reinforced concrete structures in Chile is based on the conventional code-prescribed force method. However, after the recent occurrence of significant seismic events, such as the 2010 Maule earthquake, changes to the regulation were introduced afterwards to improve the structural response of walls by ensuring the ductility of these and including recommendations for estimating structural deformations. It is well known that Chile is located in one of the most seismically active regions of the world, where the geological conditions (from a tectonic point of view) near the Chilean coast mostly consist of interplate areas where subduction events occur frequently and are generally of large magnitude and also of long duration [31]. This last feature has not been considered in the seismic-resistant design despite the local conditions; therefore, it is necessary to promote research works that include duration effects on structural behavior.

In this paper, the effect of ground motion duration on the seismic performance of RC building structures is investigated. A sample four-story RC shear wall building is used as a case study. This building represents a typical low-rise residential building located in Central Chile designed according to current Chilean seismic provisions. A 3D nonlinear finite element model of the sample structure is developed in SeismoStruct [32], which allows incorporating the in-cycle and cyclic deterioration of stiffness and strength as well as the fiber modeling approach with material inelasticity for structural members. A set of 20 spectrally equivalent pairs of long and short earthquake records is used to evaluate the effects of ground motion duration on the structural response. Particular attention is given to effects of duration on material strains and interstory drift ratios. The results in this investigation indicate that ground motion duration does not play a key role in the damage state of the low-rise building.

2. Sample Building and Model Description

2.1. General Description.
The sample structure corresponds to an existing low-rise RC shear wall building of which structural configuration is typical of residential housing built in Chile. The prototype building is a 4-story structure with a story height of 2.44 m. The building's lateral load and gravity-resisting systems comprise interior and outer RC shear walls in both longitudinal and transverse directions and 12 cm RC slabs at each floor. The typical floor plan and elevations are illustrated in Figure 1. The compressive strength of concrete is

(a)
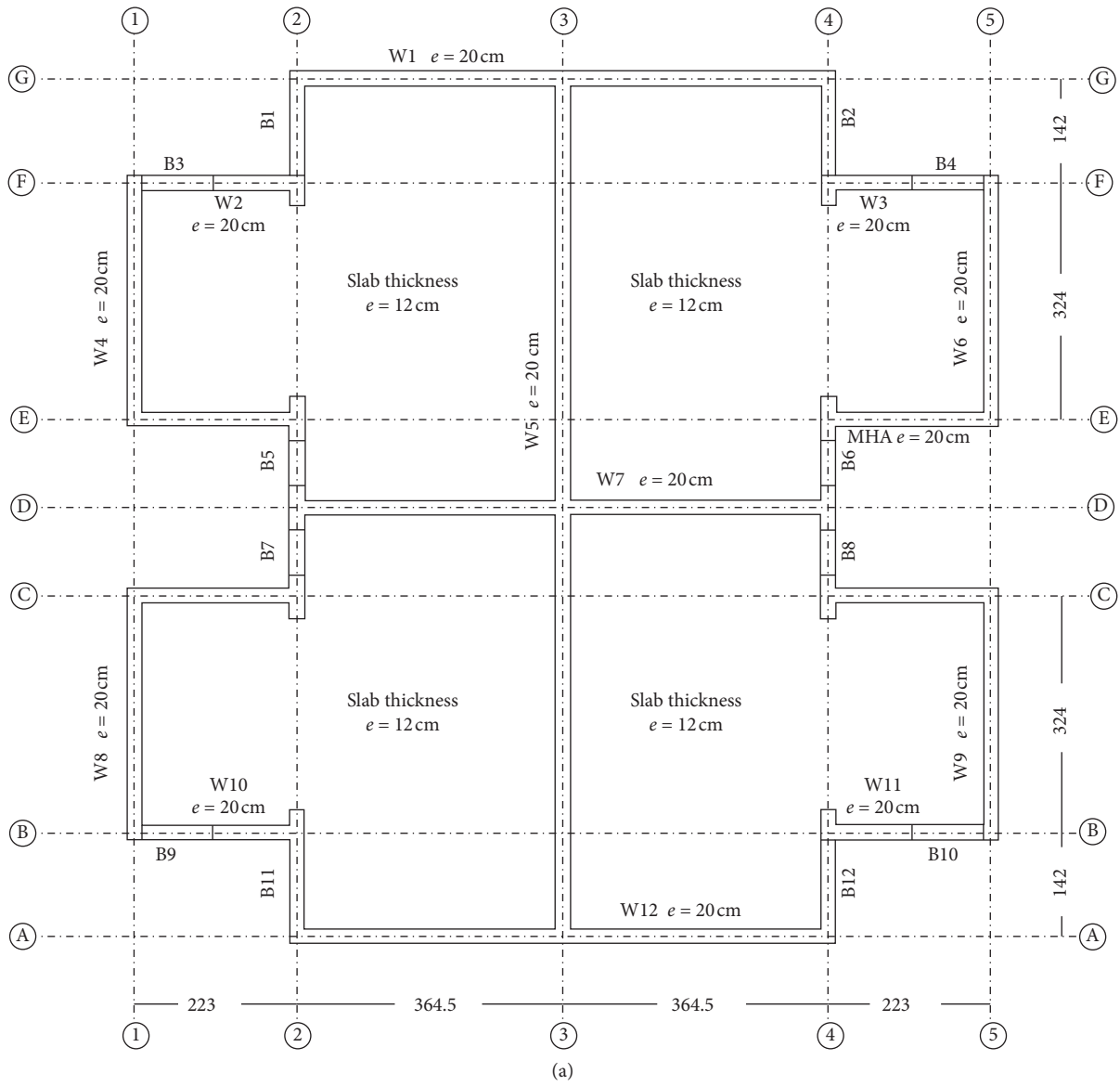
Figure 1: Continued.
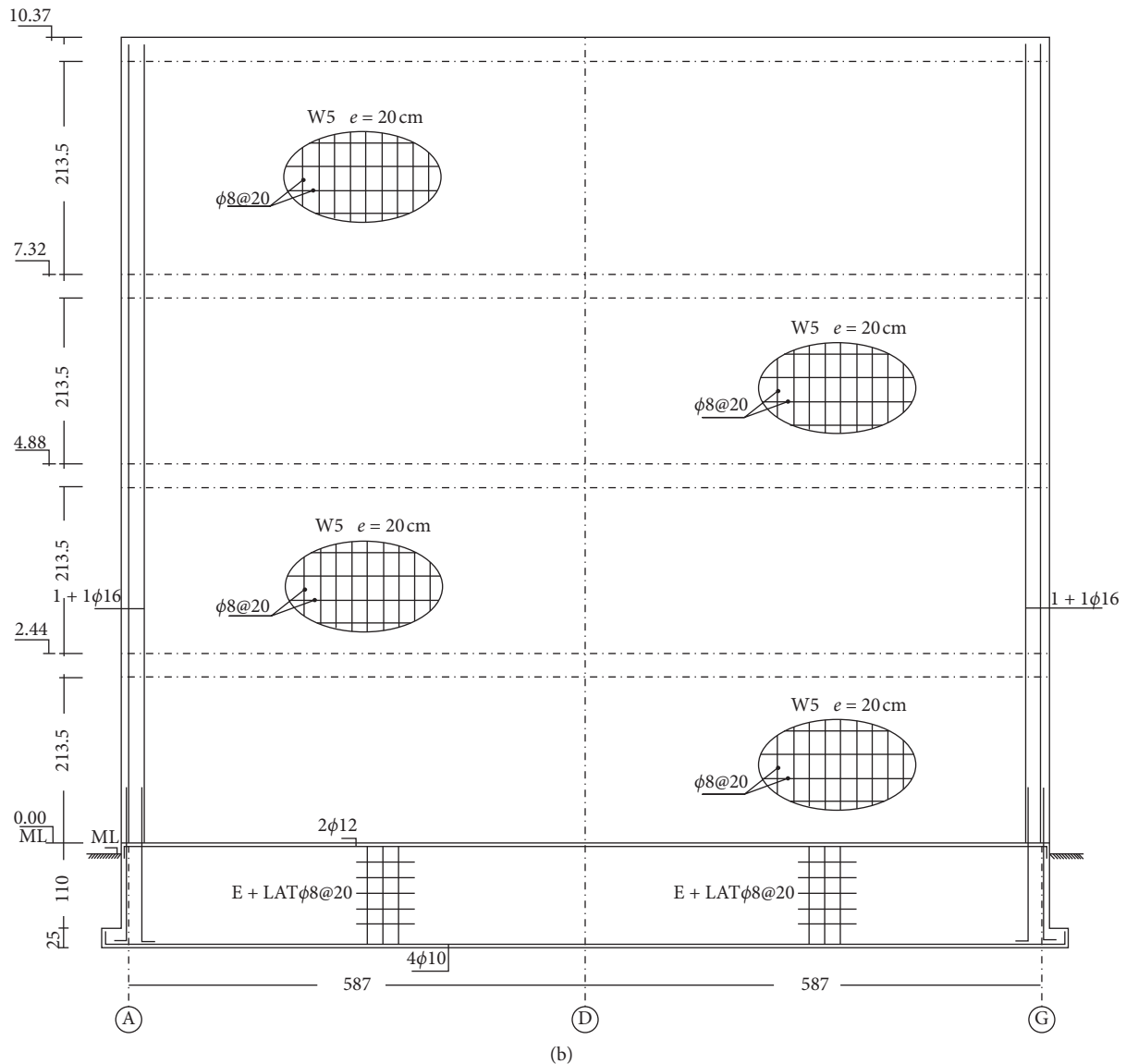
Figure 1: Sample residential housing: (a) typical floor plan of the building and (b) elevations of outer longitudinal and inner transverse shear walls.

assumed to be 20 MPa, and the tensile strength of reinforcement is 420 MPa. The floor area is about $120 \, \text{m}^2$ per story, and the dead and live loads were calculated approximately as $27.9 \, \text{kN/m}^2$ and $6.7 \, \text{kN/m}^2$, respectively. The building was analyzed as per current Chilean seismic provisions [9] and the ACI318-14 [33] requirements. The building is assumed to be located in seismic zone 3 on soil class D, according to the Chilean seismic code NCh433 [9] classification. The seismic force reduction factor (R) prescribed for this system is 4.

2.2. Modeling Approach. Linear and nonlinear numerical models were considered in this study. Given that the building already exists onsite, the structural element's design was not carried out since dimensions of the elements and the reinforcement layout for each of the elements were available.

Instead, a design check was performed, confirming that their behavior was flexural dominated. The structural drawings were therefore used for modeling the building. The 3D linear elastic model used for this study was first generated using the software package ETABS [34] to determine the structure's main dynamic properties using the response spectrum analysis as per current Chilean seismic regulations [9]. As a result, the cracked fundamental periods of vibrations obtained for the structure were 0.095 and 0.088 seconds in the x- and y-directions, respectively, for the second and third main vibration modes (the modes that accumulate 90% of the mass participation).

Despite the software's capabilities for the linear static analysis, it is not possible to conduct robust nonlinear dynamic analyses. This aspect is relevant for this study as its purpose is to evaluate the effects of ground duration on the seismic behavior of the structure. Therefore, numerical models that accurately characterize structural performance at

large nonlinear demands should be duly used. To this end, structural models that can capture the in-cycle and cyclic degradation of strength and stiffness of elements are needed [35], since it is the main factor affected by the duration of earthquake records. Therefore, the SeismoStruct software [32] was used to develop a continuous 3D nonlinear numerical model of the building. This software allows to perform, among several other options, nonlinear dynamic analysis by using accelerograms so that the corresponding loads are applied to the structure. A rigid diaphragm is assumed for each floor. Soil-structure interaction was not considered in this study. The 3D view, floor plan, and elevation of the numerical model of the structure are illustrated in Figure 2.

2.3. Material and Element Models. As previously mentioned, the nonlinear finite element model for the building was developed in SeismoStruct [32]. To this end, the reinforcement details specified in the structural drawings were included in the model. The shear walls were modeled using fiber elements with force-based (FB) formulation [36–38] and using a distributed inelasticity approach along the element length. Gauss–Lobatto numerical integration quadrature rule is used for the FB elements. The fiber-based element model used for the shear walls is presented in Figure 3. A linear elastic hinge at midheight of the walls at each story was provided to capture the elastic shear deformations. It is worth mentioning that the shear hinges' stiffness was equal to the cracked shear area of the walls multiplied by the shear modulus and divided by the story height. A factor of 0.1 was applied to the wall gross area to account for the loss of the area due to cracking [39].

The concrete material was defined using the uniaxial constant confinement model that follows the constitutive relationship proposed by Mander et al. [40] and the cyclic response theory proposed by Martinez-Rueda and Elnashai [41]. The confinement effects provided by the lateral transverse reinforcement were modeled with a confinement factor, defined as the ratio between the confined and unconfined compressive strengths of concrete. In SeismoStruct [32], the confinement factor is calculated using the confinement model proposed by Mander et al. [40]. Table 1 presents the five model-calibrating parameters defined to fully describe the mechanical features of the concrete. Regarding the reinforcing steel, it was modeled using a uniaxial steel model based on the stress-strain relationship proposed by Menegotto and Pinto [42], coupled with the isotropic hardening rules developed by Filippou et al. [43]. Nine model-calibrating parameters fully describe the mechanical characteristics of the reinforcing steel, which are presented in Table 2. These material models were generated using data calibrated in the laboratory and captured the effect of cycles on sections of reinforced concrete with transverse reinforcement and reinforcement steel elements. The reason these models were used is related to the fact that they are widely accepted by the research community in structural engineering and that they are also well adapted to the events recorded over the past several years in terms of structural performance. The hysteresis rules used for each material model are shown in Figure 4.

3. Ground Motion Sets

Two paired sets of spectrally equivalent long- and short-duration records were selected to investigate the effect of ground motion duration on the sample building model. Large-magnitude earthquakes occurred in subduction zones were chosen for the long-duration set and obtained from the 1985 Valparaiso and 2010 Maule, Chile [44], and the 2003 Hokkaido and 2011 Tohoku, Japan [45], earthquakes. Similarly, ground motions from shallow crustal events were chosen from the PEER NGA-West [46] database. Although there is still no consensus in the earthquake engineering community on a standard ground motion duration definition, in this study, the 5% to 95% significant duration ($D_{s_{5-95\%}}$) metric was used. This duration metric is defined as the time required to develop the Arias intensity [47] in the range between 5 and 95% of the total energy of the record [48], as presented in equation (1). Here, $a(t)$ corresponds to the ground motion acceleration record, T is the total duration of the recording, t_R is the desired time over which percentage of the total energy is reached (e.g., 90%), t is the time integration parameter, and R is the calculated fraction of the Arias intensity index:

$$I_A(R\%) = 100 \int_0^{t_R} (a(t))^2 \mathrm{d}t \int_0^T (a(t))^2 \mathrm{d}t. \tag{1}$$

The criterion used to categorize a ground motion as a long or short duration was based on the threshold proposed by Chandramohan et al. [22] upon which a significant duration, $D_{s_{5-95\%}}$, is higher than 25 s for long duration and lower than 25 s for a short duration. The selected long-duration ground motions are summarized in Table 3. For brevity, only the component with higher PGA is listed in the table.

To isolate the effect of duration from other ground motion characteristics such as intensity and spectral shape, the methodology proposed by Al Atik and Abrahamson [49] was used to match each ground motion set spectrally. This methodology allows us to obtain spectral equivalence between the long- and short-duration records without having to correct their baseline, which is advantageous since this method ensures the stability and convergence in the calculations. Table 4 summarizes the selected short-duration events and records. These short-duration records were obtained exclusively from worldwide shallow crustal earthquakes. Figures 5(a) and 5(b) depict the geometric mean and standard deviation spectra for the long- and short-duration records. Moreover, Figure 5(c) compares both geometric mean spectrums, indicating a good agreement between both ground motion sets.

4. Nonlinear Time-History Analysis

A dynamic time-history analysis was performed in this study. Accordingly, the two sets of ground motions were first scaled to match the NCh 433 design response spectrum for seismic zone 3 and soil class *D* [9] and then uniformly applied at the base of the building model. The resulting

(a)   (b)

(c)
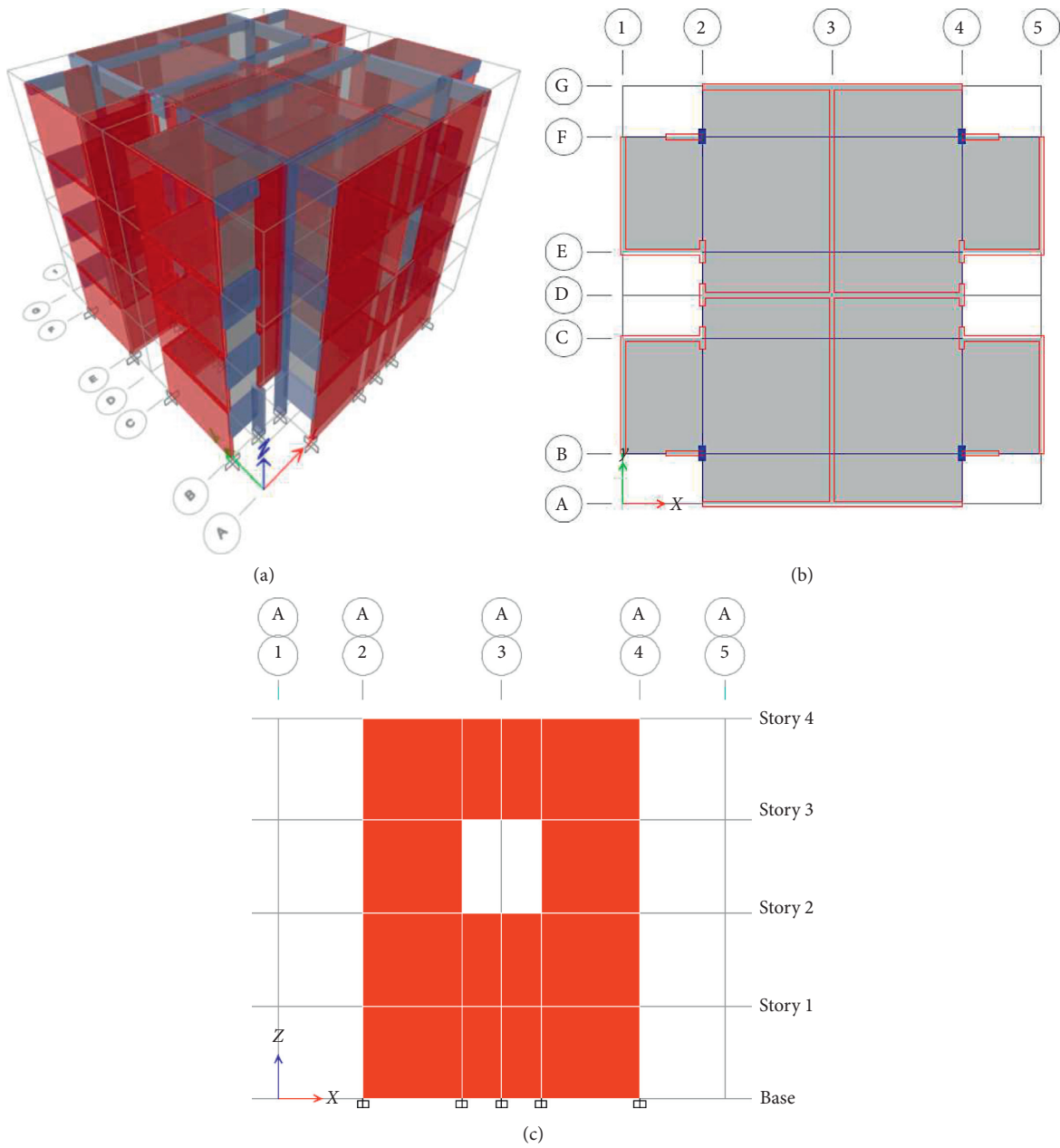
FIGURE 2: Low-rise RC building model for numerical analysis: (a) 3D view, (b) typical floor layout, and (c) elevation A1-5.

FIGURE 3: Discretized FB element model for RC shear walls.

maximum interstory drifts for the sample building are shown in Figure 6 and were obtained by gathering the available information on the nodes of the structure associated with the center of gravity of the four floors. The NCh433 [9] uses interstory drifts as a damage control parameter and limits the building to a maximum interstory drift of 0.002 of the story height for linear elastic analysis. For the immediate occupancy (IO) evaluation used in the performance-based procedure indicated in the ASCE/SEI 41-17 [11], the maximum interstory drift is limited to 0.004. As

seen in Figure 6, none of the sets surpasses these limits, which might be attributed to the great lateral stiffness of the sample building due to the significant presence of shear walls. When comparing the values obtained for both ground motion sets, there is a slight increase in the interstory drifts for the short-duration ground motion set compared to those for long-duration earthquakes. However, it should be mentioned that the values obtained in both cases are not significantly far from each other, with an increase of 20.05% for short-duration events. It is, therefore, not possible to

TABLE 1: Data required to generate the concrete stress-strain curve.

	Value	Description
f_c	25 MPa	Mean compressive strength
E_c	23,500 MPa	Modulus of elasticity
f_t	2.5 MPa	Maximum tension strength
ε_c	−0.0022	Strain at peak strength in compression
ε_t	−0.0020	Strain at peak strength in tension

TABLE 2: Data required to generate the stress-strain curve of reinforcing steel.

	Value	Description
E_s	25 MPa	Modulus of elasticity
f_y	2×10^5 MPa	Yield strength
μ	0.005	Strain hardening parameter
R_0	20	Transition curve initial shape parameter
A_1	18.50	Transition curve shape calibrating coefficient
A_2	0.15	Transition curve shape calibrating coefficient
A_3	0.00	Isotropic hardening calibrating coefficient
A_4	1.00	Isotropic hardening calibrating coefficient
b	0.1	Fracture/buckling strain

conclude that the short-duration events generate a significant increase in drifts compared to the long-duration events; thus, an incremental dynamic analysis (IDA) was then performed to have a deeper understanding of this phenomenon.

As stated previously, to better estimate the influence of ground motion duration, a series of IDAs were performed to the sample structure, obtaining results for each structural element. IDA is a parametric dynamic analysis technique used in earthquake engineering to conduct a comprehensive assessment of the seismic performance of structures under seismic loads [50]. The procedure involves multiple nonlinear dynamic analysis of a structural model under scaled ground motions until collapse, thus producing curves of engineering demand parameter (EDP) as a damage measure (DM) versus an intensity measure (IM). The ground motions are characterized by the IMs, which should be related to the structural response of interest to reduce the number of time-history analyses [51]. Among the existing IMs, the peak ground acceleration (PGA), peak ground velocity (PGV), spectral acceleration, and Arias intensity are the most widely used. The DM can be any structural parameter related to performance limit states of the structure corresponding to several damage levels. Typical options are the global and local maximum interstory drift, global and local maximum ductility, and material strain limit, among others. In this study, the spectral acceleration at the fundamental period of vibration of the structure with 5% damping S_a (T_0, 5%) while different EDPs was analyzed. Finally, the selected EDPs were the concrete and steel rebar strains for the IDA. It is worth to mention that the collapse stage was defined as the instant at which the main structural walls of the structure failed.

Given that the results for the maximum interstory drift obtained from the nonlinear time-history analysis at the design level of shaking as per Chilean seismic regulations [9] were rather low and not conclusive, the results of the IDA are presented in Figures 7 and 8 for the outer wall of the structure, identified as "A 1–4" according to the floor plan shown in Figure 2. Figure 7 shows slightly higher steel rebar peak strains for the short-duration ground motions compared to the long-duration set. In particular, there is an increase of 8% in the peak strain of the steel rebar for short-duration events. However, when observing the yield point for the reinforcement steel, 8 cases exceed this point for long-duration events, while 7 cases exceed this point for short-duration events.

Similarly, when considering concrete strains as EDP, the results showed a slight tendency to obtain higher deformations under the short-duration ground motion set. For example, Figure 8 shows 2 cases in which the cracking of concrete occurs at a deformation value exceeding the determined value of 2 per thousand. Meanwhile, for the long-duration events, there is only one case for which this limit is exceeded, as can be seen in Figure 8. The obtained peaks of concrete strain show an increase of 17% for the short-duration suite compared to the long-duration suite for a PGA of 3.8 (g).

Overall, it is generally possible to observe a slight increase in the demand on the structure under the short-duration ground motion set. In this regard, for this case study and to a slightly greater extent, the demand on the structure in terms of the chosen EDPs was higher under the short-duration earthquakes records than the long-duration earthquakes records although minimal damage is expected under both sets of records. This phenomenon should be highlighted since the previous results [22–24, 30] have shown that there are higher levels of deformations, therefore more damage induced by long-duration seismic records. However, the unlike results obtained in this research are mainly attributed to the low level of deformation exhibited by the sample structure, which can be supported by the obtained interstory drift values. It should be noted that the structure under consideration was a rather rigid building, with a large

(a)

(b)
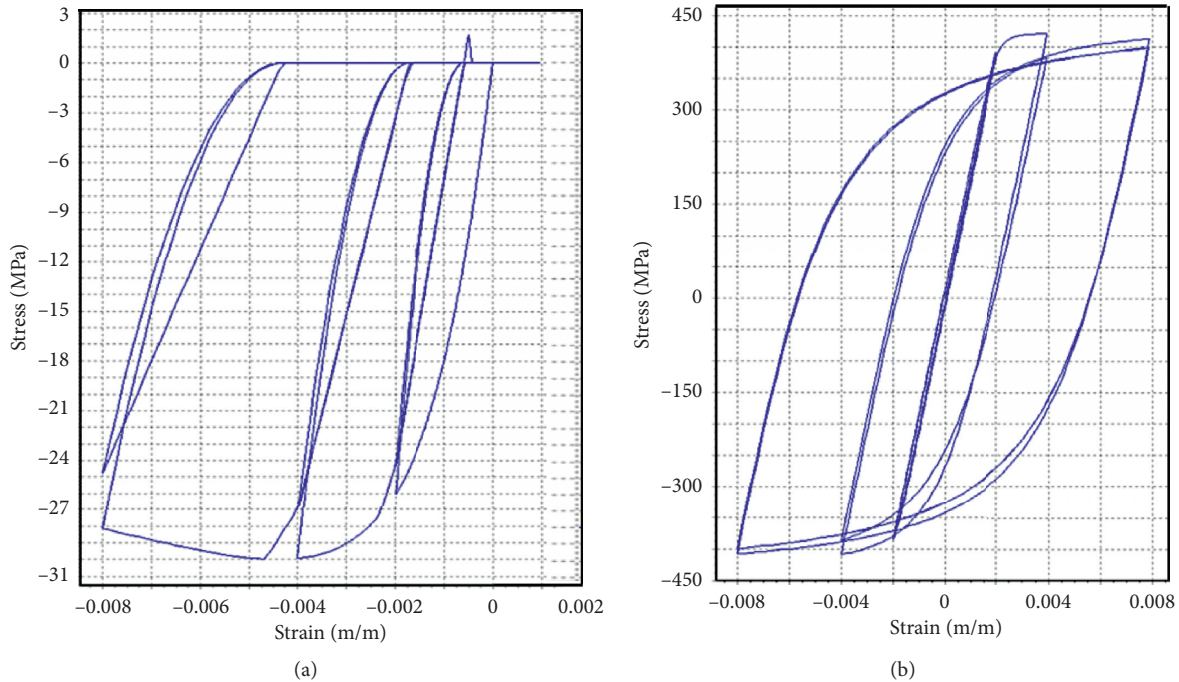
FIGURE 4: Constitutive models used in the nonlinear numerical model: (a) concrete and (b) reinforcing steel.

TABLE 3: Long-duration set summary.

Earthquake	Magnitude	Year	Station	PGA (g)	Significant duration (s)
Valparaiso, Chile	7.8	1985	Cauquenes	0.11	51.10
			Endesa	0.13	44.95
			La Ligua	0.18	28.35
Hokkaido, Japan	8.3	2003	Shibetsu	0.50	32.00
			Honbetsukai	0.48	26.96
Maule, Chile	8.8	2010	Viña Centro	0.33	25.65
			Valparaíso	0.30	27.15
			Matanzas	0.34	42.15
Tohoku, Japan	9.0	2011	Tohwa	0.81	58.20
			Okhuma	0.70	28.10

TABLE 4: Short-duration set summary.

Earthquake	Magnitude	Year	Station	PGA (g)	Significant duration (s)
Cape Mendocino, USA	7.0	1985	Rio Dell Pass	0.55	15.34
Friuli, Italy	6.5	1976	Tolmezzo	0.35	16.96
Hector Mine	7.1	1999	Hector	0.34	11.65
Imperial Valley,	6.5	1979	El Centro Array#1	0.38	17.05
Loma Prieta	6.9	1989	Gilroy Array#3	0.56	6.37
Northridge	6.7	1994	Canyon Country	0.48	5.56
Northridge	6.7	1994	Beverly Hills	0.52	9.21
San Fernando	6.6	1971	LA-Hollywood	0.21	10.49
Superstition Hill	6.5	1987	El Centro Imp. Co.	0.36	16.05
Superstition Hill	6.5	1987	Poe Road (temp)	0.45	13.81

presence of walls and a low height, which restricted the deformation capacity and energy dissipation capacity before failure considering how the building was structured. The obtained results confirmed that for structural systems with low ductility capacity, the demand would not be influenced by ground motion duration [23].

5. Conclusions

This paper examined the influence of earthquake ground motion duration on the seismic performance of a low-rise RC shear wall building typical of Chilean residential construction. A 3D nonlinear finite element model was

(a)

(b)

(c)
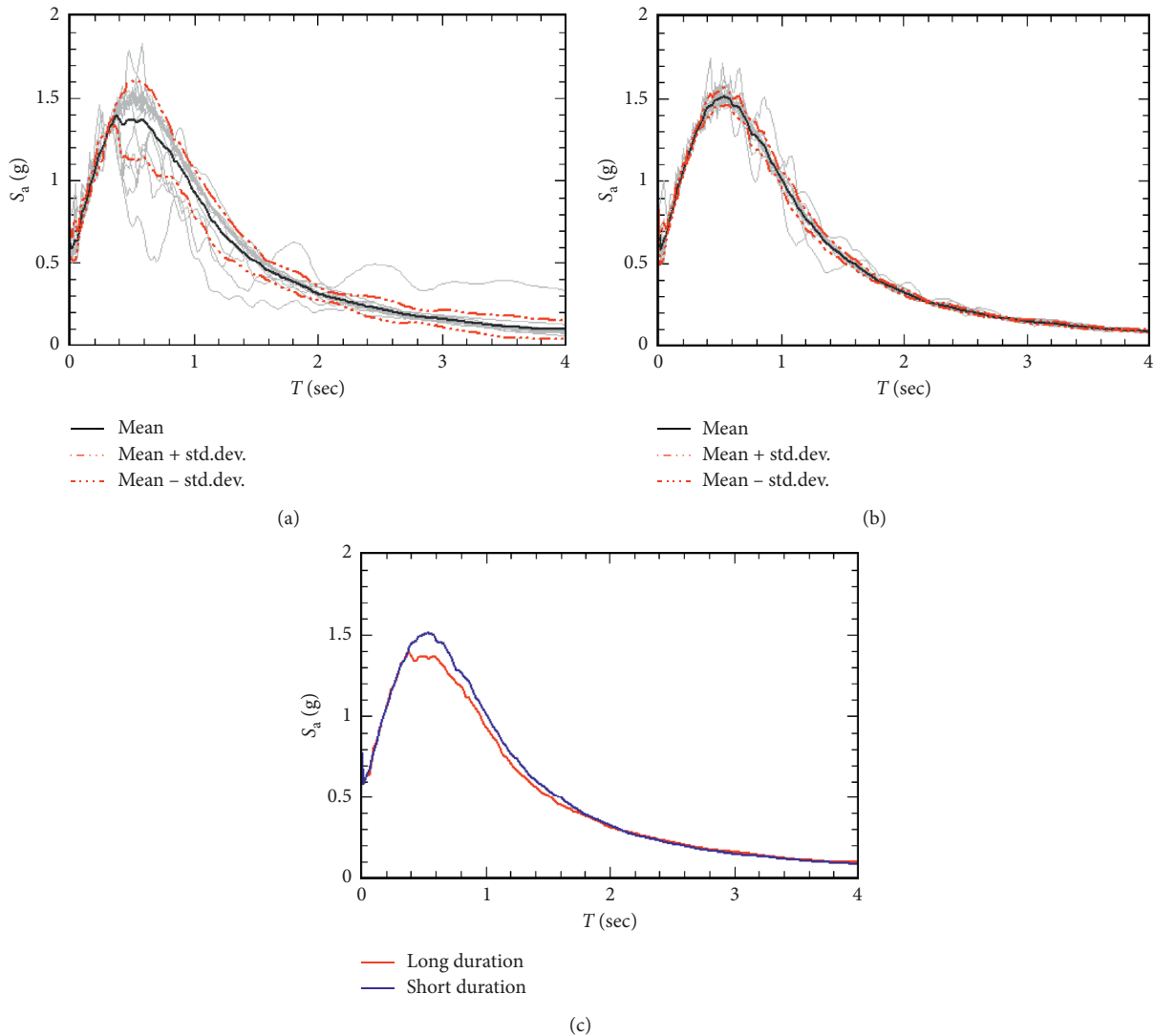
FIGURE 5: Geometric mean ± one standard deviation for spectra of (a) the long-duration set and (b) the spectrally equivalent short-duration set. (c) Comparison between geometric means for both ground motion sets.

(a)

(b)

FIGURE 6: Interstory drift results for the 4-story model as per the Chilean code shaking level for (a) the long-duration set and (b) the short-duration set.

(a)

(b)
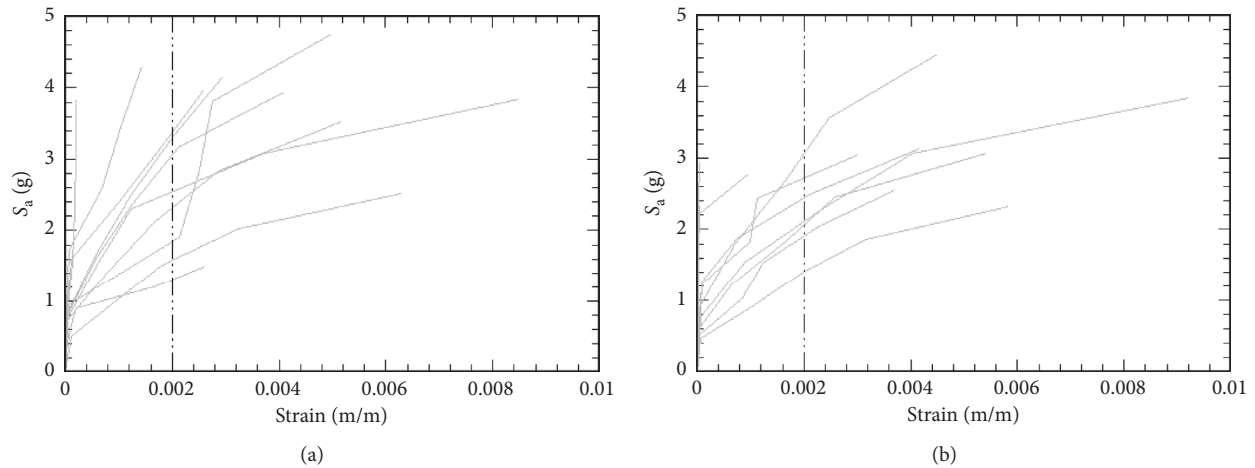
FIGURE 7: IDA curves considering steel rebar strains as EDP for (a) the long-duration set and (b) the short-duration set.

(a)

(b)
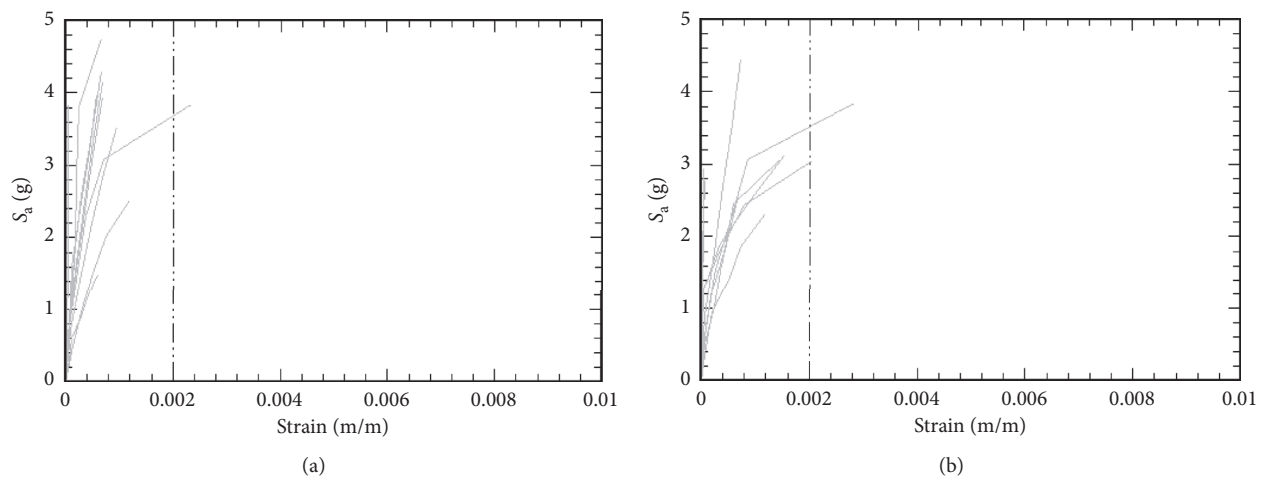
FIGURE 8: IDA curves considering concrete strains as EDP for (a) the long-duration set and (b) the short-duration set.

developed in SeismoStruct, which explicitly accounted for *P*-delta effects and inherent nonlinearities of the materials. On the other hand, two ground motion sets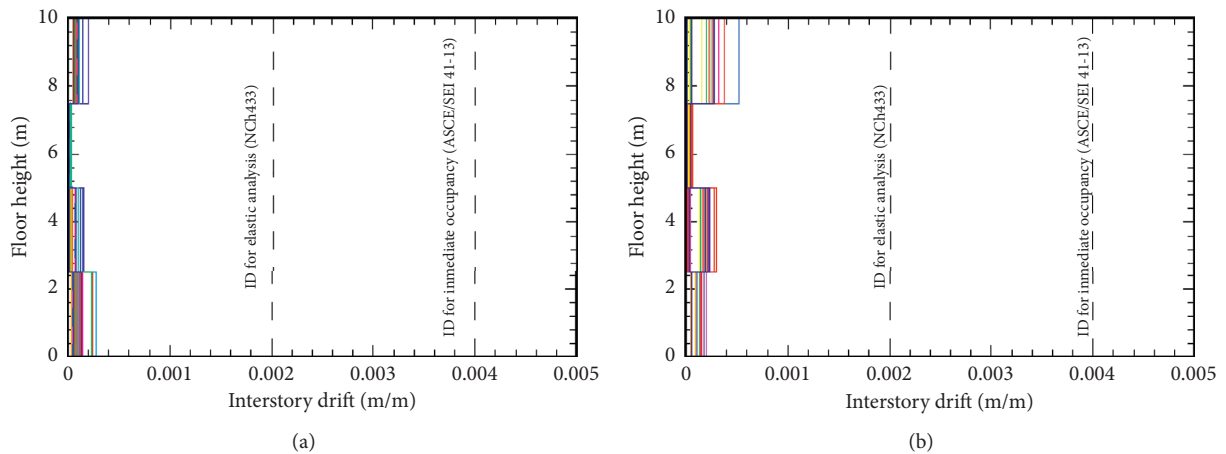 with equivalent spectral shapes but different durations were obtained to isolate the effects of ground motion duration from other ground motion characteristics. The sample building model was then subjected to time-history analysis at the design level of shaking and to extensive IDA using the long- and short-duration record sets. Overall, the influence of duration was shown to be not significant in the sample structure presented herein.

Based on the results obtained in this study, it is expected that ground motion duration does not influence significantly the peak values of EDPs in low-rise RC shear wall buildings when considering long-duration ground motion records. When comparing the maximum interstory drifts at the design level of shaking to the limits imposed by the NCh433 for linear elastic analysis and the ASCE/SEI 41-17 for performance-based evaluation, the values were found to be small and slight, which resulted in minimum damage to the sample building. Moreover, the structure's behavior regarding the drifts is generally quite similar in both situations

and slightly higher for the short-duration set than for the long-duration set. It should be mentioned that the structure was designed as per the current seismic Chilean seismic code, which resulted in a rather rigid structure. The behavior of the structure in terms of deformations was consequently restricted to its linear range, which led to low levels of deformation capacity.

To better understand the effect of the duration of earthquakes on the structure thoroughly, the sample building was subjected to incrementally scaled ground motion records to higher levels of shaking using IDA. Concrete and steel rebar strains were used as EDPs. The results showed a slight difference between the curves obtained for short-duration records and those obtained for long-duration records. Regarding the material peak strains, higher peaks by approximately 8% for reinforced steel and by approximately 17% for concrete were obtained for short-duration events. Furthermore, it should be noted that an increase in material strains for the short-duration events was generally obtained although this increase was not significant. The results obtained in this study confirmed that for structural systems with low ductility capacity, the influence

of duration is not significant due to the incapacity to reach large deformation and dissipate energy before failure.

Further research is recommended to study structures that can reach higher levels of deformation to obtain a relevant structural demand regarding seismic loading and results related to the performance of the materials considering their nonlinear behavior. Thereby, it would be possible to have a deeper and a more conclusive understanding of the effect of the duration of a seismic event since the increased number of cycles imposed by long-duration ground motions are one of the main concerns when conducting such studies.

Data Availability

Conflicts of Interest

Acknowledgments

References

[1] C. Alarcon, M. A. Hube, R. Jünemann, and J. C. de la Llera, "Characteristics and displacement capacity of reinforced concrete walls in damaged buildings during 2010 Chile earthquake," *Bulletin of Earthquake Engineering*, vol. 13, no. 4, pp. 1119–1139, 2015.

[2] K. Kawashima and I. Buckle, "Structural performance of bridges in the Tohoku-oki earthquake," *Earthquake Spectra*, vol. 29, no. 1, 2013.

[3] I. Buckle, M. Hube, G. Chen, W. H. Yen, and J. Arias, "Structural performance of bridges in the offshore maule earthquake of 27 February 2010," *Earthquake Spectra*, vol. 28, no. 1, pp. 533–552, 2012.

[4] F. Rojas, F. Naeim, M. Lew et al., "Performance of tall buildings in concepción during the 27 February 2010 moment magnitude 8.8 offshore Maule, Chile earthquake," *The Structural Design of Tall and Special Buildings*, vol. 20, no. 1, pp. 37–64, 2011.

[5] R. Saragoni and G. Hart, "Simulation of artificial earthquakes," *Earthquake Engineering & Structural Dynamics*, vol. 2, no. 3, pp. 249–267, 1973.

[6] R. Tremblay, "Development of design spectra for long-duration ground motions from Cascadia subduction earthquakes," *Canadian Journal of Civil Engineering*, vol. 25, no. 6, pp. 1078–1090, 1998.

[7] M. Sarieddine and L. Lin, "Investigation correlations between strong-motion duration and structural damage," in *Proceedings of the 2013 Structures Congress*, pp. 2926–2936, Pittsburgh, PA, USA, May 2013.

[8] ASCE, *Minimum Design Loads for Buildings and Other Structures*, ASCE/SEI 7-16 Press, Reston, VA, USA, 2016.

[9] Instituto Nacional de Normalizacion, *Diseno Sismico de Edificios*, Instituto Nacional de Normalizacion, Santiago, Chile, in Spanish, 2012.

[10] CEN, Eurocode 8: Design of Structures for Earthquake Resistance—Part 1: General Rules, Seismic Actions and Rules for Buildings, No. English, The European Union Per Regulation 305/2011, Directive 98/34/EC, Directive 2004/18/EC, 2004.

[11] ASCE, *Seismic Evaluation and Retrofit of Existing Structures ASCE/SEI 41-17*, ASCE/SEI 7-16 Press, Reston, VA, USA, 2014.

[12] FEMA P695, *Quantification of Building Seismic Performance Factors*, FEMA, Washington, DC, USA, 2009.

[13] C. Oyarzo-Vera and C. Nawawi, "Effect of earthquake duration and sequences of ground motions on structural responses," in *Proceedings of the 10th International Symposium on Structural Engineering for Young Experts ISSEYE*, pp. 1881–1886, Changsha, China, January 2008.

[14] J. Hancock and J. J. Bommer, "A state-of-knowledge review of the influence of strong-motion duration on structural damage," *Earthquake Spectra*, vol. 22, no. 3, pp. 827–845, 2006.

[15] I. Iervolino, G. Manfredi, and E. Cosenza, "Ground motion duration effects on nonlinear seismic response," *Earthquake Engineering & Structural Dynamics*, vol. 35, no. 1, pp. 21–38, 2006.

[16] A. Dutta and J. B. Mander, "Energy based methodology for ductile design of concrete columns," *Journal of Structural Engineering*, vol. 127, no. 12, pp. 1374–1381, 2001.

[17] E. Bojorquez, I. Iervolino, G. Manfredi, and E. Cosenza, "Influence of ground motion duration on degrading SDOF systems," in *Proceedings of the 16 th European Conference on Earthquake Engineering and Seismology*, pp. 3–8, Geneva, Switzerland, September 2006.

[18] C. A. Cornell, "Does duration really matter?" in *Proceedings of the FHWA/NCEER Workshop on the National Representation of Seismic Ground Motion for New and Existing Highway Facilities*, pp. 125–133, Burlingame, CA, USA, May 1997.

[19] V. Bhanu, R. Chandramohan, and T. J. Sullivan, "Investigating the influence of ground motion duration on the dynamic deformation capacity of reinforced concrete framed structures," in *Proceedings of the 11th Pacific Conference on Earthquake Engineering*, Auckland New Zealand., April 2019.

[20] J. Hancock and J. J. Bommer, "Using spectral matched records to explore the influence of strong-motion duration on inelastic structural response," *Soil Dynamics and Earthquake Engineering*, vol. 27, no. 4, pp. 291–299, 2007.

[21] M. Mashayekhi, M. Harati, M. Ashoori Barmchi, and H. E. Estekanchi, "Introducing a response-based duration metric and its correlation with structural damages," *Bulletin of Earthquake Engineering*, vol. 17, no. 11, pp. 5987–6008, 2019.

[22] R. Chandramohan, J. W. Baker, and G. G. Deierlein, "Quantifying the influence of ground motion duration on structural collapse capacity using spectrally equivalent records," *Earthquake Spectra*, vol. 32, no. 2, pp. 927–950, 2016.

[23] M. Raghunandan and A. B. Liel, "Effect of ground motion duration on earthquake-induced structural collapse," *Structural Safety*, vol. 41, pp. 119–133, 2013.

[24] A. R. Barbosa, F. L. A. Ribeiro, and L. A. C. Neves, "Influence of earthquake ground-motion duration on damage estimation: application to steel moment resisting frames,"

Earthquake Engineering & Structural Dynamics, vol. 46, no. 1, pp. 27–49, 2017.

[25] M. A. Bravo-Haro and A. Y. Elghazouli, "Influence of earthquake duration on the response of steel moment frames," *Soil Dynamics and Earthquake Engineering*, vol. 115, pp. 634–651, 2018.

[26] A. Belejo, A. R. Barbosa, and R. Bento, "Influence of ground motion duration on damage index-based fragility assessment of a plan-asymmetric non-ductile reinforced concrete building," *Engineering Structures*, vol. 151, pp. 682–703, 2017.

[27] A. Samanta and P. Pandey, "Effects of ground motion modification methods and ground motion duration on seismic performance of a 15-storied building," *Journal of Building Engineering*, vol. 15, pp. 14–25, 2018.

[28] E. Vega and L. A. Montejo, "Influence of ground motion duration on ductility demands of reinforced concrete structures," *International Journal of Advanced Structural Engineering*, vol. 11, no. 4, pp. 503–517, 2019.

[29] M. Liapopoulou, M. A. Bravo-Haro, and A. Y. Elghazouli, "The role of ground motion duration and pulse effects in the collapse of ductile systems," *Earthquake Engineering & Structural Dynamics*, vol. 49, no. 11, pp. 1051–1071, 2020.

[30] A. Mantawy and J. C. Anderson, "Effect of long-duration earthquakes on the low-cycle fatigue damage in RC frame buildings," *Soil Dynamics and Earthquake Engineering*, vol. 109, pp. 46–57, 2018.

[31] R. Dobry, I. M. Idriss, and E. Ng, "Duration characteristics of horizontal components of strong-motion earthquake records," *Bulletin of the Seismological Society of America*, vol. 68, no. 5, pp. 1487–1520, 1978.

[32] SeismoSoft, 2019, SeismoStruct 2019—A Computer Program for Static and Dynamic Nonlinear Analysis of Framed Structures, https://www.seismosoft.com/.

[33] ACI Committee 318, *Building Code Requirements for Structural Concrete*, ACI Committee 318, Farmington Hills, MI, USA, 2014.

[34] CSI, *CSI ETABS Analysis Reference Manual*, Comput. Struct. Inc., Berkeley, CA, USA, 2013.

[35] L. F. Ibarra, R. A. Medina, and H. Krawinkler, "Hysteretic models that incorporate strength and stiffness deterioration," *Earthquake Engineering & Structural Dynamics*, vol. 34, no. 12, pp. 1489–1511, 2005.

[36] E. Spacone, F. C. Filippou, and F. F. Taucer, "Fibre beam-column model for non-linear analysis of R/C frames: part I. Formulation," *Earthquake Engineering & Structural Dynamics*, vol. 25, no. 7, pp. 727–742, 1996.

[37] E. Spacone, F. C. Filippou, and F. F. Taucer, "Fibre beam-column model for non-linear analysis of R/C frames: part II. Applications," *Earthquake Engineering & Structural Dynamics*, vol. 25, no. 7, 1996.

[38] A. Neuenhofer and F. C. Filippou, "Evaluation of nonlinear frame finite-element models," *Journal of Structural Engineering*, vol. 123, no. 7, pp. 958–966, 1997.

[39] J. S. Pugh, L. N. Lowes, and D. E. Lehman, "Seismic design of slender concrete walls," in *Proceedings of the 10th U.S. National Conference on Earthquake Engineering Frontiers of Earthquake Engineering*, Anchorage, AK, USA, July 2014.

[40] J. B. Mander, M. J. N. Priestley, and R. Park, "Theoretical stress-strain model for confined concrete," *Journal of Structural Engineering*, vol. 114, no. 8, pp. 1804–1826, 1988.

[41] J. Martínez-Rueda and A. S. Elnashai, "Confined concrete model under cyclic load," *Materials and Structures*, vol. 30, no. 3, pp. 139–147, 1997.

[42] M. Menegotto and P. E. Pinto, "Method of analysis for cyclically loaded R. C. plane frames including changes in geometry and non-elastic behavior of elements under combined normal force and bending," *Proceedings of IABSE Symposium on Resistance and Ultimate Deformability of Structures Acted on by Well Defined Repeated Loads*, pp. 15–22, 1973.

[43] F. C. Filippou, E. P. Popov, and V. V. Bertero, "Effects of bond deterioration on hysteretic behaviour of reinforced concrete joints," Report, National Science Foundation, Berkeley, CA, USA, 1983.

[44] University of Chile, *Earthquakes of Chile*, University of Chile, Santiago, Chile, 2010.

[45] K-NET, Kyoshin Network Database, National Research Institute for Earth Science and Disaster Resilience, 2019.

[46] Pacific Earthquake Engineering Research Center, PEER Ground Motion Database, Shallow Crustal Earthquakes in Active Tectonic Regimes, NGA-West2, 2017.

[47] A. Arias, *A Measure of Earthquake Intensity, Seismic Design for Nuclear Power Plants*, MIT Press, Cambridge, MA, USA, 1970.

[48] M. D. Trifunac and A. G. Brady, "A study on the duration of strong earthquake ground motion," *Bulletin of the Seismological Society of America*, vol. 65, no. 3, pp. 581–626, 1975.

[49] L. Al Atik and N. Abrahamson, "An improved method for nonstationary spectral matching," *Earthquake Spectra*, vol. 26, no. 3, pp. 601–617, 2010.

[50] D. Vamvatsikos and C. Allin Cornell, "Incremental dynamic analysis," *Earthquake Engineering & Structural Dynamics*, vol. 31, no. 3, pp. 491–514, 2002.

[51] J. Kiani and S. Pezeshk, "Sensitivity analysis of the seismic demands of RC moment resisting frames to different aspects of ground motions," *Earthquake Engineering & Structural Dynamics*, vol. 46, no. 15, pp. 2739–2755, 2017.

Research Article

Typhoon Vulnerability Analysis in South Korea Utilizing Damage Record of Typhoon Maemi

Ji-Myong Kim,[1] **Kiyoung Son,**[2] **Sang-Guk Yum** ⓘ**,**[3] **and Sungjin Ahn** ⓘ[1]

[1]*Department of Architectural Engineering, Mokpo National University, 1666 Yeongsan-Ro, Cheonggye-myeon, Muan-gun, Jeonnam 58554, Republic of Korea*
[2]*School of Architectural Engineering, University of Ulsan, 93 Daehak-Ro, Ulsan 44610, Republic of Korea*
[3]*Department of Civil Engineering and Engineering Mechanics, Columbia University, 500 W. 120th Street #610, New York, NY 10027, USA*

Correspondence should be addressed to Sungjin Ahn; sunahn@mokpo.ac.kr

The purpose of this research is to identify the indicators of typhoon damage and develop a metric for typhoon vulnerability functions employing the losses associated with Typhoon Maemi. Typhoons cause significant financial damages worldwide every year. Federal and local governments, insurance companies, and construction companies strive to develop typhoon risk assessment models and use them to quantify the risks so that they can avoid, mitigate, or transfer the financial risks. Therefore, typhoon risk assessment modeling is becoming increasingly important, and in order to achieve a sophisticated evaluation, it is also important to reflect more specified and local vulnerabilities. Although several previous studies on economic loss associated with natural catastrophe have identified essential risk indicators, there has been a shortage of more specific research studies focusing on the correlation between vulnerability and economic loss caused by typhoons. In order to fill this gap, this study collected and analyzed the actual loss record of Typhoon Maemi collected and accumulated by a major insurance company in Korea. In order to create the vulnerability functions and to identify the natural hazard indicators and basic building information indicators, information from the insurance record was used in the analysis. The results and metric of this research provide a pragmatic approach that helps create vulnerability functions for abovementioned sectors and like estimating local vulnerabilities and predicting and coping with the possible damage and loss from typhoons.

1. Introduction

1.1. Background. As the incidence of severe windstorms continues to increase drastically, the resulting losses are also remarkably increasing [1]. For example, in 2005, Hurricane Katrina caused about $ 108 billion in economic losses, and this loss has been recorded as the most destructive natural disaster in the United States in economic impact wise. Hurricane Sandy and Hurricane Ike have been classified as the hurricanes of the second and third largest financial losses, respectively. That is, Hurricane Sandy in 2012 led to losses of $71.4 billion, while Hurricane Ike in 2008 led to losses of $29.5 billion [2, 3]. In December 1999, three sequence of European windstorms, i.e., Anatol, Lothar, and Martin, hit Western Europe and Central Europe with heavy rains and strong winds. The total economic damages were approximately 13 billion euros [4]. Typhoon Yolanda, a.k.a., Super Typhoon Haiyan passed over several countries in its path in 2013 and recorded as the most extreme typhoon on land. This typhoon severely devastated a wide area covering several southern Asian countries with extreme storm surges, landfall, and winds and led to total losses estimated at $ 2.88 billion.

To cope with such damages and losses, many industrialized countries have adopted and used insurance as a means to transfer the financial risks caused by typhoons. At this, it is crucial for the insurance industry to be able to accurately estimate and assess the risks. In order to achieve such accurate and reliable assessment, insurance companies use natural catastrophe models and historical loss records to

predict and manage potential economic losses in individual buildings, regions, or countries. Among these, the natural catastrophe model consists of hazard, exposure, finance, and vulnerability modules [5]. The hazard module identifies the frequency and intensity of typhoons and other typhoon information, e.g., storm surge, precipitation, and central pressure, and regenerates typhoons in specific areas and periods according to the prescribed information. The finance module estimates the economic losses based on the policy term, e.g., risk excess of loss, cat excess of loss, and limit of liability. The vulnerability module is a module that uses the vulnerability function to quantify the degree of damage by vulnerability according to the building attributes using the correlation between damage and risk indicators [6]. The vulnerability function can be found by analyzing past storm losses, and it can also be validated by the losses recorded. As can be seen, the precision of the vulnerability function, among many other factors, is substantially affected by the presence and its quality of past damage data.

However, in practice, it is difficult to develop a vulnerability function, since there is a lack of detailed loss records. Meanwhile, claim payout records of insurance companies can provide specific, accurate, and reliable loss data. That is, these claim payout records can be used to assess the vulnerability of individual buildings by taking advantage of the features of building inventory because such data includes the information of engineers' and claim adjusters' objectively inspections and their results and the information of claim payout paid accordingly.

Nonetheless, many insurance companies are tended to be hesitant to record or document the data on detailed building exposures, such as building type, building age, building height, and building materials. The reason for this is that developing a database that includes such information is considered to be inefficient, timewise and moneywise, for not only small- and medium-sized companies but also large corporations [7]. For this reason and many other related reasons, the low data quality does not follow the input level of the sophisticated vendor CAT models to date. And therefore, the current situation is that the risk assessment is relied on the basic and minimum amount of data and information available. Furthermore, in developing countries with emerging economies, in which insurance penetration rates are relatively low, it is strongly required to create vulnerability functions using historical loss records. Similarly, in certain countries, it is particularly difficult to describe the correlation between potential risk and loss, due to incoherent data or a lack of data [8]. In order to reduce the uncertainty of the evaluation model, the demand for and importance of identifying and developing work through proxy measurements of risks is increasing. Therefore, there is an urgent need for metrics and models that can easily and directly estimate and assess the vulnerabilities of the buildings to typhoons in these countries and situations.

In this study, based on the actual record of damages and the consequent financial losses caused by typhoons documented and accumulated by a major insurance company in Korea, it is first aimed to identify the statistically significant risk factors of buildings and of typhoons while relying on the objectivity and accuracy of the quantitative data. This study also intends to develop and model a local vulnerability function, which assesses the damage of buildings from the results of typhoons by conducting the statistical analysis of the risk factors, in order for many sectors including federal and local governments, insurance companies, and construction companies to utilize in their own damage assessment. Ultimately, this study was designed to provide more methodologically grounded understanding and evidence-based knowledge in minimizing the risks of typhoons to buildings.

1.2. Natural Catastrophe Model. As the demand for natural catastrophic risk modeling continues growing, several vendors such as Applied Insurance Research (AIR), EQECAT, and Risk Management Solution (RMS) [9, 10] have developed their own models. These models are also used by insurers and reinsurers around the world to assess the risks of natural disasters such as hurricanes, tsunamis, typhoons, floods, earthquakes, tornadoes, and winter storms, and they are considered to be the standard methodologies for natural disaster risk management. However, such models are hardly applicable for all companies and cases due to their high annual fees and also limitations for specifics. More specifically, it is a problem that models can only be developed and evaluated in a limited number of countries, such as the United States, China, and Japan, which often suffer large losses due to natural disasters and large insurance industries. For small- and medium-sized countries, it is not possible to utilize the models in their own risk evaluations in the same way due to the limitations for specifics. In addition, the modeling firms encourage insurers and reinsurers to create an independent in-house model with which to apprehend and assess portfolios and risks. It is dangerous to conclude the risk solely with the existing standard models alone. One of the reasons for this is that different insurance companies may show results unlike those from the standardized model due to the diverse business preference, portfolio, and capital. They should be able to judge whether the outcome is optimistic, pessimistic, or conservative, depending on their exposure. Therefore, insurers and reinsurers require in-house models that can verify the results of the standard models to their exposure.

Furthermore, many international organizations, e.g., HAZUS Multi-Hazard (MH) in the United States, the Florida Pubic Hurricane Loss Model (FPHLM) in the state of Florida, the Central American Probability Risk Assessment (CAPRA) in South America, the new Multi-Risk and Multi-Risk Assessment Method (MATRIX) in Europe, and the RiskScape in New Zealand, are investing a lot of resources in developing natural catastrophe models to be able to better predict, respond, and mitigate the risks associated with natural disasters. These models can assess direct and indirect damages at the national or community level due to tropical cyclones, earthquakes, floods, and storm surges. Nonetheless, these models are not designed to be adopted in the insurance industry because there are no finance modules that consider insurance concepts such as layers, deductible,

and so on. For this, this study adopted the various indicators that can be straightforwardly computed and easily accessed, found on Crichton's risk triangle [11].

1.3. Significance of Analyzing Typhoon Maemi. After major record-breaking hurricanes, such as hurricanes Katrina, Ike, and Sandy, insurance companies had to shut down, due to unexpected tremendous losses, and the companies that survived had to quickly modify their coverage and rates [12]. For this reason, insurers and reinsurers analyze extreme natural disasters in order to prepare reserves for losses from such extreme natural disasters.

They allocate portfolios to avoid emergencies and worst-case scenarios. They also set up catastrophe zones and limit amounts in order to minimize the damage caused by these extreme disasters. The records of previous extreme disasters are used as essential bases to establish the zone and limit.

Furthermore, the potential risk of natural disaster is the one of the major points used to determine the premium. The premium consists of the pure premium, expense, and profit. The pure premium is a combination of modeled cat risk, nonmodeled cat risk, and noncat risk such as FLEXA (i.e., fire, lighting, explosion, and aircraft). The historical loss records from previous extreme disasters guide the modeled cat risk and nonmodeled cat risk as well. Hence, analyzing extreme disasters makes a significant contribution in assigning risk and determining pricing.

In addition, the maximum amount of loss caused by a catastrophic disaster is a very vital number in the insurance industry. For example, insurers and reinsurers should assess probable maximum loss (PML), excess of loss reinsurance (XOL), liability limit (LOL), and retention. The PML is the amount of maximum loss an insurance company is likely to sustain. It also stands for the amount of loss expected from the worst-case scenario. Probable maximum loss (PML) has to be taken into account by an underwriter when taking risks. Underwriters must consider PML in order to determine whether to take the risk and also to determine the premium [13]. XOL and LOL are meaningful for allocating and limiting financial risk [14]. Retention is the responsibility of the insurer to limit the scope of the risk; it is an important management indicator for an insurance company because it is set as the amount of one's own responsibility, the amount of holding, and the amount of holding limit. The elementary guidelines are based on damage analysis of extreme disasters. Therefore, in order to plan for unanticipated damage and compute maximum losses, it is necessary to analyze extreme disasters.

In the New Oxford American Dictionary, the term typhoon is defined as "a tropical storm in the region of the Indian or western Pacific oceans" [15]. Among the two types of typhoons, straight and recurving, in areas such as Philippines, southern China, and Vietnam, are threatened by straight-moving typhoons, while recurving typhoons are threats to Korea, northern China, and Japan [16].

Typhoon Maemi in 2003 caused the most extreme damages in South Korea, as it was the largest in size and intensity since the record-keeping had begun in the country in 1904. Typhoon Maemi was generated as a tropical cyclone in the sea near Guam on September 4, 2003 and landed on the southern coast of the Korean peninsula on September 11 after passing through Okinawa Prefecture, Japan. After its rapid penetration of the southeastern part of the Korean Peninsula, it disappeared on September 14 in the East Sea. Among all the typhoons that have affected the Korean peninsula, it was the most destructive at the time of landing. The typhoon updated the record in various ways; the central pressure was 910 hPa, the maximum wind speed was 54 m/s, and the maximum size was 460 km (radius). The damage was also enormous due to its severe wind speed, storm surge, and precipitation. Ultimately, 135 people died, there were 61,000 victims, and the overall property damage was about $ 4.3 billion (in 2003 year). In terms of the strength and consequent damage of Typhoon Maemi, the distribution of the loss record indicated the southern part of the Korean Peninsula, such as Busan and Gyeongnam province, was particularly devastated by the typhoon. In particular, the loss distribution shows that in the right side area of the Gyeongnam province, more damage has occurred than in the left side area of the province. The reason for this was that the typhoon landed directly on the midcoast of Gyeongnam province, and the right side of the area had more influence than the left side of the area by the strong wind and rainfall of the typhoon [17, 18]. The World Meteorological Organization decided to remove the name Maemi from circulation and substituted it with Mujigae in 2006 due to the extreme damage and death caused by the typhoon [19].

2. Review of Literature

Several previous studies have focused on hurricane/tornado damage, damage assessment, and vulnerability analysis. This section will refer to a few most recent studies that specifically examined hurricane/tornado damage in terms of vulnerability analysis.

Chock looked into hurricane damage on Hawaii residential buildings gathered and georeferenced on the GIS. Data on property tax records, which included construction type attributes and property valuation, were also adopted, in order to specify residential building fragilities in relation to comprehensive reconstruction cost. As a result, this study suggested risk relativity factors and developed loss functions, which contributed to estimating hurricane damage to various Hawaii buildings [20]. Zhang suggested the concept of socioeconomic vulnerability and provided six vulnerability indicators (population density, population of coastline, GDP, primary industry export, annual disposable income of urban residents, and annual disposable income of rural residents) to assess the socioeconomic vulnerability to typhoon surges [21]. Heneka and Ruck focused on German winder storm events in 2000s and the damage from them to residential buildings. Using physical evidence and logical assumptions, this study derived a model that calculates number and financial values of damage, while assessing and simulating the spatial distribution and total damage [22].

In 2014, Zhang et al. examined wind risk of residential buildings in Japan caused by typhoons and developed a

provisional reliability-based vulnerability model to assess the risk. Although provisional, the model this study presents found that it is the resistance of roof tile and the correlation of trajectories of flying debris that takes an important part in the vulnerability [23]. Gautam et al. conducted a vulnerability analysis of damage to residential buildings and infrastructure caused by extreme windstorms in southcentral Nepal in 2019. Based on the field observations and forensic interpretations, this study presents fragility functions obtained from damage statistics for wattle and daub houses [24].

Previous studies on wind speed and precipitation in Korean peninsula have been conducted with similar yet various focuses: typhoon risk assessment wind speed from the GIS (Geographic Information System) [25], natural hazard prediction modeling based on a wind speed of typhoon and precipitation [26], characteristics of the damage scale and risk management system by strong wind speed of typhoon [27], damage analysis of meteorological disasters for each district considering the regional characteristics [28], and measuring typhoon damage by wind speed in the rural area properties [29].

These abovementioned studies have similarities with this study in the sense that most of them relied on the past record of financial information and data in measuring the damage and vulnerability from hurricanes/windstorms/typhoons of residential or industrial buildings in their analyses. In addition, all of these studies aimed to suggest a loss function or a model to adopt in an attempt to estimate and simulate the damage and loss in other areas in the event of future hurricanes/windstorms/typhoons.

Similar to the mentioned studies, this study conducted a vulnerability analysis in order to present the valid risk factors related to building vulnerability based on the accumulated past data and statistics. Although many similarities, however, this study distinguishes itself from other studies especially in terms of the data source it selected. In order to ascertain the actual damage and loss to the commercial, residential, and industrial buildings from Typhoon Maemi, this study made use of the claim payout data accumulated and provided by a major Korean insurance company. This was to achieve the quantification of the damage in numerical, especially in financial values. To be more specific, the monetary data was adopted because of its definiteness and objectivity [30]. This quantification of damage data represented in the insurance claim payout record can be especially helpful because of the detailed and specified information about each case of damage of the buildings, which also enables engineers and insurance underwriters, for logical and accurate, and thus more reliable review estimation of the damage.

3. Research Methodology

3.1. Loss Records.
The purpose of this study is to determine the significant factors, i.e., typhoon loss, natural hazard factors, and basic building information factors in the damage of buildings from the results of typhoons and to identify the relationship among the factors. This study also aims to assess the loss reflecting the regional vulnerability and to build a systematic method to measure other extreme cases and countries to predict the typhoon loss. In order to reach this goal, this study used Typhoon Maemi loss record from a primary insurance company in South Korea. The research scope is limited to South Korea. The amount of loss is the claim payout based on ground-up loss, which is the pure loss not accounting for insurance. Typhoon Maemi hit the Korean Peninsula on 11th September in 2003, as shown in Figure 1(a). The typhoon landed on the south coast on the Korean peninsula, through the inland, to the east coast, causing extreme economic losses in many cities on the south coast, as shown in Figure 1(b).

Table 1 shows the distribution of loss per province from Typhoon Maemi. In particular, the provinces located in the southern part of the Korean peninsula, Busan and Gyeongnam, were vastly damaged by the typhoon. Gyeongnam was damaged by the typhoon to the dollar amount of loss (48.0%) and the number of losses (35.4%). Busan was also significantly devastated by the typhoon to the dollar amount of damages (43.8%) and the number of losses (45.0%).

3.2. Data Availability.
This study gathered the loss record from a major insurance company of Construction All Risk (CAR) in South Korea from Typhoon Maemi's damage. The records received include information such as the date of the accident, location, occupancy, structure type, construction period, floor, underground, detail of loss, loss amount, and so on. Yet, due to the nature of the data, although any customer information is hardly included, the public access to the data is not permitted to avoid any possible problems.

3.3. Dependent and Independent Variables

3.3.1. Dependent Variable.
In this study, a regression analysis was first used to determine the significant loss indicators for building vulnerability and then to evaluate the relationship between the indicators and loss ratio. This loss ratio is a concept and a term established in this study; loss ratio is the amount of occurred losses to indemnifying typhoon damages divided by the property value of the damaged building. The property value of the building in this study was measured by the total sum insured. This concept is entered into the following equation (1):

$$\text{Loss ratio} = \frac{\text{Claim} - \text{payout}}{\text{Total sum insured}}. \tag{1}$$

Because in each case, the loss from typhoon damages was relatively small, compared to the total sum insured, most loss ratio were inclined toward zero when presented by equation (1), and for this reason, the dependent variable was converted by log transformation in order to fit the normal distribution. The dependent variable value used in the regression model is shown in equation (2):

$$\text{Transformed loss ratio} = \text{Ln} \, (\text{loss ratio}). \tag{2}$$
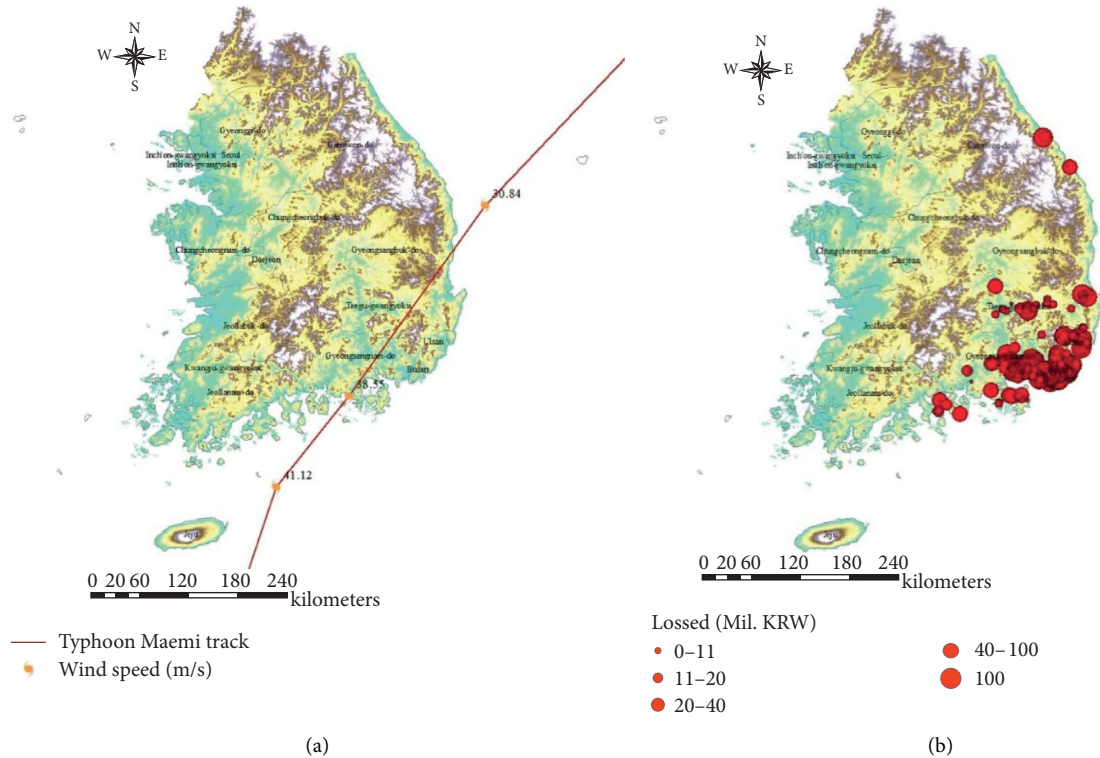
(a)

(b)

Figure 1: Typhoon Maemi: (a) track of typhoon and (b) distribution of losses.

Table 1: Loss records per province from Typhoon Maemi.

Province	Total claim payouts (mil. KRW)	No. of claim payouts
Gyeongnam	11,224	110
Busan	10,245	140
Ulsan	928	28
Gyongbuk	530	21
Kangwon	239	4
Jeonnam	135	3
Daegu	91	5

3.3.2. Independent Variables. The loss records are consisted of two categories: (1) accident details, e.g., details of the accident, the address, the amount of loss, and the date of the accident, and (2) basic building information, e.g., the total amount of the property, construction type, number of floors, and number of underground floors.

Based on the existing location information, the wind speed and distance from the property centroid to the coastline are estimated. The various properties information of the typhoon directly affects the damage [31]. Wind speed is an important indicator of the intensity of typhoons and causes damage such as floods, storm surge, landslides, and missile impacts [32, 33]. The wind speeds of the individual buildings that suffered damage were collected based on the date of the accident and the address information in the loss records using the Geographic Information System. Wind speed information is collected from the Japan Meteorological Administration's (JMA's) maximum wind speed (10 min sustained) record. The distance from the property

centroid to the coastline is also estimated based on the address information using the Geographic Information System. The distance between the building and coastline also plays an important role in describing a building's vulnerability to windstorms. Highfield et al. estimated the distance from the building to the coastline to identify the relationship between the distance and loss caused by Hurricane Ike on Galveston Island and the Bolivar Peninsula. They indicated that the loss decreased as the distance from the coastline increased [34]. The results reveal that a building farther from the coastline is less vulnerable to windstorms than a building closer to the coastline.

The basic building information, e.g., total amount of the property, construction type, number of floors, and number of underground floors, is used as indicators to reveal the typhoon vulnerability according to the building inventory. The total amount of the property is also substantial in terms of the losses associated with windstorms. Kim et al. indicated that windstorm loss increases as the total amount of the building decreases. The correlation with the total amount of the properties and windstorm loss are negative [7]. The construction type is also an important indicator of the building's typhoon vulnerability. For instance, when construction types can be divided into wood, stone, steel, and reinforced concrete, they are generally vulnerable to typhoons in the following ascending order: reinforced concrete, steel, stone, and wood [6, 35, 36]. The building height is regarded as a vital indicator of vulnerability quantification against windstorms [6, 37]. The reason for this is that the building height is statistically correlated with the degree of financial loss, so it can be used as a vulnerability index to

TABLE 2: Descriptive statistics of the variables.

	N	Mean	Std. deviation	Minimum	Maximum
Dependent variable					
Loss ratio (%)	312	1.68	5.03	0.01	47.14
Independent variables					
Total value of property (mil. KRW)	312	25,677.16	39,814.96	100.00	358,397.00
Construction type (number)†	312	1.32	0.74	0.00	4.00
Floors (number)	312	13.75	9.06	1.00	30.00
Underground floors (number)	312	0.52	0.94	0.00	6.00
Maximum wind speed (m/s)	312	37.58	1.22	31.24	38.56
Distance from coastline (km)	312	33.42	18.80	1.31	117.88

"†" denotes (1) reinforced concrete building, (2) steel structure building, (3) wood, and (4) steel plate roof.

quantify a building's vulnerability to hurricanes. For instance, the correlation between building height and typhoon loss is negative, which means that as building height increases, typhoon loss decreases [37, 38]. Table 2 defines the loss and data. The central trends in each category are expressed as a mean.

4. Results

4.1. Multiple Regression Analysis. Table 3 shows the typhoon information and basic building information related to the loss ratio for the line of business (LOB): commercial, residential, and industrial, as assessed through the regression models, correspondingly. The LOB is typically used as a risk indicator to quantify the building vulnerability in the risk assessment model [7, 39]. The LOB is a term that is a commonplace in the insurance industry and denotes a tightly linked product or service that is a business necessity. This terminology from insurance is also stated to relate policies in provision and book-keeping, such as the fact that injury and property policies can be classified as commercial, residential, and industrial. As a result, the LOB category can classify buildings as physical and financial functions. This study adopts this classification to reveal information in a practical manner.

Table 3 displays the typhoon information and basic building information to loss ratios for Typhoon Maemi as assessed through regression analysis. In the regression analysis of the commercial building, the adjusted R^2 value is 0.332, which indicates that 33.2% of the variant of the loss ratio can be described by the regression model. Two significant variables, total value of property and construction type, are branded as meters of the ruthlessness of typhoon loss. By contrast, the other indicators are not associated with the loss ratio of commercial building. The values of the variance inflation coefficient (VIF) ranged from 1.016 to 1.293. These values indicate that there is no substantial multicollinearity between variables. The indicators can be hierarchical in the descending order of their beta coefficients. Following the scale of the coefficient, the indicators are (1) the total value of property (beta coefficient = –0.549) and (2) construction type (beta coefficient = 0.241).

In the regression analysis of the residential building, the Adj-R^2 value is 0.587, which indicates that 58.7% of the variant of the loss ratio can be described by the regression model. Four significant variables, maximum wind speed, distance from coast, total value of property, and floors, are identified as indicators of the severity of typhoon loss. However, the other indicators are not associated with the loss ratio of residential building. The values of the variance inflation coefficient (VIF) ranged from 1.048 to 1.1. The values show that there is no significant multicollinearity between variables. The indicators can be ranked in the descending order of their beta coefficients. According to the number of the coefficient, the indicators are (1) maximum wind speed (beta coefficient = –0.509), (2) total value of property (beta coefficient = 0.328), (3) distance from coast (beta coefficient = –0.248), and (4) floors (beta coefficient = 0.113).

In the regression analysis of the industrial building, the Adj-R^2 value is 0.403, which indicates that 40.3% of the variant of the loss ratio can be clarified by the regression model. Three significant variables, distance from coast, total value of property, and construction type, are recognized as indicators of the sternness of typhoon loss. Nevertheless, the other indicators are not related with the dependent variable of residential building. The values of the variance inflation coefficient (VIF) ranged from 1.109 to 2.190. These values show that there is no noteworthy multicollinearity between variables. The indicators can be listed in the descending order of their beta coefficients. Following the scale of the coefficient, the indicators are (1) the total value of property (beta coefficient = –0.622), (2) floors (beta coefficient = 0.227), and (3) distance from coast (beta coefficient = –0.222).

5. Discussion

The models are statistically significant because the P values (0.000) are less than 0.05. This means that there is a significant relationship between the dependent and independent variables. In each regression model, according to the LOB classification, the adjusted R^2 values and the significant indicators were also different. The adjusted R^2 value of the commercial building model was 0.332, indicating that 33.2% of the variance of the dependent variable can be explained by two indicators (total value of property and construction type). However, the remaining 66.8% caused by some unconfirmed indicators was not considered in this study. The adjusted R^2 value of the residential building model is 0.587,

TABLE 3: Results with the regression models.

Variables	Commercial				Residential				Industrial			
	Coefficient	Beta coefficient	$p > |z|$	VIF	Coefficient	Beta coefficient	$p > |z|$	VIF	Coefficient	Beta coefficient	$p > |z|$	VIF
Typhoon information												
Maximum wind speed	0.089	0.060	0.612	1.022	0.484	0.509	0.000	1.101	0.402	0.092	0.338	1.200
Distance from coast	−0.013	−0.107	0.363	1.016	−0.015	−0.248	0.000	1.057	−0.035	−0.222	0.021	1.165
Basic building information												
Total value of property	$-3.137E-005$	−0.549	0.000	1.027	$-1.413E-005$	−0.328	0.000	1.085	$-4.260E-005$	−0.622	0.000	2.190
Construction type	1.094	0.241	0.050	1.073	—	—	—	—	0.214	0.130	0.163	1.109
Floors	0.028	0.083	0.531	1.293	0.033	0.113	0.027	1.048	0.083	0.227	0.080	2.147
Underground floors	0.082	0.055	0.673	1.271	0.024	0.018	0.726	1.055	0.678	0.106	0.267	1.182
Number of observations	51				173				78			
F	5.147				47.811				9.785			
Adj-R^2	0.332				0.587				0.403			

Coefficient designates the nonstandardized coefficients that reflect the unit scale of the independent variable. Beta coefficient designates standardized coefficients that disregard the unit scale of independent variable, which helps comparisons among the independent variables. The higher value of the beta coefficient means a more significant effect on the dependent variable.

indicating that 58.7% of the change in the dependent variable can be explained by four indicators: maximum wind speed, distance from coast, total value of property, and floors. However, the volatility of 41.3% due to unverified indicators was not considered in this study. The adjusted R^2 value of the industrial building model was 0.403, indicating that 40.3% of the difference of the dependent variable can be described by three indicators (distance from coast, total value of property, and construction type). Nevertheless, the remaining 59.7% caused by some unproven indicators was not considered in this study. The reason why the significant indicators and adjusted R^2 are different among the regression model is that they have different damage vulnerabilities against typhoon damage. It reinforces the previous study indicating that the LOB grouping can categorize buildings as physical and financial functions [7].

Among the key indicators of the variables, the value of property is the significant indicator that is shared among the three models. The value of property is negatively associated with the degree of loss caused by a typhoon. This indicates that the rate of loss increases as the value of property decreases. The lower the property value of a building, the more vulnerable it is to typhoons. This is also consistent with the results of prior studies [20, 24]. Former studies have stated that the value of property affects the degree of loss caused by typhoons and is a valuable factor for loss valuation.

The distance from the coast has also been proven to play a vital role in describing vulnerability to windstorm. The distance from the coast is adversely related with the amount of loss caused by a typhoon. This signifies that the degree of loss rises as a building is closer to the coast. The closer a building is to the coast, the more devastated it is to typhoons [34]. This confirms the results of the initial study and shows that the distance from the coast is an imperative indicator for assessing losses caused by typhoons.

The maximum wind speed and loss due to the typhoon are positively interrelated. This means that the loss increases as the wind speed intensifies. This also supports early research that reported that maximum wind speed is an essential indicator for predicting loss due to typhoons [12, 33, 40].

The construction type also shows a main indicator of the building's typhoon vulnerability. There is a positive correlation between the type of construction and the extent of loss, which suggests that the type of construction affects the magnitude of the loss, which is consistent with the results of previous studies; in the ascending order of construction type, reinforced concrete, steel, stone, and wood, it was found that they are vulnerable to typhoons [6, 36].

The number of floors has a positive relationship with the loss, which suggests that as the number of floors increases, the degree of loss increases. This again confirms that the number of floors is a vital indicator of quantifying typhoon, and it also strengthens the results of previous studies [37, 38].

6. Conclusion

This study conducted a statistical analysis on the damages caused by Typhoon Maemi, which was categorized as an extreme disaster, in order to identify the natural hazard indicators and basic building information indicators and to develop a vulnerability function. The buildings were categorized into three different types, i.e., commercial, residential, and industrial. Variables for natural hazard indicators included maximum wind speed and distance from coast. Variables for basic building information indicators included total value of property, number of floors and underground floors, and construction types.

The statistical analysis found that, in the case of commercial buildings, total value of property and construction type are the two significant vulnerability indicators among the variables of both the natural hazard indicators and the basic building information indicators. For residential buildings, maximum wind speed, distance from coast, total value of property, and number of floors are significant indicators. Last, in the case of industrial buildings, the significant indicators were found to be distance from coast, total value of property, and number of floors.

In this study, the vulnerability function of the typhoon risk assessment models has also been developed and validated based on the statistical analysis of the actual loss claim payout data kept by an insurance company. The models were also developed in specification of various types of buildings including commercial, residential, and industrial, so that the particular and practical application of these models are possible.

Every year, typhoons such as Typhoon Maemi cause serious financial losses worldwide. Therefore, it would be necessary for public and private disaster management agencies to estimate the possible amount of damage by using typhoon risk assessment models. Therefore, findings and results of this research can serve as references and provide vital directions to abovementioned sectors such as federal and local governments, insurance companies, and construction companies in predicting typhoon losses. For example, federal and local governments can refer to this research in an effort to reducing future typhoon damages by predicting financial losses with the models reported in this study and establish mitigation strategies based on expected losses.

Insurance and reinsurance companies can use the model from this research to improve their own business model using the methodologies to measure latent risks. More specifically, they can use modeling to assess risks and make judgments and use the base rate of insurance policies as a percentage of experience with expected losses. Furthermore, they can appraise the event limits and probable maximum loss, delineate premiums, estimate risk accumulation from typhoons, and institute business strategies found on the outcome of the metric. The building construction companies are also able to improve their design guidelines by planning storm-resistant buildings and by assessing building loss based on the predicted total value of property, construction type, and the number of floors of the building.

Furthermore, the frameworks and indicators of this study can also be used for a further similar research, especially in developing countries with few data on loss caused by windstorms and building characteristics to predict windstorms. These countries can assess windstorm losses by

adopting the frameworks and indicators used in this study, although the weight of the indicator should be adjusted by the weight of each province and the coefficient to reflect the local building vulnerability for use in other areas. However, this study solely focused on the one typhoon case, Typhoon Maemi. Therefore, there is a need for a more comprehensive loss data using the damages associated with various categories of typhoons for development of the vulnerability function in future studies, in order to support the results of this study.

In addition, constructing vulnerability curves in further research can make much contribution in the field. That is, based on the data used and the significant factors found in this study, vulnerability curves can be created in a subsequent research. In other words, in catastrophe modeling, vulnerability curves define the degree of vulnerability according to, e.g., types of the buildings, and thus can serve as an important part of the modeling. For example, the vulnerability curve for typhoons describes the link between average damage rate and wind speed and determines the degree of damage, depending on the types of buildings. The average damage rate of the vulnerability curve indicates the building's storm vulnerability. Hence, constructing the vulnerability curves referring to the data and meaning factors from this research can enhance future studies with the similar focus and approach.

Again as to future research, the values of adjusted R^2 were 0.332 for commercial buildings, 0.587 for residential buildings, and 0.403 for industrial buildings, which indicate that the residual variability of the damage is described by some indeterminate indicators. Therefore, in future studies, other possible indicators should be identified and added to the model.

Data Availability

This study gathered the loss record from a major insurance company of Construction All Risk (CAR) in South Korea from Typhoon Maemi's damage. The records received include information such as the date of the accident, location, occupancy, structure type, construction period, floor, underground, detail of loss, loss amount, and so on. Yet, due to the nature of the data, although any customer information is hardly included, the public access to the data is not permitted to avoid any possible problems.

Conflicts of Interest

The authors declare that there are no conflicts of interest regarding the publication of this paper.

Acknowledgments

References

[1] K. T. Bhatia, G. A. Vecchi, T. R. Knutson et al., "Recent increases in tropical cyclone intensification rates," *Nature Communications*, vol. 10, no. 1, pp. 1–9, 2019.

[2] E. S. Blake, E. N. Rappaport, and C. W. Landsea, *The Deadliest, Costliest, and Most Intense United States Tropical Cyclones from 1851 to 2006 (And Other Frequently Requested Hurricane Facts*, NOAA/National Weather Service, National Centers for Environmental Prediction, National Hurricane Center, Miami, FL, USA, 2007.

[3] E. S. Blake, T. B. Kimberlain, J. B. Robert et al., *Hurricane Sandy: October 22-29, 2012 (Tropical Cyclone Report)*, United States National Oceanic and Atmospheric Administration's National Weather Service, Silver Spring, MD, USA, 2013.

[4] U. Ulbrich, A. H. Fink, M. Klawa, and J. G. Pinto, "Three extreme storms over Europe in December 1999," *Weather*, vol. 56, no. 3, pp. 70–80, 2001.

[5] E. E. Koks, B. Jongman, T. G. Husby, and W. J. W. Botzen, "Combining hazard, exposure and social vulnerability to provide lessons for flood risk management," *Environmental Science & Policy*, vol. 47, pp. 42–52, 2015.

[6] A. C. Khanduri and G. C. Morrow, "Vulnerability of buildings to windstorms and insurance loss estimation," *Journal of Wind Engineering and Industrial Aerodynamics*, vol. 91, no. 4, pp. 455–467, 2003.

[7] J.-M. Kim, T. Kim, and K. Son, "Revealing building vulnerability to windstorms through an insurance claim payout prediction model: a case study in South Korea," *Geomatics, Natural Hazards and Risk*, vol. 8, no. 2, pp. 1333–1341, 2017.

[8] H. Ryu, K. Son, and J.-M. Kim, "Loss prediction model for building construction projects using insurance claim payout," *Journal of Asian Architecture and Building Engineering*, vol. 15, no. 3, pp. 441–446, 2016.

[9] D. E. A. Sanders, B. Anders, D. Paul et al., "The management of losses arising from extreme events," Convention General Insurance Study Group GIRO, London, UK, 2002.

[10] H. Kunreuther, R. Meyer, C. Van den Bulte, E. Robert, and Chapman, *Risk Analysis for Extreme Events: Economic Incentives for Reducing Future Losses*, US Department of Commerce, Technology Administration, National Institute of Standards and Technology, Gaithersburg, MD, USA, 2004.

[11] D. Crichton, "The risk triangle," in *Naturalc Disaster Management*, J. Ingleton, Ed., pp. 102-103, Tudor Rose, London, UK, 1999.

[12] C. C. Watson, M. E. Johnson, and S. Martin, "Insurance rate filings and hurricane loss estimation models," *Journal of Insurance Regulation*, vol. 22, no. 3, pp. 39–64, 2004.

[13] P. Grossi, H. Kunreuther, and D. Windeler, "An introduction to catastrophe models and insurance," in *Catastrophe Modeling: A New Approach to Managing Risk*, P. Grossi and H. Kunreuther, Eds., pp. 23–42, Springer, Boston, MA, USA, 2005.

[14] D. Cummins, C. Lewis, and R. Phillips, "Pricing excess-of-loss reinsurance contracts against cat as trophic loss," in *The Financing of Catastrophe Risk*, pp. 93–148, University of Chicago Press, 1999.

[15] E. McKean, *The New Oxford American Dictionary*, Oxford University Press, New York, NY, USA, 2005.

[16] J. Elsner and K. Liu, "Examining the ENSO-typhoon hypothesis," *Climate Research*, vol. 25, no. 1, pp. 43–54, 2003.

[17] W. J. Platt, R. F. Doren, and T. V. Armentano, "Effects of Hurricane Andrew on cypress (Taxodium distichum var. nutans) in south Florida," *Journal of Coastal Research*, no. 17, pp. 184–196, 1995.

[18] J. M. Kim, P. K. Woods, Y. J. Park, and K. Son, "Estimating the Texas windstorm insurance association claim payout of commercial buildings from hurricane Ike," *Natural Hazards*, vol. 84, no. 1, pp. 405–424, 2016.

[19] National Typhoon Center, *Typhoon White Book*, National Typhoon Center, Pearl Harbor, Hawaii, 2011, http://typ.kma.go.kr/TYPHOON/down/2011/%C0%CE%B8%ED%B9%D7%C0%E7%BB%EA%C7%C7%C7%D8.pdf.

[20] G. Y. K. Chock, "Modeling of hurricane damage for Hawaii residential construction," *Journal of Wind Engineering and Industrial Aerodynamics*, vol. 93, no. 8, pp. 603–622, 2005.

[21] J. Zhang, "A vulnerability assessment of storm surge in Guangdong province, China," *Human and Ecological Risk Assessment: An International Journal*, vol. 15, no. 4, pp. 671–688, 2009.

[22] P. Heneka and B. Ruck, "A damage model for the assessment of storm damage to buildings," *Engineering Structures*, vol. 30, no. 12, pp. 3603–3609, 2008.

[23] S. Zhang, K. Nishijima, and T. Maruyama, "Reliability-based modeling of typhoon induced wind vulnerability for residential buildings in Japan," *Journal of Wind Engineering and Industrial Aerodynamics*, vol. 124, pp. 68–81, 2014.

[24] D. Gautam, R. Adhikari, P. Jha, R. Rupakhety, and M. Yadav, "Windstorm vulnerability of residential buildings and infrastructures in south-central Nepal," *Journal of Wind Engineering and Industrial Aerodynamics*, vol. 198, p. 104113, 2020.

[25] S.-Su Lee and E.-Mi Chang, "Application of GIS to typhoon risk assessment," *Spatial Information Research*, vol. 17, no. 2, pp. 243–249, 2009.

[26] S. I. Lee, A "study on damage scale prediction by rainfall and wind velocity with typhoon," Master thesis, Sunchon National University, Suncheon, Korea, 2013.

[27] J. S. Kim, "On the characteristics of damage scale and risk management system by strong-wind speed of typhoon," Master thesis, Inje University, Gimhae, Korea, 2013.

[28] H.-D. Jun, P. Moo-Jong, and G.-Y. Kim, "Damage analysis of meteorological disasters for each district considering the characteristics of a district," *Journal of the Korean Society of Hazard Mitigation*, vol. 8, no. 2, pp. 75–82, 2008.

[29] D.-Y. Lee and Il-J. Kim, "A Study on typhoon damage prevention measures about the facility of the rural areas-Focused on Jeollabuk-do area," *Journal of the Korean Institute of Rural Architecture*, vol. 14, no. 4, pp. 117–124, 2012.

[30] H. A. Odeyinka, "An evaluation of the use of insurance in managing construction risks," *Construction Management and Economics*, vol. 18, no. 5, pp. 519–524, 2000.

[31] Z. Huang, D. V. Rosowsky, and P. R. Sparks, "Hurricane simulation techniques for the evaluation of wind-speeds and expected insurance losses," *Journal of Wind Engineering and Industrial Aerodynamics*, vol. 89, no. 7-8, pp. 605–617, 2001.

[32] J.-M. Kim, P. K. Woods, and Y. J. Park, K. T. Kim and K. Son, Predicting hurricane wind damage by claim payout based on Hurricane Ike in Texas," *Geomatics, Natural Hazards and Risk*, vol. 7, no. 5, pp. 1513–1525, 2016.

[33] C. G. Burton, "Social vulnerability and hurricane impact modeling," *Natural Hazards Review*, vol. 11, no. 2, pp. 58–68, 2010.

[34] W. E. Highfield, W. G. Peacock, and S. Van Zandt, "Determinants & characteristics of damage in single-family island households from Hurricane Ike1," in *Proceedings of the Association of Collegiate Schools of Planning Conference*, pp. 7–10, Minneapolis, MN, USA, October 2010.

[35] D. D'Ayala, C. Alex, and H. Wang, "A conceptual model for multi-hazard assessment of the vulnerability of historic buildings," in *Proceedings of the Fifth International Conference, Structural Analysis of Historical Constructions: Possibilities of Numerical and Experimental Techniques*, pp. 121–140, New Delhi, India, November 2006.

[36] J.-M. Kim, K. Son, and Y.-J. Kim, "Assessing regional typhoon risk of disaster management by clustering typhoon paths," *Environment, Development and Sustainability*, vol. 21, no. 5, pp. 2083–2096, 2019.

[37] D. G. De Silva, J. B. Kruse, Y. Wang, and Y. Wang, "Spatial dependencies in wind-related housing damage," *Natural Hazards*, vol. 47, no. 3, pp. 317–330, 2008.

[38] J.-M. Kim, K. Son, Y. Yoo, D. Lee, and D. Kim, "Identifying risk indicators of building damage due to typhoons: focusing on cases of South Korea," *Sustainability*, vol. 10, no. 11, p. 3947, 2018.

[39] F. A. Cummins, *Building the Agile Enterprise: with SOA, BPM and MBM*, p. 193, Elsevier, Amsterdam, Netherlands, 2010.

[40] P. J. Vickery, P. F. Skerlj, J. Lin, L. A. Twisdale Jr, M. A. Young, and F. M. Lavelle, "HAZUS-MH hurricane model methodology. II: damage and loss estimation," *Natural Hazards Review*, vol. 7, no. 2, pp. 94–103, 2006.

Research Article

An Analysis of Factors Affecting Flowslide Deposit Morphology Using Taguchi Method

Zhao Duan,[1,2] Yan-Bin Wu [ID],[1,2] Hao Tang,[1,2] Jian-Quan Ma [ID],[1,2] and Xing-Hua Zhu[3]

[1]*College of Geology and Environment, Xi'an University of Science and Technology, Xi'an 710054, China*
[2]*Shaanxi Provincial Key Laboratory of Geological Support for Coal Green Exploitation, Xi'an 710055, China*
[3]*College of Geological Engineering and Geomatics, Chang'an University, Xi'an 710064, China*

Correspondence should be addressed to Yan-Bin Wu; 19209071021@stu.xust.edu.cn

Flowslides, as one type of landslides, are becoming a research hotspot due to their high speed and long runout distance, which can cause tremendous damage and economic loss. The scale of damage and deposit morphology of flowslide is closely related to factors like deposit volume, slope height, and slope angle. In order to assess the influence of these factors, a sandbox apparatus is developed, and the Taguchi method is used to design an experimental scheme to analyze the results of factors affecting the deposit morphology of flowslide. The results show that the factor that has the greatest impact on flowslide deposit morphology is slope angle, followed by the influence of volume and slope height. As slope angle increases, the maximum width, maximum length, area, and length-width ratio of the deposit first increase and then decrease. In addition, there should be a critical angle in the changes of deposit morphology that is between 60° and 70° under the experimental conditions. When the volume is $5.4 \times 10^{-3} \, \text{m}^3$, the slope angle is 70°, the slope height is 0.90 m, and the changes of deposit morphology of the flowslide are the largest. In this study, considering the slope angle as a single variable, there is a single upheaval for a slope angle of 40° and 50° and a double upheaval at 60° and 70°. The formation mechanism of the upheaval is analyzed based on the Mohr-Coulomb criterion and considered properties of the material. The apparent friction coefficient of a flowslide is spatially and lithologically different and increases nonlinearly as the slope angle increases. The initial benchmark of the slope angle and apparent friction coefficient curve are affected by the friction coefficient of the material; the position of the inflection point at which the curve increases rapidly is affected by the coefficient of velocity restitution.

1. Introduction

Landslides including slide and flowslide are often seen in the Loess Plateau of northwest China since the loess features metastable microstructure, high porosity, and water sensitivity. The hazards associated with flowslides are often closely related to volume, slope angle, slope height, and so on, because these conditions significantly affect a flowslide's moving distance [1–4]. Flowslides are becoming a research hotspot recently since it has the characteristics of high speed and long runout distance as well as leading to tremendous damage and economic loss. A large number of field investigations have shown that the runout and area of a

flowslide increase with an increase in volume and slope height, but decrease with an increase in slope angle [5–9]. In fact, each flowslide is unique and nonrepeatable, and, as a result, the characteristics and parameters of each are different. Therefore, in field research, it is impossible to separate out the various influencing factors for single factor research. Similarly, data obtained through field investigations cannot accurately reflect the impact of various factors on the characteristics of flowslide movement. To make up for the shortcomings of field investigations, physical model tests were introduced to study the deposit morphology and movement rules of flowslides [10–12]. In the course of these investigations, some rules and interesting characteristics of

deposits that were in line with reality were reproduced well by model tests. These modeling studies provide a reference for understanding the dynamic characteristics of flowslides. The rationality of experimental method directly determines the accuracy of experimental results [10, 13–15]. It is prevailing to study the runout distance, influencing factors, stress during movement, and other characteristics of flowslides using model experiments [11]. However, in the research involving the field of flowslides currently, the method is relatively monotonous, and those studies are conducted to the movement and deposit characteristics under the influence of a single factor [4]. In addition, when the order of influencing factors was obtained, a deep excavation on the change laws of deposit morphology and the possible internal mechanical mechanism under the greatest influencing factor has not been performed.

The flowslide flows to the slope break where a change in its flow direction will inevitably cause collision and shearing; the intensity of this effect increases with an increase in slope break angularity and sharpness [13]. The duration of a flowslide increases with angle and volume and decreases with aspect ratio [16]. In the study of the deposit morphology of flowslides, scale effects would affect the overall shape of the deposit including leading edge, highest point, and trailing edge positions, but could be minimized by accurately controlling the test variables [17]. Longitudinal ridges developed on the surface of flowslide deposits caused by radial propagation of the flowslide during movement, as discussed by Dufresne and Davies [18]. The properties of granular materials are also an important factor affecting the characteristics of flowslide deposits, including the granular diameter, the grading index, and the roundness. Different granular materials can lead to different granular effects, which can increase the accumulation area and runout distance [19, 20]. The apparent friction coefficient is an important parameter used to characterize the movement of a flowslide, which has been widely studied under different variable conditions [5, 7, 9, 21]. It is generally believed that the apparent friction coefficient decreases with increasing volume and increases with increasing slope angle, but the related general relationship has not been proposed [3, 22]. Flowslide on alien planets shares the above-mentioned characteristics and rules [23–25] but shows longer runout. At present, research methods used in the study of flowslide are limited, and research schemes are not systematic enough. In addition, better knowledge of the overall rules governing changes in and causes of flowslide deposit morphology is needed.

In this paper, the Taguchi method [15, 26–29] is used to design an experimental scheme and analyze the results of factors affecting the deposit morphology of flowslide. The Taguchi method can be used to quantify test results and to obtain the combination factors that cause the greatest morphological changes in the deposits under test conditions. The specific objectives of this study are to (1) determine the maximum influencing factors of flowslide deposit morphology and the combination of factors that cause the largest change in the morphology of a deposit using the Taguchi method; (2) analyze the changes of the surface and profile

morphology of the deposit under the most influential factors and compare them with actual flowslides; (3) explain the rules governing changes in flowslide deposit morphology and carry out the necessary stress analyses for particular morphologies; (4) obtain and confirm the distribution characteristics of the apparent friction coefficient by combining test results with natural flowslides.

2. Material and Method

2.1. Sandbox Experiment Setup. A sandbox experiment was conducted to study flowslide deposit morphology. Plexiglass was chosen for the experimental devices, which were composed of four parts: a sand container, an inclined plate, a horizontal plate, and high-speed cameras. The length of both the inclined plate and the horizontal plate is 1.5 m, and the width of each is 1.2 m (Figure 1(a)). The specification volumes of each sand container with a gate in the bottom are $1.8 \times 10^{-3} \, \text{m}^3$, $3.6 \times 10^{-3} \, \text{m}^3$, and $5.4 \times 10^{-3} \, \text{m}^3$. The angle of the inclined plate can be adjusted freely through a rear bracket, and the center gravity height of the sand container can be adjusted through a track on the inclined plate. High-speed cameras (120 frames/s) were used to record images during the experiment.

During the experiment, medium-fine sand density was controlled to $1.51 \, \text{kg} \cdot \text{m}^{-6}$. The material flowed down an inclined plate with no boundary constraints to the horizontal plate when the gate was opened. When the sliding material stopped moving, a millimeter-level three-dimensional scanner was used to collect digital elevation model (DEM) data of the deposit surface (Figure 1(b)) through calibrated and extracted key point coordinates to obtain flowslide deposit morphology data.

2.2. Material. A medium-fine sand (Figure 2) was used as the sliding material in the simulated sandbox experiment because it shows a similar flow characteristic during sliding compared with natural flowslides [30, 31]; its particle-size distribution curve is shown in Figure 3. The uneven coefficient C_u is 2.39, the curvature coefficient C_c is 1.19, the average diameter is 2×10^{-4} m, and the specific surface area is $0.02 \, \text{m}^2 \cdot \text{kg}^{-4}$. The cumulative percentage of the particle size in the range 0.075–0.5 mm is 87.71%, the internal friction angle φ is 36°, the cohesion c is zero, and the interface friction parameter of plexiglass and sand is 0.538.

2.3. Method. The experimental scheme was designed using the Taguchi orthogonal method (Table 1) to comprehensively analyze the influence of flowslide volume, slope angle, and slope height on deposit morphology. The following design variables were used to assess influencing factors: volumes $1.8 \times 10^{-3} \, \text{m}^3$, $3.6 \times 10^{-3} \, \text{m}^3$, and $5.4 \times 10^{-3} \, \text{m}^3$; slope angles 50°, 60°, and 70°; and slope heights 0.7 m, 0.9 m, and 1.1 m.

The principle of variable selection was as follows: A K-means clustering of volume and slope height data from 28 flowslides [30] in the Jingyang South platform, Shaanxi province, China, was conducted. Results showed that the
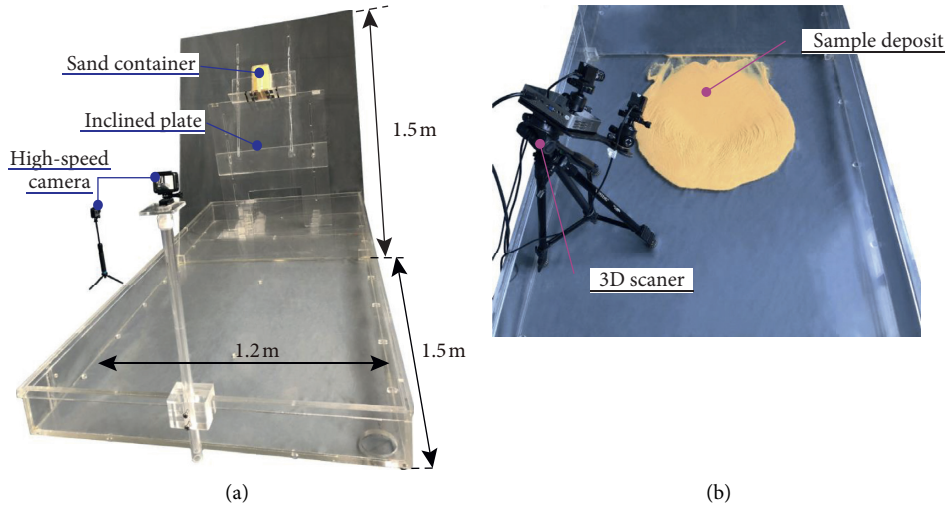
(a)

(b)

FIGURE 1: Flowslides experimental research design: (a) structural of the experimental device; (b) 3D scanner for acquisition of deposit data.
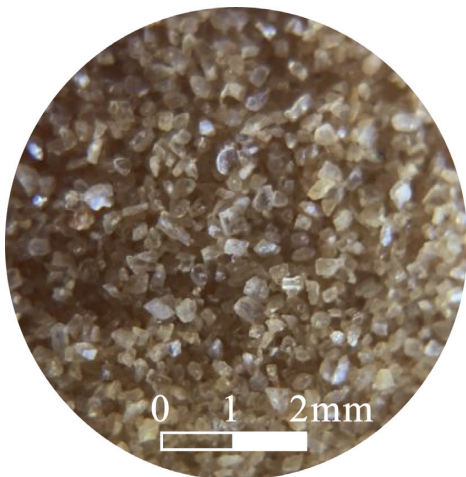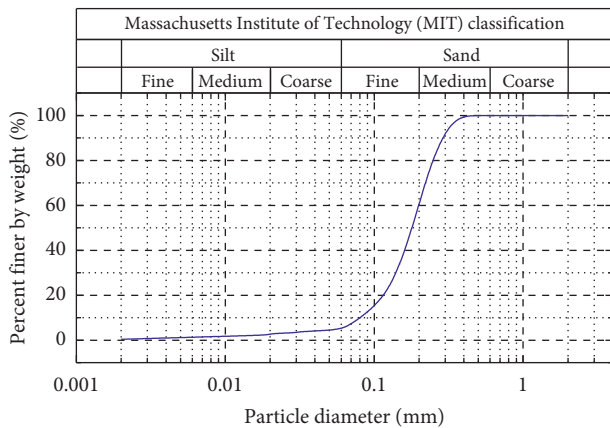

FIGURE 2: Experimental material.

FIGURE 3: Particle-size distribution curve for the experimental material.

deposit volume was divided into three levels of $1317.75 \times 10^3 \, \text{m}^3$, $545.44 \times 10^3 \, \text{m}^3$, and $184.82 \times 10^3 \, \text{m}^3$, respectively, so the similarity ratio was approximately $1 : 2 \times 10^8$. Slope height was divided into three levels of $113.45 \, \text{m}$, $84.27 \, \text{m}$, and $63.07 \, \text{m}$, with a similarity ratio of approximately $1 : 100$. The slope angle of the Jingyang South platform was mainly within $40°–70°$ [31]. There were, in total, nine groups of experiments; two parallel experiments were carried out for each group. If the experimental results were greater than millimeter-level in difference, a third experiment was conducted, eventually taking the average value of two small differences in the results to determine the deposit morphology of the flowslide.

3. Results

3.1. Sandbox Experiment Results. The Taguchi method is a test method commonly used in steel casting and other fields within materials science to maximize production and reduce consumables. Its greatest advantage is to determine the order of significance of evaluation indexes using fewer tests and to determine an optimized combination scheme of influencing factors [15, 26, 27, 29]. The direct basis for the analysis of the results is the signal-to-noise ratio (S/N), which can be divided into three categories according to three characteristics: larger-the-better, smaller-the-better, and nominal-the-better (washing the test results closest to the target value). The larger the value of (S/N), the greater the signal that the dependent variable responds to the change of factors. Therefore, the larger-the-better characteristic is used in this paper, and the calculation expression is as follows:

$$\left(\frac{S}{N}\right)_i = -10\lg\left(\frac{1}{n}\sum_{j=1}^{n} Y_{ij}^2\right), \qquad (1)$$

TABLE 1: Orthogonal experimental scheme.

Number	Orthogonal combination	Flowslide volume (10^{-3} m^3)	Slope angel (°)	Height (m)
1	$A_1B_1C_1$	1.8	50	0.7
2	$A_1B_2C_2$	1.8	60	0.9
3	$A_1B_3C_3$	1.8	70	1.1
4	$A_2B_1C_2$	3.6	50	0.9
5	$A_2B_2C_3$	3.6	60	1.1
6	$A_2B_3C_1$	3.6	70	0.7
7	$A_3B_1C_3$	5.4	50	1.1
8	$A_3B_2C_1$	5.4	60	0.7
9	$A_3B_3C_2$	5.4	70	0.9

Note: A, B, and C denote flowslide volume, Slope angle, and height, respectively.

where (S/N) denotes the signal-to-noise ratio; n denotes the repeatable time of each variable combination; Y_{1j} denotes the observed data of evaluation index; i denotes a different evaluation index, and j is the test number from 1 to n.

It is necessary to establish an evaluation index to analyze the influencing factors of flowslide deposit morphology by the Taguchi method, because the deposit morphology of flowslide (Figure 4(a)) can be characterized by five elements, maximum length (L_d), maximum width (W_d), maximum thickness (D_d), area (A), and length-width ratio (L_d/W_d) denoted by Y_{1j}, Y_{2j}, Y_{3j}, Y_{4j}, and Y_{5j}, respectively. The five indexes used as evaluation indexes along with statistical results and signal-to-noise ratio calculation results are shown in Tables 2 and 3.

It can be seen from Table 3 that when the volume is 5.4×10^{-3} m^3, the slope angle is 70°, the slope height is 0.9 m, and the signal-to-noise ratio values of L_d, W_d, and A are the largest: 40.55, 40.49, and −0.6, respectively. Therefore, under the influence of this combination, the change responses of L_d, W_d, and A are the largest. It can also be seen that when the volume is 5.4×10^{-3} m^3, the slope angle is 50°, the slope height is 1.1 m, and the change response of D_d is the largest. When the volume is 1.8×10^{-3} m^3, the slope angle is 60°, the slope height is 0.9 m, and the change response of (L_d/W_d) is the largest. Based on a comprehensive comparison of a combination of influencing factors $A_3B_3C_2$—namely, when the volume is 5.4×10^{-3} m^3, the slope angle is 70°, and the slope height is 0.9 m—the change response of the flowslide deposit morphology is the largest.

3.2. Morphology of the Flowslide. The calculation results of the Taguchi method and multivariate analysis of variance both indicate that slope angle has the greatest influence on the deposit morphology of flowslide. To further analyze the morphology of flowslide under the change of slope angle only, an experiment using four sets of sandboxes with a constant volume of 3.6×10^{-3} m^3, a constant slope height of 0.9 m, and slope angles of 40°, 50°, 60°, and 70° was carried out (Figure 4(b)).

(1) Analysis based on Taguchi method: According to the signal-to-noise ratio values of different combinations determined using equation (1) as listed in Table 3, the values of the maximum minus minimum (extreme difference) of the signal-to-noise ratio between the three levels under the same factor are obtained (Table 4) and shown in Figure 5. The bigger the extreme difference value of the influencing factors, the greater the influence of this factor on the results [26, 28].

The results show that the values of extreme difference of L_d, D_d, A, and (L_d/W_d) are 2.77, 5.51, 4.54, and 1.7, respectively. The largest value reflects the influence of slope angle as compared with other factors. The next largest value of extreme difference reflects the influence of flowslide volume. The value of extreme difference as influenced by slope height is relatively the smallest. The value of W_d is most affected by volume; the corresponding value of extreme difference is 2.78. In summary, the most significant factor affecting the deposit morphology of flowslide is slope angle, followed by volume and slope height.

(2) Multivariate analysis of variance: To further verify and analyze the impact of flowslide volume, slope angle, and slope height on deposit morphology, a multifactor analysis of variance is conducted on five evaluation indexes influenced by the three factors (Figure 5); the statistical results are shown in Table 5. Partial η^2 (the ratio of the within-group variance to the overall variance of an independent variable) indicates the significance of the effect caused by the influence factor, where the larger the value, the more obvious the effect of the influence factor. The results of multivariate analysis of variance are consistent with the calculation results of the Taguchi method. The values of L_d, D_d, A, and (L_d/W_d) corresponding to the biggest partial η^2 are 0.64, 0.79, 0.56, and 0.73, all as a result of the effect of slope angle, while for W_d, the biggest value is 0.87, which is the effect of volume of the flowslide. Similarly, the value of partial η^2 under the influence of slope height is relatively the smallest among the five evaluation indexes, which are 0.1, 0.24, 0.45, 0.06, and 0.05, respectively. Therefore, slope angle is the factor that has the greatest influence on the deposit morphology of flowslide, followed by volume and slope height.
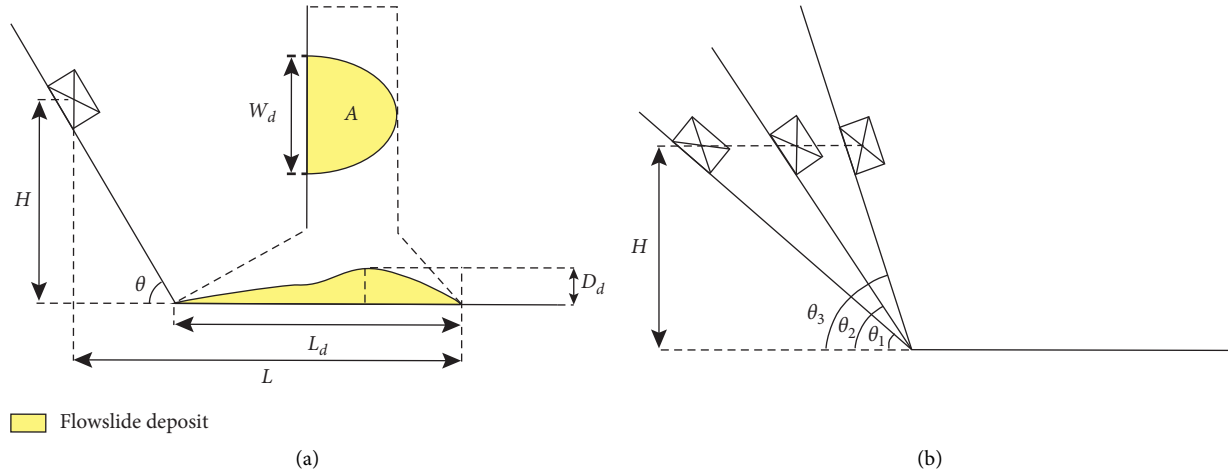
FIGURE 4: Schematic illustration of devices: (a) The flowslide deposit characteristics; L_d Maximum sliding length of flowslide deposit on the surface; W_d Maximum width of flowslide deposit; D_d Maximum depth of flowslide deposit; A Area of flowslide deposit projected on horizontal plane; θ slope angle; H Height of sandbox measuring from center of gravity; L Total sliding distance of flowslide deposit. (b) The process of center gravity constantly.

TABLE 2: Statistics on flowslide deposit morphology.

Orthogonal combination	$Y_{1j}L_d (10^{-2}\text{m})$	$Y_{2j}W_d (10^{-2}\text{m})$	$Y_{3j}D_d (10^{-2}\text{m})$	$Y_{4j}A (\text{m}^2)$	$Y_{5j}(L_d/W_d)(1)$
$A_1B_1C_1$	65.42	61.55	2.88	0.36	0.94
$A_1B_2C_2$	68.33	70.51	1.40	0.43	1.03
$A_1B_3C_3$	74.63	75.01	1.32	0.47	1.01
$A_2B_1C_2$	73.33	52.00	2.79	0.32	0.71
$A_2B_2C_3$	94.13	90.00	1.37	0.78	0.96
$A_2B_3C_1$	79.27	64.51	3.23	0.44	0.81
$A_3B_1C_3$	88.12	67.36	4.29	0.43	0.76
$A_3B_2C_1$	95.08	88.50	2.68	0.71	0.93
$A_3B_3C_2$	105.76	106.50	2.78	0.93	1.01

Note: L_d, maximum sliding length of flowslide deposit on the surface; W_d, maximum width of flowslide deposit; D_d, maximum depth of flowslide deposit; A, area of flowslide deposit projected on horizontal plane; θ, slope angle; (L_d/W_d), length-width ratio.

TABLE 3: The signal-to-noise ratio of elements of deposits morphology.

Orthogonal combination	Signal-to-noise ratio (dB)				
	$L_d (10^{-2}\text{m})$	$W_d (10^{-2}\text{m})$	$D_d (10^{-2}\text{m})$	$A (\text{m}^2)$	$(L_d/W_d)(1)$
$A_1B_1C_1$	35.79	36.31	9.19	−8.76	−0.53
$A_1B_2C_2$	36.97	36.69	2.92	−7.29	0.27
$A_1B_3C_3$	37.5	37.46	2.41	−6.51	0.04
$A_2B_1C_2$	34.32	37.31	8.91	−9.91	−2.99
$A_2B_2C_3$	39.09	39.48	2.73	−2.1	−0.39
$A_2B_3C_1$	36.19	37.98	10.18	−7.08	−1.79
$A_3B_1C_3$	36.57	38.9	12.65	−7.3	−2.33
$A_3B_2C_1$	38.94	39.56	8.56	−2.95	−0.62
$A_3B_3C_2$	40.55	40.49	8.88	−0.6	0.06

Note: L_d, maximum sliding length of flowslide deposit on the surface; W_d, maximum width of flowslide deposit; D_d, maximum depth of flowslide deposit; A, area of flowslide deposit projected on horizontal plane; θ, slope angle; (L_d/W_d), length-width ratio.

3.3. Planar Morphology at Different Angles. After correcting the digital elevation model (DEM) data obtained by the scanner, the three-dimensional coordinates of the flowslide deposit are extracted and the contour maps of the surface morphology are drawn (Figure 6). At smaller slope angles of 40° and 50°, the deposit surface is relatively flat, its long axis lies along the width of the flowslide, and it is generally tongue-shaped. At 40°, the length, width, length-width ratio, and area are 0.53 m, 0.70 m, 0.76, and 0.29 m², respectively. At 50°, the length, width, length-width ratio, and area are 0.89 m, 0.80 m, 1.11, and 0.44 m², respectively, while at larger slope angles of 60° and 70°, the deposits tend to be thickest at

TABLE 4: The main factors of influence.

Morphological elements of deposit	Influencing factors	Level1 (dB)	Level2 (dB)	Level3 (dB)	Extreme difference (dB)	Influence order
L_d (m)	A	36.75	36.52	38.69	2.16	2
	B	35.56	38.33	38.08	2.78	1
	C	36.97	37.28	37.72	0.75	3
W_d (m)	A	36.82	38.25	39.65	2.78	1
	B	37.51	38.58	38.64	1.08	2
	C	37.95	38.16	38.66	0.71	3
D_d (m)	A	4.82	7.28	10.03	5.21	2
	B	10.25	4.74	7.16	5.51	1
	C	9.31	6.91	5.93	3.38	3
A (m^2)	A	−7.52	−6.37	−3.62	3.90	2
	B	−8.66	−4.11	−4.73	4.54	1
	C	−6.27	−5.93	−5.31	0.96	3
(L_d/W_d) (1)	A	−0.07	−1.72	−0.97	1.65	2
	B	−1.95	−0.25	−5.61	1.70	1
	C	−0.98	−0.90	−0.89	0.09	3

Note: A, B, and C denote flowslide volume, slope angle, and height, respectively. L_d, maximum sliding length of flowslide deposit on the surface; W_d, maximum width of flowslide deposit; D_d, maximum depth of flowslide deposit; A, area of flowslide deposit projected on horizontal plane; θ, slope angle; (L_d/W_d), length-width ratio.
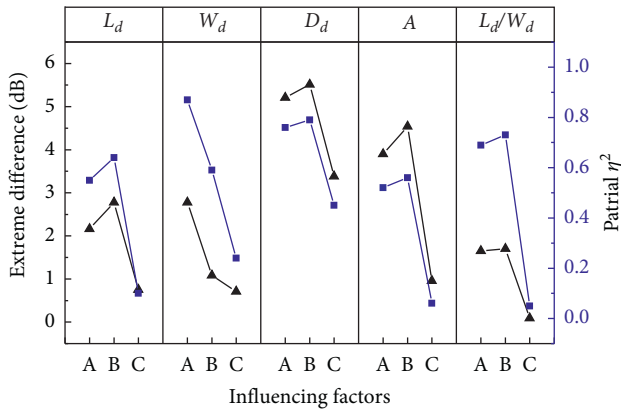

FIGURE 5: Statistical results using Taguchi method and multivariate analysis of variance.

the front and back and are nearly round; upheaval and wash are arranged alternately on the surface. At 60°, the length, width, length-width ratio, and area are 0.90 m, 0.90 m, 1.0, and 0.57 m^2, respectively. At 70°, the length, width, length-width ratio, and area are 0.74 m, 0.75 m, 0.99, and 0.42 m^2, respectively. The morphologies of the flowslides formed at each of the four angles are symmetrically distributed about the sliding central axis.

Comparing the shape of the deposits formed at each of the four angles, we can see that, with an increase in slope angle, the values of L_d, W_d, A, and (L_d/W_d) for the flowslide deposit first increase and then decrease. The main reason is that, by increasing slope angle from 40° to 60°, the sum of kinetic energy loss by the sliding body due to friction and collisional energy loss on the slope break is reduced. However, in increasing the slope angle from 60° to 70°, the sum of the kinetic energy loss and the collisional energy loss increases. In the experiment, the slope height was kept at a constant value of 0.90 m to each of the four angles, so the initial potential energy was the same for each (Figure 4(b)).

The smaller the slope angle, the greater the moving displacement of the sliding body on the inclined plate, resulting in greater kinetic energy loss caused by friction. When the flowslide flows to a slope break where there is a change in the direction of motion to a horizontal direction, and kinetic energy loss will inevitably occur; kinetic energy loss is positively related to the slope angle [32]. Under the condition of changing angles, the increase in the length of the flowslide deposit is significantly higher than the width. This is explained by the feature of straightness [33], which the flowslide has during high-speed movement.

These laboratory findings can be examined in the context of flowslides that occurred naturally. In Xihetan, Shaanxi province, China, a low-angle flowslide deposit formed at a 45° slope angle and had a length of 289 m, a width of 329 m, and a length-width ratio of 0.88 (Figure 7). Another low-angle deposit formed in Shenzhen, China [34, 35], on a slope angle of 24° with a length of 700 m, a width of about 550 m, and a length-width ratio of about 1.27 (Figure 8). A large slope angle (more than 60°) slide on the steep cliffs along the coast of Northern Europe is shown in Figure 9. The following are shown: in Figure 9(a), the deposit with a length 330 m, in Figure 9(b), the deposit with a length 150 m, in Figure 9(c), the deposit with a length 150 m and width 120 m, in Figure 9(d), the deposit with a length 270 m and width 300 m, all of these deposits with a length-width ratio close to 1, alternating upheaval and wash on the surface of the deposit, and an overall circular shape (Figure 9) [36, 37]. The actual flowslides at small angles and large angles are similar to the deposit morphology and state of motion formed during the current experiment. However, due to the difference in topography and the scale of the actual flowslides, it is difficult to compare in terms of dimensional parameters, such as the length and width of the deposit, leaving the dimensionless length-width ratio, surface morphology, and overall shape for comparison. In both the natural and the modeled deposit morphology, a flat surface and a generally

TABLE 5: Variance analysis statistics.

Morphological elements of deposit	Factors	Quadratic sum	DOF	Mean square error	Partial η^2
L_d (m)	A	686.28	2	343.14	0.55
	B	987.32	2	493.66	0.64
	C	59.7	2	29.85	0.1
	Error	564.58	2	282.29	
	Total	2297.87	8		
W_d (m)	A	1083.03	2	541.51	0.87
	B	224.48	2	112.24	0.59
	C	48.97	2	24.49	0.24
	Error	158.35	2	79.17	
	Total	1514.83	8		
D_d (m)	A	2.89	2	1.44	0.76
	B	3.42	2	1.71	0.79
	C	0.73	2	0.37	0.45
	Error	0.91	2	0.45	
	Total	7.95	8		
A (m^2)	A	0.11	2	0.06	0.52
	B	0.13	2	0.07	0.56
	C	0.01	2	0	0.06
	Error	0.11	2	0.05	
	Total	0.36	8		
(L_d/W_d) (1)	A	0.04	2	0.02	0.69
	B	0.05	2	0.03	0.73
	C	0	2	0	0.05
	Error	0.02	2	0.01	
	Total	0.11	8		

Note: L_d, maximum sliding length of flowslide deposit on the surface; W_d, maximum width of flowslide deposit; D_d, maximum depth of flowslide deposit; A, area of flowslide deposit projected on horizontal plane; θ, slope angle; (L_d/W_d), length-width ratio.

tongue-shaped deposit form at low angles, while alternating upheaval and wash on the deposit surface and a generally circle-shaped deposit form at large angles.

3.4. Profile Morphology at Different Angles. Multidimensional analysis of the morphology of flowslide deposit can help researchers gain a deeper understanding of morphology characteristics. Figure 10 shows the profiles of the four flowslides depicted in Figure 6. Combining the profile (Figure 10) with planar morphology (Figure 6), it can be seen that, at smaller slope angles of 40° and 50°, a generally single upheaval with heights of 0.027 m and 0.018 m can be recognized with corresponding peak positions of 0.28 m and 0.50 m, respectively, although the surface of each deposit is slightly undulated. The position of the center of gravity is consistent with the peak position of the upheaval. At larger slope angles of 60° and 70°, the surfaces of the deposits are undulated and there is double upheaval. The maximum height differences between adjacent upheaval and wash are 0.005 m and 0.023 m, respectively. The heights of the front upheaval are 0.009 m and 0.026 m with corresponding peak positions of 0.67 m and 0.40 m, respectively. The heights of the back upheaval are 0.012 m and 0.035 m with corresponding peak positions of 0.10 m and 0.06 m, respectively. The heights of the middle wash are 0.006 m and 0.011 m with corresponding positions of 0.41 m and 0.22 m, respectively. The positions of the center of gravity are relatively consistent with the position of the middle wash.

Comparing the four profiles shows a single upheaval shape at smaller angles of 40° and 50° and a double upheaval shape at larger angles of 60° and 70°. In the flowslides with double upheaval, the height of the front upheaval is smaller than that of the back upheaval. As the slope angle increases, the average thickness of the deposit first decreases and then increases, and the position of the center of gravity first advances and then retreats. Based on the above comparison, it can be considered that there should be a key angle in the change laws of flowslide deposit morphology. If the slope angle is less than or larger than the key angle under the same conditions, the length and width of the deposit will decrease. The key angle is between 60° and 70° under the experimental conditions in the paper. However, actually, the key angle of flowslides should be different values depending on the material of the sliding body and the terrain conditions.

The profile figures of chalk flows [36] on the steep cliffs of the European coast show similarities with the profile morphology of the sandbox experiment for the larger angles, especially the feature of double upheaval (Figures 11 and 12). These two deposits shown in Figures 11 and 12 are 320 m and 200 m in length, respectively. It can be seen from the picture that the leading edge of the flowslide deposit is flat and the surface shows double upheaval. The front upheaval is lower than the back upheaval. The height difference between the middle wash and the back upheaval is greater than that of the front upheaval. The center of gravity is located slightly in front of the middle wash. It is noticed that there is a difference although the morphology of the double
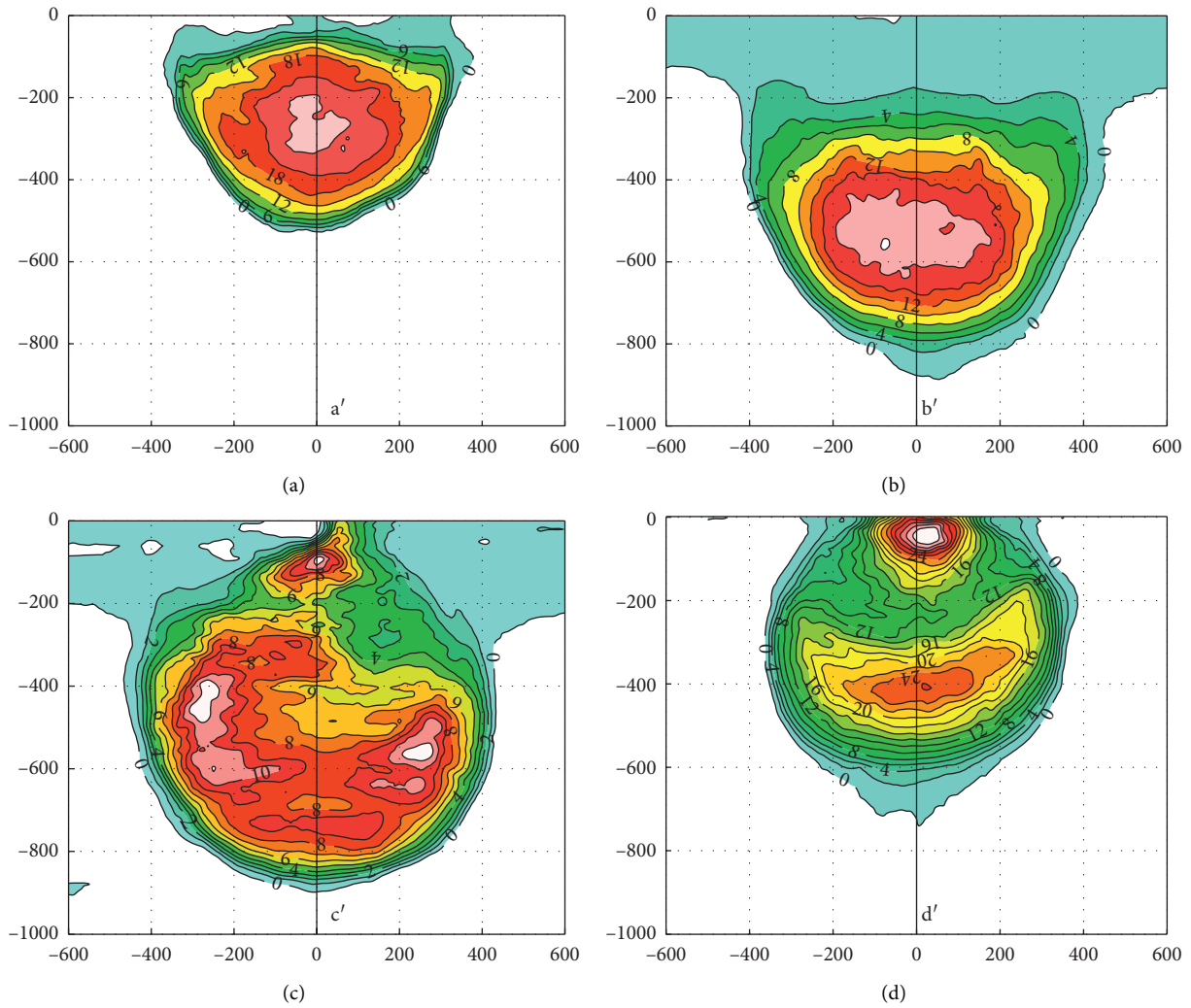
(a)

(b)

(c)

(d)

FIGURE 6: Contour map of flowslides topography at different slope angles: (a), (b), (c) and (d) corresponding to 40°, 50° 60° and 70°, respectively.

FIGURE 7: Xi Hetan flowslide, in China (34°29′32″ N 108°50′13″ E).

FIGURE 8: Shenzhen flowslide. Source: Aerial image form Souhu.com, in China (22°43′04″ N 113°56′31″ E).

upheaval is the same. The center of gravity of flowslide deposit is located in the middle wash in experimental conditions. However, the center of gravity is located in front of the middle wash in actual flowslides. The possible reason mainly is the difference of properties of granular materials, because the movement and accumulation process of flowslides are also affected by internal factors such as the particle size and roundness of sliding body materials [14].

3.5. *Mechanical Analysis of the Deposit Morphology.* Before the mechanical analysis, the properties of the medium-fine sand and plexiglass should be noticed as a basis for this analysis. The friction coefficient 0.727 of the medium-fine sand is larger than 0.538 of the interface of
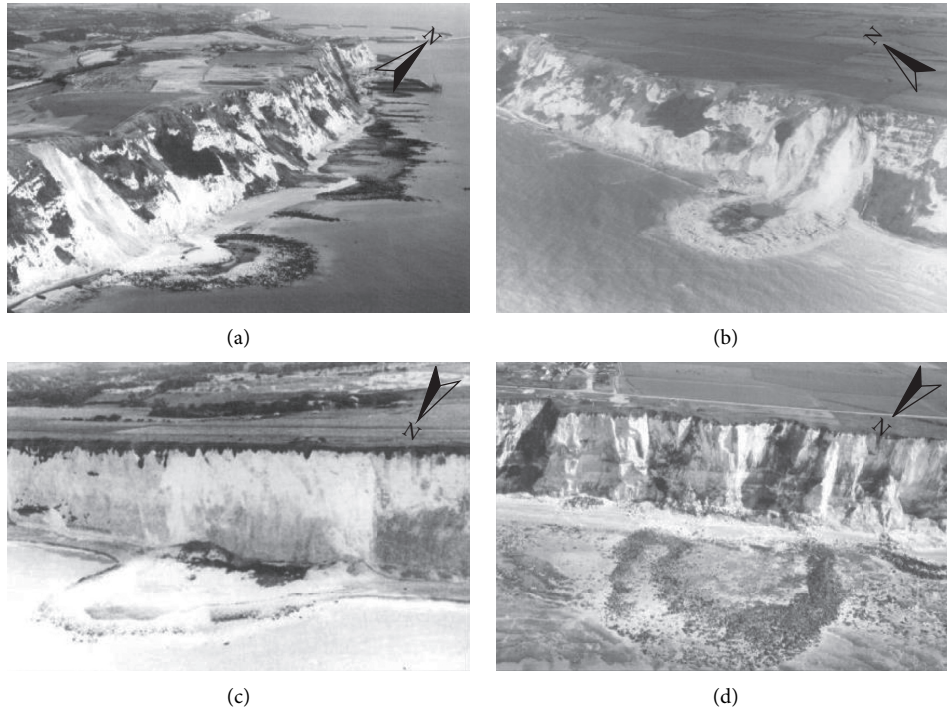
(a)

(b)

(c)

(d)

FIGURE 9: Topography of typical flowslides. (a) and (b) located in Folkestone Warren (51°05′03″ N 1°20′36″ E), (c) and (d) located Dover, Kent (51°07′53″ N 1°20′36″ E). Source from Hutchinson [36].
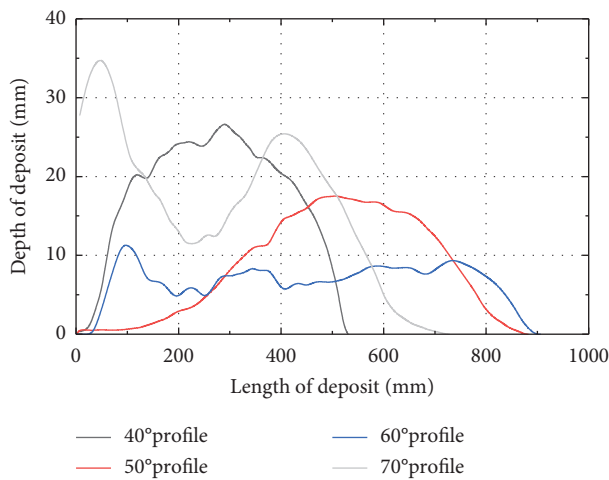
FIGURE 10: The deposit profiles of flowslides at different angles.

FIGURE 11: Flowslide occurred in May 1981 at Le Chien Neuf (49°46′59″ N 0°25′19″ E). Source from Hutchinson [36].

FIGURE 12: Flowslide occurred in May 1958 at Wissower Klinken, Rügen, Germany (54°32′09″ N 13°40′42″ E). Source from Hutchinson [36].

the plexiglass with the medium-fine sand. The difference of the friction coefficient between the interface and the sliding body itself also existed in actual flowslides because the interface will be lubricated by water or the liquefaction effect [30, 38]. Therefore, the sliding body tends to flow along the interface of the plexiglass, and the sand forms a thin sand layer like an erodible bed before the main sliding body arrived on both inclined and horizontal plates [39, 40]. It provides an essential condition of the shear action. Figure 13 shows the cross-sectional state of the sliding body at three phases, in which phase 3, indicated by a solid line, represents the final deposit state of the
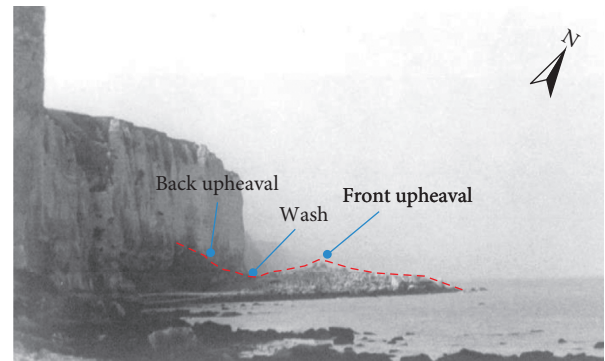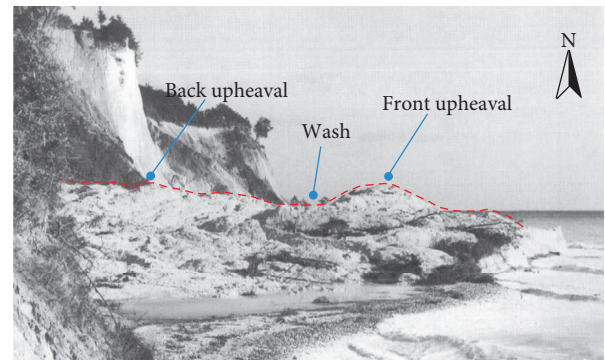
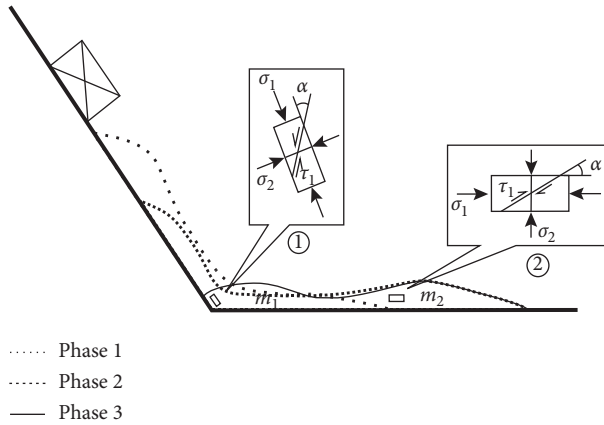...... Phase 1
...... Phase 2
—— Phase 3

FIGURE 13: Schematic illustration of shear force of flowslide.

sliding body. In this paper, the Mohr-Coulomb criterion is used in the analysis of the formation of single and double upheaval as follows:

$$\tau = c + \sigma \tan \varphi. \tag{2}$$

Taking the numbers ① and ② as two microelements in the sliding body, under a stress condition whereby the maximum principal stress σ_1 of the microelement at the slope break is parallel to the direction of the inclined plate and the confining pressure $\sigma_2 = \sigma_3$ is perpendicular to the direction of the inclined plate (the microelements are small enough, so it is considered that $\sigma_2 = \sigma_3$), shear behavior occurs [22, 30, 31].

The angle between the shear plane and the maximum principal stress is defined as $45° - (\varphi/2)$, and the friction angle φ in the sand material is 36°. For a microelement ① at smaller slope angles of 40° and 50°, the counterclockwise angles between the shear action direction and the overall movement direction of the flowslide are 167° and 157°, respectively, tending to horizontal, which is approximately the same as the direction of the maximum principal stress in the state of the microelement ②, which will be a source of power for the morphology of single upheaval. Afterwards, the microelements located on the horizontal plate move along the shear plane at an angle of 27° counterclockwise with the movement direction of the sliding body on the horizontal plate under the obstruction of the other particles in the front and the push of rear particles, similar to a thrust nappe in macroscopic performance, resulting in deposit morphology as a single upheaval.

The formation of double upheaval is more complicated. Here, it will be described according to the order of the front upheaval, the wash, and the back upheaval. First, based on the same calculation method as for the smaller angles, the counterclockwise angles between the shear-action direction of the microelement ① and the movement direction of the sliding body on the horizontal plate are 93° and 83° at the larger slope angles of 60° and 70°, respectively. At this point, the sliding body deposits part of its load under the actions of shear force and thrust force to form a rudiment of the front upheaval, while the part of the sliding body on the horizontal plate keeps moving under the inertial force and the thrust

force of the back part sliding body (the force state is similar to the microelement ②) and continues development of the front upheaval gradually. Next, the microelements at the back of the front upheaval stop their shearing motion when the equilibrium condition of equation (3) is satisfied; climbing is stopped, and the wash is formed. However, mechanical conditions still allow the microelements to move horizontally. When the equilibrium condition of equation (4) is satisfied, the horizontal movement stops. Assuming that the microelements are small enough, the equilibrium condition can be listed as follows:

$$m \cdot g = \tau \cdot \sin\left(45° - \frac{\varphi}{2}\right), \tag{3}$$

$$m \cdot a = \tau \cdot \cos\left(45° - \frac{\varphi}{2}\right), \tag{4}$$

where m is the mass of the microelement, g is the acceleration of gravity, τ is shear stress, a is the horizontal acceleration of the microelement, and φ is the friction angle of sand material.

Eventually, under the balance of equations (3) and (4), the sliding body that is still moving at the trailing edge is very small, as the speed, so the shear force provided can be reduced accordingly. At this time, if the internal shearing force of the sliding body at the trailing edge is greater than the shearing strength of the sliding body, the subsequent sliding body is deposited at the foot of the slope to form the back upheaval and conducts a localized shear motion based on the shear force similar to the microelement ①; however, if the shear force is less than the shear strength of the sliding body, then the sliding body deposits at the slope break to form the back upheaval. In general, the order of the formation process of the double upheaval is front upheaval, wash, and back upheaval.

The formation of double upheaval morphology is also owing to properties of the granular material. In this study, there is a double upheaval morphology; nevertheless, this is not in the study by Hu [14]. The range of the granular particle from 5×10^{-6}m to 4×10^{-4}m in this article is obviously less than the range of the granular particle from 10^{-3}m to 1.6×10^{-2}m in the research by Hu [14]. Therefore, the internal friction angle and cohesion of the experimental material in this study are larger than those in the research by Hu [14]. The more the internal friction angle and cohesion of granular materials are, the more the difficult to disturb the state of the deposit morphology [19] is. When the front upheaval is formed, the granular material with a particle size of 5×10^{-6}m to 4×10^{-4}m is more likely to keep its morphology of the front upheaval in the disturbance of the back sliding body compared with a particle size of 10^{-3}m to 1.6×10^{-2}m. If the backsliding body can not disturb the formed front upheaval, it will accumulate in the slope break forming the back upheaval meanwhile, whereupon the double upheaval is formed.

For these change laws, as the slope angle increases, the maximum width, maximum length, and area of the deposit first increase and then decrease, similar to the results by Hu [14] at the condition of the mass of fine particles changes.

Based on those results, a conclusion was proposed that there is an optimum proportion of fine and coarse particles in the granular materials, because the shear strength and friction coefficient are increasing with the mass of fine particles increases [41, 42]. In the condition that the internal friction angle and cohesion are the smallest, the maximum width, maximum length, and area are maximum. Hence, the deduction mentioned before is reasonable that there should be a critical slope angle in the changes of the deposit morphology.

3.6. Apparent Friction Coefficient. To further understand the rules that govern changes in the apparent friction coefficient with slope angle and the distribution characteristics of the apparent friction coefficient in different lithologies and different regions, the apparent friction coefficients and corresponding slope angle data were collected for research from three places. There are 28 soil flowslides in the Jingyang South platform (34°29′32″ N, 108°50′13″ E), Shaanxi province, China [30], consisting of loess. The accumulation area is the even river terrace, comprised of the loess deposit, underlain by the silty clay deposit with interbedded sand layers occasionally. Along the coast of northern Europe(51°05′03″ N, 1°20′36″ E), there are 27 chalk flows [22] with a porosity ranging from 9% to 52% and dry density ranging from 24.13 to 12.65 kN/m^3. In Wenchuan (31°00′00″ N, 103°40′00″ E), Sichuan province, China [2], there are 44 rock flowslides that occurred in the mountainous area and consisted of the sand-mudstone mainly. The accumulation area is relatively flat though it is hard to compare with flowslides that occurred in Jingyang and coast of northern Europe. An important reason why the above three flowslide groups are taken as research objects is that they have similar flow characteristic and long runout distance. In addition, the topographical condition of the accumulation area is similar to the model test conditions. It can be seen from Figure 14 that the overall relationship between the apparent friction coefficient of flowslide and the slope angles shows a nonlinear growth relationship. This conclusion is consistent with Crosta [22]. The growth relationship is as follows:

$$\frac{H}{L} = \frac{\tan\theta}{1 + \left[(\cos\theta + \varepsilon\sin\theta)^2 \cdot ((\tan\theta/\mu) - 1)\right]}, \quad (5)$$

where θ represents the slope angle; H represents the slope height; L represents the moving distance of the flowslide; ε is the coefficient of velocity restitution when the sliding body reaches the slope break to change its moving direction to horizontal; μ is the friction coefficient.

The difference in regional lithology determines the difference between the friction coefficient μ and the coefficient of velocity restitution ε, so two different μ values and three different ε values are set in this paper. When μ is 0.2 and ε is 0, 0.2, or 0.4, the curve better reflects the overall trend of the three natural flowslide groups. When the friction coefficient, μ, between the inclined plate and the experimental material is 0.55 and ε is 0.4, the curve shows good correlation with the experimental points. It can be said that the friction coefficient determines the height of the initial benchmark of the curve. The larger the value of the friction coefficient, the higher the initial
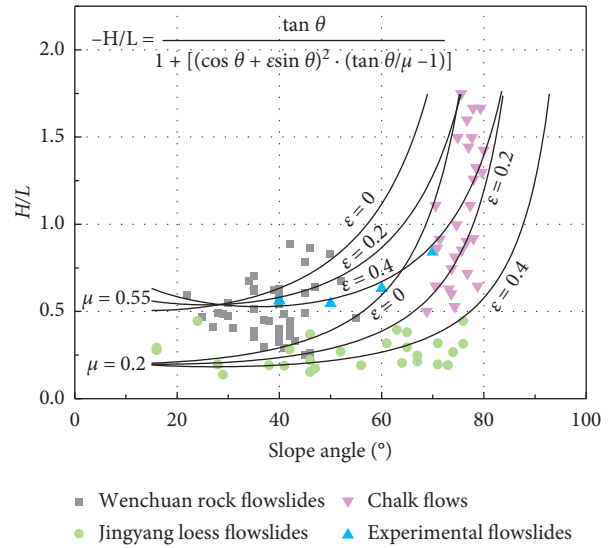

FIGURE 14: Comprehensive relationship between slope angle and apparent friction coefficient. Formula comes from Crosta [22].

benchmark of the curve. The coefficient of velocity restitution determines the change of the inflection point when the curve changes from flat to rapid. The larger the value of the coefficient of velocity restitution, the larger the horizontal coordinates of the inflection point.

From the point of energy conversion, energy loss at the slope break is closely related to terrain and lithology. The kinetic energy loss is small when the junction of slope and the accumulation area is a curved slope break; when the junction has sharp edges, the kinetic energy loss is larger [13, 22]. Under the experimental conditions, in which slope height H and volume are constant, as the slope angle increases, energy loss also increases due to the collision of the flowslide and the horizontal plate at the slope break [43, 44], which results in shorter distance of movement of the sliding body. The slope angle in the chalk flow area is too large, and the energy loss is excessive though the sliding path is lubricated by water beneath the accumulation area 1-2 m. The flowslides in Wenchuan affected by lubrication due to water are few. Besides, there are many obstacles in the movement path because these flowslides are located in a mountainous area though the accumulation area is relatively flat, so energy loss is large. However, for the flowslides in Jingyang, the path is flat and straight as well as lubricated by the liquefied effect [31], and the energy loss is small. The flowslides in the model experiment fall between the three natural flowslide groups, to the left of chalk flows, above loess flowslides, and intersecting with rock flowslides. The apparent friction coefficient in the condition of this model experiment is not the smallest although the condition is ideal flat, for the reason that there are no lubrications. Therefore, the lubrication effect plays a key role in affecting the apparent friction coefficient.

4. Discussion

In this paper, the Taguchi method was employed innovatively to study quantitatively the order of significance

and the maximal responses of combinations of factors affecting flowslide deposit morphology. The calculation results in Figure 5 confirm that slope angle is the most influential factor. The maximum influencing combination is a volume of 5.4×10^{-3} m^3, at a slope angle of 70°, and a slope height of 0.90 m, which will be useful to evaluate the hazards of potential flowslides. Based on the accepted knowledge that slope angle is the largest influencing factor, further experimental research was performed. The conditions of small slope angles and large slope angles show interesting phenomena of single upheaval and double upheaval, respectively; the Mohr-Coulomb criterion is used to explain the action of the shear motion during the process. The comprehensive study of apparent friction coefficient shows a nonlinear increase with slope angle as well as spatial and lithological differences in distribution, which are affected by the friction coefficient and the coefficient of velocity restitution.

Similar model experiments have been carried out to analyze the movement rule of flowslide [4, 12, 21] and deposit morphology [3, 16, 18, 22, 25]. Previous studies focused on the influence of a single factor, and the research content is more in-depth [8, 11, 45, 46], but the research process is not systematic enough, as flowslide movement and deposit morphology are determined by multiple factors, including volume, slope angle, slope height, sliding body material, and slip bed material. Of course, some scholars have conducted multifactor experiments; for example, Manzella [13] studied the influence of flowslide volume, initial height, slope of slip bed, and the slope break on movement characteristics, but the relative significance of various factors governing the movement of flowslide has not been revealed although the factors considered are comprehensive. An orthogonal experiment was used to study the motion characteristics (velocity, acceleration) of flowslide under the influence of various factors and found that slope angle was the largest influencing factor [33], which is consistent with the findings of this article though the research content was different.

The morphology of the double upheaval of flowslide was also observed in an experiment similar to the current study [1], which examined wave propagation in the macroscopic view. That experiment was also carried out with bulk materials. A wave would be formed when the experimental materials slid or fell into the accumulation area; the initial wave would accelerate suddenly as it was pushed by a subsequent wave propagating forward. The wave crest formed when motion stopped due to resistance may be one of the reasons for the formation of upheaval, and the wave trough can be regarded as wash [1] in this paper. According to the motion rule of the object, the flowslide is partially reflected at the slope break [22] and then propagates in the form of waves, which were observed somewhat during the experiment of larger slope angles. Macroscopic wave propagation may be the cause of the formation of upheaval and wash on the surface of flowslide, but if the phenomenon is deeply understood from the interior of sliding body, the internal shear behavior in the movement of flowslide may be reasonable. In addition, the morphology of actual flowslides

is also affected by properties of sliding materials [14, 19, 20]. With an increase of the mass of fine particles, the length and width of the flowslide deposit increase first and then decrease [14]. Therefore, the difference of properties of granular materials is contributing to the formation of the double upheaval.

The apparent friction coefficient is often involved in the study of flowslide, but the focus here is on its relationship with volume [5, 7, 9, 21, 38]. There are few studies that use slope angle as a variable, including Lied and Bakkehoi [47] and Okura [3], both of which proposed that the apparent friction coefficient of flowslide was directly proportional to the slope angle, but the results were based on the analysis of only about 20 flowslides, so the conclusion was limited. The analysis in this paper involved 99 landslides in three areas, and the conclusion is consistent with the viewpoint of Crosta [22] in finding that the apparent friction coefficient increases nonlinearly as the slope angle increases. In the comparison made in this study, spatial and lithological differences in the apparent friction coefficient are also found.

In this paper, an experimental idea of constant height of the center of gravity is provided, but when the angle changes, the sliding distance of the flowslide on the inclined plate (Figure 4(b)) will inevitably increase, and the loss of kinetic energy due to friction will increase accordingly. Therefore, further improvement of the experimental device is needed to reduce the kinetic energy loss due to the increase in the sliding distance on the inclined plate. Modeling should also include more influencing factors.

5. Conclusions

(1) The combined influence factor obtained by the Taguchi method demonstrates that when flowslide volume is 5.4×10^{-3} m^3, the slope angle is 70°, the slope height is 0.90 m, and the changes of deposit morphology of the flowslide is the largest. The extreme differences of maximum length (L_d), maximum thickness (D_d), area (A), and the length-width ratio (L_d/W_d) at three different levels under various factors are 2.77, 5.51, 4.54, and 1.7, respectively. The calculation results indicate that the factor that has the greatest impact on the deposit morphology of flowslide is slope angle, followed by volume and slope height.

(2) With an increase in slope angle, the width, length, area, and length-width ratio of flowslide deposits first increase and then decrease, and the maximum accumulation thickness first decreases and then increases. And, there should be a critical angle in the change laws of the flowslide deposit morphology, that is, between 60° and 70° under the experimental conditions. When the volume is 3.6×10^{-3} m^3 and the slope height is 0.90 m, the slope angles at 40° and 50° both result in a single upheaval, while slope angles of 60° and 70° both result in a double upheaval, which has been explained by shear behavior in the sliding body based on the Mohr-Coulomb criterion.

(3) The apparent friction coefficient of flowslide increases nonlinearly as the slope angle increases and shows spatial and lithological difference. The greater the friction coefficient of the sliding material, the higher the initial benchmark of the curve; the larger the coefficient of velocity restitution, the larger the abscissa corresponding to the position of inflection point when the curve changes from flat to rapid.

Data Availability

The data used to support the findings of this study are available from the corresponding author upon request.

Conflicts of Interest

The authors declare that they have no conflicts of interest.

Acknowledgments

Supplementary Materials

In this section, the data on the slope angles and the apparent friction coefficients are provided as a formation of table. These data are related to 44 rock flowslides in the Wenchuan, Sichuan province, China, 28 soil flowslides in in the Jingyang South platform, Shaanxi province, China, and 27 chalk flowslides along the coast of northern Europe. (*Supplementary Materials*)

References

[1] O. Roche, M. Attali, A. Mangeney, and A. Lucas, "On the runout distance of geophysical gravitational flows: insight from fluidized granular collapse experiments," *Earth Planetary Science Letters*, vol. 311, no. 3-4, pp. 375–385, 2011.

[2] D. Guo, M. Hamada, C. He, Y. Wang, and Y. Zou, "An empirical model for landslide travel distance prediction in Wenchuan earthquake area," *Landslides*, vol. 11, no. 2, pp. 281–291, 2014.

[3] Y. Okura, H. Kitahara, A. Kawanami, and U. Kurokawa, "Topography and volume effects on travel distance of surface failure," *Engineering Geology*, vol. 67, no. 3-4, pp. 243–254, 2003.

[4] Z. Han, Y. Li, J. Huang et al., "Numerical simulation for runout extent of debris flows using an improved cellular automaton model," *Bulletin of Engineering Geology and the Environment*, vol. 76, no. 3, pp. 961–974, 2017.

[5] F. Guzzeti, F. Ardizzone, M. Cardinali, M. Rossi, and D. Valigi, "Landslide volumes and landslide mobilization rates in Umbria, Central Italy," *Earth Planetary Science Letters*, vol. 279, no. 3-4, pp. 222–229, 2009.

[6] J. D. Chaytor, S. Uri, A. R. Solow, and B. Andrews, "Size distribution of submarine landslides along the US Atlantic margin," *Marine Geology*, vol. 264, no. 1-2, pp. 16–27, 2009.

[7] H. Qiu, P. Cui, A. D. Regmi et al., "Influence of topography and volume on mobility of loess slides within different slip surfaces," *Catena*, vol. 157, pp. 180–188, 2017.

[8] J. Hu, J. Peng, G. Wang, I. Javed, Y. Wang, and W. Li, "Distribution and characteristics of landslide in Loess Plateau: a case study in Shaanxi province," *Engineering Geology*, vol. 236, pp. 89–96, 2018.

[9] L. Xu, F. C. Dai, Q. M. Gong, L. G. Tham, and H. Min, "Irrigation-induced loess flow failure in Heifangtai Platform, north-west China," *Environmental Earth Sciences*, vol. 66, no. 6, pp. 1707–1713, 2012.

[10] R. Q. Huang, W. H. Liu, J. P. Zhou, and X. J. Pei, "Rolling tests on movement characteristics of rock blocks," *Journal of Geotechnical Engineering*, vol. 29, no. 9, pp. 1296–1302, 2007, in Chinese.

[11] I. Manzella and V. Labiouse, "Physical modelling to better understand rock avalanches," in *Physical Modelling in Geotechnics, Two Volume Set: Proceedings of the 7th International Conference on Physical Modelling in Geotechnics (ICPMG 2010)*, vol. 2, pp. 1259–1265, Taylor & Francis Group, London, UK, 2010.

[12] G. B. Crosta, F. V. De Blasio, M. De Caro, G. Volpi, S. Imposimato, and D. Roddeman, "Modes of propagation and deposition of granular flows onto an erodible substrate: experimental, analytical, and numerical study," *Landslides*, vol. 14, no. 1, pp. 47–68, 2017.

[13] I. Manzella and V. Labiouse, "Empirical and analytical analyses of laboratory granular flows to investigate rock avalanche propagation," *Landslides*, vol. 10, no. 1, pp. 23–36, 2013.

[14] Y.-X. Hu, H.-B. Li, S.-C. Qi, G. Fan, and J.-W. Zhou, "Granular effects on depositional processes of debris avalanches," *KSCE Journal of Civil Engineering*, vol. 24, no. 4, pp. 1116–1127, 2020.

[15] I. Goktepeli, U. Atmaca, and A. Cakan, "Investigation of heat transfer augmentation between the ribbed plates via Taguchi approach and computational fluid dynamics," *Journal of Thermal Science*, vol. 29, no. 3, pp. 647–666, 2020.

[16] M. Farin, A. Mangeney, and O. Roche, "Fundamental changes of granular flow dynamics, deposition, and erosion processes at high slope angles: insights from laboratory experiments," *Journal of Geophysical Research: Earth Surface*, vol. 119, no. 3, pp. 504–532, 2014.

[17] M. Kesseler, V. Heller, and B. Turnbull, "A laboratory-numerical approach for modelling scale effects in dry granular slides," *Landslides*, vol. 15, no. 11, pp. 2145–2159, 2018.

[18] A. Dufresne and T. R. Davies, "Longitudinal ridges in mass movement deposits," *Geomorphology*, vol. 105, no. 3-4, pp. 171–181, 2009.

[19] T. De Haas, L. Braat, J. R. F. W. Leuven, I. R. Lokhorst, and M. G. Kleinhans, "Effects of debris flow composition on runout, depositional mechanisms, and deposit morphology in laboratory experiments," *Journal of Geophysical Research: Earth Surface*, vol. 120, no. 9, pp. 1949–1972, 2015.

[20] C. Goujon, N. Thomas, and B. Dalloz-Dubrujeaud, "Monodisperse dry granular flows on inclined planes: role of roughness," *The European Physical Journal E*, vol. 11, no. 2, pp. 147–157, 2003.

[21] X.-Y. Fan, S.-J. Tian, and Y.-Y. Zhang, "Mass-front velocity of dry granular flows influenced by the angle of the slope to the runout plane and particle size gradation," *Journal of Mountain Science*, vol. 13, no. 2, pp. 234–245, 2016.

[22] G. B. Crosta, F. V. D. Blasio, M. Locatelli, S. Imposimato, and D. Roddeman, "Landslides falling onto a shallow erodible

substrate or water layer: an experimental and numerical approach," *IOP Conference Series: Earth and Environmental Science*, vol. 26, no. 1, Article ID 012004, 2015.

[23] C. Quantin, P. Allemand, and C. Delacourt, "Morphology and geometry of valles marineris landslides," *Planetary and Space Science*, vol. 52, no. 11, pp. 1011–1022, 2004.

[24] B. K. Lucchitta, "Landslides in valles marineris, mars," *Journal of Geophysical Research*, vol. 84, no. B14, pp. 8097–8113, 1979.

[25] B. K. Lucchitta, "Morphology of chasma walls, Mars," *Journal of Research of the U.S. Geological Survey*, vol. 6, no. 5, pp. 651–662, 1978.

[26] J. J. Wu, Z. W. Xie, Y. L. Huang, and X. M. Wu, "Sensitivity analysis on stress of flexible hinges to design parameters based on Taguchi method," *Journal of Mechanical Strength*, vol. 38, no. 2, pp. 252–258, 2016.

[27] S. D. Kumar, P. R. Vundavilli, A. Mandal, S. Mantry, and M. Chakraborty, "Erosion response of thixoformed A356-5TiB2 in situ composite using Taguchi's experimental design," *Tribology Transactions*, vol. 60, no. 1, pp. 39–46, 2017.

[28] M. Bagci and H. Imrek, "Application of Taguchi method on optimization of testing parameters for erosion of glass fiber reinforced epoxy composite materials," *Materials & Design*, vol. 46, pp. 706–712, 2013.

[29] M. Bagci and H. Imrek, "Erosion wear performance of borax filled novel hybrid composites by using the Taguchi experimental design," *Industrial Lubrication and Tribology*, vol. 68, no. 1, pp. 134–140, 2016.

[30] Z. Duan, W.-C. Cheng, J.-B. Peng, Q.-Y. Wang, and W. Chen, "Investigation into the triggering mechanism of loess landslides in the south Jingyang platform, Shaanxi province," *Bulletin of Engineering Geology and the Environment*, vol. 78, no. 7, pp. 4919–4930, 2019.

[31] P. Ma, J. Peng, Q. Wang, Z. Duan, Z. Meng, and Z. Jianqi, "Loess landslides on the South Jingyang platform in Shaanxi province, China," *Quarterly Journal of Engineering Geology and Hydrogeology*, vol. 52, no. 4, pp. 547–556, 2019.

[32] P. Asteriou, H. Saroglou, and G. Tsiambaos, "Geotechnical and kinematic parameters affecting the coefficients of restitution for rock fall analysis," *International Journal of Rock Mechanics and Mining Sciences*, vol. 54, pp. 103–113, 2012.

[33] R. Q. Huang and W. H. Liu, "In-situ test study of characteristics of rolling rock blocks based on orthogonal design," *Chinese Journal of Rock Mechanics Engineering Geology*, vol. 28, no. 5, pp. 882–891, 2009, in Chinese.

[34] L.-T. Zhan, Z. Zhang, Y.-M. Chen et al., "The 2015 Shenzhen catastrophic landslide in a construction waste dump: reconstitution of dump structure and failure mechanisms via geotechnical investigations," *Engineering Geology*, vol. 238, pp. 15–26, 2018.

[35] C. S. Chen, Q. Q. Li, J. S. Zhu et al., "Formation of the 2015 Shenzhen landslide as observed by SAR shape-from-shading," *Scientific Reports*, vol. 7, no. 1, Article ID 43351, 2017.

[36] J. N. Hutchinson, S. G. Evans, and J. V. Degraff, "Chalk flows from the coastal cliffs of Northwest Europe," in *Catastrophic Landslides*, vol. 15, pp. 257–302, Geological Society of America, Boulder, Colo, USA, 2002.

[37] A. Hénaff, Y. Lageat, S. Costa, and E. Plessis, "Le recul des falaises crayeuses du Pays de Caux:détermination des processus d'érosion et quantification des rythmes d'évolution/ Retreat of chalk cliffs in the Pays de Caux: processes and rates," *Géomorphologie: Relief, Processus, Environnement*, vol. 8, no. 2, pp. 107–118, 2002.

[38] A. Lucas, A. Mangeney, and J. P. Ampuero, "Frictional velocity-weakening in landslides on earth and on other planetary bodies," *Nature Communications*, vol. 5, no. 1, pp. 1–9, 2014.

[39] A. N. Edwards and J. M. N. T. Gray, "Erosion-deposition waves in shallow granular free-surface flows," *Journal of Fluid Mechanics*, vol. 762, pp. 35–67, 2015.

[40] E. D. Fernández-Nieto, J. Garres-Díaz, A. Mangeney, and G. Narbona-Reina, "A multilayer shallow model for dry granular flows with the μ (I) rheology: application to granular collapse on erodible beds," *Journal of Fluid Mechanics*, vol. 798, pp. 643–681, 2015.

[41] J.-J. Wang, H.-P. Zhang, S.-C. Tang, and Y. Liang, "Effects of particle size distribution on shear strength of accumulation soil," *Journal of Geotechnical and Geoenvironmental Engineering*, vol. 139, no. 11, pp. 1994–1997, 2013.

[42] L. J. Su, W. H. Zhou, W. B. Chen, and X. Jie, "Effects of relative roughness and mean particle size on the shear strength of sand-steel interface," *Measurement*, vol. 122, pp. 330–346, 2018.

[43] L.-P. Li, S.-Q. Sun, S.-C. Li, Q.-Q. Zhang, C. Hu, and S.-S. Shi, "Coefficient of restitution and kinetic energy loss of rockfall impacts," *KSCE Journal of Civil Engineering*, vol. 20, no. 6, pp. 2297–2307, 2015.

[44] K. Sharma, S. S. Mallick, and A. Mittal, "A study of energy loss due to particle to particle and wall collisions during fluidized dense-phase pneumatic transport," *Powder Technology*, vol. 362, pp. 707–716, 2020.

[45] H. Qiu, A. D. Regmi, P. Cui, S. Hu, Y. Wang, and Y. He, "Slope aspect effects of loess slides and its spatial differentiation in different geomorphologic types," *Arabian Journal of Geosciences*, vol. 10, no. 15, p. 344, 2017.

[46] C. M. Lo, M. L. Lin, C. L. Tang, and J. C. Hu, "A kinematic model of the Hsiaolin landslide calibrated to the morphology of the landslide deposit," *Engineering Geology*, vol. 123, no. 1-2, pp. 22–39, 2011.

[47] K. Lied and K. Bakkehøi, "Empirical calculations of snow-avalanche run-out distance based on topographic parameters," *Journal of Glaciology*, vol. 26, no. 94, pp. 165–177, 1980.

Research Article

Physical Modeling Test on Deformation and Failure of Rock Slope with New Support System

Zhigang Tao [1,2] **Tongxing Zhang,** [1,2] **Daoyong Zhu,** [1,2] **Weili Gong,** [1,2] **and Manchao He** [1,2]

^{1}*State Key Laboratory for Geomechanics & Deep Underground Engineering, China University of Mining & Technology, Beijing 100083, China*
^{2}*School of Mechanics and Civil Engineering, China University of Mining & Technology, Beijing 100083, China*

Correspondence should be addressed to Zhigang Tao; taozhigang@263.net

In order to explore the monitoring and control method of rock slope, indoor physical model testing of collapse control and monitoring were carried out with the example of a rock slope collapse area project in Jietai Temple in Beijing, China, as the prototype. Based on the similarity theory, in this study, a new structural support with Negative Poisson's Ratio bolt and flexible anchored net was utilized to reinforce the rock slope. Following a graded loading sequence, the collapse failure characteristics and the overall control effect of energy absorption reinforcement measures were explored. The experimental results demonstrated that the entire process of slope collapse presented four distinct stages of failure: fracture generation, fracture propagation, partial collapse, and overall collapse. The full-field displacement nephogram and the displacement monitoring point of the collapse area indicated that the large deformation and failure of the collapsed surrounding rock were effectively controlled, while the Negative Poisson's Ratio bolt and the flexible anchored net had good reinforcement effects. The experimental stress record presented that the change of pressure curve was an apparent regularity in the entire process of slope collapse, which reflects the change state of internal force of surrounding rock; it includes the function of monitoring of slope collapse. It was indicated that the Negative Poisson's Ratio bolt along with the large-deformation flexible anchored net had good reinforcement monitoring effect on the rock slope collapse disaster.

1. Introduction

Under the effects of rainfall, earthquake, and weathering, the strength of rock mass becomes weak, causing the engineering collapse [1–4], which was extremely destructive and with high potential for dangers of tunnel, roadway, and slope [5–9]. The failure of rock slope with multijoints was a kind of prominent geological hazards; its failure mode is complicated, and the treatment is difficult [10–12]. At present, the treatment measures were mainly based on the traditional support methods such as anchorage. Its resistance to slope mass large deformation and anti-impact were poor. Its deficiency was a major scientific problem limiting the on-site safety of the slope. Therefore, it is necessary to conduct in-depth research.

Currently, most of the research studies on slope collapse were on site. Harry used reinforced piles to increase slope stability [13]. Shi et al. utilized prestressed cable bolt and concrete frame to reinforce the collapse of steep-high slope of hydropower station [14]. Dong et al. researched the collapse of high cutting slope with horizontal soft-hard alternant strata and adopted anchorage, bolt-shotcrete for reinforcement [15]. Lin et al. researched reinforcement measures for the high and steep slope with weak rock mass structures with a rock bolt and long anchor reinforcement measures [16]. The treatment method of slope collapse was mainly based on bolt and bolt-shotcrete support; its materials are all common rebar. It has the low deformation characteristics which are difficult to meet the safety requirements of slope treatment. He et al. [17–20] developed a new type of structural bolt; it was used in roadway and slope reinforcement and has achieved good results. The structural bolt called "Negative Poisson's Ratio bolt (NPR bolt)" has ultra-high-energy-absorbing capacity by deforming with an

extraordinarily large elongation at high constant resistance [21]. To sum up, it was found that most of the control and treatment of slope collapse were carried out in the order of pretreatment, emergence, and retreatment. At present, the main indoor research method was physical model test; it has the strong intuitive characteristics, and the qualitative or quantitative analysis that is applied to the rock slope stability analysis [22–25]. Friedmann et al. studied the physical behavior of rock debris flow after collapse by model experiment [26]. Alzo'ubi et al. studied the effect of tensile strength on the toppling failures of the rock collapse by centrifuge test [27]. Bourrier et al. compared and analyzed the rebound model of the rock collapse by simulation test [28]. By means of shaking table tests associated with numerical analyses, Li et al. discussed the effect of seismic wave on response of jointed antidip rock slopes [29]. At present, the physical model test mainly studied the failure mechanism of the collapse, but there was no in-depth study on the collapse support.

This paper takes Jietai Temple in Beijing, China, as the research object. Aiming at the problem of slope collapse, the paper proposes a support method utilizing "NPR bolt + anchored net." On the basis of field application, we carried out the physical model test, the deformation characteristics were studied under the condition of the new support system, and the improved supporting measures and monitoring methods were put forward, which provided a theoretical reference for the comprehensive prevention and control of the multijoint slope.

2. Geological Settings

The geological structure around Jietai Temple in Mentougou, Beijing, China, is complex and rich in minerals, such as clay and limestone. Especially in the last ten years, with the application of modern mining tools, the disturbance of large-scale mining activities to mountain was further intensified, which led to rock mass loosening, local goaf collapses, and cracks.

As shown in Figure 1, Jietai Temple was located at the northern foot of Ma'an Mountain in the southwestern mountainous area of Beijing. Its front was a ridge with a north-south direction, located in the transition zone in-between middle-low mountain and plain, while belonging to the low mountain denudation geomorphic unit. The southern Ma'anshan Mountains were generally nearly east-west, slightly inverse "S" curve, and the ridges were low towards the east and high towards the west. According to regional geological data analysis, the average elevation of the collapse mass was about 46 m, the slope direction is 254°, the slope is about 80°, and the width is about 52 m.

As shown in Figure 2, the upper lithology of the slope area was sandy shale, which belonged to soft rock, with joint fissures in rock mass and thick weathering layer. The range of dangerous rock mass was mainly concentrated on the steep slope surface, with a thickness of approximately 1 m. The slope rock mass structure was unstable and the structural plane was developed. These structural planes cut the rock mass into lump structures, and there were local rock collapses and fell blocks. The lower part was sandstone, with dense and hard

medium-thick layers, which could be utilized as a stable bearing layer; the lithology of the collapse area was mainly sandy shale.

This geological section reflects the typical characteristics of the surrounding rock of the slope in the area around Jietai Temple. The surrounding rock has obvious joint fissures, and the slope is in an unstable state with potential danger of collapse. The construction and design of the model test can better simulate the structural characteristics of the surrounding rock of the slope and greatly enhance the authenticity of the physical model test, which is of representative significance for the study of the slope collapse support in the Jietai Temple area.

3. Model Test

3.1. Model Design

3.1.1. Test Device.
In this experiment, the geological conditions of rocky slope surrounding Jietai Temple in Mentougou, Beijing, were taken as the research background, while the plane stress loading model experimental device of the State Key Laboratory for Geomechanics and Deep Underground Engineering, China University of Mining and Technology-Beijing, was adopted. As presented in Figure 3, the experimental system consisted of main parts, such as main engine structure and hydraulic control platform. The framework size was 3310 mm × 970 mm × 3010 mm, which could accommodate the physical model size of 1600 mm × 400 mm × 1600 mm. Six groups of hydraulic jacks were distributed within each boundary direction. Each hydraulic jack could be pressurized separately. The loading range of modeling the hydraulic cylinder is 0–5 MPa, realizing step-by-step loading of the physical model working face.

3.1.2. Similar Design.
The section size of the site collapse was as follows: length × height = 52 m × 46 m; combining the size of the site collapse and the experimental model, the geometric similarity ratio of the model experiment was finally determined [30, 31]:

$$C_L = \frac{L_p}{L_m} = 30, \tag{1}$$

where L_p are the geometric parameters of the prototype and L_m are the geometric parameters of the model. The similarity ratio of the bulk density was determined through indoor proportioning tests:

$$C_\gamma = \frac{\gamma_p}{\gamma_m} = 1, \tag{2}$$

where γ_p is the bulk density of the prototype; γ_m is the bulk density of the model. Therefore, the stress similarity ratio was finally determined as

$$
\begin{aligned}
C_\sigma &= C_L C_\gamma = 30, \\
C_\varepsilon &= C_f = C_\mu = 1, \\
C_E &= C_\sigma = 30,
\end{aligned}
\tag{3}
$$

where C_ε is the similarity ratio of strain, C_f is the similarity ratio of friction coefficient, C_μ is the similarity ratio of
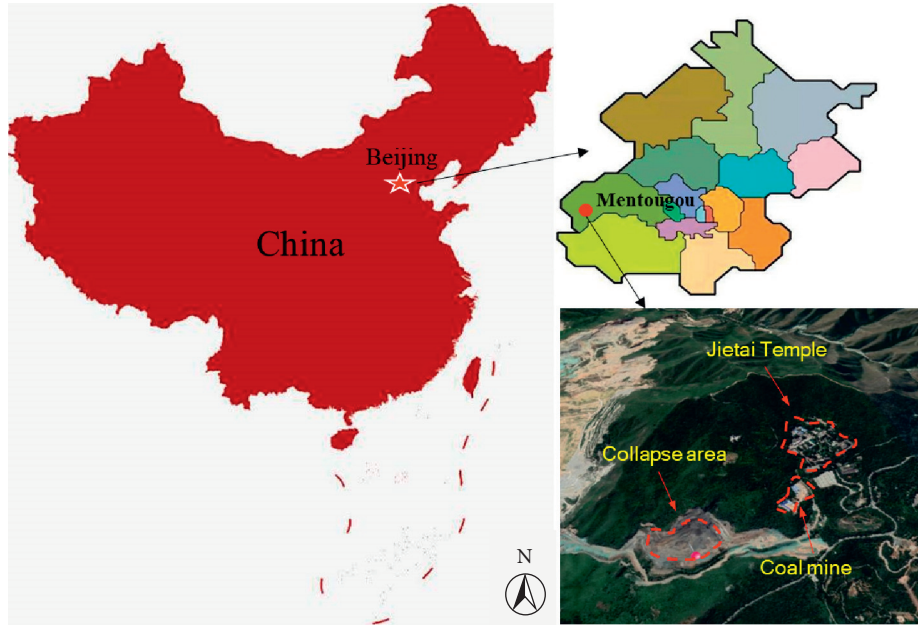
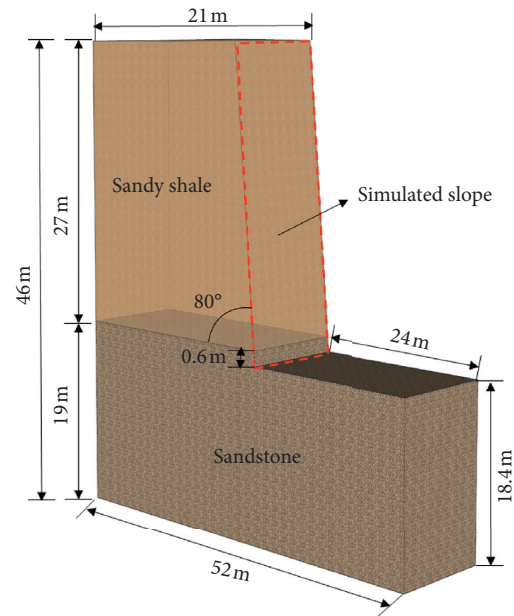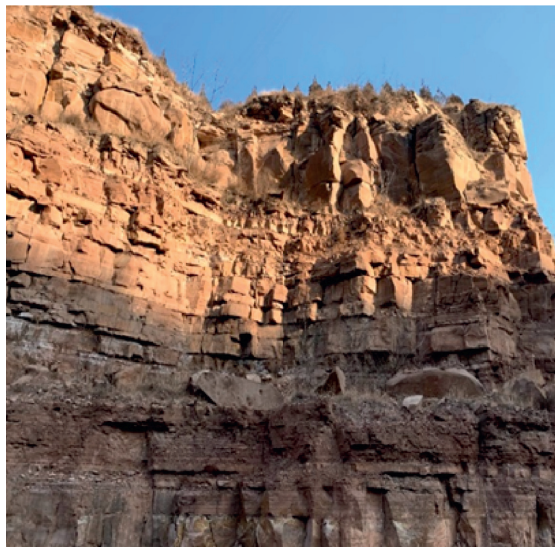FIGURE 1: Location of the Jietai Temple slope.

FIGURE 2: Site slope and model diagram of Jietai Temple.

Poisson's ratio, and C_E is the similarity ratio of elastic modulus.

3.1.3. Slope Model Construction. As presented in Figure 4, the rock strata in the model were laid out by unit plates made of water, gypsum powder, fine river sand, and barite powder. The similar materials mechanics parameters meet the requirements through laboratory rock mechanics experiments, and there were slight differences that could be ignored; the mechanical parameters were presented in Table 1.

As presented in Figure 5, the range of dangerous rock mass was mainly concentrated on the steep slope surface. Combining the actual geological conditions in the field, the structural surface and secondary fracture surface of rock layers were simulated through using the layering of unit plates made of similar materials to restore the real structure of the slope rock. The weak structural plane between each layer of unit plates could be regarded as bedding in the rock mass, and the vertical crack between unit plates could be regarded as joint fissure in the rock mass. The small-size unit plate was utilized to build slope model to simulate the joint-
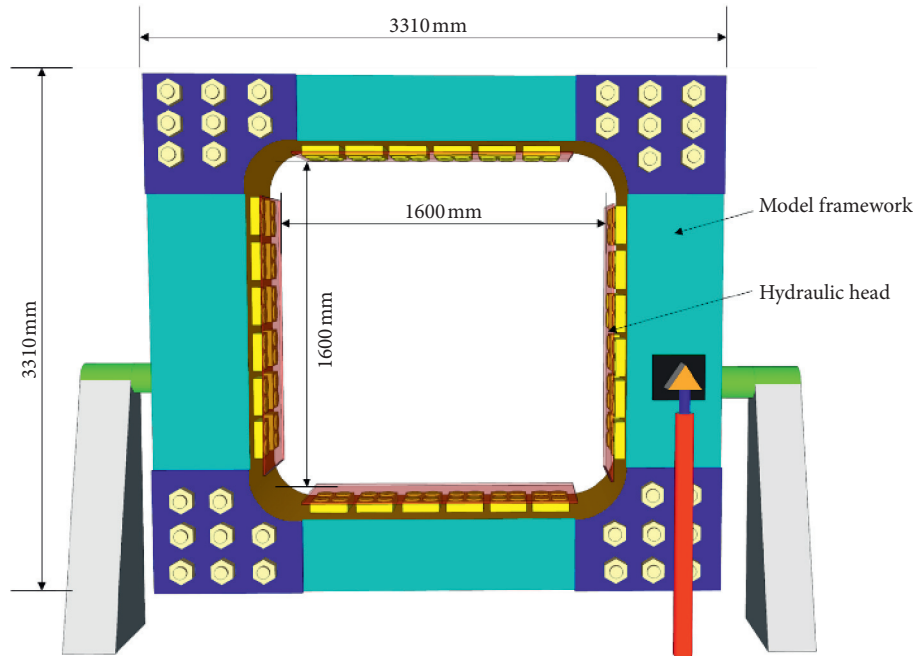
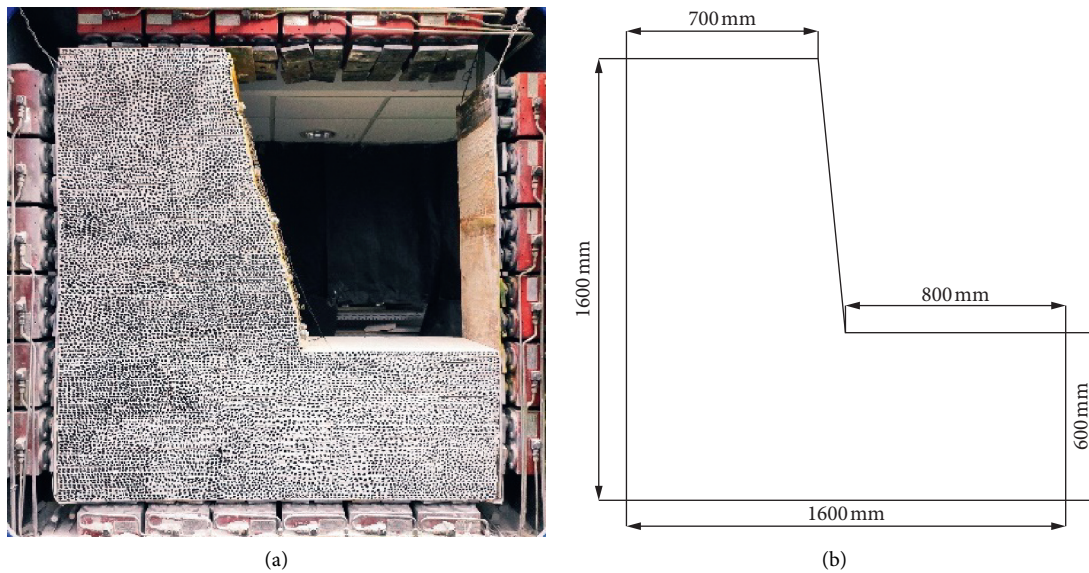FIGURE 3: Plane strain loading experiment device.

(a)

(b)

FIGURE 4: Physical model test diagram: (a) lateral view; (b) model geometry.

intensive area in the slope fractured rock mass zone; the width of the zone was 60 mm.

3.1.4. Load Design. In the first stage, as presented in Figure 6(a), the horizontal pressure $\sigma_x = 0.2$ MPa and the vertical pressure $\sigma_y = 0.2$ MPa were applied to the entire model, while the pressure remained unchanged for 20 minutes subsequently to preloading. In the second stage, as presented in Figure 6(b), the top of the model was continuously loaded step by step, with 0.1 MPa as the loading step, and the horizontal pressure on both sides remained unchanged. Finally, horizontal pressure $\sigma_x = 0.2$ MPa and

vertical pressure $\sigma_y = 0.6$ MPa were applied to the entire model. The entire process lasted 100 minutes in five stages. The experimental loading steps are presented in Figure 6(c).

3.2. Reinforcement Design

3.2.1. NPR Bolt and Its Reinforcing Principle

(1) NPR Bolt Structure. Figure 7 presents the NPR bolt, consisting of a constant cone, a sleeve pipe, a shank rod, a bearing plate, and a tightening nut [32, 33]. The larger end diameter of the cone was slightly bigger than the inner

TABLE 1: Physical and mechanical parameters of rock mass and model materials.

Lithology		Bulk density (kN/m³)	UCS (MPa)	Tensile strength (MPa)	Elastic modulus (GPa)	Internal friction angle (°)	Cohesion (MPa)	Poisson's ratio
Sandy shale	Prototype	25.2	18.6	0.86	18.8	35	9.62	0.19
	Model	25.9	0.68	0.03	0.6	32	0.34	0.14
	Similarity ratio	1	27	29	31	1	28	1
Sandstone	Prototype	26.5	23.8	1.13	25.4	38	12.14	0.26
	Model	27.1	0.81	0.04	0.85	34	0.42	0.23
	Similarity ratio	1	29	28	30	1	29	1
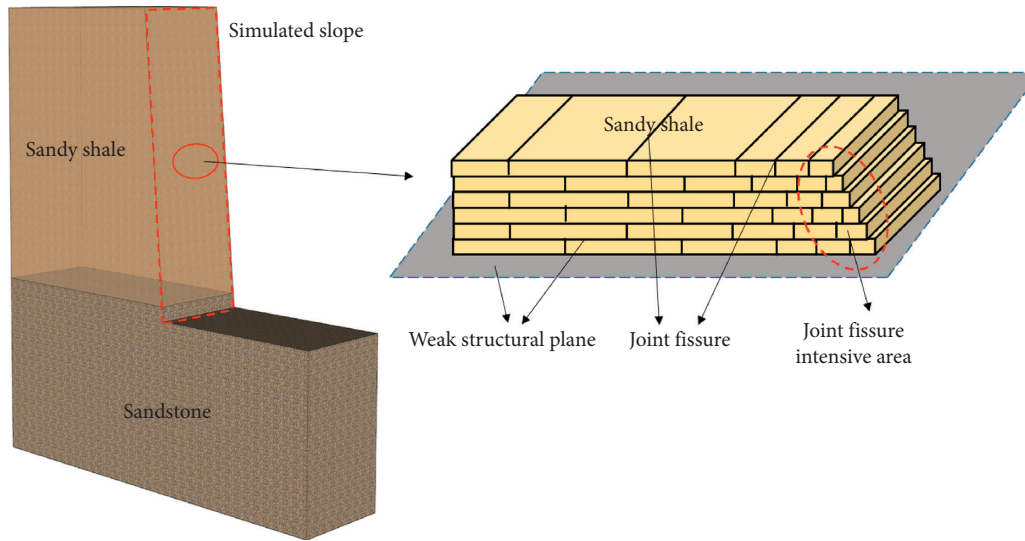
FIGURE 5: Joint fissure simulation diagram of slope model.

diameter of the sleeve pipe. When the cone and the sleeve pipe slip were relative to each other, the frictional resistance (such as the working resistance of the bolt) was generated. The inner surface of the sleeve pipe was screw thread structure, which increased friction along with the cone. When the axial external load (tension) acted in the opposite direction to the anchored end on the working bearing plate, the sleeve pipe displacement was relative to the cone, while the NPR bolt was extended as a whole.

(2) Working Principle of NPR Bolt. Figure 8 presents the NPR static stretch diagram. Its working was divided into three stages. In the elastic deformation stage, when the deformation energy of surrounding rock was low and the axial force applied on the shank rod was lower than the design constant resistance of bolt, the constant resistance device did not move. At this time, the bolt relied on the elastic deformation of the bolt body material to resist the deformation and failure of rock mass. The structural deformation stage, which, with the gradual accumulation of deformation energy of surrounding rock, the axial force applied on the bolt body was higher than or equal to the design constant resistance of the NPR bolt. The cone in the sleeve pipe slid along the inner wall of the casing; the constant resistance was furnished during the slip process, relying on the structural deformation

of the constant resistance device to resist the deformation and failure of rock mass. After the bolt deformation of material and structure, the deformation of surrounding rock could be fully released, while the surrounding rock was again in a relatively stable state. In the destruction stage, the surrounding rock continued to deform, while the displacement of the NPR bolt constant resistance body continued to increase beyond its ultimate tensile length; also, the NPR bolt lost its reinforcing effect.

3.2.2. Model Bolt Design. Due to the large geometric similarity, the model NPR bolt design could only satisfy the similar scale in the length direction, while the dimension of the cross-sectional direction was satisfied as high as possible on the basis of satisfying the mechanical similarity characteristics. Therefore, the length of the designed bolt was

$$L_M = \frac{L_p}{L_m} = \frac{1800}{30} = 60 \, \text{mm}, \tag{4}$$

where L_P is the geometric parameter of the prototype; L_m is the geometric parameter of the model. The mechanical similarity ratio of anchor bolt in experimental design was

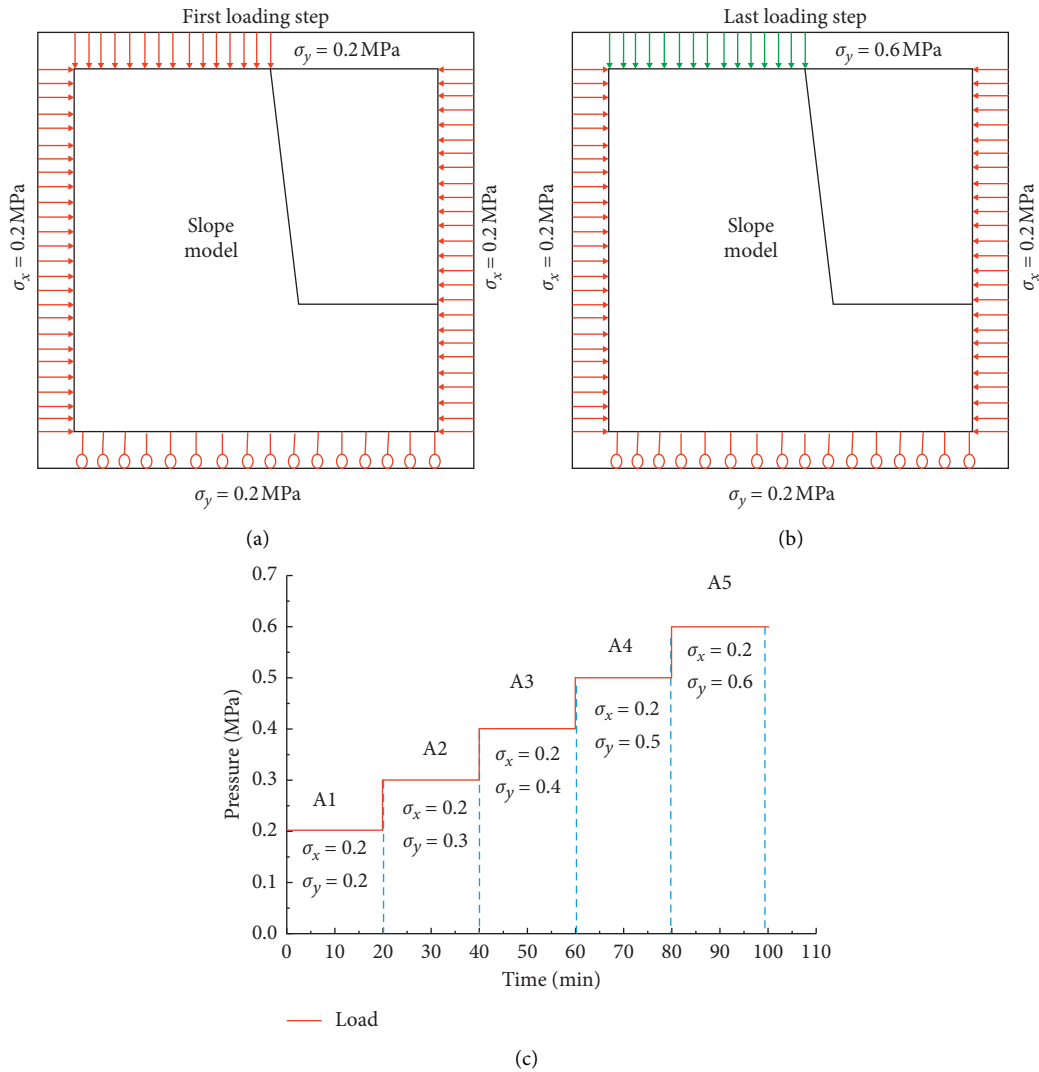$$C_F = C_L^3 C_\gamma = 30^3 \times 1 = 27000, \tag{5}$$

FIGURE 6: Loading path of physical model test: (a) first loading stage; (b) last loading stage; (c) hierarchical loading diagram.
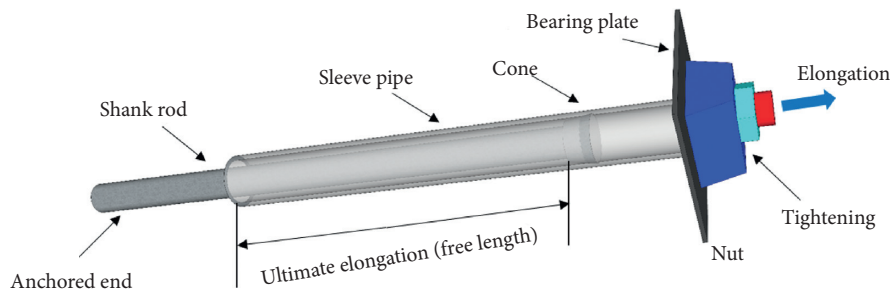

FIGURE 7: Schematic of three-dimensional view of NPR bolt.

where C_L is geometric similarity ratio; C_γ is bulk density similarity ratio. Therefore, constant resistance could be obtained as

$$P_M = \frac{P}{C_F} = \frac{160\,\text{kN}}{27000} \approx 6\,\text{N}, \quad (6)$$

Due to the model size limitation, if the reinforcement was carried out according to the calculation results of

similarity ratio, the bolt installation spacing would be too low. Finally, one bolt was determined to replace six bolts. This signified that the constant resistance of the bolt in the design model was

$$P'_M = P_M \times 6 = 6\,\text{N} \times 6 = 36\,\text{N}. \quad (7)$$

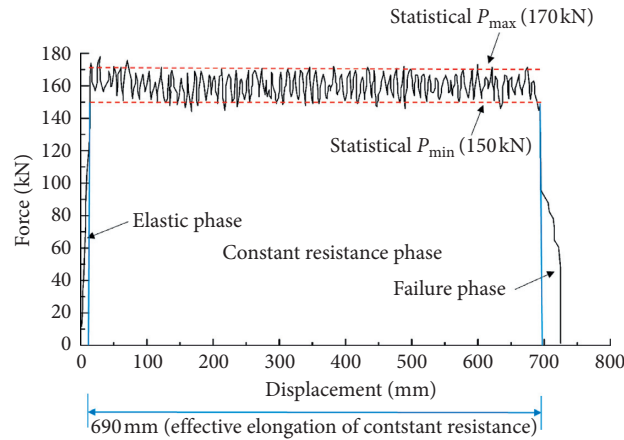The mechanical parameters of engineering-scale NPR bolts and model-scale NPR bolts are presented in Table 2.

FIGURE 8: Static tension diagram of NPR bolt.

TABLE 2: Physical and mechanical parameters of engineering-scale and model-scale bolts.

Bolt type	Length (mm)	Elongation indicator (mm)	Maximum tensile force (N)	Minimum tensile force (N)	Average value (N)
Engineering-scale NPR bolts	1800	700	17000	150000	160000
Model-scale NPR bolts	135	56	43	33	37

Figure 9 presents the NPR bolt model: (1) was a sleeve pipe of 8 mm in inner diameter, the external diameter was 10 mm, and the length was 65 mm; (2) was a cone of 4.8 mm in small end diameter and 8.1 mm in large end diameter. The diameter of the large end was higher than the inner diameter of the constant resistance sleeve, while a small hole mounting rod was left at the top of the cone and the cone was mounted inside the sleeve pipe to form a constant resistance device; (3) was a tightening nut, which was installed at the top of the sleeve pipe, prestressing the NPR bolt; (4) was a bearing plate to transfer prestressing force; (5) was a shank rod, for which one end was connected to the top of the cone, while the other end was anchored to the rock mass. The cone was pulled by the shank rod to produce friction in the sleeve pipe as constant resistance. The model NPR bolt was composed of these five parts. The material of the sleeve, tightening nut, and bearing plate was resin, made through 3D printing SLA (Stereo Lithography Apparatus) technology, which restored the constant resistance reinforcement characteristics of NPR bolt.

Figure 10 presents the static tension curve of the model NPR bolt. It could be observed that bolt reinforcement deformation could be divided into elastic stage, constant resistance stage, and failure stage. Tensile displacement was 2 mm in elastic stage and 55 mm in the constant resistance stage. The maximum resistance of model bolt was 43 N, for which the minimum was 33 N and the average value was 37 N, which was basically the same as the design value of model bolt.

3.2.3. Reinforcement Monitoring Design. Figure 11 presents the reinforcement layout design; a total of 8 bolts were designed to be installed in 5 rows (i.e., rows A, B, C, D, and E), two bolts were installed in rows A, C, and E, and one bolt

was installed in rows B and D, respectively. The pressure sensor was installed between the bearing plate and the tightening nut for whole-course pressure monitoring, while the anchored net was fixed under the bearing plate. The pressure sensor could monitor the pressure change of the bolt in real time.

Figure 12 presents the structure of anchored net; it was made of spiral iron wire. Its static tensile curve was presented in Figure 13. The iron of anchored net could bear the maximum tension of 25 N in the deformation stage of its own structure, while its yield strength was 190 N. When the collapse failure occurred, the anchored net was forced to produce tensile deformation, while absorbing the instantaneous impact force generated through the collapse mass to prevent the anchored net from being destroyed; then the anchored nets were pulled up and deformed. It was extended as a whole and produced "net pocket" effect to encapsulate the falling rocks. Also, it could prevent the falling rocks causing damage.

4. Analysis of Experimental Results

4.1. Failure Process Analysis. Figure 14 presents the stress record of B1 and C1 pressure sensors for the entire loading process of the model slope. Due to the pressure generated after prestressing, it was necessary to reset the pressure sensor to zero so as to observe the pressure change during the test.

According to the stress change of the monitoring curve, the reinforcement could be divided into three stages: the elastic stage, the constant resistance stage, and the failure stage. In the elastic stage, no large deformation exists in the surrounding rock of the slope and the axial force applied on the bolt body was lower than the constant resistance of the
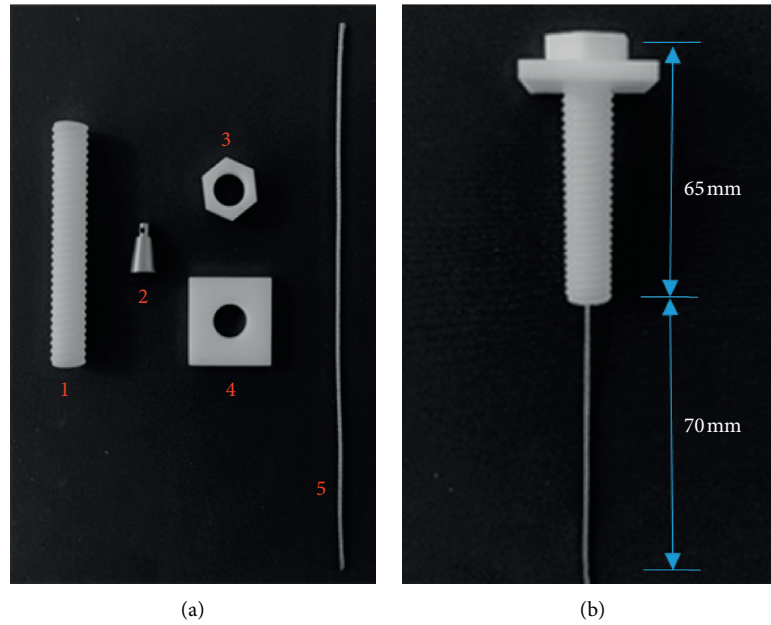
(a)   (b)

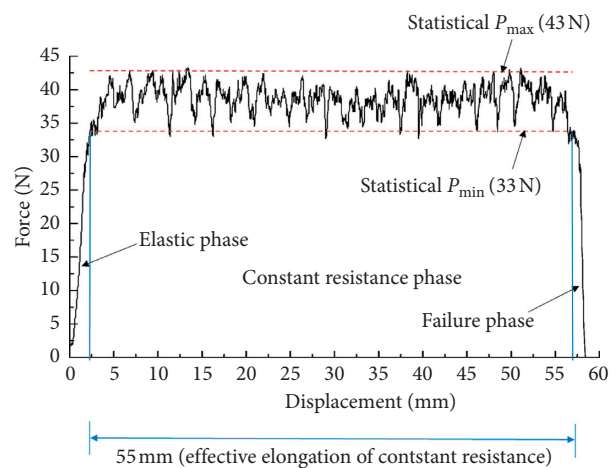FIGURE 9: NPR bolt model: (a) bolt components; (b) NPR bolt assembled.

FIGURE 10: Model NPR bolt static tension curve.

model NPR bolt. The constant resistance device did not slip. The bolt relied on the elastic deformation of the bolt body material to resist the deformation and failure of the rock mass, while the pressure monitoring curve continued to decline. In the constant resistance stage, with the accumulation of deformation energy of the surrounding rock of the slope, the surrounding rock displaced, while the axial force applied on the bolt body was higher than the constant resistance of the bolt. The constant resistance body in the constant resistance device slid. After the deformation of the material and structure of the bolt, the surrounding rock was again in a relatively stable state, while the pressure monitoring curve remained relatively stable for a period of time subsequently to fluctuation. In the failure stage, as the surrounding rock continued to deform beyond its ultimate tensile length, the anchor broke and the pressure monitoring

curve dropped sharply to zero. According to the collapse process of the experimental model, combined with the stress of the monitoring curve, the pressure monitoring curve was divided into five processes, namely, OA, AB, BC, CD, and DE.

The curves AB and BC correspond to the elastic phase of the model NPR bolt. The pressure curve continued to descend and then remained relatively stable, but there was no significant fluctuation, indicating that the axial force applied on the bolt was lower than the constant resistance of the model NPR bolt. The constant resistance device did not slip. The bolt relied on the elastic deformation of the bolt material to resist the deformation and collapse of the rock mass. The curves CD and DE correspond to the constant resistance phase of the bolt. The pressure curve began to fluctuate following a sharp drop and then fluctuated sharply after
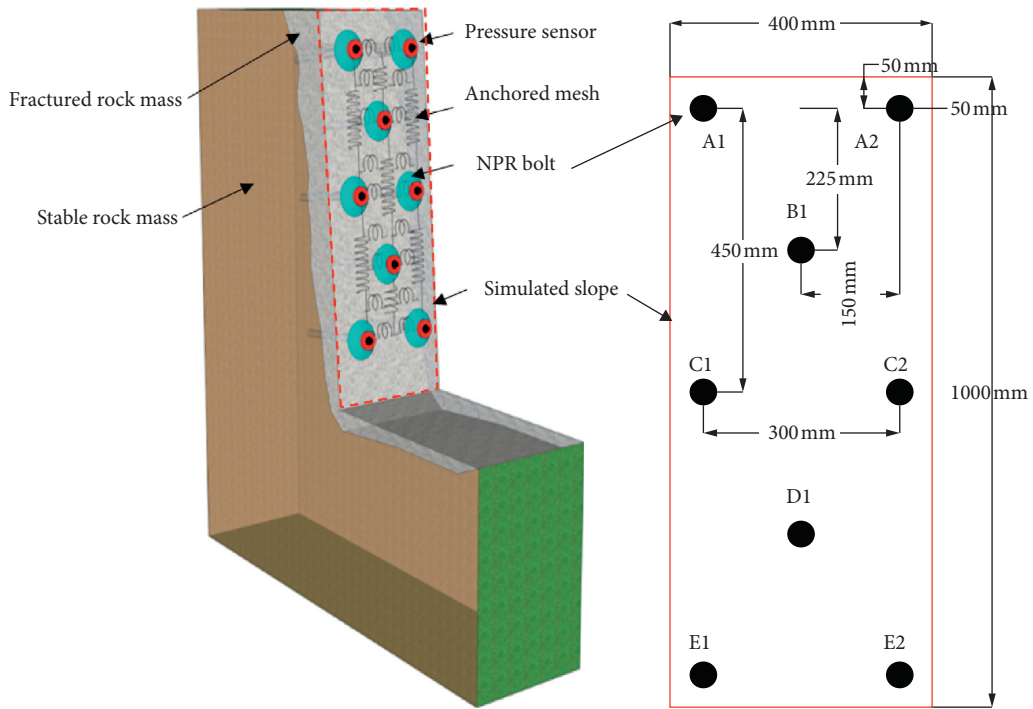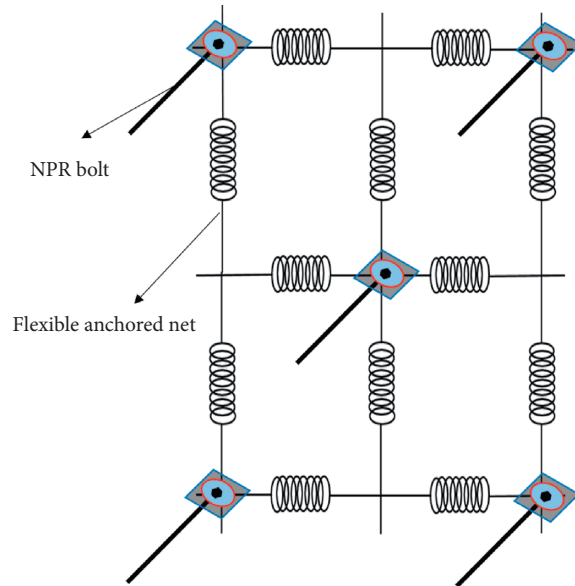
FIGURE 11: NPR bolt support system layout.

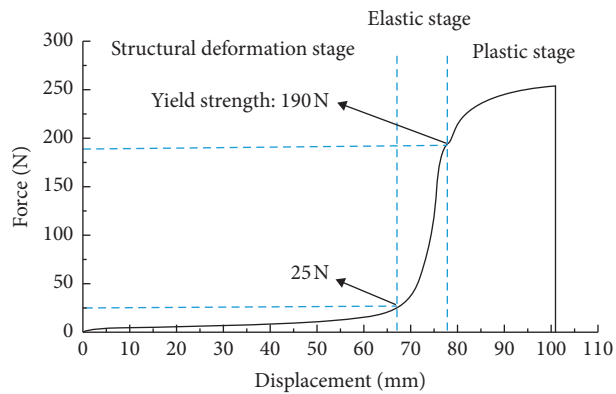FIGURE 12: Anchored net structure support system layout.

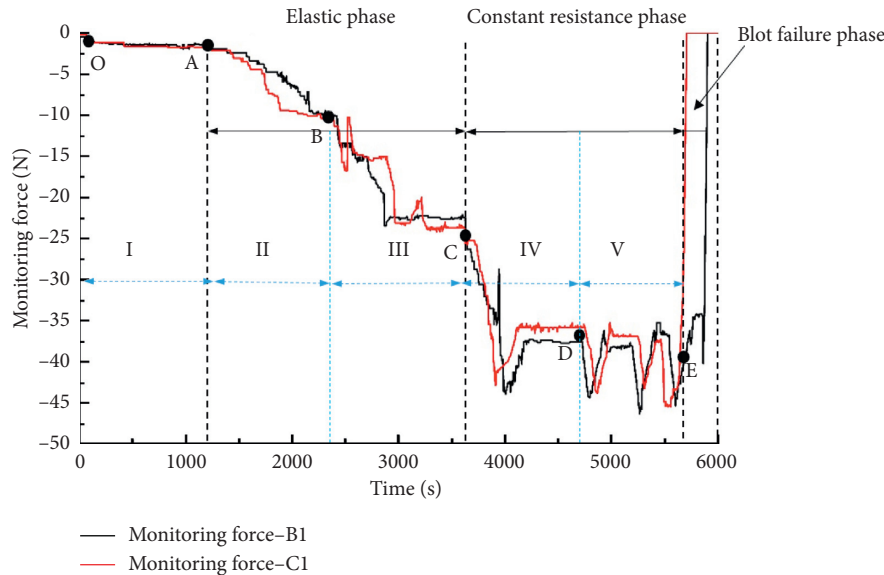FIGURE 13: Static tension curve of the single anchored net.

FIGURE 14: Stress record of the whole test process.

remaining relatively stable for a period of time. It indicated that the cone had slid and the bolt had structural deformation. After the curve point E, the bolt removal stage was corresponding. The pressure curve rises sharply to zero. It presented that the bolt reached its ultimate tensile length; the bolt was broken and lost its function.

Figure 15(a) presents the model picture of compaction stage. The horizontal pressure and the vertical pressure were applied to the model, corresponding to the OA phase of the stress record. At this stage, the model had no apparent change. Small cracks existed in the middle of each layer of the unit plate during the model building stage. When the slope model was pressurized as a whole, the interlayer cracks were gradually compacted and the model became an entity. The record of the section OA presents that the pressure was unchanged basically; this indicated that the slope was stable.

Figure 15(b) presents the model picture of fracture generation stage. The horizontal pressure and the vertical pressure were applied to the model, corresponding to AB section of stress record. At this stage, many microcracks occurred in the model. As presented in Figure 15(b) (i), the vertical microcracks were generated near the slope surface, such as in the red solid line marking position. Many cracks occurred near the slope in the lower part of the model of 1 mm in width. As presented in Figure 15(b) (ii), bulges and cracks existed in the middle and lower parts of the slope, along with small cracks and breakage in other parts, without deformation in the anchored net. The record of section AB presented the continuous increase of pressure. It means that the internal stress of rock mass changed, which was the first stage of slope collapse monitoring.

Figure 15(c) presents the model picture of fracture propagation stage. The horizontal pressure and vertical pressure were applied to the model, corresponding to the BC section of the stress record. As presented in Figure 15(c) (i), the cracks in the upper part of the model section near the slope surface extended to the deep part of the slope; the

maximum width of the cracks was 7 mm, while the width of the cracks in the middle part was 2 mm. Two circular protrusions occurred on the upper surface of the model section; the diameter was 1 to 2 cm. As presented in Figure 15(c) (ii), the upper part of the slope was severely damaged, with the surface spalling within a large area. A low amount of collapse blocks was wrapped by the anchored net, while the anchored net was deformed by punching. A high amount of cracks occurred in the middle and lower parts, while a low amount of surface spalls occurred. From record of section BC, it could be observed that the increase remained stable following a sharp drop. It indicates that the internal stress of rock mass continued to increase, which constituted the second stage of slope collapse monitoring.

Figure 15(d) presents the model picture of local collapse stage. The horizontal pressure and the vertical pressure were applied to the model, corresponding to the CD section of the stress record. At this stage, the upper part of the model collapsed and the entire model was unstable. As presented in Figure 15(d) (i), the cracks in the upper part of the model section near the slope extended to the middle; the widest part of the cracks was 10 mm. A large number of cracks in the upper part of the model had a width of 1–5 mm. There are 5 circular bulges with a diameter of 1–5 mm in the upper part of the slope. As presented in Figure 15(d) (ii), the upper and middle parts of the slope collapsed, resulting in large pieces of collapse peeling off and wrapping by anchor mesh, leading to severe deformation of the anchored net. The collapse in the lower part of the model was lighter than that in the upper part; the surface spalling within a large area and the anchored net produced a low amount of deformation. The record of section CD presents that the pressure curve rose slightly after a sharp drop and then remained stable; it means that the NPR bolt began to produce structural deformation.
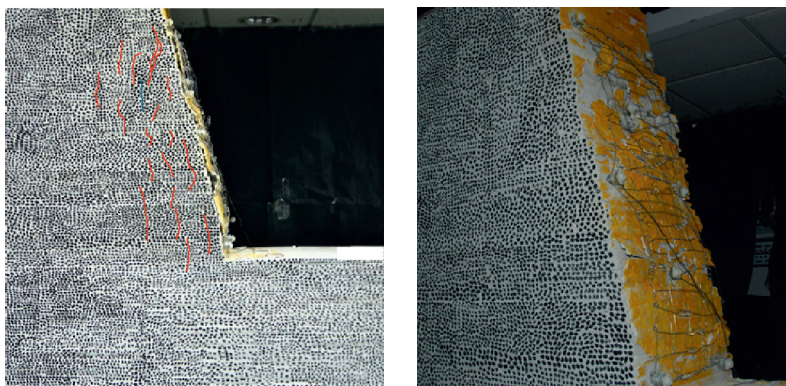
Figure 15(e) presents the model picture of the entire collapse stage. The horizontal pressure and vertical pressure
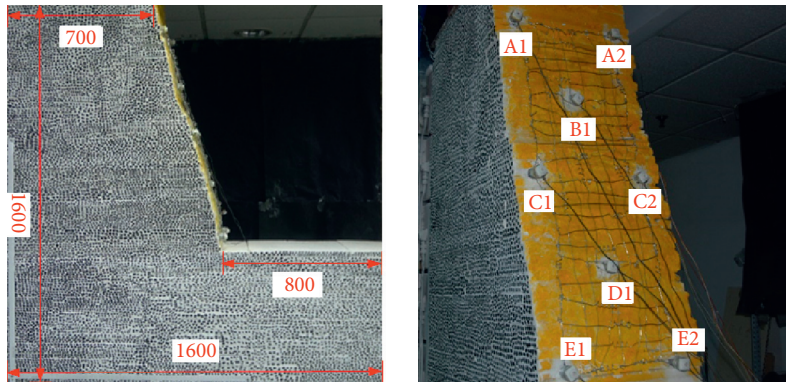
(a)
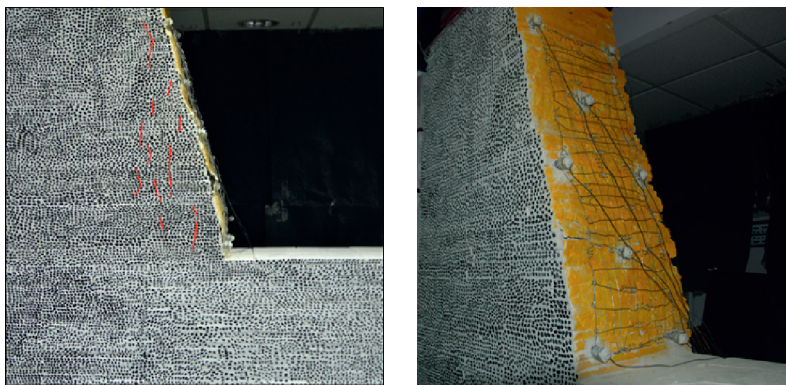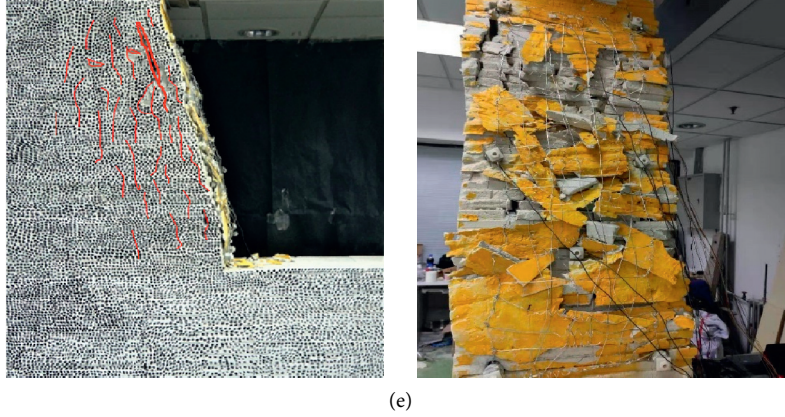
(b)

(c)

(d)

Figure 15: Continued.

(e)

FIGURE 15: . Photograph of model collapse process: (a) compaction stage: (i) lateral view and (ii) side view; (b) fracture generation stage: (i) lateral view and (ii) side view; (c) fracture propagation stage: (i) lateral view and (ii) side view; (d) local collapse stage: (i) lateral view and (ii) side view; (e) entire collapse stage: (i) lateral view and (ii) side view.

were applied to the model, corresponding to the DE section of the stress record. At this stage, the model occurs the large area collapse. As presented in Figure 15(e) (i), the cracks in the upper part of the model section extended around the slope with a maximum crack width of 15 mm. Also, a high amount of cracks occurred in the middle and upper parts of 1 mm to 5 mm in width, while a low amount of spalling occurred on the upper surface. As presented in Figure 15(e) (ii), the entire slope was collapsed; in addition, serious deformation occurred on the slope, and a large amount of collapse spalling was wrapped by the anchored net. This led to severe deformation of the anchored net. It could be seen from the CD segment record that the pressure fluctuates with a high frequency; it presented that the NPR bolt continued to produce structural deformation.

4.2. Digital Speckle

4.2.1. Principle.
In this model experiment, the MTI-2D digital image measurement system was utilized to quantify the full-field displacement [33–35]. This system was also called noncontact strain measurement and parameter reverse analysis system. It was composed of MTI-2D two-dimensional measurement and simulation optimization analysis software, AVT-CCD industrial camera, and lighting system (halogen lamp or LED), along with fixture and calibration board. The two-dimensional measurement and simulation optimization analysis software constituted the postprocessing software of the system, used to process the acquired image information. The image acquisition control software was connected to the industrial camera through a computer device to perform real-time image acquisition on the experimental target. The industrial camera had a maximum resolution of 5 million pixels and a frequency of ≥ 30 Hz. The displacement pixel accuracy measured by the system was 0.001–0.01, the displacement resolution was 0.1 μm, and the strain resolution was 20–50 $\mu\varepsilon$, while the strain measurement range was 0.005%–2000%.

Prior to experimentation, the speckles were made on the model section. The entire speckle pattern had high contrast, high anisotropy, and nonrepetition [36]. The basic principle of the system was to use the scattered spots randomly distributed on the surface of the model as the information carrier. Contrast analysis of the speckle pattern provided information, such as the displacement field.

The center point coordinates of a surface of an object were let to be $P(x, y)$ and any point of $Q(x_i, y_i)$ nearby. When the object was deformed, the corresponding coordinates of two points were $P'(x_0', y_0')$ and $Q'(x_i', y_i')$.

P' and P had the following relationships:

$$\begin{aligned} x_0' &= x_0 + \mu, \\ y_0' &= y_0 + v. \end{aligned} \tag{8}$$

Q and Q' had the following relationships:

$$\begin{aligned} x_i' &= x_i + \mu_Q, \\ y_i' &= y_i + v_Q, \end{aligned} \tag{9}$$

where μ and v represent the displacement components of point P on the x- and y-axes, respectively; μ_Q and v_Q represent the displacement components of point Q on the x- and y-axes, respectively.

Let the gray scale of point p prior to and following deformation be

$$\begin{aligned} f(Q) &= f(x_i y_i), \\ g(Q') &= g(x_i', y_i'). \end{aligned} \tag{10}$$

It could be concluded that

$$\begin{aligned} \mu_Q &= \left(\mu + \mu_x \Delta x + \mu_y \Delta y \right), \\ v_Q &= \left(v + v_x \Delta x + v_y \Delta y \right), \\ \Delta x &= (x_i - x_0), \\ \Delta y &= (y_i - y_0). \end{aligned} \tag{11}$$

Among these, f represents the gray scale function of the image before deformation and g represents the gray scale

function of the image after deformation. $\mu, \mu_x, \mu_y, \nu, \nu_x, \nu_y$ are displacement vectors.

In order to determine the displacement correspondence before and after deformation, $C(f, g)$ is introduced to determine the degree of similarity of the images before and after the displacement as

$$C(f, g) = C(x_i, y_i, x_i', y_i') = C(P). \tag{12}$$

From the above equation, it could be observed that $C(f, g)$ is a function of P and its minimum value was found as

$$\frac{\partial C}{\partial P} = 0. \tag{13}$$

4.2.2. Displacement Nephogram Analysis. Figure 16(a) presents the displacement nephogram of the model compaction stage, in which the direction of horizontal displacement was the same as that of the *x*-axis. As presented in Figure 16(a) (i), the entire model produced low displacement, while the displacement of the top part of the model was apparent. The displacement presented a decreasing trend from the upper part to the middle part of the model, while the displacement of the lower part had no apparent difference. As presented in Figure 16(a) (ii), no apparent difference existed in the displacement. This indicated that the model had reached the compact state. The maximum displacement of the top part of the model was 1.9 mm and the displacement of other areas was 1.3 mm.

Figure 16(b) presents the displacement nephogram of the model fracture generation stage. As presented in Figure 16(b) (i), the horizontal displacement of the model increased significantly, while the displacement from the right side (near the slope) to the left side of the model presented a decreasing trend, while the displacement change region also presented a decreasing trend. As presented in Figure 16(b) (ii), there was a gradual increase of displacement in the central region, while it decreased in the upward and downward directions. The displacement of the middle position of the model was 6.2 mm.

Figure 16(c) presents the displacement nephogram of the model fracture propagation stage. As presented in Figure 16(b) (i), the displacement trend changed highly and the maximum displacement region shifted to the upper part of the model compared to the fracture generation stage, and the horizontal displacement significantly increased. The displacement variation of nephogram was divided into four grades, while the displacement gradually decreased from top to bottom and the displacement increment of the upper part of the model near the slope surface was the highest. As presented in Figure 16(c) (ii), the trend of displacement had no major change in the nephogram compared to Figure 16(b) (i). The displacement growth area of the upper part of the model expanded downwards, especially on the side close to the slope, where the growth was faster and the displacement could be up to 30 mm.

Figure 16(d) presents the displacement nephogram of the partial collapse stage of the mode. As presented in Figure 16(d) (i), the trend of displacement change was lower compared to the fracture propagation stage. As presented in Figure 16(d) (ii), the displacement of the upper part of the model near the slope increased rapidly, while the growth region was extended along the slope to the middle. No apparent change existed in the displacement of the lower part of the model or the upper part of model slope, while the displacement of the model reached 32 mm.

Figure 16(e) presents the displacement nephogram of the overall collapse stage of the model. As presented in Figure 16(e) (i), the trend of displacement change in this stage was lower compared to the local collapse stage, while the displacement change region was mainly concentrated on the upper part of the model near the slope, diffusing outwards. As presented in Figure 16(e) (ii), the horizontal displacement of the model increased slowly, while the area of displacement growth expanded downwards. The maximum horizontal displacement of the upper and middle parts near the slope was 41 mm.

Derived from the displacement cloud map during the model experiment, the horizontal displacement was mainly concentrated on the upper part of the model near the side of the slope. The displacement growth area extends downwards along the side slope, gradually decreasing from top to bottom. The maximum displacement region extended downwards along the slope and the horizontal displacement of surrounding rock reached 41 mm. The maximum increase of displacement was in the fracture propagation stage, but the surrounding rock did not collapse in an instant. In the stage of local collapse and entire collapse, the displacement increased slowly until the overall collapse of the slope.

4.2.3. Displacement Analysis of Monitoring Points. As presented in Figure 17, column A and column B monitoring points were taken parallel to the slope direction in the slope model; the horizontal distance between column A and the slope was 5 cm, while column B was 15 cm. The distance between points A1 and B1 and the top of the slope was 10 cm, and the vertical distance between each monitoring point was 25 cm. The monitoring points were selected to analyze the change rule of horizontal displacement.

The horizontal axis coordinates of the following displacement curves represented pictures of different states corresponding to different moments taken through the speckle system during the entire experiment. Stages I, II, III, IV, and V in the displacement curves represented the model compaction stage, the fracture generation stage, the fracture expansion stage, the partial collapse stage, and the overall collapse stage, respectively.

In Figure 18, it could be observed that the horizontal displacement trends of column A and column B were roughly the same. The horizontal displacement curve of each monitoring point increased apparently, but the displacements of measuring points of A5 and B5 were unchanged. The increasing range of displacement of each monitoring point (except point A2) grew gradually from the bottom to top, especially for monitoring point A2. The fracture expansion stage had a high influence on the
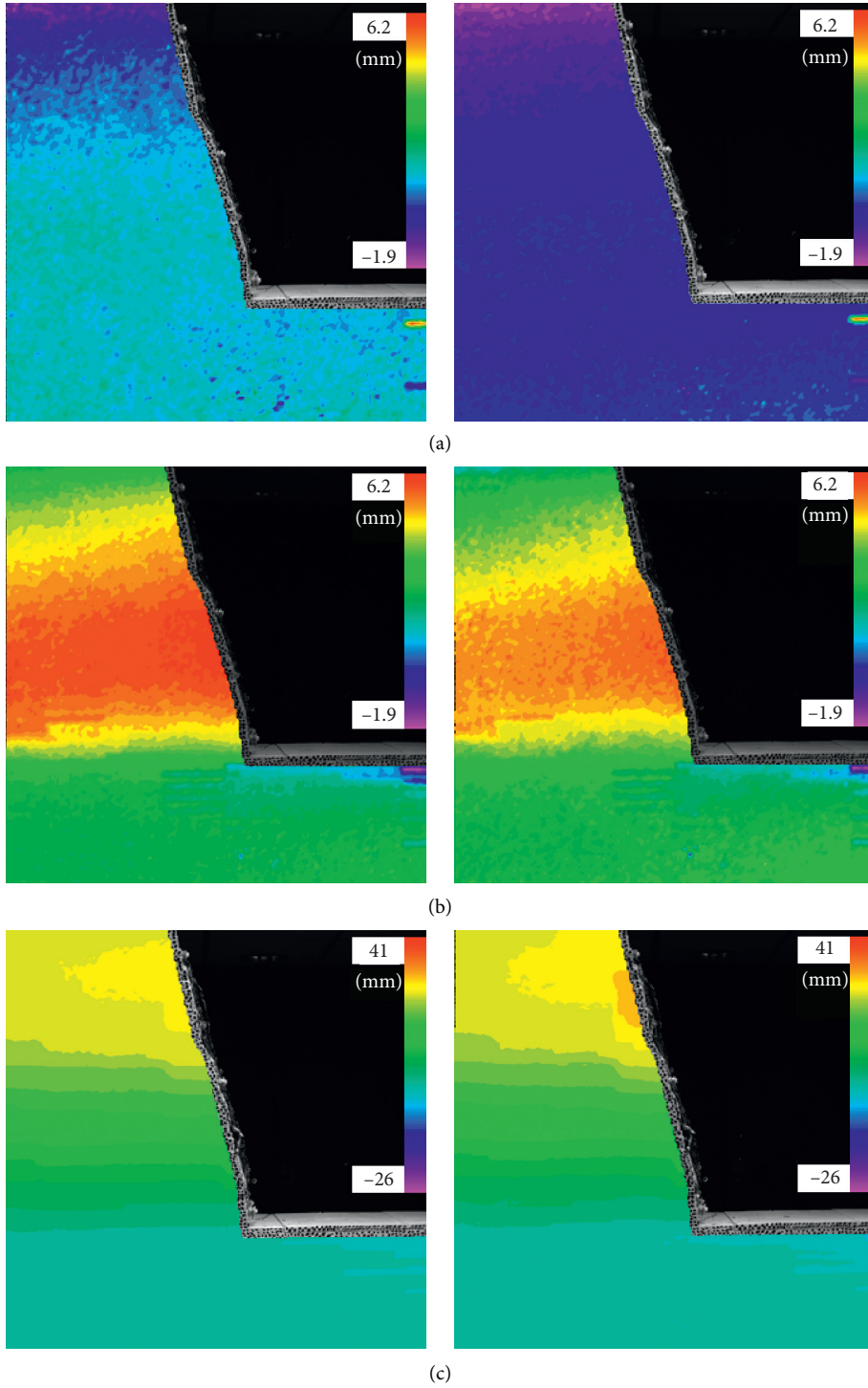
(a)
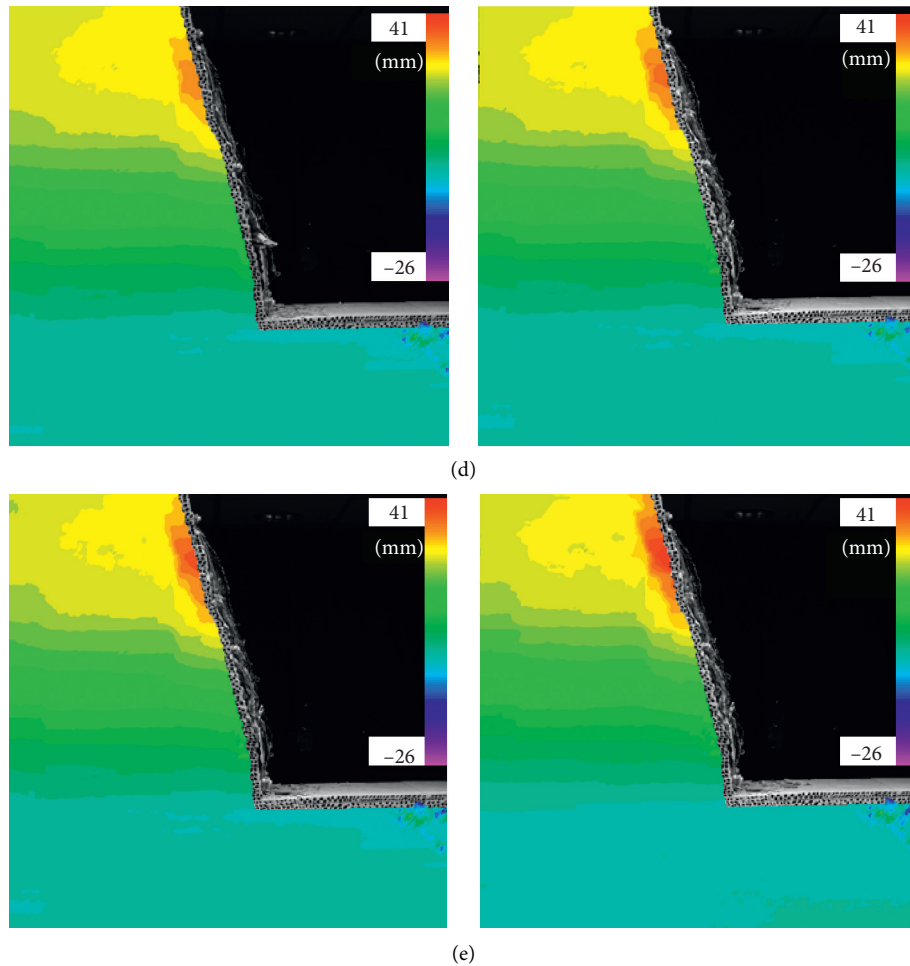

(b)

(c)

FIGURE 16: Continued.

(d)

(e)

FIGURE 16: Displacement nephogram of slope model: (a) compaction stage: (i) prior to load application and (ii) after loading; (b) fracture generation stage: (i) prior to load application and (ii) after loading; (c) fracture propagation stage: (i) prior to load application and (ii) after loading; (d) local collapse stage: (i) prior to load application and (ii) after loading; (e) entire collapse stage: (i) prior to load application and (ii) after loading.

horizontal displacement of the model, but, after this stage, the displacement was raised slightly with the loading path. The displacement of the monitoring points A1, A2, B1, and B2 were higher than others; this indicated that the collapse was mainly concentrated in the middle and upper parts of the slope. The horizontal displacement of column A was larger than that of column B as a whole; this indicated that the closer to the slope area, the more serious the rock mass collapse. The maximum horizontal displacement of column A was 35 mm, while that of column B was 28 mm.

5. Discussion

As an important research method, the physical model test has some difficulties and limitations in quantitative research, but this method can directly reflect the real process of slope collapse under support conditions. The physical model is mainly adopted with simplified geological conditions. Although the physical model presupposes the surrounding rock joints, it is unable to simulate the joints widely distributed in the rock mass. The joint setting in the physical model will lead to some differences between the test results and the field observation results, which is one of the challenges faced by the current physical model test methods. In order to solve this problem, the model block made of similar materials is used to establish the test model, and the interface between the model blocks is used to simulate the nodes.

The model test phenomenon should well reflect the deformation of slope under the support of NPR bolt system. The failure characteristics of the slope agree well with the displacement monitoring results. Through the monitoring of NPR anchor pressure, the supporting effect is verified, especially the change rule of pressure record, which has certain reference value for rock slope collapse monitoring. The experiment reproduces the collapse process of rock slope and reveals the supporting effect of NPR anchor. In this paper, the physical model test method is proposed to provide an effective method for the study of rock slope collapse support and monitoring.
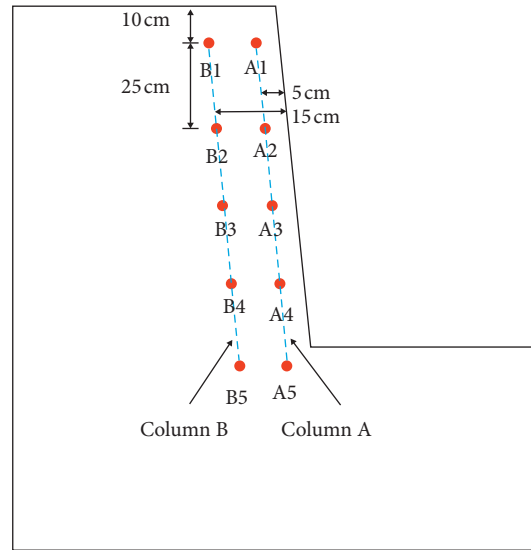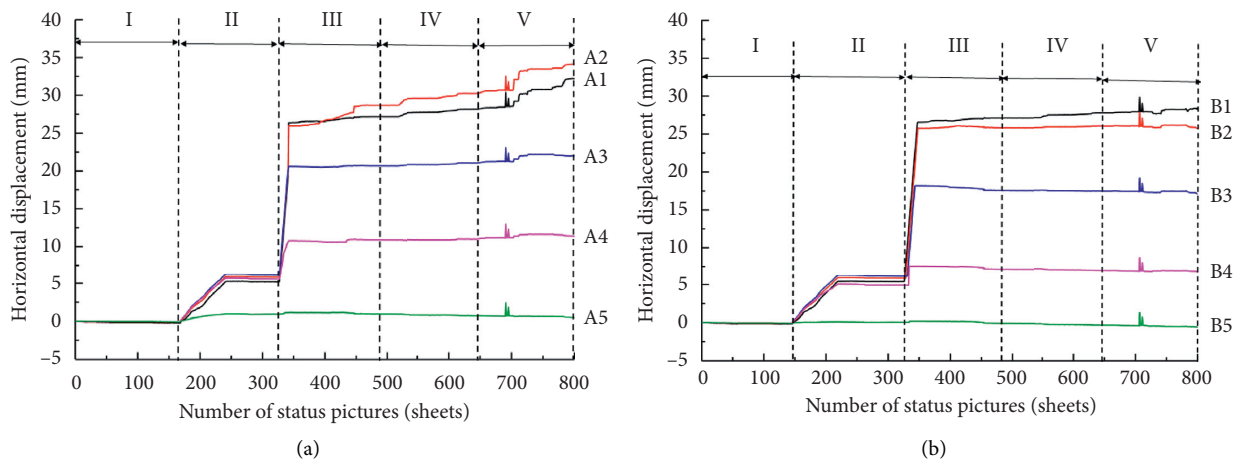
FIGURE 17: Displacement measuring points layout.

(a)

(b)

FIGURE 18: Horizontal displacement curves of displacement measuring points: (a) A1–A5 measuring points; (b) B1–B5 measuring points.

6. Conclusions

Physical model tests and pressure sensor and displacement nephogram analyses were carried out to investigate the effects of NPR bolt system, characteristics of collapse, and monitoring of rock slope. Based on the test and the numerical results, the following conclusions may be drawn:

(1) According to the analysis of the slope failure characteristics, the slope model collapse can be divided into four distinct stages: fracture generation stage, fracture propagation stage, local collapse stage, and overall collapse stage.

(2) The displacement nephogram of the slope and the displacement change trend of the monitoring points show that the displacement increases the most in the fracture propagation stage, but the surrounding rock did not collapse in an instant. Then, the displacement increased slowly until the whole slope collapsed. It

indicated that the NPR bolt had a constant resistance effect after being subjected to the instantaneous impact force, effectively preventing the instantaneous overall collapse of the surrounding rock; that realized the stable reinforcement of surrounding rock and highly reduced the potential safety hazards of rock slope collapse. Flexible anchored net absorbed the instantaneous impact force of the falling rocks, while wrapping it to prevent falling.

(3) From the comprehensive analysis of slope failure characteristics and stress records, it could be concluded that the change of pressure curve presented apparent regularity in the entire process of slope collapse and reflected the change state of the internal force of surrounding rock. The curve in section AB was decreased apparently. It means that the internal stress of rock mass changed, which was the first stage of slope collapse monitoring. The curve of section BC

presents declined sharping and then maintains a transitory stable stage. This was the second stage of collapse monitoring; this monitoring stage of slope was particularly important; this indicated that the slope was imminent collapse.

(4) Through the comprehensive analysis of model test, the new support system has good support effect on the deformation and failure of rock slope with joints and has the function of slope monitoring, which can catch the stress change of surrounding rock timely and without delay, and has high monitoring accuracy for the test slope, thus providing a theoretical basis for the support and monitoring of other similar rock slopes.

Data Availability

All data are available and have been explained in this article; readers can access the data supporting the conclusions of the study.

Disclosure

The funders had no role in the design of the study; in the collection, analyses, or interpretation of data; in the writing of the manuscript; or in the decision to publish the results.

Conflicts of Interest

The authors declare that they have no conflicts of interest.

Authors' Contributions

Zhigang Tao and Daoyong Zhu conceptualized the study; Zhigang Tao contributed to methodology; Tongxing Zhang and Weili Gong provided software; Manchao He contributed to formal analysis; Daoyong Zhu was responsible for data curation; Tongxing Zhang wrote and prepared the original draft; Zhigang Tao and Tongxing Zhang wrote, reviewed, and edited the manuscript.

Acknowledgments

References

[1] N. Wu, Z. Z. Liang, J. R. Zhou, Y. Z. Zhang, Y. Q. Hu, and X. H. Li, "Energy evolution characteristics of coal specimens with preformed holes under uniaxial compression," *Geomechanics and Engineering*, vol. 20, no. 1, pp. 55–66, 2020.

[2] G. Feng, Y. Kang, and X. C. Wang, "Investigation on the failure characteristics and fracture classification of shale under Brazilian test conditions," *Rock Mechanics and Rock Engineering*, pp. 1–16, 2020.

[3] Z. Qin, H. L. Fu, and X. X. Chen, "A study on altered granite meso-damage mechanisms due to water invasion-water loss cycles," *Environmental Earth Sciences*, vol. 78, no. 14, p. 428, 2019.

[4] N. Jiang, C. X. Wang, H. Y. Pan, D. W. Yin, and J. B. Ma, "Modeling study on the influence of the strip filling mining sequence on mining-induced failure," *Energy Science & Engineering*, pp. 1–17, 2020.

[5] A. Li, Y. Liu, F. Dai, K. Liu, and M. D. Wei, "Continuum analysis of the structurally controlled displacements for large-scale underground caverns in bedded rock masses," *Tunneling and Underground Space Technology*, vol. 97, Article ID 103288, 2020.

[6] D. Z. Ren, D. S. Zhou, D. K. Liu, F. Dong, S. Ma, and H. Huang, "Formation mechanism of the upper triassic Yanchang formation tight sandstone reservoir in Ordos basin—take Chang 6 reservoir in Jiyuan oil field as an example," *Journal of Petroleum Science and Engineering*, vol. 178, pp. 497–505, 2019.

[7] S. J. Chen, D. W. Yin, N. Jiang, F. Wang, and Z. Zhao, "Mechanical properties of oil shale-coal composite samples," *International Journal of Rock Mechanics and Mining Sciences*, vol. 123, Article ID 104120, 2019.

[8] J. Wang, P. Qiu, J. Ning, L. Zhuang, and S. Yang, "A numerical study of the mining-induced energy redistribution in a coal seam adjacent to an extracted coal panel during longwall face mining: a case study," *Energy Science & Engineering*, vol. 8, no. 3, pp. 817–835, 2020.

[9] J. Wang, J. G. Ning, P. Q. Qiu, S. Yang, and H. F. Shang, "Microseismic monitoring and its precursory parameter of hard roof collapse in longwall faces: a case study," *Geomechanics and Engineering*, vol. 17, no. 4, pp. 375–383, 2019.

[10] N. Zhang, W. Liu, Y. Zhang, P. Shan, and X. Shi, "Microscopic pore structure of surrounding rock for underground strategic petroleum reserve (SPR) caverns in bedded rock salt," *Energies*, vol. 13, no. 7, p. 1565, 2020.

[11] X. Wang, W. Yuan, Y. T. Yan, and X. Zhang, "Scale effect of mechanical properties of jointed rock mass: a numerical study based on particle flow code," *Geomechanics and Engineering*, vol. 21, no. 3, pp. 259–268, 2020.

[12] H. Huang, T. BabadagliLin, X. Chen, H. Li, and Y. Zhang, "Performance comparison of novel chemical agents for mitigating water-blocking problem in tight gas sandstones," *SPE Reservoir Evaluation & Engineering*, pp. 1–9, 2020.

[13] G. Harry, "Design of reinforcing piles to increase slope stability," *Canadian Geotechnical Journal*, vol. 32, no. 5, pp. 808–818, 1995.

[14] G. B. Shi, J. H. Yang, S. X. An, and N. Li, "Collapse mechanism analysis of steep-high rock slope of Shiquan hydropower station and reinforcement design," *Rock and Soil Mechanics*, vol. 7, pp. 1186–1192, 2004, in Chinese.

[15] J. Y. Dong, J. H. Yang, F. Q. Wu, D. Wang, and G. X. Yang, "Research on collapse of high cutting slope with horizontal soft-hard alternant strata in Three Gorges reservoir area," *Rock and Soil Mechanics*, vol. 31, pp. 151–157, 2010, in Chinese.

[16] P. Lin, X. Liu, W. Zhou, R. Wang, and S. Wang, "Cracking, stability and slope reinforcement analysis relating to the Jinping dam based on a geomechanical model test," *Arabian Journal of Geosciences*, vol. 8, no. 7, pp. 4393–4410, 2015.

[17] M. C. He, C. Li, W. L. Gong, L. R. Sousa, and S. L. Li, "Dynamic tests for a constant-resistance-large-deformation bolt using a modified SHTB system," *Tunnelling and Underground Space Technology*, vol. 64, pp. 103–116, 2016.

[18] Q. Wang, M. C. He, J. Yang, H. K. Gao, B. Jiang, and H. C. Yu, "Study of a no-pillar mining technique with automatically formed gob-side entry retaining for longwall mining in coal

mines," *International Journal of Rock Mechanics and Mining Sciences*, vol. 110, pp. 1–328, 2018.

[19] Z. G. Tao, C. Zhu, X. H. Zheng, and M. C. He, "Slope stability evaluation and monitoring of Tonglushan ancient copper mine relics," *Advances in Mechical Engineering*, vol. 10, pp. 1–16, 2018.

[20] Z. Tao, Y. Wang, C. Zhu, H. Xu, G. Li, and M. He, "Mechanical evolution of constant resistance and large deformation anchor cables and their application in landslide monitoring," *Bulletin of Engineering Geology and the Environment*, vol. 78, no. 7, pp. 4787–4803, 2019.

[21] M. He, W. Gong, J. Wang et al., "Development of a novel energy-absorbing bolt with extraordinarily large elongation and constant resistance," *International Journal of Rock Mechanics and Mining Sciences*, vol. 67, pp. 29–42, 2014.

[22] W. L. Gong, J. Wang, Y. X. Gong, and P. Y. Guo, "Thermography analysis of a roadway excavation experiment in 60° inclined stratified rocks," *International Journal of Rock Mechanics and Mining Sciences*, vol. 60, pp. 134–147, 2013.

[23] Y. Zhang, S. J. Cao, N. Zhang, and Z. Z. Zhao, "The application of short-wall block backfill mining to preserve surface water resources in northwest China," *Journal of Cleaner Production*, vol. 261, pp. 57–68, Article ID 121232, 2020.

[24] F. Huang, H. Zhu, Q. Xu, Y. Cai, and X. Zhuang, "The effect of weak interlayer on the failure pattern of rock mass around tunnel—scaled model tests and numerical analysis," *Tunnelling and Underground Space Technology*, vol. 35, pp. 207–218, 2013.

[25] P. F. Shan and X. P. Lai, "An associated evaluation methodology of initial stress level of coal-rock masses in steeply inclined coal seams, Urumchi coal field, China," *Engineering Computations*, vol. 37, no. 6, pp. 2177–2192, 2020.

[26] S. J. Friedmann, N. Taberlet, and W. Losert, "Rock-avalanche dynamics: insights from granular physics experiments," *International Journal of Earth Sciences*, vol. 95, no. 5, pp. 911–919, 2006.

[27] A. K. Alzo'ubi, C. D. Martin, and D. M. Cruden, "Influence of tensile strength on toppling failure in centrifuge tests," *International Journal of Rock Mechanics and Mining Sciences*, vol. 47, no. 6, pp. 974–982, 2010.

[28] F. Bourrier, F. Berger, P. Tardif, L. Dorren, and O. Hungr, "Rockfall rebound: comparison of detailed field experiments and alternative modelling approaches," *Earth Surface Processes and Landforms*, vol. 37, no. 6, pp. 656–665, 2012.

[29] L.-q. Li, N.-p. Ju, S. Zhang, X.-x. Deng, and D. Sheng, "Seismic wave propagation characteristic and its effects on the failure of steep jointed anti-dip rock slope," *Landslides*, vol. 16, no. 1, pp. 105–123, 2019.

[30] Q. Wang, B. Jiang, R. Pan et al., "Failure mechanism of surrounding rock with high stress and confined concrete support system," *International Journal of Rock Mechanics and Mining Sciences*, vol. 102, pp. 89–100, 2018.

[31] M. C. He and Z. B. Guo, "Mechanical property and engineering application of anchor bolt with constantre-sistance and large deformation," *Chinese Journal of Rock Mechanics and Engineering*, vol. 33, pp. 1297–1308, 2014, in Chinese.

[32] Z. G. Tao, Z. Zhu, W. S. Han et al., "Static tension test and the finite element analysis of constant resistance and large deformation anchor cable," *Advances in Mechanical Engineering*, vol. 10, no. 12, Article ID 1687814018810638, 2018.

[33] S. P. Ma, X. H. Xu, and Y. H. Zhao, "The GEO-DSCM system and its application to the deformation measurement of rock materials," *International Journal of Rock Mechanics and Mining Sciences*, vol. 41, no. 3, pp. 411–412, 2014.

[34] F. Hild and S. Roux, "Digital image correlation: from displacement measurement to identification of elastic properties—a review," *Strain*, vol. 42, no. 2, pp. 69–80, 2006.

[35] B. Pan, K. M. Qian, H. M. Xie, and A. Asundi, "Two-dimensional digital image correlation for in-plane displacement and strain measurement: a review," *Measurement Science and Technology*, vol. 20, no. 6, pp. 1–17, 2009.

[36] Y. Yu and S. T. Acton, "Speckle reducing anisotropic diffusion," *IEEE Transactions on Image Processing: A Publication of the IEEE Signal Processing Society*, vol. 11, no. 11, pp. 1260–1270, 2002.